

COMBUSTION DYNAMICS OF ORGANIC- GELLANT-LADEN ETHANOL FUELS

Ph.D. Thesis

By

JANMEJAI SHARMA

2006103002



**DEPARTMENT OF MECHANICAL ENGINEERING
INDIAN INSTITUTE OF TECHNOLOGY INDORE**

JUNE 2023

COMBUSTION DYNAMICS OF ORGANIC- GELLANT-LADEN ETHANOL FUELS

A THESIS

*Submitted in partial fulfillment of the
requirements for the award of the degree*

of

DOCTOR OF PHILOSOPHY

by

JANMEJAI SHARMA

2006103002



**DEPARTMENT OF MECHANICAL ENGINEERING
INDIAN INSTITUTE OF TECHNOLOGY INDORE**

JUNE 2023



INDIAN INSTITUTE OF TECHNOLOGY INDORE

I hereby certify that the work which is being presented in the thesis entitled **COMBUSTION DYNAMICS OF ORGANIC-GELLANT-LADEN ETHANOL FUELS** in the partial fulfillment of the requirements for the award of the degree of **DOCTOR OF PHILOSOPHY** and submitted in the **DEPARTMENT OF MECHANICAL ENGINEERING, INDIAN INSTITUTE OF TECHNOLOGY INDORE**, is an authentic record of my own work carried out during the time period from August 2020 to June 2023 under the supervision of **Dr. ANKUR MIGLANI**, Associate Professor, Department of Mechanical Engineering.

The matter presented in this thesis has not been submitted by me for the award of any other degree of this or any other institute.

Sharma
21-NOV-2023.

JANMEJAI SHARMA

This is to certify that the above statement made by the candidate is correct to the best of my knowledge.

ankur
21 Nov. 2023

Dr. ANKUR MIGLANI

JANMEJAI SHARMA has successfully given his/her Ph.D. Oral Examination held on

ankur
21 Nov. 2023

Dr. ANKUR MIGLANI

ACKNOWLEDGEMENT

*“No one who achieves success does so without acknowledging the help of others.
The wise and confident acknowledge this help with gratitude.”*

- *Alfred North Whitehead*

It is a well-known fact that no matter how big or small the work is, it takes not only effort but also the assistance of many people to achieve its fruition. During the endeavor of my Ph.D. research, there are many people who are steppingstones in the quest for success. Their support is undeniably crucial, and I am forever grateful and obliged to have these people in my ventures.

To begin with, I would like to convey my sincere regards to my mentor Dr. Ankur Miglani for providing me the perpetual assistance and guidance during my entire journey of doctoral studies. Dr. Miglani not only mentored me regarding the crucial aspects of research but also taught me various life skills for which I am, and I will be forever obliged to him. Dr. Miglani apart from being a person of tremendous technical acumen has a congenial personality which was an asset in carrying out vital discussions and research effectively. I am destitute of words to convey my gratitude to my mentor who has not only helped me in achieving various technical skills but also shaped my personality in uncountable ways. Dr. Miglani is one of a kind, and I am so fortunate that he is my Ph.D. supervisor. He is and will always remain a role model in my life. Thank you so much for everything.

I am also grateful to our collaborators Dr. Jerin John (Concordia University, Montreal, Quebec, Canada) and Dr. Purushothaman Nandagopalan (Hindustan University, Chennai, Tamil Nadu, India) for providing their critical and insightful inputs during the research.

I want to convey my gratitude to the PSPC members Dr. Pavan Kumar Kankar and Dr. Bhargav Vaidya for their crucial insights during the assessment of this research work.

I am also thankful to Dr. Eswara Prasad Korimilli, Dr. Vinod Kumar, and Dr. Indrasen Singh whose teachings that I inculcated during the MTech helped me in my doctoral work.

I would like to express my gratitude to my family away from home i.e., my friends which include Dr. Abhinav Sharma, Dr. Vinod Singh Thakur, Dr. Nagendra Singh Ranawat, Dr. Jatin Prakash, Mr. Bhupendra, Mr. Dnyanesh Mirikar, Mr. Rahul Suryawanshi, Mr. Prince Kaushik, Mr. Nishchay Saurabh, Mr. Rajat Kumar, Mr. Aaditya Gaur, Mr. Niteen Sapkal, Mr. Anoop K R, Mr. Isparsh Chauhan, Mr. Sourav Jha, Mr. Aayush Pathak, Mr. Anshul Choudhari, Mr. Sushil Bagle, Mr. Shrish Tiwari, Mr. Rishabh Gupta and Mr. Yogendra Sharma for their support during the entire journey.

I want to convey my regards to our lab manager Mr. Suresh Bhagore for aiding me in the official matters.

I am thankful to my flat mates Mr. Manish Badole, Mr. Pradyuman Kumar Arya, Mr. Hari Narayanan Vasavan, and Mr. Vivek Rana for their help and support.

I want to convey my thanks to my family for their indomitable support which includes my grandfather Shri Bhawani Shankar Sharma, father Shri Gyanendra Sharma, uncle Shri Girjesh Sharma, Aunt Shrimati Kriti Sharma, Annu, brother Bhanujai Sharma, and sister Vaibhavi Sharma.

Lastly, I want to convey sincere regards to IIT Indore for providing me with the learning experience of a lifetime.

Janmejai Sharma

DEDICATION

I would like to dedicate this work to my mother Late Mrs. Sushma Sharma, my father Late Mr. Gyanendra Sharma, brother Late Tilak Sharma, my supervisor, family, friends, country, and almighty God.

ACRONYMS

TGA	Thermogravimetric Analysis
DTG	Derivative Thermogravimetry
DSC	Differential Scanning Calorimetry
SEM	Scanning Electron Microscopy
HPMC	Hydroxypropyl Methylcellulose
MC	Methylcellulose
HTPB	Hydroxy-Terminated Polybutadiene
DCPD	Dicyclopentadiene
ICBMs	Intercontinental Ballistic Missiles
UDMH	Unsymmetrical Dimethyl Hydrazine
MMH	Monomethyl Hydrazine
IRFNA	Inhibited Red-Fuming Nitric Acid
TMEDA	Tetramethyl Ethane Diamine
DMAZ	Dimethyl Ethanamine Azide
WFNA	White-Fuming Nitric Acid
RFNA	Red-Fuming Nitric Acid
JP	Jet Propellant
NTO	Nitrogen Tetroxide
HPC	Hydroxypropyl Cellulose
UDMH	Unsymmetrical Dimethyl Hydrazine
PLIF	Planar Laser-Induced Fluorescence

DC	Direct Current
CWT	Continuous Wavelet Spectra
DI	De-Ionized
HED	Holistically Nested Edge Detection
CNN	Convolutional Neural Network
AR	Aspect Ratio
K-H	Kelvin-Helmholtz
BSE	Backscatter Electron
NP	Nanoparticles
EDX	Energy-Dispersive X-Ray Spectroscopy
AMMO	Azidomethyl-S-Methyloxetane
LiF	Lithium Fluoride
NMMO	3-Nitramethyl-3-Methyloxene
GAP	Glycidyl Azide Polymer
GOX	Gaseous Oxygen
OFB	Opposed Flow Burner
ADD	Agency of Defense Development
ID	Inner Diameter
SEF	Solidified Ethanol Fuels

NOMENCLATURE

ε	Angular ray deflection
n	Refractive index
ρ	Density of the medium
k	Gladstone-Dale coefficient
A_p	Projected area of the gel droplet
D	Diameter of gel droplet of equivalent projected area
C	Centroid of gel droplet
AR	Aspect ratio
H_{max}	Maximum height of gel droplet
W_{max}	Maximum width of gel droplet
c	Gel droplet circumference
t_a	Active jetting period
t_{ia}	Inactive jetting period
f_{cycle}	Oscillation frequency
A_{OVR}	Overlapping rupture area between successive cycles
A_{TCAS}	Total rupture area of the cascade
t_b	Gel droplet lifetime
T	Instantaneous temperature
T_g	Glass transition temperature
T_m	Melting temperature
\dot{r}_b	Regression rate

ρ_b	Bulk density
G_{ox}	Oxidizer mass flux
Δx	Burnout length
Δt	Burning duration
Re	Reynolds Number
\dot{r}_{gas}	Gasification rate
\dot{r}_{ent}	Entrainment rate
$\dot{r}_{o_{SEF}}$	Regression rate of solidified ethanol fuel
\dot{r}_{jet}	Regression rate due to active jetting

TABLE OF CONTENTS

ACKNOWLEDGEMENT.....	I
ACRONYMS.....	V
NOMENCLATURE.....	VII
LIST OF FIGURES	XIII
LIST OF TABLES	XXIII
ABSTRACT.....	XXV
LIST OF PUBLICATIONS.....	XXVII
CHAPTER 1: INTRODUCTION.....	1
1.1 Rockets and propulsion technology: Brief history and overview	1
1.2 Gelled fuels: Background and Overview	6
1.3 Gel Propellants: An Outlook.....	9
1.3.1 Gel propellants vs Liquid propellants	9
1.3.2 Gel propellants vs Solid propellants	10
1.4 The Organization of Thesis.....	11
CHAPTER 2: LITERATURE REVIEW	13
2.1 Literature Review.....	13
2.2 Objectives of the Thesis.....	21
CHAPTER 3: EXPERIMENTAL METHODOLOGY	25
3.1 Fuel formulation.....	25
3.2 Experimental setup.....	26
3.2.1 The Droplet Imaging using ultra-high-speed camera	26
3.2.2 The Flame Scale Imaging using Schlieren.....	27

3.3 Computation of geometric parameters	32
3.3.1 Droplet Scale geometric parameter extraction	32
3.3.2 Flame Scale geometric parameter extraction	36
3.4 Thermoanalytical methods	39
3.4.1 Thermogravimetric analysis (TGA) and Derivative thermogravimetry (DTG).....	39
3.4.2 Differential scanning calorimetry (DSC).....	39
3.5 Scanning electron microscopy (SEM): Combustion residue analysis	40
CHAPTER 4: DYNAMICS OF VAPOR JETTING.....	41
4.1 Introduction.....	42
4.2 Results and Discussion.....	45
4.2.1 Jetting Modes	48
4.2.2 Jetting Events	51
4.2.3 Effect of the gellant type on the jetting events.....	62
4.3 Conclusions.....	67
CHAPTER 5: COMBUSTION STAGES OF ORGANIC-GELLANT-LADEN FUEL DROPLETS	69
5.1 Introduction.....	70
5.2 Results and Discussion.....	74
5.2.1 Stage I: Transient heat up	74
5.2.2 Stage II: Disruptive Burning	75
5.2.3 Stage III: Carbonization	84
5.2.4 Bulk motion of gel fuel droplets: Centroidal Shift.....	88
5.2.5 Effect of droplet rupture due to jetting at flame scale.....	90
5.2.6 Burn rate estimation of combustion stages	93
5.2.7 Combustion residue characterization	95
5.3 Conclusions.....	99

CHAPTER 6: TIME-VARYING OSCILLATORY RESPONSE DURING DISRUPTIVE BURNING PHASE	105
6.1 Introduction.....	106
6.2 Results and Discussion	109
6.2.1 Data Reduction	109
6.3 Conclusions.....	121
CHAPTER 7: EVOLUTION OF THE GELLANT SHELL	123
7.1 Introduction.....	123
7.2 Results and Discussion	125
7.3 Conclusions.....	132
CHAPTER 8: REGRESSION RATE ANALYSIS OF SOLIDIFIED ETHANOL FUELS FOR HYBRID ROCKETS.....	133
8.1 Introduction.....	134
8.2 Materials and Methods.....	138
8.2.1 Materials	138
8.2.2 Fuel Formulation.....	140
8.2.3 Opposed Flow burner test rig for linear regression rate studies	143
8.3 Results and Discussion	145
8.3.1 Regression rate measurements.....	145
8.3.2 Regression behavior of nano-Al laden solid fuels	151
8.4 Conclusions.....	156
CHAPTER 9: CONCLUSIONS & FUTURE SCOPE	159
9.1 Major Conclusions	159
9.1 Future Scope	161
REFERENCES.....	165

LIST OF FIGURES

Figure 2. 1. Schematic representation of combustion behavior of organic gel fuels.
 14

Figure 3. 1. Schematic representation of the setup with its detailed components used for studying the droplet scale dynamics of the gel fuels during the combustion.
 27

Figure 3. 2. (Top) Diagrammatic representation of the test facility showing the top view of dual-mirror Z-type Schlieren system for characterization of the jetting behavior of the gel fuels during combustion. **(Bottom)** The orthographic view of the test facility for flame visualization..... 30

Figure 3. 3. Effect of the knife-edge position on the Schlieren image..... 31

Figure 3. 4. A representative image of a flame distortion event. At $t=0\text{ms}$ is the steady flame with the gel droplet at its center (**O**). At $t= 5\text{ms}$ **(a)** jet of length initiates and impacts the flame. At $t=9\text{ms}$ **(b)** flame distortion initiates. At $t=10\text{ms}$ **(c)** flame distorts further and jetting diminishes. Therefore, jet velocity is given as $v = R\Delta t$ where R is the length of the jet impacting the flame periphery and Δt is the duration of the jet impacting the flame periphery. The scale bar equals 2 mm.
 32

Figure 3. 5. (A) Sequential steps for processing of droplet image when no jetting or rupture takes place. (a.) HED-based non-binary image (b). Color thresholding and droplet localization. (c) Morphological transformation, (d). Parameter extraction. **(B)** Sequential steps for processing of droplet image when jetting or rupture takes place. (a). HED-based non-binary image for a droplet rupture event, (b). Color thresholding and droplet localization. (c). Convex hull operation, (d). Parameter extraction. 35

Figure 3. 6.A sequential method of image processing for extraction of the flame perimeter from the raw Schlieren images. 38

Figure 4. 1. High-magnification images (**top**) and the accompanying schematic representations (**bottom**) of the precursor events that lead to the initiation of jets. (a) Formation of gellant crust/shell and bubble nucleation, (b) bubble growth and droplet expansion (**b1**: initial bubble growth, **b2**: bubble expansion occupying large droplet vapor fraction, and **b3**: swelled droplet state prior to rupture, and (c) shell rupture and jetting of unreacted fuel vapors (**c1**: formation of rupture site, and **c2**: expansion of rupture site due to viscoelastic nature of the gellant shell. The scale bar equals 1 mm. 47

Figure 4. 2. High-speed images showing a representative jetting event and its interaction with the droplet flame envelope. The scale equals 10 mm. 48

Figure 4. 3. A classification chart showing the jetting modes and events that govern the combustion behavior of organic-gellant-laden gel fuel droplets. 49

Figure 4. 4. Rupture sequence of a combusting gel fuel droplet undergoing oscillatory bursting. The scale bar equals 1mm. 50

Figure 4. 5. High-magnification images showing the random bursting of a burning gel fuel droplet. (a). Gel droplet with the gellant shell. (b) Bubble nucleation on the inside surface of the gellant shell. (c,d) Bubble growth inside the droplet. (e) Initiation of droplet burst at a single rupture site. (f) Droplet bursting at multiple random locations. The resultant jetting and its interaction with the flame envelope are shown on the right. The red arrows indicate the directions of jetting at the droplet and flame scale respectively. The scale bar equals 1 mm for the droplet images and 10 mm for the flame image. 51

Figure 4. 6. (Top) Time-frozen snapshots of a jet causing flame distortion. The scale equals 12 mm. **(Bottom)** Temporal variation in the normalized flame perimeter characterizing the flame envelope disruption. Each point in the plot corresponds to the respective image in the top figure. 54

Figure 4. 7. (Top) Time-frozen snapshots of a jet forming a fire ball outside the flame envelope. The scale bar equals 5 mm. **(Bottom)** Temporal variation in the normalized flame perimeter for characterizing the flame envelope disruption. Each point in the plot corresponds to the respective image in the top figure. 55

Figure 4. 8. (Top) Time-frozen snapshots of a jet breaking the flame front. The scale bar equals 10 mm. **(Bottom)** Temporal variation of the normalized flame perimeter for characterizing the flame envelope disruption. Each point in the plot corresponds to the respective image in the top figure..... 56

Figure 4. 9. (Top) Time-frozen snapshots of a double-jet event comprising two flame distortion events aligned at two different angular locations. The scale bar equals 15mm. **(Bottom)** Temporal variation of the normalized flame perimeter characterizing the flame envelope disruption. 57

Figure 4. 10. (Top) Time-frozen snapshots of a triple-jet event comprising two fire balls and one flame distortion event, each aligned at a different angular location. The scale bar equals 20 mm. **(Bottom)** Temporal variation of the normalized flame perimeter for characterizing the flame envelope disruption. 58

Figure 4. 11. Time-frozen snapshots of multiple jetting events caused by the random bursting of a gel fuel droplet. The scale bar equals 5 mm. 59

Figure 4. 12. Temporal variation of the normalized flame perimeter resulting from the disruption caused by a random bursting event with multiple jets..... 60

Figure 4. 13. The variation in the jet velocities as a function of time during the combustion of a gel fuel droplet: **(a)** HPMC-3 and **(b)** MC-9. The range of the velocities (vertical double-headed arrows) is shown for all three jetting events and are color-coded as black for the flame distortion events, blue for fireball events, and red for pin ejection events, alongside their average values (horizontal dotted lines) to show the range over which the jet velocities are distributed. 63

Figure 4. 14. (a) Histograms showing a one-to-one comparison of the variation in the average velocities of three types of jetting events for both the gel fuels. **(b)** The number of each type of jetting event (flame distortion, pinhole ejection, and fireball) for both the gel fuels. 64

Figure 4. 15. Representative images of rupture site (dashed red circle) formation during a jetting event: **(a)** HPMC-3, **(b)** MC-9. The scale equals 1 mm..... 66

Figure 5. 1. Combustion stage characterization based on droplet diameter and time histories for ethanol-based gel fuels droplet of **(A)**. HPMC-3% **(B)** MC-9 %..... 75

Figure 5. 2. Bursting dynamics of a precursor transient burst event for ethanol based HPMC-3% gel fuel. **(a)** Swollen droplet at $t= 0$ ms. **(b to c)** localization of bubbles at the preferential site $t=5$ to 18ms. **(d)** Sudden rupture due to drastic pressure build-up and beginning of precursor transient burst at $t=23$ ms. **(e to f)** Initiation and progression of burst from multiple locations at $t= 25$ and 26ms respectively of the ruptured gellant shell (red arrows). **(g to h)** Beginning of formation of shell following shell retraction from $t=30$ to 33ms. **(i)** Completely recovered gellant shell after the precursor random burst. At $t=40$ ms. The scale bar equals 0.7 mm. 79

Figure 5. 3. Temporal variation of droplet diameter during a precursor transient burst in sync with the bursting dynamics for ethanol-based HPMC-3% gel fuel. 80

Figure 5. 4. (Top) Bursting dynamics of a precursor transient burst ethanol-based MC-9% are as follows: **(a)** swollen droplet state at $t=0$ ms. **(b)** Initiation of burst at $t=4.5$ ms (red arrows). **(c)** Rupturing of droplet causing it to open at $t= 5$ ms. **(d to e)** retraction of the gellant shell at the site of the rupture at $t= 5.5$ to 6ms. **(f)**. Complete closure of the rupture site at $t= 7$ ms. The scale bar equals 1mm. 81

Figure 5. 5. Temporal variation of droplet diameter during a precursor transient burst in sync with the bursting dynamics for ethanol-based MC-9% gel fuel..... 81

Figure 5. 6. Sequential progression of jetting due to oscillatory rupture cascades consisting of 6 bursting cycles of HPMC-3% based ethanol gel fuel droplet fuel. The corresponding schematic of each image is shown beneath for clarity. Out of the 6 cycles, the first 2 cycles **(a to f and g to l respectively)** have been represented. Cycle 1 **(a)** Swelling of droplet due to pressure surge $t=0$ ms. **(b)** Formation of a jet hole at $t=3$ ms. **(c to e)** retraction of jet hole at $t=5.5$ ms to 10ms. **(f)** complete shell recovery and closure of the jet hole and inflation of droplet begins $t=12$ ms. **(g)** The onset of cycle 2 at $t= 18$ ms **(h)** formation of the jet hole at $t=20$ ms. **(i to k)** retraction of the jet hole at $t=22$ ms and 24ms respectively **(l)**. Complete closure of hole and further initiation pressure build-up for subsequent rupture cycles $t=30$ ms. The scale bar represents 1mm. 82

Figure 5. 7. Dynamic rupture sequence of single burst for ethanol based HPMC-3% gel fuel. **(a)** Swelled droplet at $t= 0$ ms **(b)** Creation of rupture site to release

pressure via jetting $t=7$ ms. **(c to e)** Initiation of hole retraction from $t=14$ to 24ms. **(f)**. Complete closure of hole at $t=30$ ms. The scale bar equals 0.7mm..... 83

Figure 5. 8. Representative Image sequence demonstrating the double bursting of HPMC-3% gel droplets causing double jets. **(a)** gel fuel droplet at the initial position with a pre-existing hole at $t=0$ ms. **(b)** Rupture initiation and formation of two simultaneous holes for jetting at $t=4$ ms. **(c to e)** initiation of hole closure via retraction at $t=7$ to 14 ms **(f)**. closure of the holes at $t= 25$ ms. The scale bar equals 0.7mm. 83

Figure 5. 9.The dynamic single burst sequence for MC-9% follows: **(a)**. Inflated droplet state at $t= 0$ ms. **(b)**. Starting of rupture at $t=1$ ms (black dashed circle). **(c)**. Initiation of jetting hole $t=6$ ms. **(d & e)** hole retraction at $t =13$ and 14ms. **(f)**. complete closure of hole at $t= 16$ ms. The scale equals 0.5mm..... 84

Figure 5. 10. The carbonization sequence of HPMC-3% ethanol-based gel fuel shows the sequential progression of the carbonization front. **(a)**. The gellant shell has a localized appearance of carbonaceous regions along with hard-striated and soft regions in coexistence at $t=0$ ms. **(b)**. Formation of the jet hole at $t= 1.7$ ms. **(c)**. Initiation of hole closure via retraction at $t=2.1$ ms. **(d to e)** Hole closure continues at $t= 2.5$ to 3.3ms. **(f)** Closure of hole at $t= 3.3$ ms. The scale bar equals 1 mm. .. 86

Figure 5. 11.The bursting dynamics of the carbonization sequence for MC-9% ethanol-based gel fuel is represented as **(a)**. The appearance of the localized carbonaceous region at $t=0$ ms. **(b to c)**. Growth of the carbonization front $t= 160$ and 212ms respectively. **(d)**. Formation of the jet hole at $t=380$ ms. The scale bar equals 1 mm. 86

Figure 5. 12. **(Top)** The TGA **(A)** and DTG **(B)** thermograms for HPMC-3 gel fuel. **(Bottom)** The TGA **(C)** and DTG **(D)** thermograms for MC-9 gel fuel. In both cases, gel fuel samples were subjected to a heating rate of $10^{\circ}\text{C}/\text{min}$ in an inert nitrogen atmosphere..... 87

Figure 5. 13. Dynamic spreading of the area swept (A_s) by the droplet centroid due to jetting induced bulk motion. The spreading area is shown across the three stages of combustion during the droplet lifespan (t_b) for **(A)**. HPMC-3% **(B)** MC-9 %. 88

Figure 5. 14. Histograms of variation of velocities of flame disruptions caused by jetting during the individual combustion stages of ethanol-based HPMC-3% and MC-9% gel fuels. 92

Figure 5. 15. The temporal variation of areas of rupture sites during the combustion of ethanol-based (A) HPMC-3% and (B) MC-9% gel fuels across the combustion stages. 93

Figure 5. 16. Variation of burn rates across the combustion stage for ethanol-based (A) HPMC-3% and (B) MC-9% gel fuels. 93

Figure 5. 17. SEM micrographs showing the combustion residue during stage I of the combustion for HPMC-3% (a & b) and MC-9% (c & d). (a). Overall view showing crumpled and striated shell for HPMC-3% (122X magnification). (b). Magnified view of the striations in HPMC-3% shell (501X magnification). (c). Overall view illustrating the blistered MC-9% shell (27X magnification). (d). Magnified view of blistered MC-9% droplet surface (85X magnification). 96

Figure 5. 18. SEM micrographs showing the combustion residue during stage II of the combustion for HPMC-3% (a & b) and MC-9% (c to f). (a). Overall view showing crumpled and striated shell for HPMC-3% with jetting holes in softer regions (yellow dots) (100X magnification). (b). Bottom view of the jet holes in softer regions (yellow dot) striations in HPMC-3% shell (80X magnification). (c). Overall view illustrating the blistered MC-9% shell with jet holes. (82X magnification). (d). Magnified view of blistered MC-9% droplet surface with jet holes (white dashed rectangle) (200X magnification). (e). Overall view illustrating the MC-9% shell with jet cracks and jet holes. (35X magnification). (f). Magnified view of the MC-9% shell with jet cracks and jet holes. (200X magnification).... 97

Figure 5. 19. SEM micrographs (a & b) and EDX mapping spectra (c & d) show the representative combustion residue during stage III of the combustion for MC-9%. (a). Overall view showing carbonized porous region with jetting holes (100X magnification). (b). Magnified view of the carbonized porous region with jetting holes (dashed white rectangle) for MC-9% shell (201X magnification). (c & d). EDX surface mapping spectra of the carbonized region. 98

Figure 5. 20. SEM micrographs showing the non-homogenous thickness and hollow combustion residue for (a). HPMC-3% (180X magnification) and (b.) MC-9% (84X magnification). The red arrows represent the locations of thickness measurements along the periphery of the shell residue.	99
Figure 5. 21. Characterization of combustion stages of HPMC-3% and MC-9% gel fuel compositions.	102
Figure 5. 22 Comparison of droplet bursting modes of HPMC-3% and MC-9% gel fuel droplets.	103
Figure 6. 1.(a) Diameter time history of HPMC-based ethanol gel fuel droplet. (b) Continuous wavelet spectra (CWT) or scalogram of the diameter time signal showing frequencies for diametrical fluctuations.	112
Figure 6. 2. High-magnification images of a burning gel fuel droplet undergoing a single rupture–recovery cycle. The accompanying schematics are shown at the bottom of each image. (a1) Rupture of the gellant shell and (a2–a7) jetting of unreacted fuel vapors from the rupture site. (b) Recovery of the rupture site. (c1–c4) Bubble growth and droplet expansion. The time stamps are shown on each image, and the scale bar equals 1 mm.....	113
Figure 6. 3.(a) Spatial movement of the centroid coordinates (x_r , y_r) of rupture sites with time for each cascade. The double-headed arrows on the top show the time duration of each cascade. The vertical bars indicate the extent of spatial shifting. (b) The total distance traversed by both the centroid coordinates during each cascade.	115
Figure 6. 4. Schematic diagram showing the key geometrical parameters for analyzing the temporal evolution of the gellant shell. (a) Spatial movement of the rupture site centroid (x_r , y_r) during a single rupture–recovery cycle for a representative case. (b) The maximum rupture area of each cycle, with the rupture area overlapping between successive cycles ($A_{O,2}$ and $A_{O,3}$), and the total rupture area for the cascade ($A_{T,CAS}$).	116

Figure 6. 5. A comparison of the total rupture area for each cascade: (a) graphical representation and (b) schematic representation showing the area relative to the initial droplet area.119

Figure 6. 6. The variation of the normalized overlap area of the rupture sites (A_{OVR}/A_0) between successive cycles with each cascade. Solid bars represent the rupture site area for each cycle while the shaded bars represent the percentage overlap between successive cycles. The horizontal red dotted lines represent the average overlap for each cascade..... 120

Figure 7. 1. High-magnification representative images showing the temperature-dependent structural variation of gellant shell during the disruptive combustion of gel fuel droplet. The scale bar equals 1mm at the droplet scale and 6mm at the flame scale..... 126

Figure 7. 2. Schematic illustration depicting the variation of jetting behavior due to temperature-dependent gellant shell changes during combustion. 127

Figure 7. 3. The DSC thermograms for HPMC-3% and MC-9% gel fuel compositions depict their respective glass transition and melting temperatures. 129

Figure 7. 4. (a) Distribution of velocities of flame disruption events caused by jetting during the combustion of ethanol-based HPMC-3% and MC-9% gel fuels. **(b).** One-to-one comparison of flame disruptions events for HPMC-3% and MC-9%. 131

Figure 8. 1. Experimental test facility. (a) Schematic diagram of the flow loop for measurement of regression rates of solidified-ethanol fuel. Inset at the bottom shows the image of a MC 13 sample pressed into the quartz tube (pellet holder) for combustion experiments. Scale bar corresponds to 10 mm. 143

Figure 8. 2. The linear burning rate of HPMC 10 using gaseous oxygen at 1.95 kg/m²-s. (a) Displacement-time trace of the pellet top surface obtained from the 50-fps video, whose slope in the steady-state burning period is used to determine the regression rate (rb). (b) The corresponding burning sequence of the solidified fuel

pellet. The time stamps corresponding to images starting from left to right and top down are: 3.15s (ignition), 3.27s, 3.75s, 5.55s, 7.25s, 10.08s, 13.38s, 15.3s, 16.05s, 16.78s, 17s, 17.42s (oxidizer cut-off). 148

Figure 8. 3. Mean linear regression rate of MC and HPMC-based unloaded fuel at varying oxidizer flux conditions. 149

Figure 8. 4. Burning sequence of the HPMC 10 fuel pellet at $1.95 \text{ kg/m}^2\text{-s}$ with the accompanying schematics showing bubble formation below the melt layer. Red arrows show the key events including bubble, nucleation, growth, coalescence, and subsequent collapse to release unreacted fuel vapors in form of jets. The time stamps of the images from top to bottom and left to right in order are: 7s, 8s, 8.75s, 9s, 10s, 11s, 12s. 150

Figure 8. 5. Linear regression rate of (a) HPMC, and (b) MC based nano-Al loaded fuel at varying oxidizer flux conditions. 152

Figure 8. 6. Burning sequence of HPMC 10 Al-6 fuel pellet at an oxidizer flux of $11.7 \text{ kg/m}^2\text{-s}$ in turbulent flow regime: (a) pre-ignition, (b) ignition, (c) nano-aluminum particles/particle aggregate combustion near pellet, (d), ejection of burning particles/particle aggregates, (e) continued burning of particles/particle aggregates in end stages, and (f) extinction. The time stamps of images in order from top to bottom and left to right is 0s, 2s, 3s, 6s, 7s, 8s, 9s, 10s, 13s, 14s, 17s, 20s, 22s, 25s, 26s, 29s..... 154

Figure 8. 7.Burning sequence of HPMC 10 Al-6 fuel pellet at an oxidizer flux of $11.7 \text{ kg/m}^2\text{-s}$ in turbulent flow regime: (a) pre-ignition, (b) ignition, (c) nano-aluminum particles/particle aggregate combustion near pellet, (d), ejection of burning particles/particle aggregates, (e) continued burning of particles/particle aggregates in end stages, and (f) extinction. The time stamps of images in order from top to bottom and left to right are 0s, 2s, 3s, 6s, 7s, 8s, 9s, 10s, 13s, 14s, 17s, 20s, 22s, 25s, 26s, 29s..... 155

Figure 9. 1 Combustion dynamics of ethanol-based organic gel fuel droplets.. 162

Figure 9. 2 The combustion dynamics of solidified ethanol-based organic gel fuel tested in an opposed flow burner facility for the evaluation of regression rates. 163

LIST OF TABLES

Table 2. 1 Flow models (constitutive equations) for gel propellant rheology in shear flows.	18
Table 3. 1 Relative composition (in weight %) and yield stress of test fuels	26
Table 3. 2 Characterization of gel droplet shape variation with time.....	33
Table 4. 1 Velocities of jets of flame-disrupting events.....	52
Table 8. 1 The chemical composition, density, and yield stress of solid ethanol fuel samples both with and without aluminum nanoparticles.....	142

ABSTRACT

Modern-day aerospace propulsion systems are scaling new heights of innovation in technology and performance. Alongside performance, parameters like reusability, ease of processing, reliability, and ecological safety of fuel sources are of prime concern. Gelled propellants have the potential to replace conventional solid and liquid fuels by integrating their benefits and concurrently negating their disadvantages, therefore they are considered promising candidates for hybrid rocket and ramjet propulsion systems. The liquid propellant is widely used as either a mono or bipropellant. It is pumped/fed under pressure and an atomization system is used to spray the liquid into the combustion chamber. Thus, ease of throttle control makes liquid propellants superior to solid propellants, but they have their inherent drawbacks. A major issue to be considered with all the classes of liquid propellants is sloshing in the storage tanks. Another major disadvantage of the typical liquid propellants is the likelihood of leakage and spills during handling, this becomes a key concern specifically in the case of hazardous hypergolic liquids. Modern-day high-performance and energy-dense cryogenic liquid propellants have their utility, but they are more difficult to handle and suffer from high evaporation losses, embrittlement of the storage vessel, and difficulty in storage under zero gravity. The liquid propellant is vulnerable to accidents due to leakage during the flight or on the ground. Hence, incorporating gelling into all the above liquid propellants can nullify or mitigate these disadvantages to a certain extent. Solid propellants do not have issues with storage and handling, but they also have certain disadvantages. The solid propellants are vulnerable to impact, friction, and electrostatic discharge and are susceptible to accidental ignition. The gel propellants are relatively less sensitive to accidental ignition. Moreover, the viscoelasticity associated with the gel propellants aids during the storage and solid-to-liquid transformation within the delivery system thereby eliminating the possibility of cracks in the propellant structure and thus preventing uncontrolled combustion.

Gel propellants have proved excellent storability without settling or separation. The high viscosity of the gel fuels facilitates the stable suspension of metal additives like Boron (B), Aluminum (Al), Magnesium (Mg), etc. into the fuel matrix to increase energy density and specific impulse. Alternatively, liquid-like behavior at high shear (shear-thinning) offers thrust modulation and re-ignitability because gel fuels can be pumped with ease like liquids.

Despite the benefits, gel fuels exhibit a complex rheological and combustion behavior compared to solid/liquid counterparts due to their multi-component nature. Existing studies have hypothesized that during combustion the low-

volatility gellant separates from the gel and forms a viscoelastic shell on the droplet surface, which governs droplet vaporization and burn rate. However, this hypothesis has been limited to qualitative observations, inferred based on mainly bulk droplet temperature measurements and visualizations at ambient temperature and pressure. So far, the existing literature lacks experimental studies featuring high-fidelity diagnostic measurements at the droplet surface and at the droplet-flame scale that can provide a mechanistic understanding of the thermo-physical processes which govern the combustion behavior of gel fuel droplets.

To decipher the combustion dynamics of the gel fuels, for this study organic-gellant-laden ethanol fuels of different formulations are taken. The organic gellants are cellulose i.e., Hydroxypropyl methylcellulose (HPMC) and methylcellulose (MC). The assessment of combustion dynamics is investigated at droplet and flame scales by using ultra-high-speed imaging. The jetting dynamics at flame scale can suitably be tracked and quantified by using Schlieren imaging. The droplet scale ultra-high-speed videos provided high-fidelity evidence to demarcate the combustion into stages which are further supported by TGA and DSC. The TGA and DSC techniques are used to identify phases like carbonization and glass transition in gellant shells. Furthermore, combustion residue analysis is also carried out using SEM which provides crucial qualitative insights into the nature of shells. Apart from this, regression burn rate studies have also been done for metalized solidified gelled ethanol fuel. It is observed that these fuel formulations exhibited superior regression rates over conventional solid fuels like HTPB and DCPD. Overall, the current study provides a detailed perspective into the combustion dynamics of organic gellant-based ethanol fuels which can be beneficial in fabricating gel fuel compositions to obtain superior burn rates and to further utilize them for potential applications like sounding rockets, tactical missiles, and hybrid rocket motors.

LIST OF PUBLICATIONS

Publications from thesis work

Published journal articles:

- **Janmejai Sharma**, Ankur Miglani, Jerin John, Purushothaman Nandagopalan, Javed Shaikh, and Pavan Kumar Kankar. "Jetting Dynamics of Burning Gel Fuel Droplets." *Gels* 8, no. 12 (2022): 781.
- **Janmejai Sharma**, and Ankur Miglani. "Time-Varying Oscillatory Response of Burning Gel Fuel Droplets." *Gels* 9, no. 4 (2023): 309.
- John Jerin, **Janmejai Sharma*** (equal contribution as first author), Ankur Miglani, Purushothaman Nandagopalan, Javed Shaikh, and Seung Wook Baek. "Structural characterization and regression rate of solidified ethanol fuels for hybrid rocket applications." *Fuel* 336 (2023): 127152.
- **Janmejai Sharma**, Purushothaman Nandagopalan, Jerin John, and Ankur Miglani. "The characterization of disruptive combustion of organic gellant-laden ethanol fuel droplets." *Combustion and Flame* 257 (2023): 113018.

Journal articles under preparation

- **Janmejai Sharma**, and Ankur Miglani. "The evolution of gellant shell of burning organic gellant-laden ethanol fuel droplet". To be submitted to Applied Physics Letters
- **Janmejai Sharma**, Het Sekhalia, and Ankur Miglani. "Regression rate studies of organic gellant-laden gel fuels in an opposed burner facility". To be submitted to Combustion Science and Technology.

Publications not a part of the thesis work

- John Jerin, Purushothaman Nandagopalan, **Janmejai Sharma**, and Ankur Miglani. "Hypergolic ignition delay studies of reaction driven solidified ethanol fuels with hydrogen peroxide." To be submitted to Combustion and Flame.
 - Book chapter
- Ankur Miglani, **Janmejai Sharma**, Shravan Kumar Subramanian, and Pavan Kumar Kankar. "The Effect of Thermal Interaction Between Boiling Parallel Microchannels on Flow Distribution." In *Recent Advances in Fluid Dynamics: Select Proceedings of ICAFFTS 2021*, pp. 483-493. Singapore: Springer Nature Singapore, 2022.

CHAPTER 1: INTRODUCTION

A brief history and overview of rockets and propulsion technology are presented in this chapter. The discussion about the origins, development, and potential applications of a new category of propellants i.e., gelled propellants is done. A comparative perspective on the advantages and potential of gelled propellants to existing solid and liquid propellants is elucidated. In the end, the organization of the thesis is given in correspondence with the chapters.

1.1 Rockets and propulsion technology: Brief history and overview

Contemporary rockets and propulsion technology are an incredible culmination of human ingenuity that have its roots in the science and technology of the past. They are natural consequences of literally thousands of years of experimentation and research on rockets and rocket propulsion. One of the first successful devices to employ the principles of rocket flight was a wooden pigeon as per the writings of a Roman named Aulus Gellius. He reported that a Greek named Archytas around 400 B.C. flew a steam-propelled wooden pigeon. Around three hundred years later, another Greek named Hero of Alexandria developed a steam-propelled device called the Aeolipile that transformed the thrust produced by steam into rotary motion [1]. The first recorded military use of rockets was in 1232 A.D. during the battle of Kai-Keng between the Chinese and Mongols. It is said that the Chinese deterred the Mongol invaders with a barrage of “arrow of flying fire”. These fire arrows were one of the simplest forms of solid-propellant rocket. Its design comprised of a tube, capped at one end, which contained gunpowder. The other end of the tube was left open and was attached to a long stick. Upon the ignition of gunpowder, the rapid burning of the powder produced fire, smoke, and gas that escaped out the open end and produced a thrust. The stick acted as a simple guidance system that kept the rocket headed in one general direction during its flight [1], [2]. The Mongols following the Chinese developed their rocket-like

weapon and claimed Magyar (Hungary) in 1241 A.D. This led to the introduction of rockets to European countries and by the 13th to 15th centuries there were accounts of many rockets propelled experiments. In England, a monk named Roger Bacon improved the existing gunpowder which led to an increase in the range of rockets. In France, Jean Froissart introduced the launching of rockets from long tubes for improved flight. This idea paved the way for developing the modern-day rocket launcher. In Italy, Joanes de Fontana designed a rocket-propelled surface-running torpedo for setting enemy ships on fire. In 1591, a German fireworks maker, Johann Schmidlap invented the “step rocket” a first-of-its-kind multi-staged rocket to lift fireworks to higher altitudes. A large rocket (1st stage) carried the smaller rocket (2nd stage). During operation, when the larger rocket burned out, the smaller one continued its higher altitude before raining the sky with glowing cinders. Schmidlap’s idea is the foundation for launching modern-day rockets into outer space [1], [3], [4].

In the 17th century, the scientific foundations for modern-day rockery were laid by Sir Isaac Newton in his book named *Principia* which contains the three laws of motion. These laws provide practical insights into the working of rockets both in Earth’s atmosphere and outer space today[1], [4]. During the late 18th and early 19th centuries the revival of rockets as weapons took place. The historical account reflects the use of rocket barrages in India against the British in 1792 and 1799 by the father-son duo of Hyder Ali and Tipu Sultan. Their rockets had a range of 2-3 km which was considered exceptional at those times [5]. This caught the attention of the British military and an artillery expert Colonel William Congreve and he set out to design rockets as a weapon of war. The Congreve rockets were successful in battle due to their sheer numbers however they lacked accuracy [1], [4]. To circumvent this issue, in 1844 William Hale developed a spin stabilization technique. In this method, the escaping exhaust gases struck small vanes at the bottom of the rocket, causing it to spin like a bullet while airborne and thereby, making the rocket more stable and accurate. Modifications of this principle are still employed today for spin stabilization[1], [4].

The modern-day age of rocketry began in 1898 when a Russian school teacher, Konstantin Tsiolkovsky, proposed space exploration via rocket. A report published by Tsiolkovsky in 1903 suggested the utility of liquid propellants for rockets to attain greater range. According to Tsiolkovsky, the speed and range of a rocket were constrained only by the exhaust velocity of escaping gases. Hence, for his ideas, thorough research, and great vision, Tsiolkovsky has been named the father of modern astronautics [1], [3], [4]. Furthermore, in 1915, an American, Robert H. Goddard conducted experiments on solid fuels and estimated the exhaust velocities of the burning gases. During the operation of solid fuels, Goddard realized that to have a controlled and safe combustion, bulk solid particle fuel must be replaced. It eventually led him to test small quantities of powdered fuel in the combustion chamber. Ultimately, Goddard achieved the first successful flight with a liquid-propellant (liquid oxygen and gasoline) on March 16, 1926. The experiments in liquid-propelled rockets by Goddard continued for years. Consequently, the rockets became bigger and flew higher. Apart from this, he developed a gyroscope system for flight control and a payload compartment for scientific instruments. Therefore, for his contributions, Robert H. Goddard has been referred to as the father of modern rocketry. Similarly, another space pioneer Hermann Oberth from Germany, and a team of scientists developed the V-2 rocket which was used against London during World War II. The V-2 rocket was smaller in comparison to its modern-day counterparts. However, it achieved a thrust of 56,000 pounds which gave the rocket a maximum range of 220 miles at a speed of 3400 mph [1], [3], [4]. These performance parameters were accomplished by burning a liquid propellant which consisted of a mixture of oxygen and alcohol. This mixture was burnt at a rate of 1 ton every 7 seconds. The V-2 rocket is said to be the first ballistic missile and the world's first operational liquid-fuel rocket. However, with the defeat of Germany in World War II the unused V-2 rockets and their components were seized by the allied forces. Moreover, many German scientists defected to the United States of America and the Soviet Union which paved the way development of rocketry as military and research explorations. Eventually, with the help of defected German scientists and rocket engineers, in 1946 the United States of America began the

utilization of V-2 rockets as sounding rockets to take measurements in the atmosphere at high altitudes [6].

Since the inception of 1947, the world witnessed the Cold War between the USA and the Soviet Union. The Cold War led to unprecedented developments in rocketry which included the development of Intercontinental ballistic missiles (ICBMs), satellite launching, and sending humans to space. At first in the 1950s the USA developed three ICBMs: Redstone, Atlas, and Titan. All three ICBMs were liquid-propelled with Redstone having liquid oxygen and alcohol while Atlas and Titan were propelled by liquid oxygen and Kerosene (RP-1)[1], [4]. Eventually, the development of these ICBMs paved the way for launching astronauts into space. In the context of satellite launching and earth-orbit exploration, the Soviets were the first to incorporate the liquid-fueled (liquid oxygen and kerosene) R-7 ballistic missile to carry the Sputnik-1 satellite into the earth's orbit successfully in 1961[7]. In return, in 1969 the USA successfully launched Apollo 11 with the help of a three-staged liquid-fueled Saturn-5 rocket [1], [4]. This mission led to the first-ever moon landing and it is often coined as one giant leap of mankind. In the year 1981, NASA developed a reusable vehicle i.e., the space shuttle named Columbia. The space shuttle had solid rocket boosters containing ammonium perchlorate and aluminum. The shuttle's main engine during the launch was fueled by liquid oxygen and liquid hydrogen. The space shuttle's significant contribution was the development of the International Space Station, which remains in orbit today to conduct hundreds of science experiments annually on human health, engineering, and other matters[1], [3].

In the 21st century, rocket and propulsion technology is not confined to the countries like USA and Russia. There are various other countries and organizations like India, Japan, China, and the European Space Agency who are in pursuit of sending exploration probes and people not only to the Moon and Mars but also beyond. Private organizations like SpaceX, Orbital ATK, Virgin Galactic, and Blue Origin have also sprung up and are actively and successfully assisting the space

industry[3]. The involvement of private players has led to the introduction of the space tourism industry.

Even though rocket and propulsion technology has scaled new heights of innovation and technology, it is still marred by infamous and fatal accidents that have led to both losses of life and property. These accidents have occurred in the past due to both solid and liquid propellants. To begin with, in 1975 the Apollo-Soyuz test project (a joint venture of the U.S. and Soviet) during re-entry suffered from a malfunction of the reaction control system that controls the altitude. Consequently, the malfunctioning caused leakage of poisonous nitrogen tetroxide in the cabin which caused fatal injuries to the Apollo astronauts[8]. In 1986, the space shuttle named Challenger exploded shortly after its launch. It was the first deadly accident concerning an American spacecraft during a flight. The malfunction in the spacecraft's O-rings (rubber seals that separated its rocket boosters) caused a fire to start that destabilized the boosters and spread up the rocket itself. Consequently, Challenger's solid rocket boosters flew uncontrollably after the breakup of the external tank separated them from the shuttle stack. The disaster led to the deaths of all astronauts on board [8], [9]. Furthermore, in 2003 in Alcántara, Brazil during the lift-off, the solid fuel detonation led to a catastrophic explosion, due to which 21 people succumbed to death[10].

Apart from these, conventional solid and liquid propellants also pose a severe threat to the environment. For instance, Unsymmetrical dimethyl hydrazine (UDMH) is referred to as the "Devil's Venom" by the Soviets as it is responsible for turning a vast area of the Kazakh Steppe into an ecological disaster. The carcinogenic UDMH got soaked into the soil and rendered it dangerous for decades. In the case of solid rocket motors which are used during the lift-off typically contain ammonia and aluminum which is not eco-friendly. It has been reported that the cloud generated during the lift-off often contains reactive chemicals like hydrochloric acid and aluminum oxide. This cloud then spreads in the vicinity and severely impacts the soil water quality, aquatic life, and vegetation. There are also reports of exhaust plumes of solid rocket motors that have led to the formation of localized ozone

holes. Although these holes eventually healed, still a threat of ozone layer depletion exists in the future considering the increase in the number of space flights [11], [12].

Thus, considering the issues prevailing with currently available solid and liquid fuels there is a need to explore an alternative that is safe, reliable, eco-friendly, and has high-performance characteristics. One such promising candidate is gel fuel. A brief perspective on the development and characteristics of gel fuel is given in the subsequent section.

1.2 Gelled fuels: Background and Overview

Gelled fuels, monopropellants, and oxidizers are fluids whose rheological properties are altered by incorporating gelling agents or gellants so that they behave as solids during storage and offer superior atomization like liquid fuels when flowing under shear. Globally, multiple research and development projects are being carried out on different aspects of gel fuels and are continuously growing. In the following section, brief historical background and overview are presented.

The history of the development of gelled propellants dates to the 1930s. In 1936, Arthur B Ray in the USA patented a solidified gel fuel consisting of gellants such as silicic acid, silica, and titanitic acid while the base liquid fuels used were methanol, ethanol, and ketones. It was claimed that the gel fuel can be safely stored and transported[13]. In 1962, Claude G Long patented the use of gelled propellants analogous to solid propellants and claimed it to be potentially used for rocket motor applications. It was also claimed that the addition of micron size metal particles like aluminum, Boron, Magnesium, etc. has led to an increase in the specific impulse [14]. The thixotropic behavior of gel fuels was claimed and patented by Tarpley in the years 1969 and 1979[15], [16]. Furthermore, Mckinney and Tarpley in 1966, conducted the gelation of liquid hydrogen with the addition of ultrafine particles of lithium and lithium borohydride[17]. The gelation of hydrogen was done to improve the storability by reducing the rate of vaporization. In 1969 Rapial and

Daney [18] merged the benefits of slush hydrogen (a mixture of solid and liquid hydrogen) and hydrogen gel into slush hydrogen gel by incorporating silica (7nm size) as gellant. The program for the development of space-storable gelled propellants came to fruition in 1970. These gel propellants comprised oxygen difluoride as an oxidizer and micrometric particles of chlorine trifluoride as the gellant. The resulting gels were storable for 30 days and demonstrated extreme shear thinning behavior[19] . In the 1980s Varma and coworkers examined the gelation and rheological characteristics of hypergolic unsymmetrical dimethyl hydrazine (UDMH) and red-fuming nitric acid with methyl cellulose and sodium silicate respectively[20]–[22]. The research on gel propulsion in the later part of the 1980s was picked up by NASA and TRW[23], [24].

The studies at NASA led to the characterization of gels as non-Newtonian fluids [23]. Thus, the atomization studies of gel propellants began. The year 1999 proved to be a marquee event in the development of gel propulsion as a successful flight test conducted by TRW. The gel propellant used in this flight test had carbon-loaded gelled monomethyl hydrazine (MMH) and gelled-inhibited red-fuming nitric acid (IRFNA)[24]. In the mid-1990s and early 2000s scientific studies based on three facets of gelled propellants: rheology, atomization, and combustion were conducted at Technion, Israel [25]. All these studies provided critical insights into the development of gel propellants. For instance, the rheological properties of gel propellants proved vital in understanding the atomization which eventually led to the development of new injector designs [26], [27]. The developmental work at Rafael led to the formulation and combustion characterization at the laboratory scale for hydrazine-based gel propellants [28]. In 2000 the cooperation between DLR-Germany and Technion-Israel provided a pathway to further scientific achievements in gel propulsion technology. Research conducted by this joint venture provided an understanding of atomization regimes (formation of sheets, ligaments, threads, and droplets) dependent on rheological properties, jet velocity, and generalized Weber and Reynolds numbers[29]. The Fraunhofer Institute for Chemical Technology achieved significant advancement in gelled nitromethane which eventually led to the successful launch of a rocket by Bayern Chemie in 2009

[30]. A significant number of German efforts in the development of gel propulsion technology have appeared as proposals for applications, environmental and health impact assessment of 'green' gel propellants [31], [32]. Moreover, these studies also include the scalability of a gel propellant combustion from laboratory-scale to sounding rocket in the thrust range of 0-20 kN[33]. In Israel, hypergolic ignition of kerosene gelled with hydrogen peroxide and reactive particles was proposed. These hypergolic propellants are non-toxic, and enhanced ignition can be obtained due to gelation enabling particle suspension [34] The application of metalized gel fuel was investigated in Germany and Israel for the ramjet engine [35], [36]. This study involved the suspension of boron particles in gelled Jet A1 fuel. The theoretical potential of boron loaded Jet A1 gelled fuel-powered ramjet missile has shown superior performance in comparison to a typical aluminum-loaded solid rocket motor with the aid of bypassing air to enhance the efficiency of energy extraction [36]. This enhancement can be attributed to the longer range of the missile due to the less weight of the payload of the boron-loaded gel-fuel ramjet missile in comparison to its solid-fueled counterpart.

At the beginning of 2008 in the USA, various universities carried out basic research on gelled hypergolic fuels and oxidizers. The hypergolic fuels included monomethyl hydrazine (MMH), tetramethyl ethane diamine (TMEDA), and dimethyl ethanamine azide (DMAZ). While the oxidizers utilized were white-fuming nitric acid (WFNA), red-fuming nitric acid (RFNA), and nitrogen tetroxide. The gelation of these hypergolic fuel-oxidizer combinations was attained by fumed silica[37]–[40]. Moreover, these studies have provided key insights into the various characteristics of hypergolic gel propellants like ignition, atomization, and jet impingement. In the 21st century, studies have been conducted in different parts of the world which includes India, China, and Russia. These countries have explored different avenues of gel propellants which include formulation, atomization, flow characterization, and combustion [41]–[52]. Overall, the research carried out across the globe provides an idea about the status of the development of gel propulsion technology and future scenarios.

1.3 Gel Propellants: An Outlook

A gel is a ‘soft matter’ having a tendency to behave like a solid and liquid depending upon the level of shear. The applications of gels can be found in various fields. A gel can also be defined as a three-dimensional solid phase that encloses the liquid phase with some degree of elasticity which is its most relevant feature [53]. These properties of gel propellants enable them to merge the advantages of both solid and liquid counterparts. The advantages of gel propellants over solid and liquid propellants are discussed below:

1.3.1 Gel propellants vs Liquid propellants

Liquid propellants are often used as either monopropellant or bipropellant and possess exceptional atomization behavior. Its combustion is easier to control therefore, it also offers superior thrust control [54]. Despite the advantages, certain inherent drawbacks are needed to be addressed. For instance, conventional liquid propellants are susceptible to leakage and spillage during handling which becomes a major concern in the case of hazardous hypergolic liquids [32], [54]–[59]. The handling of cryogenic liquid propellants is a cumbersome task as they suffer from high boil-off losses, embrittlement, and storage difficulty under zero gravity [54]. Moreover, liquid propellants are vulnerable to sloshing in storage tanks[60]. The sloshing of liquid propellant caused major issues during the moon landing Apollo 11 lunar module [54]. The metal particles are often added to enhance the performance of liquid propellant, but it is observed that particle sedimentation occurs over time which invariably affects the combustion performance [61]. Liquid propellants due to their effective thrust control are also used in propelling missiles but they are vulnerable to external stimuli like heat, shock, bullet, and fragment impacts that are often encountered during operation [24], [54]. The gelation of liquid propellants in the cases can mitigate these shortcomings to an extent.

Gel propellants have demonstrated superior storage and handling characteristics in comparison to liquid propellants. Unlike liquid propellants, it enables the safe storage of hypergolic propellants due to gelation [54]. The gel propellants have

demonstrated longevity in terms of safe storage without settling or phase separation for more than 10 years [23], [24], [62], [63]. Moreover, the occurrence of phase separation takes place only at high levels of acceleration [23]. The ease of throttle control like liquid propellant can also be achieved by gel fuel due to its shear-thinning behavior [26], [27], [35], [64], [65]. The three-dimensional gelled network enables stable suspension (without sedimentation) of metal particles which enhances the specific impulse and energy density [36], [57]. Furthermore, gelation can help in damping the sloshing behavior [19], and in the case of gelled cryogenic propellants it can mitigate the evaporation losses during storage [17], [18], [54]. The use of gel propellants has shown promise as an insensitive munition and hence it can be considered as an alternative to liquid propellants in tactical missiles [24].

1.3.2 Gel propellants vs Solid propellants

Solid propellants, unlike liquid propellants, offer superior storability, handling, and transportation characteristics [55]–[57], [66]. However, solid propellants have their inherent set of disadvantages. The solid propellants are vulnerable to accidental ignition, detonation, deflagration, or thermal runaway, due to sensitivity to friction and electrostatic discharge [32]. The large-size casting of solid propellants needs rigorous manufacturing to obtain defect-free propellant grain. However, the possibility of cracks and voids always exists during manufacturing. Moreover, during operation at high temperatures these defects (cracks and voids) can severely affect the propellant structure and thereby cause uncontrolled combustion [57].

Gel propellants, on the other hand, are less sensitive to impact, friction electrostatic discharge and hence can negate the abovementioned drawbacks of solid propellants [54]. Furthermore, due to the viscoelastic nature during storage and transformation from solid-like to liquid-like during the delivery system eliminates the possibility of cracks and voids in the propellants structure and consequent uncontrolled combustion [57], [66]. The shear-thinning behavior of gel propellants enables thrust control akin to liquid propellants unlike solid propellants [67].

1.4 The Organization of Thesis

The chapter-wise organization of the thesis is as follows:

Chapter 1: It contains a brief overview of the history and overview of the development of rockets and propulsion technologies. An overview of the origins and development of the new category of propellants i.e., gel propellants is also done. A brief comparative perspective of gel propellants to conventional solid and liquid propellants is illustrated.

Chapter 2: The chapter deals with the literature survey of existing studies. It also mentions the objectives and significance of the research.

Chapter 3: In this chapter, the experimental methodology utilized to carry out the study is explained.

Chapter 4: In this chapter, the dynamics of jetting behavior of organic gel-based fuel at droplet and flame scales are studied. The visualization and assessment of jetting behavior at the flame scale are done via Schlieren Imaging.

Chapter 5: This chapter aims to investigate the disruptive combustion behavior of organic gel fuel droplets with the help of high-speed imaging at droplet and flame scales. Further, the combustion is demarcated in stages based on visual evidence from droplet scale video data.

Chapter 6: In this chapter, the time-dependent analytical assessment of the evolution of the gellant shells is done.

Chapter 7: In this chapter, the DSC (differential scanning calorimetry) is used to decipher the temperature-dependent structural changes in the gellant shell during combustion. It is seen that the gellant shell undergoes glass transition which not only affects the gellant shell bursting but also the jetting behavior.

Chapter 8: This chapter deals with the regression rate studies of solidified gelled ethanol fuel by using an opposed flow burner facility, followed by a comparison of regression rate with conventional solid fuels.

Chapter 9: It contains the key conclusions of the present study along with the future scope.

CHAPTER 2: LITERATURE REVIEW

In this chapter, a comprehensive review of the existing studies is presented on the development of gel propellants from the point of view of formulation, combustion, rheology, and atomization. Further, in this chapter, the objectives of the current study are discussed.

2.1 Literature Review

Currently, numerous studies have been conducted to assess the behavior of gel propellants from multiple aspects of fuel formulation, combustion, rheology, and atomization. In this section, a comprehensive survey of existing studies is illustrated.

To begin with, Nachmoni and Natan [68] conducted pendant droplet experiments to assess the combustion dynamics of gelled JP-5 fuel via videography. They also conducted tests to examine the variation of droplet burn rates as a function of pressure and oxygen mass fraction. It was observed that the burn rate showed an increment with an increase in pressure and oxygen mass fraction. The videography revealed the ignition and flame behavior at varying pressures. The ignition was easier at high pressures due to the smaller flame size which enabled the burning almost at the droplet surface. Furthermore, another study performed by Nachmoni and Natan in 2000 [69] gave insights into the various parameters like ignition delay, heat input for ignition, droplet temperature, and heat of vaporization as a function of gellant content and ambient pressure for JP-5 gels. They observed that due to an increase in gellant content, ignition delay, heat input for ignition, droplet temperature, and heat of vaporization increases. Furthermore, due to the increase in ambient pressure all the above parameters except droplet temperature demonstrated a decreasing trend. Solomon et.al. [70] utilized high-speed imaging to record and analyze the combustion dynamics of JP-8 metalized (boron) and non-metalized organic gel fuel droplets. It was reported that in both cases a non-

permeable elastic layer of gellant is formed which prevents the evaporation of base fuel and traps it inside it. Consequently, the fuel vapors are formed underneath the gellant layer which causes the droplet to swell. Eventually, the gellant layer ruptures and fuel vapors escape out as jets. This process occurs periodically till the end of the droplet's lifetime. This study introduced the jetting behavior of gel fuel droplets which further paved the way for the combustion characterization of organic gel fuel droplets (Figure 2.1). The research examined by Solomon et.al [71] in 2009 proposed the combustion mechanism of organic gel fuel droplets. They stated that the combustion of organic gel occurs in four stages: classic droplet combustion, phase separation of gel fuel components, viscous gellant shell formation which undergoes swelling and jetting due to subsequent rupturing, and lastly, the combustion of the gellant shell.

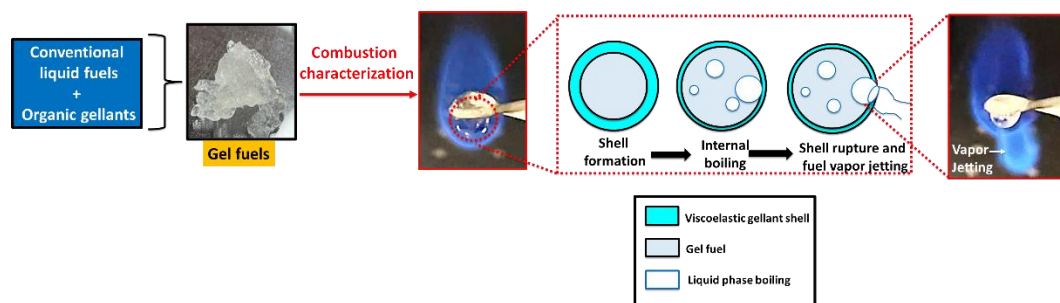


Figure 2. 1. Schematic representation of combustion behavior of organic gel fuels.

Inorganic gellants like fumed silica have also been used to formulate gel fuels. Arnold and Anderson[72] studied the rheological and combustion traits of JP-8 turbine fuel gelled with fumed silica. They reported that the gel fuel demonstrated shear-thinning behavior. Moreover, during combustion, the formation silica shell takes place which cracks and acts as a preferential site for jetting of unreacted fuel vapor. A time-dependent theoretical model for the combustion of organic gel fuel droplets was proposed by Kunin et.al.[73] which described a relationship between droplet diameter and the gellant layer formed during combustion. It was reported that the larger the droplet diameter, the thicker the gellant layer. Furthermore, due

to the bubble growth underneath, the gellant layer experiences tensile stress, and as the bubble growth increases the gellant layer reaches its tensile limit and ruptures, leading to jetting of fuel vapors.

The combustion behavior of organic and inorganic gel fuels differs substantially. One such study was conducted by Solomon et.al in 2011 [38] which investigated hypergolic organic and inorganic gel-based propellants. The base fuel used was Monomethyl hydrazine (MMH) with nitrogen tetroxide (NTO) as an oxidizer. The organic and inorganic gellant used were Hydroxypropyl cellulose (HPC) and fumed silica respectively. In both cases the gellant shell/ layer forms. However, the organic gellant (HPC) forms an elastic shell while the inorganic gellant (silica) forms a porous layer due to silica clustering. Reportedly, the organic gel fuel demonstrated typical swelling and jetting while the inorganic gel fuel had a rigid silica shell which led to micro explosions.

The studies performed by D.P. Mishra et.al. [41], [42] revealed that parameters like gellant concentration, initial droplet diameter, and ambient pressure influence burn rates. It was reported that at ambient pressure, with an increase in gellant concentration, the burn rate initially decreases and then stabilizes. This can be attributed to a decrease in the calorific value of the fuel due to an increase in the gellant concentration. Moreover, it was seen that with an increase in droplet diameter and ambient pressure, the burn rate was found to increase. Further, due to the increase in pressure a suppression in microexplosion intensity was seen due to increased diffusion resistance in the vicinity of the gel droplet. They also proposed a four-staged combustion behavior of organic gel droplets: (1) Initial transient period with phase separation. (2) Gellant layer formation, bubble nucleation, and initiation of microexplosions. (3) Vigorous microexplosion. (4) Subsequent uniform regression of the droplet. Similarly, Liu et. al[74] conducted freely falling droplet experiments for unsymmetrical dimethyl hydrazine (UDMH) gelled with organic hydroxypropyl cellulose (HPC) and reported that the combustion occurs in three distinct stages: formation of gellant layer, bubble formation and growth, vapor jetting and microexplosion. It was also reported that vapor jetting led to a horn-

shaped luminous flame. This indicated that vapor jetting causes flame disruptions. Furthermore, the researchers Cho et. al.[39], [40] investigated the disruptive burning behavior of the gel fuel droplets at the flame scale by utilizing the high-speed OH-PLIF experiments to characterize the trimodal behavior of flame-disrupting jets as: first, the jets that cause corrugations in the flame envelope. Second, the jets that cause the localized extinction of the flame envelope. Third, jets form a localized fireball outside the flame envelope. It was proposed that these jets arise from the same location recurrently which can be attributed to the weakening of the viscoelastic gellant shell during subsequent jetting.

Feng et.al.[75] investigated the burning behavior of gelled UDMH droplets in an oxidative conductive environment. Further, the assessment of burning characteristics and flame structure was also done. The combustion behavior was broken into four stages based on differences in the phenomenon: (1) Heating and swelling period. (2) Initial combustion period. (3) violent combustion period. (4) Extinguished combustion period. They reported that disruptive combustion behavior occupied nearly 70% of the burning time. Ghamari and Ratner [76] blended diesel and Jet A fuel with polybutadiene and proposed that gelation can be fruitful in the suppression of splashing behavior upon spillage and hence can improve fire safety. Research performed by Miglani et.al [47] provided mechanistic insights into the bursting and jetting behavior of ethanol-based organic gelled droplets of varying gellant concentrations. Their findings affirmed that due to the viscoelasticity of the gellant shells, volumetric fluctuations occur due to the oscillatory bursting of the gel droplets. They reported that the lower concentration of gellant exhibited an oscillatory bursting behavior in the form of rupture cascades that occurred in the same region of the droplet. On the contrary, for the high concentration of gellant, the ruptures took place at dispersed locations of the droplet surface. Cao et. al. [48] conducted studies to investigate the combustion characteristics of kerosene-based inorganic gel fuel droplets and reported a mechanism for the morphological changes of inorganic gel fuel droplets during combustion. The mechanism is characterized by stable evaporation and combustion of gel droplets, formation and rupture of bubbles, rigid silica shell formation,

exfoliation of silica shell, and combustion inside the silica shell. D.O. Glushkov et.al.[49]–[52] developed a new category of gel fuels i.e., cryogels, and conducted combustion studies in high-temperature oxidizing medium. These cryogels were laden with different additives in the form of metals (copper, iron, and aluminum) and non-metals (coal and silica). They have also reported that the cryogels exhibit disruptive combustion behavior occurring in the form of vapor jetting and microexplosions.

The gel fuels exhibit shear thinning traits which enables effective atomization like the liquid fuels. Hence, the rheological and atomization aspect of gel fuels becomes crucial in their development. The rheological properties of the gelled propellants are pivotal in deciphering the key parameters like processibility, storage life (shelf life) and flow characteristics. In practice, rocket propellants are typically a blend of two or more components. Hence, their rheological characterization is of prime concern in understanding the propellants response in real time applications by correlating them with lab scale studies [77]. Thus, from the context of application, it is important to determine the rheological parameters like yield stress and apparent viscosity (via simple shear flow) and time dependent dynamic properties using oscillation tests [46]. The physical stability of gel propellants is a key property which enables retention of solid-like phase behavior during storage or flight conditions. Yield stress is primarily dependent on strong gelation network. Further, it helps in determining the optimal mechanical strength and propellant formulation[54], [57], [67]. Several studies have been conducted which addressed these prospects. The determination of yield strength was done by Boger et.al. [78][]. They incorporated both experimental and theoretical methods for the yield stress estimation. The theoretical methods employed an extrapolative technique based on several models namely, Herschel-Bulkly (H-B), Casson, Bingham and Tsheuschner (TSCH) models [46], [67], [78].

Furthermore, the shear effects on rheology are often described with the help of theoretical models and constitutive equations. Some of the most used flow models are Oswald-de Waele ‘power law’, Herchel-Bulkly law, Cross model, Carreau

model etc. The equations in these models are written in shear viscosity (η)- shear rate ($\dot{\gamma}$) and can be further modified into an equivalent shear stress (τ)- shear rate ($\dot{\gamma}$). Oswald-de Waele ‘power law’, is one of the simplest models which relies on two constants i.e., the flow consistency index (K) and dimensionless flow behavior index ‘n’ (pseudoplasticity index). The power law can be used for modeling shear-thinning and shear-thickening fluids. For all practically useful gel propellants, $0 < n < 1$, with $n \rightarrow 1$ indicating a nearly Newtonian behavior such that $K \rightarrow \eta$ in the Newtonian sense. Similarly, $n \rightarrow 0$ indicates a dominant pseudoplasticity (shear thinning). The relation give in table 2.1 can be used to estimate the viscosity and non-Newtonian character of gel propellants. The Oswald-de Waele ‘power law’ has a drawback that for shear thinning fluids the predicted viscosity tends to zero as shear rate goes to infinity.

Table 2. 1 Flow models (constitutive equations) for gel propellant rheology in shear flows.

Flow Model	Constitutive Equation
Oswald-de Waele ‘power law’	$\eta = K\dot{\gamma}^{n-1}$
Herschel-Bulkly (H-B)	$\eta = K\dot{\gamma}^{n-1} + \eta_{\infty}$
Cross model	$\eta = \eta_{\infty} + \frac{\eta_0 - \eta_{\infty}}{1 + (a + \dot{\gamma})^m}$
Carreau model	$\eta = \eta_{\infty} + \frac{\eta_0 - \eta_{\infty}}{[1 + (a\dot{\gamma})^2]^{m/2}}$

If the flow conditions involve the effects of yield stress, then it should be taken into consideration in the flow model. In such cases Herschel-Bulkley (HB) equation models are used (Table 2.1). In HB model, the flow of a yield stress is shear thinning because the term η_0 (zero shear) is the apparent shear viscosity at the yield point. η_0 is estimated as part of a curve-fitting procedure and in its τ - $\dot{\gamma}$ form, the HB equation indirectly produces τ_{yield} .

Another flaw of the power law, which is shared by the Herschel-Bulkley model, is that the prophesied values tend to infinity at low shear rates, whereas experimentation proposes that the viscosity remains finite. This led to the advancement of more elaborate models, including the extensively used Cross and Carreau models. These models are stated in table 2.1 and, using η_0 and η_∞ , both include limiting values for the viscosity at zero and infinite shear. They further make use of the relaxation time a (in s) and the dimensionless power index 'm'. The Cross and Carreau models provide a notably better regression of the data than the other two models (Herschel-Bulkley and Oswald-de Waele 'power law'), which suggests that it is important for the model to include a parameter that limits the viscosity to a finite value at zero shear rate. Moreover, the final value predicted by the Herschel-Bulkley model for the viscosity at infinite shear rate is an unrealistic value. This highlights the limitations of this model and emphasizes that it should only be used to model the gel within the range of examined shear rates. The Carreau and Cross models, in contrast, offer more realistic values for the limit viscosity at increasing shear rates.

Viscoelasticity refers to the comparative influence of viscous and elastic components in a gel propellant. Overall, this rheological behavior is demarcated between purely elastic and purely viscous at yield point. The viscoelasticity of gel propellant not only enables ease of storage and transportation but also it aids in preventing leakage spills provided the yield point is not reached. Furthermore, the viscoelastic response at applied stress less than the yield point indicates the possibility of partial or full recovery. The viscoelasticity is often determined by loss (G'') and storage moduli (G'). The loss modulus provides an indication to the energy needed for initiation of flow irreversibly lost due to shear induced heat dissipation. Storage modulus gives an indication to store energy due to stress. The viscoelastic properties are also determined by creep-recovery experiments which provide details on approximate value yield stress from creep response of gel propellant under prolonged steady shear stress[54]. In a creep-recovery experiment the results are plotted as creep strain (γ) and time (t). The creep recovery test provides crucial insights into the viscoelasticity and response of gel propellants at time scales

analogous to actual processes. Furthermore, the assessment of creep properties provides a better understanding of the stability of gel propellants when subjected to system vibrations and combustion[46], [47].

The studies conducted by Rahimi et.al.[67] provided crucial insights into the rheological behavior of different organic and inorganic gel fuels. They proposed a generalized classification of gel propellants into three categories: Category A: pseudoplastic, shear-thinning, and low yield. Category B: Viscoelastic. Category C: yield, thixotropic. Among the three categories, A and C demonstrated superior atomization, while the difficulty in the flow behavior of B gel fuels makes them inferior for atomization. The rheological characterization of different formulations of gel fuels was done by Dennis et.al. [79]. They incorporated viscometry, yield stress, and small shear strain oscillation experiments on monomethyl hydrazine (MMH) gelled with hydroxypropyl cellulose (HPC) and fumed silica. It was proposed that HPC gels behave like linear viscoelastic liquids under a critical strain value. On the contrary, the fumed silica gel with noticeable yield stress behaves akin to a viscoelastic solid. The goal of this research was to formulate a gel fuel having measurable yield stress under low-shear conditions and shear-thinning behavior at shear rates representative of typical rocket injectors. John et.al. [46] investigated the rheological behavior of solid-like ethanol-based fuels gelled with Methylcellulose (MC) and Hydroxypropyl Methylcellulose (HPMC). The rheological studies incorporated shear flow and dynamic oscillation tests with varying concentrations of gellant and nanoparticles. It was observed that the solidified ethanol-based fuels exhibited a strong shear thinning behavior and high yield thixotropic behavior. They also proposed the utilization of these fuels for hybrid rocket engines.

Studies have been conducted to visualize and characterize the atomization of gel fuels. The impinging jet investigations done by Jejurkar et.al [43], [44] provided crucial insights into the sheet breakup of the nanoparticle-laden gel fuel. It was reported that atomization occurs in two regimes (1) open rim with holes. (2) Impact wave with longitudinal ligaments. The reason for the hole formation was attributed

to the clustering of nanoparticles which also led to recurring webbed structure. The webbed structure further disintegrated into longitudinally oriented ligaments. These sheet atomization characteristics were observed due to shear thinning and viscoelasticity. The viscosity and complex rheological properties due to gellants and particle loading can lead to poor quality of atomization and injector clogging. Therefore, to negate this issue, an optimal design of the injector is the need of the hour. Recently (2022) one such design is proposed by Li et.al. [80] which demonstrated the spray characteristics of nanoparticle-laden gel fuel. The design consists of a cone-like structure inside the nozzle which enhances the shearing rate and a gradually decreasing cross-sectional area from inlet to outlet which ensures a continuous decrease in the apparent viscosity till the nozzle outlet. Furthermore, they compared this new design of the nozzle with the conventional direct current (DC) nozzle and reported an improvement in atomization, fineness, and uniformity of the spray field for the nanoparticle-laden gel fuel.

2.2 Objectives of the Thesis

The dissertation aims to provide physics-based insights into the disruptive combustion behavior of organic-gellant-laden ethanol fuels, which are in the form of the following objectives:

- To study and characterize the jetting dynamics as a function of gellant type and investigate their influence on the droplet flame.
- To study and develop mechanistic insights into the progression of disruptive combustion behavior of organic gel fuel droplets by correlating the droplet bursting behavior and its effect on the jetting behavior at the flame scale.
- To investigate the temporal evolution of the gellant shell during the combustion lifetime of the gel droplet.
- To study the thermally induced evolution of the shell morphology from a material and structure viewpoint and analyze its influence on the jetting behavior.

- To formulate both metalized and non-metalized solidified gel fuels and characterize the regression burn rates in a range of oxidizer fluxes followed by a comparative evaluation of performance in terms of their regression rate with conventional solid fuels.

The attainment of the objectives is done in the following ways:

- Development of an in-house High-speed imaging facility to visualize the combustion dynamics at droplet and flame scales. For droplet scale visualization, backlit imaging was done while for assessing the jetting dynamics at flame scale, Schlieren imaging was performed.
- The characterization of the disruptive combustion behavior was done for ethanol-based organic gel fuel droplets. The combustion behavior is demarcated into three stages namely, Stage I Transient heat up, Stage II disruptive burning, and Stage III Carbonization. The demarcation of stages is based on high-speed and high-fidelity video data. Furthermore, variation jetting behavior at the flame scale across the stages, and its subsequent effect on burn rate was also done. The identification of the carbonization phase was done using Thermogravimetric analysis (TGA). The combustion residue analysis was also performed to assess the variation in gellant shell morphology across the stages.
- An analytical assessment of the temporal evolution of the gellant shell is done for the oscillatory bursting mode of jetting. This includes the extraction of droplet oscillation frequency with the aid of continuous wavelet spectra (CWT). Further, an estimation of the area and overlap of rupture sites along with their centroidal movement as a function of time was done.
- The phenomenological study related to the thermally induced structural evolution of gellant shells is done via Differential Scanning Calorimetry (DSC). It is observed that the gellant shells during combustion undergo thermally induced glass transition. This transition leads to the

transformation of gellant shells from a soft to a hard brittle state which significantly affects the bursting behavior.

- The assessment of regression burn was done in an opposed flow burner setup in an environment of varying oxidizer flux. The comparison of the fuel formulations was done with conventional hybrid propellants (HTPB, DCPD, and paraffin wax).

CHAPTER 3: EXPERIMENTAL METHODOLOGY

The chapter contains details of the experimental methodology incorporated to assess the combustion dynamics of the ethanol-based organic gel fuels.

The chapter contains a detailed explanation of the experimental methodologies utilized to carry out the research studies which include fuel formulation, droplet scale backlit imaging, flame scale Schlieren imaging setups, geometrical parameter extraction from ultra-high-speed droplet and flame scale videos, thermal gravimetric analysis (TGA), differential scanning calorimetry (DSC) and scanning electron microscopy (SEM).

3.1 Fuel formulation

The gel fuel combinations investigated in this research are non-metalized ethanol-based fuels containing organic gellants. Gelled ethanol fuel is a tri-component fuel consisting of two different organic gellant combinations having :(1). Research grade ethanol (99.8% pure; CAS No. 64-17-5) as the base fuel. (2). The gelling agents or gellants i.e., Hydroxypropyl methylcellulose (HPMC; CAS No. 9004-65-3, bulk density $\rho_b \sim 689.19 \text{ kg/m}^3$) and Methylcellulose (MC; CAS No. 9004-67-5, bulk density $\rho_b \sim 503.92 \text{ kg/m}^3$). The methoxy group in MC ranges from 27.5 to 31.5%. On the contrary, HPMC consists of both hydroxyl and methoxy groups ranging between 7-12% and 28-38 % respectively [46], [81]. (3). De-ionized (DI) water is used as the base solvent for organic gellants. All the above three components were procured from Sigma Aldrich Co. It is noteworthy that both HPMC and MC-based gel fuels were prepared over a range of concentrations. In the case of HPMC, it was from 3 to 6% while for MC the range was 8–9%. The rheological properties and compositions of both fuel formulations are detailed in Table 3.1.

Table 3. 1 Relative composition (in weight %) and yield stress of test fuels

Test sample	Ethanol (wt. %)	DI Water (wt. %)	Gellant (wt. %)	Yield stress (Pa)
HPMC-3	82	15	3	23.23±2.62
HPMC-6	84	10	6	120.58±5.22
MC-8	78	14	8	353.085±4.72
MC-9	77	14	9	398 ± 4.2

During the preparation of the gel fuels, a key consideration is taken that the gel fuel should have maximum fuel content alongside a stable gel phase. In this regard, all the formulations in Table 3.1 fit the criterion. To obtain a stable gel fuel, three steps were employed. Firstly, the organic gellants (HPMC or MC) were added to ethanol and subjected to manual stirring for ~2 min at room temperature. Secondly, the solvent i.e., de-ionized water is added to achieve a gel state. The gel formed after the addition of the solvent is further mechanically stirred by using a three-blade impeller at 500 rpm for the duration of ~2 min. Finally, to get the gel phase stability, the gel fuel is left undisturbed for nearly 48 hours at room temperature.

3.2 Experimental setup

3.2.1 The Droplet Imaging using ultra-high-speed camera

The combustion of the gel fuels was performed in a pendant mode set up under the conditions of ambient temperature, pressure, and normal gravity. A calibrated μ -syringe of fixed volume is used for the droplet suspension over the cross-wire arrangement. The syringe dispenses ~2.8 μ l of gel. The suspension of the gel fuel droplet is done on fused quartz fiber of 80 μ m. The quartz wire is chosen because of its small size (diameter less than 100 μ m) and low thermal conductivity

(1.4W/mK at 293 K) as it offers the least thermal and physical interference during combustion. The ignition of the droplet is carried out using a 150 μ m nichrome wire powered via a DC supply. The droplet scale imaging was done to record and observe the bursting dynamics associated with the combustion of gel fuel droplets. For this purpose, an ultra-high-speed PHOTRON FASTCAM -X2 camera attached with a 6.5 \times Navitar Zoom lens was used to capture high-speed video at 10,000 fps with an exposure time of 60 μ s and at the spatial resolution of 3.9 μ m/pixel. Due to the viscosity of gel fuel attaining the spherical shape of the gel fuel droplet was a complex task. Hence a projected area of an equivalent sphere was taken. The initial diameters of $\sim 1.65 \pm 0.1$ mm obtained in both cases were averaged over 6 experimental trials for all formulations of HPMC and MC gel fuels. The error in the accuracy of measurements of the droplet diameter was in the range of $\pm 3\%$. The schematic of the setup is given in Figure 3.1.

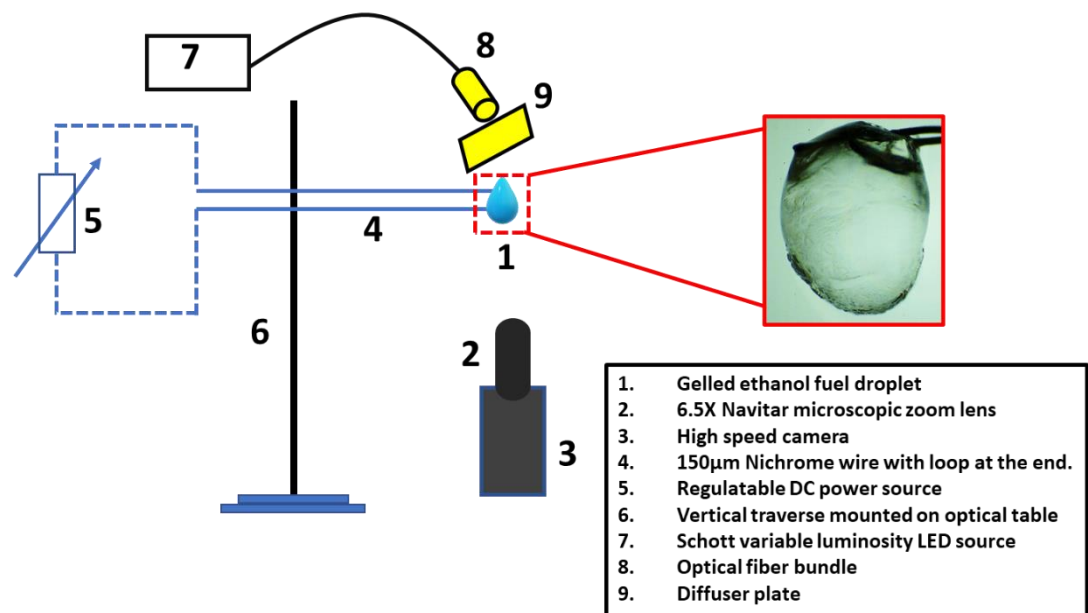


Figure 3. 1. Schematic representation of the setup with its detailed components used for studying the droplet scale dynamics of the gel fuels during the combustion.

3.2.2 The Flame Scale Imaging using Schlieren

Schlieren imaging is extensively used for visualizing and studying variable density gradients. It is one of the most sought-after methods that has paved its way in the

fields of aerodynamics, ballistics, boundary layer studies, combustion studies, materials processing, etc.[82]–[86] . Apart from this, the Schlieren method has been used in providing monumental insights into the use of face masks and their efficacy during the covid-19 pandemic[87] . Not only this, the Schlieren visualization is being effectively incorporated into the study of auditory response produced by the aerodynamics of labial, nasal, and vocalic processes [88].

As mentioned earlier, Schlieren is used for flow visualization. The subtle changes in density gradients provide key insights into the phenomenon associated with it. In Schlieren, due to density gradients, the refractive index gradients also get affected. These gradients of the refractive index can be in one, two, or three dimensions. To observe the schlieren in one or two dimensions, the orientation should match the X and Y axes for best visibility. The three-dimensional Schlieren, although certainly observable, cannot be completely characterized by 2D methods. Hence, methods like Holographic, tomographic, and stereoscopic are used for this purpose[89] . The Schlieren effect occurs in solids, liquids, and gases. The effect results from temperature gradients, high-speed flows, or the mixing of dissimilar materials. In glass or plastics, it can be due to the inclusion of variable density or due to non-uniform thickness in an otherwise homogenous material.

From the view of geometric optics, in Schlieren's visualization, the interest lies in the bending or refraction of light rays. In a cartesian coordinate system, the X & Y planes represent the planes perpendicular to the normal Z- direction. It can be demonstrated that the optical inhomogeneities refract or bend the light in proportion to the gradients of the refractive indices in an X-Y plane [90].

The resulting ray curvature is given by:

$$\frac{\partial^2 x}{\partial z^2} = \frac{1}{n} \frac{\partial n}{\partial x} \quad \frac{\partial^2 y}{\partial z^2} = \frac{1}{n} \frac{\partial n}{\partial y} \quad (1)$$

The angular ray deflection is given by:

$$\varepsilon_x = \frac{1}{n} \int \frac{\partial n}{\partial x} dz \quad \varepsilon_y = \frac{1}{n} \int \frac{\partial n}{\partial y} dz \quad (2)$$

For a 2D Schlieren of an extent “L” along the optical axis, the angular ray deflection from equation 2 becomes:

$$\varepsilon_x = \frac{L}{n} \frac{\partial n}{\partial x} \quad \varepsilon_y = \frac{L}{n} \frac{\partial n}{\partial y} \quad (3)$$

Moreover, for gases and air, the relationship between the refractive index (n) and the gas density (ρ) is given by:

$$n - 1 = k\rho \quad (4)$$

Thus, $k\rho$ is smaller than 1, so the refractive index (n) varies only in the third or fourth decimal places. Therefore, very sensitive optics are required to detect such subtle changes in the density of gases. Hence Schlieren visualization is the preferred mode for the study of changes in flow behavior due to density changes. Also, from eq.1 and eq.2, light rays bent towards the region of a higher refractive index (n). Significantly, for gases, the bending of light rays takes place towards a region of higher density as evident from eq.4 [89], [90].

Currently, flame scale imaging of gel fuel formulations was done by incorporating Schlieren imaging technique. An ultra-high-speed PHOTRON FASTCAM SA-X2 coupled with a Canon EF 100mm 2.8L Macro lens was used to record and assess the combustion behavior. The flame data for the fuel combinations were recorded at 3000fps at a spatial resolution of 126.3 μ m/pixel. The schematic of the setup is given in Figure 3.2.

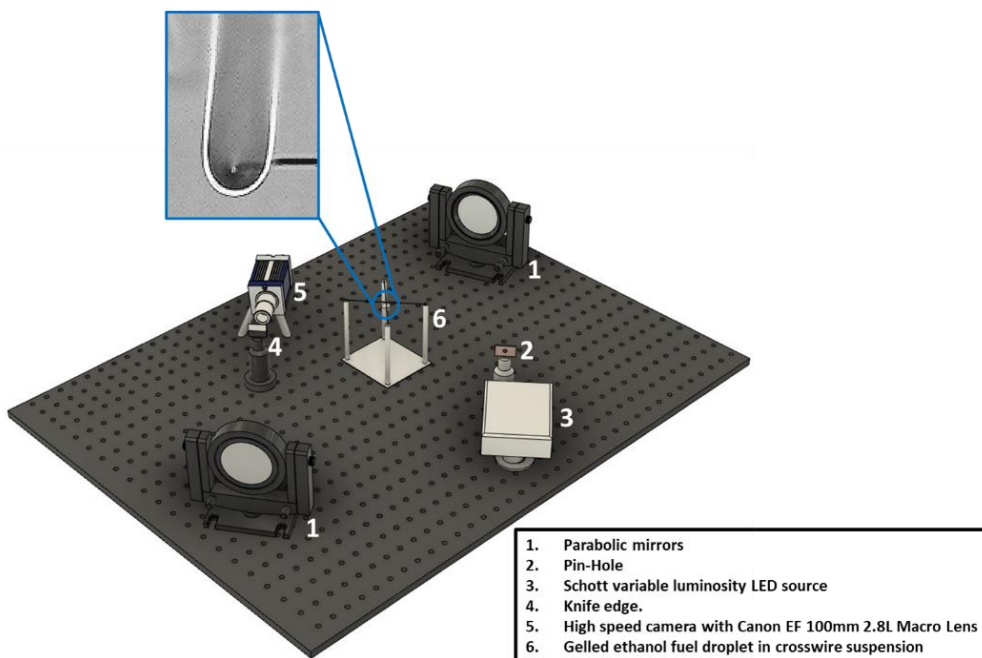
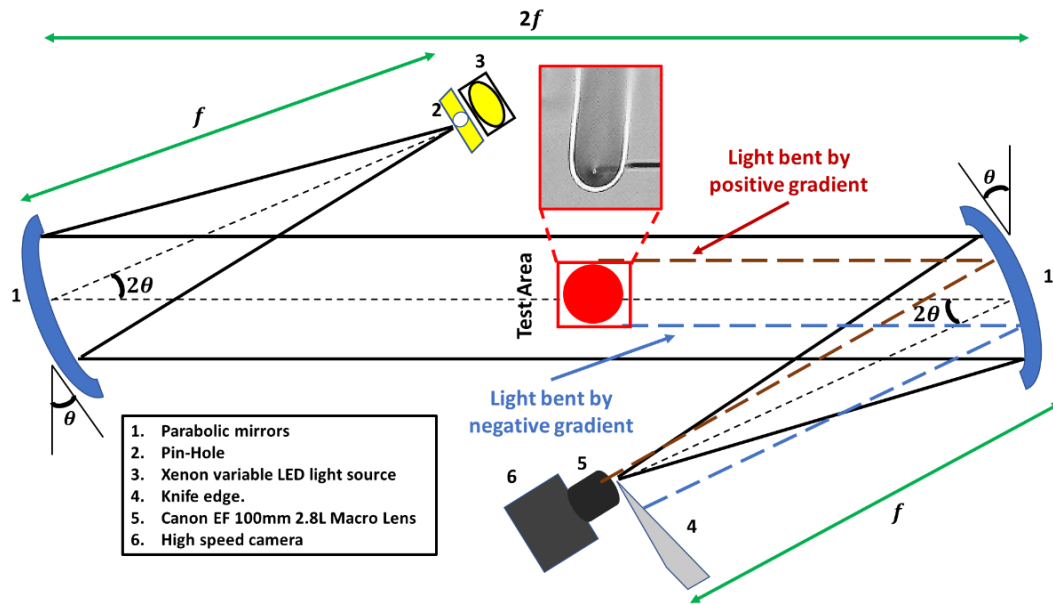


Figure 3. 2. (Top) Diagrammatic representation of the test facility showing the top view of dual-mirror Z-type Schlieren system for characterization of the jetting behavior of the gel fuels during combustion. **(Bottom)** The orthographic view of the test facility for flame visualization.

In Figure 3.2 the Schlieren system HOLMARC HO-SDIS-150 was utilized which contains two parabolic mirrors mounted on gimble mounts, a pointed LED light source, a knife-edge adjuster, and a high-speed camera as discussed in the previous section. The gimble mounts of the parabolic mirror eliminate the unwanted linear beam translation during the adjustment. The parabolic mirrors project the collimated beam of light rays on the object under study to visualize the changes or non-uniformities in the refractive index occurring due to changes in the density of air. This change in the density of air surrounding the object is caused by changes in temperature and pressure. During the imaging, a lighter or darker field is generated by the knife edge (figure 3.3) [89], [90]. The temperature of the diffusion flame along its periphery is higher and thus it has a lower density of air surrounding it. While the inner and the surrounding region of the diffusion flame is at lower temperature and thus has a higher density. This difference in density is reflected as brighter and darker regions in the Schlieren imaging setup. Furthermore, the jets of unreacted fuel vapors have a variation in density in comparison to their vicinity. Therefore, Schlieren imaging is a suitable technique to visualize the flame scale disruption caused by jetting in this study. Moreover, the flame disruptions events lead to changes in the flame periphery, and therefore Schlieren imaging can be utilized to track these events. The velocities of the disrupting jets are calculated by measuring the length of the jets issuing from the flame center (droplet) to the flame periphery occurring during a specified jetting period (Figure 3.4).

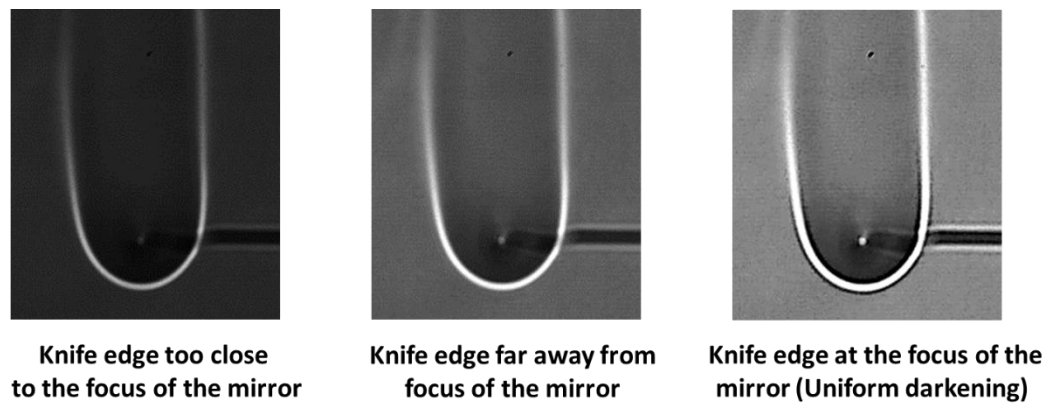


Figure 3. 3. Effect of the knife-edge position on the Schlieren image

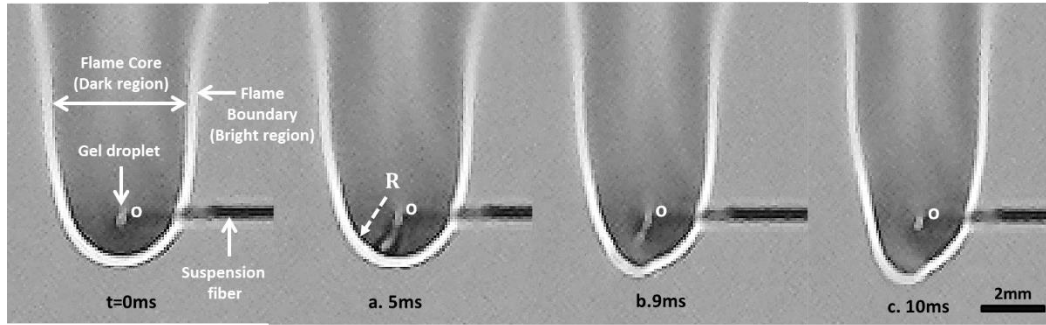


Figure 3. 4. A representative image of a flame distortion event. At $t=0\text{ms}$ is the steady flame with the gel droplet at its center (O). At $t= 5\text{ms}$ (a) jet of length R initiates and impacts the flame. At $t=9\text{ms}$ (b) flame distortion initiates. At $t=10\text{ms}$ (c) flame distorts further and jetting diminishes. Therefore, jet velocity is given as $v = \frac{R}{\Delta t}$ where R is the length of the jet impacting the flame periphery and Δt is the duration of the jet impacting the flame periphery. The scale bar equals 2 mm.

3.3 Computation of geometric parameters

3.3.1 Droplet Scale geometric parameter extraction

The geometrical parameters for characterizing the droplet scale shape variation during the combustion are done with the help of an in-house developed algorithm [91]–[93]. The combustion of gel fuel droplets has a characteristic jetting behavior that occurs asymmetrically throughout the droplet lifespan. Along with this, the droplet also undergoes drastic shape changes like swell and shrink cycles or abrupt droplet bursts. Consequently, to construct a single droplet periphery, recognition of all such events must be taken into consideration. Hence, the deep learning-based Holistically Nested Edge detection (HED) method is used to consider all the droplet shape variation and rupture events. To provide insights into the combustion behavior of a gel fuel droplet, the following parameters were analyzed which include projected area, diameter, centroid of the droplet, radial distance to the droplet edge, aspect ratio, and droplet circumference. The significance of these parameters in the combustion analysis of gel fuel droplets is given in Table 3.2.

The Deep learning-based image processing method utilizes Convolutional Neural Network (CNN) which overcomes the challenges faced by conventional image processing methods like the edge detection method. These conventional methods require visual validation and manual feedback for threshold values of the intensity gradient to retain the edge which makes them time-consuming and ineffective for large datasets. On the contrary, CNN-based deep learning involves filters for pattern recognition. Such rich hierarchical filter features enable image detection with a human-like approach and thereby help in overcoming the uncertainty associated with natural image edge and object boundary detection.

Table 3. 2 Characterization of gel droplet shape variation with time

S.No.	Parameter	Symbol	Significance
1	Projected area	A_p	Droplet diameter and modifications in the surface area occurring from disruptive events can be determined
2	Diameter	D	Calculation of droplet burn rate from the slope of diameter-time history based on the D^2 law model
3	Droplet centroid	C	Determines the bulk movement of the gel droplet in response to vapor jetting
4	Aspect ratio	H_{max} / W_{max}	Estimation of droplet deformity due to jetting events
5	Droplet circumference	c	

In the deep learning-based HED method a non-binary edge map is generated corresponding to each frame of the droplet video (Figure 3.5A). These maps are rich in turbulence and require restructuring. Furthermore, for noise removal and droplet localization, binary bit masking, and color thresholding is applied. Consequently, the image gives a set of points that surrounds the gel fuel droplet, these points are then filtered depending on their location and further classified as boundary and non-boundary points. Among these, the non-boundary points are discarded, and boundary points are used for creating the binary map. Consequently, the binary map aids in the contour detection of the gel fuel droplet.

During a jetting event, the droplet behaves as a discontinuous entity. Thus, to fabricate a continuous droplet envelope, convex hull operation is used on boundary points. The discontinuity arising due to jetting results in unresolved shell boundaries. To keep track of such events the algorithm keeps a count of the number of connected components in the image and the position of their respective centroids. During a jetting event, the centroid fluctuates, and it lies outside the component area or droplet image (Figure 3.5B). The convex hull operation thus enables the algorithm to construct the droplet boundary with the help of a convex polygon around the given point which binds the area. The droplet boundary constructed needs to be refined into a defined orientation by using morphological transformations.

Finally, after the demarcation of the droplet boundary, parameter extraction is done which includes droplet area, droplet perimeter, Coordinates of the centroid, maximum height (H) and width (W), Aspect ratio (H/W), and radial distance from the centroid to droplet edge across 1000 angles. The steps involved in the algorithm for the droplet's geometrical data extraction are depicted in Figure 3.5. The dataset obtained from the application of this algorithm is further utilized for the classification of combustion stages at the droplet scale in chapter 5.

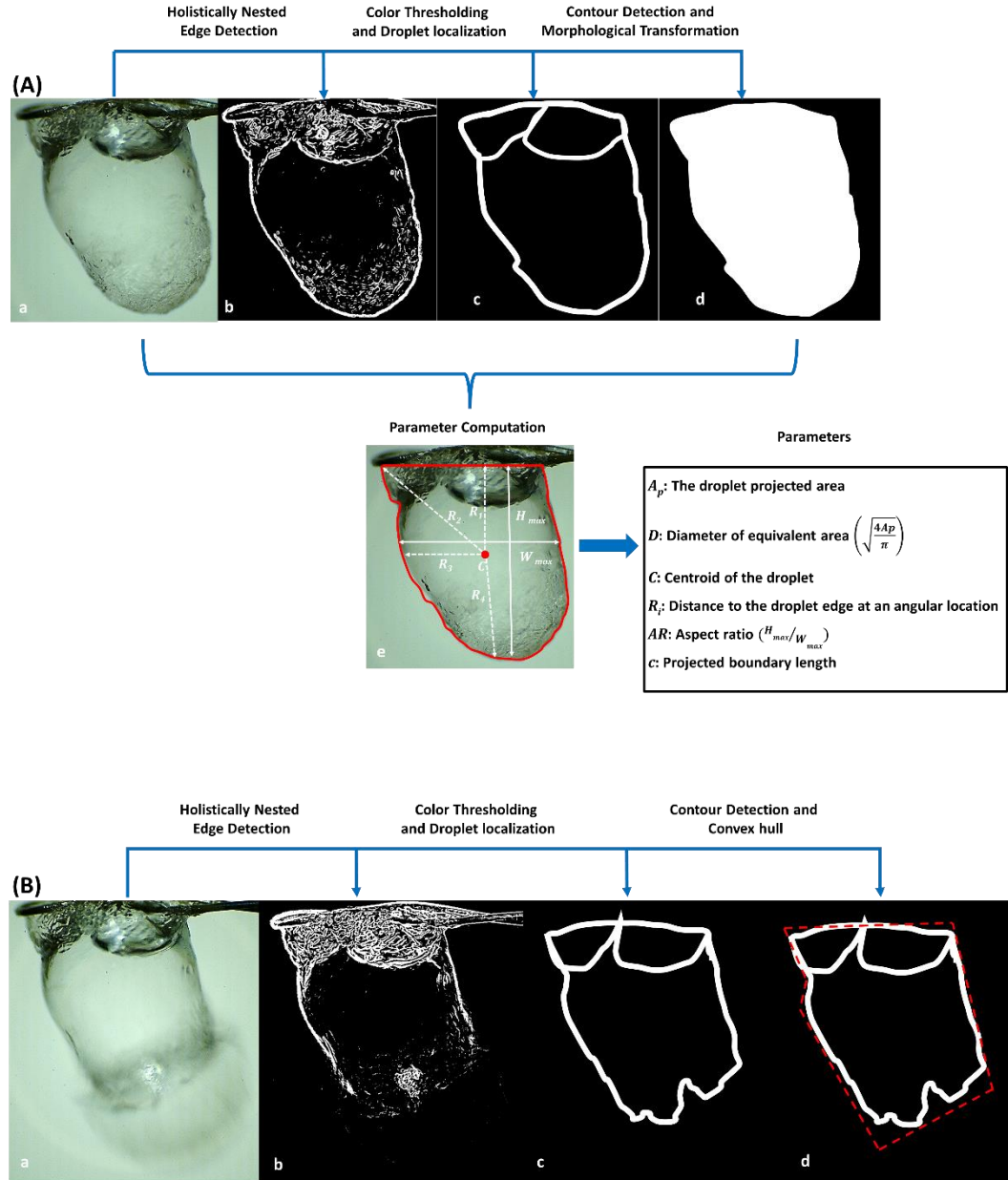


Figure 3. 5. (A) Sequential steps for processing of droplet image when no jetting or rupture takes place. (a.) HED-based non-binary image (b). Color thresholding and droplet localization. (c) Morphological transformation, (d). Parameter extraction. (B) Sequential steps for processing of droplet image when jetting or rupture takes place. (a). HED-based non-binary image for a droplet rupture event, (b). Color thresholding and droplet localization. (c). Convex hull operation, (d). Parameter extraction.

3.3.2 Flame Scale geometric parameter extraction

Schlieren imaging produces high-contrast images that demarcate the regions based on the density gradients (Figure 3.4). However, due to the occurrence of vortex roll-up at the shear layer between the droplet flame envelope and its surrounding area and the occurrence of the jetting events, the symmetrical tear-drop shape of the flame is continuously disrupted. This results in flame images with a discontinuous periphery, thereby making it difficult to track and reconstruct the complete flame envelope, which is a prerequisite condition for calculating the flame area and perimeter. Therefore, a multi-step image-processing algorithm was developed, which combines the discontinuous entities across multiple images to generate a smooth and continuous flame envelope. This algorithm calculates the quantitative attributes of the flame envelope, i.e., the area and perimeter as a function of time, for any desired flame height.

Figure 3.6 shows the step-by-step method through which the image processing algorithm is implemented on individual frames for the tracking and reconstruction of the flame envelope. First, color thresholding is applied to the images using a predetermined threshold value to localize the area being monitored and create its binary mask (Figure 3.6 a and b). The fact that the high-temperature (or low-density) flame boundary appears as a bright region and forms the flame periphery helps us to determine the threshold value. The pixels with values lower than the threshold have an extremely low chance of being present on the flame boundary and, therefore, are set to zero. The resulting image (see Figure 3.6b) displays a mask of potential but discontinuous flame edges. In the second step, since the generated masks occupy a finite area (represented by the thickness of the flame envelope), the contours are constructed around the highlighted areas in the mask to extract the coordinates of a set of points that encapsulate these areas (Figure 3.6c). The points on the outer edge of the contours are useful, as they represent boundary points; however, the points on the inner edge (non-boundary points) are redundant and, therefore, must be filtered.

To achieve this, only the points corresponding to the minimum and maximum values of the x -coordinate are stored for each vertical location of the image, while the remaining ones are discarded. The final set of boundary points is shown in Figure 3.6d. Subsequently, the boundary points must be connected to form a uniform contour that encapsulates the flame. However, because the flame boundary is irregular, with multiple concave and convex curves, there is no preset criterion that provides the order in which the points must be joined to form a continuous contour. To enable this, the image is divided into horizontal sections (see Figure 3.6e) of a fixed small height such that the effects of the shape irregularities are eliminated, and the points in these regions are processed and reconstructed to create a section of the flame. In these horizontal sections, the points are sorted in a clockwise order using the centroid as the reference point, i.e., $(x_{max} + x_{min}) / 2$ at each height. These ordered points generate smaller sections within the flame, as shown in Figure 3.6f. While the horizontal sections are mostly accurate, some faulty cases may occur when the points are not detected. For instance, in Figure 3.6e, no points are detected on the flame boundary on the right-hand side. To resolve such cases, the points on the other side of the flame boundary in the given horizontal section are mirrored. The mirroring axes are considered as the vertical axis passing through the moving average of the centroid over five frames. The resolved flame sections are shown in Figure 3.6f, where the moving averages of the centroids are marked, and each horizontal section is ten pixels thick. Next, to join the horizontal sections to create a structured body, all the sections are drawn in a blank binary frame one after the other. The resulting image (see Figure 3.6g) nearly resembles the actual shape of the flame envelope, except for a few discontinuities. Therefore, to refine the shape of the flame envelope with smooth, rounded curves, morphological transformations are performed, with the original flame image and the circular kernel being used as inputs. The shape of the final flame envelope is obtained by performing two operations, namely, opening and closing. The opening operation involves erosion followed by the dilation of the binary image, which aids in the removal of the scattered noise from the image. The closing operation involves dilation followed by the erosion of the binary image. This helps to close the small

holes inside the objects in the foreground and the small black points on the object. The final reconstructed image of the flame envelope obtained after the morphological transformations is shown in Figure 3.6h. The exact boundary of the flame envelope that is tracked and used to calculate the flame perimeter and the area is shown in Figure 3.6i. Note that in the area beyond the blue boundary, the vortex roll-up, due to K-H instability, disturbs the flame shape and, therefore, is not considered in the calculation of the flame area in this study.

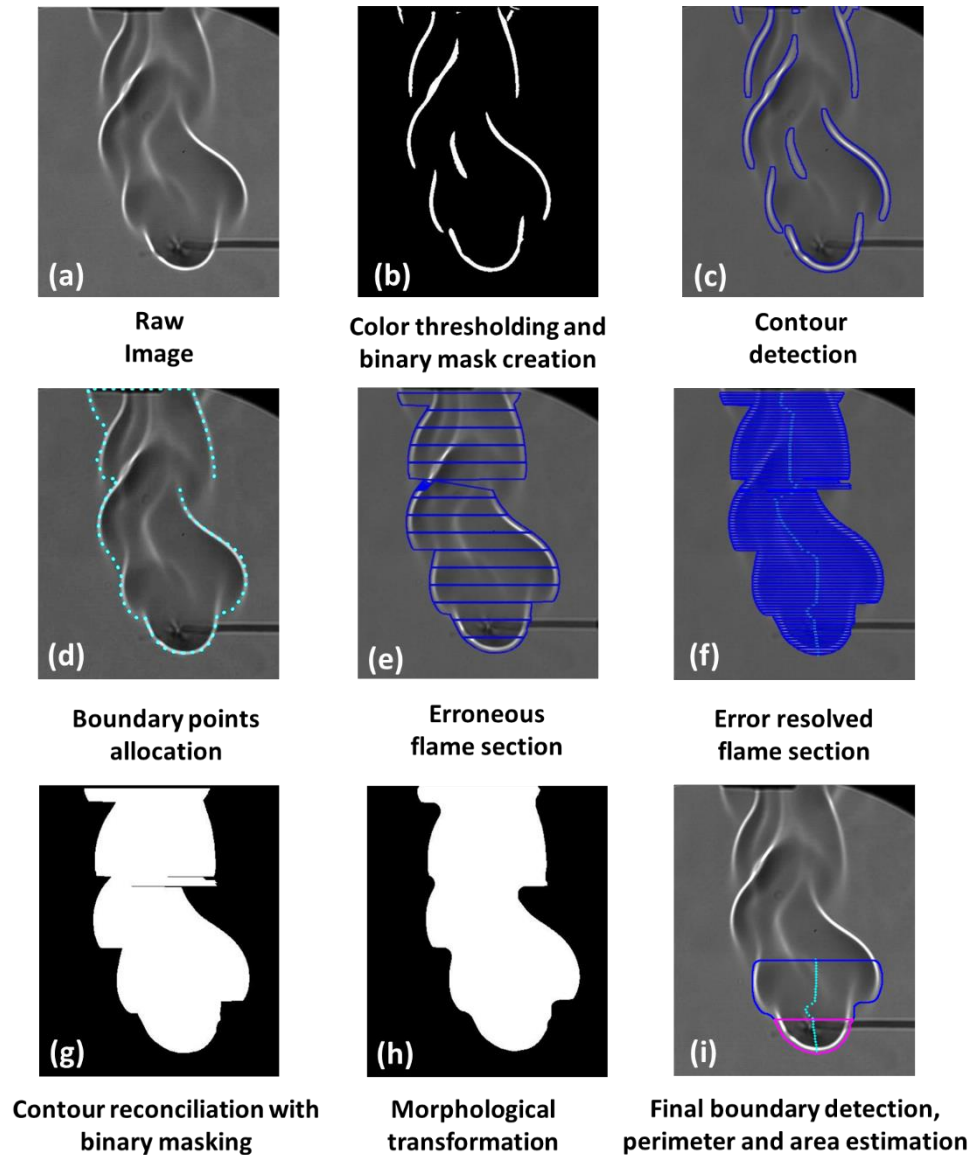


Figure 3. 6.A sequential method of image processing for extraction of the flame perimeter from the raw Schlieren images.

3.4 Thermoanalytical methods

3.4.1 Thermogravimetric analysis (TGA) and Derivative thermogravimetry (DTG)

Thermogravimetric analysis (TGA) is a thermoanalytical method in which variations in the mass of the samples are measured as a function of temperature or time at a specified heating rate. TGA is generally used in the determination of mass loss due to decomposition, loss of volatiles (e.g., moisture), or mass gained due to oxidation. The TGA is generally utilized for analysis of the decomposition behavior of materials, determination of moisture, and organic and inorganic content in the samples, and to study the degradation mechanisms and reaction kinetics. In DTG the first derivative of mass change is measured as a function of temperature or time which provides an assessment of temperature or time of significant mass change.

In this study, thermogravimetric analysis of the ethanol-based organic gel fuel samples is done to determine and estimate the phase transitions that can occur during combustion. A thermogravimetric analyzer (TGA; Perkin Elmer STA 8000) is utilized to assess the thermal stability of the gel fuel samples. The samples of 20mg mass are heated in an alumina crucible from an initial temperature of 30 to 500°C in an inert atmosphere of nitrogen. The samples are subjected to a heating rate of 10°C/min. The thermograms depicting the mass loss of the gel fuel samples as a function of increasing temperature are obtained using the TGA machine's built-in Pyris software.

3.4.2 Differential scanning calorimetry (DSC)

The thermoanalytical technique i.e., differential scanning calorimetry (DSC) measures the heat flow into or out of a sample as a function of temperature or time at a constant heat rate. In DSC the rate of heat flow is measured and compared between the reference material and the test sample. DSC helps in the evaluation of material properties like phase transitions, melting, crystallization, and glass transition.

In this study, The DSC analysis was carried out using a Perkin Elmer STA 8000 analyzer. The samples of 30 mg were loaded onto the ceramic pan and heated in the alumina crucible from 30 to 500 °C in an inert nitrogen atmosphere. The nitrogen was purged at 20ml/min and DSC thermograms were obtained by using the machine's built-in Pyris software.

In this study, differential scanning calorimetry (DSC) was performed for the gel fuels which provided crucial insights into the temperature-dependent phenomenon like phase transitions, glass transitions, and melting of the gellant shells formed during the combustion. Note that it is extremely difficult to predict the variation of gellant shell structure as a function of temperature in a dynamic combustion environment. Hence, the DSC technique can be viable tool in this regard.

3.5 Scanning electron microscopy (SEM): Combustion residue analysis

The post-combustion residue analysis is carried out to assess the morphological transformation of gellant shells for HPMC-3% and MC-9% gel fuel compositions. This was done by using scanning electron microscopy (SEM), carried out under a high vacuum and backscattering mode. The samples were made conducting by gold coating for the duration of ~2min under a vacuum-sealed chamber. The gellant shells featured many significant morphological traits like striations, jetting holes, blisters, and cracks. Hence, the incorporation of backscatter mode in SEM is essential and beneficial in enhancing the above-mentioned morphological traits as it utilized high-energy electrons to obtain high-resolution images as Backscatter Electron (BSE) imaging detects differences in atomic number on and below the surface of the sample.

CHAPTER 4: DYNAMICS OF VAPOR JETTING

Jetting in burning gel fuel droplets is an important process that, in addition to pure vaporization, enables the convective transport of unreacted fuel vapors from the droplet interior to the flame envelope. This aids in accelerating the fuel efflux and enhancing the mixing of the gas phase, which improves the droplet burn rates. In this study, Schlieren imaging was used to characterize different jetting dynamics that govern the combustion behavior of organic-gellant-laden ethanol gel fuel droplets. To initiate jetting, the gellant shell of the burning gel fuel droplet was subjected to either oscillatory bursting or isolated bursting, or both. However, irrespective of the jetting mode, the jets interacted with the flame envelope in one of three possible ways. Based on the velocity and the degree to which a jet disrupts the flame envelope, it is classified as either a flame distortion, a fireball outside the flame, or a pinhole jet (localized flame extinction), where the pinhole jets have the highest velocity (1000–1550 mm/s), while the flame distortion events have the lowest velocity (500–870 mm/s). Subsequently, the relative number of the three types of jetting events during the droplet lifetime was analyzed as a function of the type of organic gellant. It was demonstrated that the combustion behavior of gel fuels (hydroxypropyl methylcellulose: HPMC at 3 wt.%) that tend to form thin-weak-flexible shells is dominated by low-velocity flame distortion events, while the gel fuels (methylcellulose: MC at 9 wt.%) that facilitate the formation of thick-strong-rigid shells are governed by the high-velocity fireball and pinhole jets. Overall, this study provides critical insights into the jetting behavior and its characterization, which can help us to tune the droplet gasification and the gas phase mixing to achieve an effective combustion control strategy for gel fuels.

4.1 Introduction

The realization of future rocket motor engines will depend on their adaptability to next-generation fuels that are environmentally friendly, operationally safe, easy to process, and reliable [55]–[57]. In this regard, gel fuels have attracted significant interest as high-performance alternatives to traditional rocket fuels. This is due to their improved rheological and physical properties that bring together the key functional traits of solid and liquid fuels, as demonstrated by Hodge K. et al. [24]. For example, gel fuels behave in a solid-like manner at low shear, which mitigates the chances of an accidental hazard due to a leak or spillage, especially in the case of hypergolic and toxic fuels, as per the findings of Ciezki H.K. et al. [66]. During storage, the high viscosity allows the energetic nanoparticles to be suspended stably in the fuel matrix, which aids in the enhancement of the energy density of the fuel and the engine's specific impulse, as per the studies of Rahimi S and Natan B[26]. At the other end, the liquid-like behavior at high-shear stresses due to the shear-thinning property enables easier pumping and atomization when the gels are forced through injectors at high pressures [25], [26], [64], [65], [94], [95]. These liquid-like characteristics can provide critical functionalities, such as re-ignitability and thrust modulation in rocket engines [25], [26], [64], [65], [94], [95]. While gel fuels are an attractive alternative to their solid and liquid counterparts, their implementation has been limited due to the lack of understanding of their complex combustion behavior, which is highlighted by the disruptive vapor-jetting events. The jetting of fuel vapors, or simply jetting, as proposed by Solomon Y et al. [70], [71] refers to the discharge of unreacted fuel vapor from the droplet interior, which occurs aperiodically and asymmetrically during the droplet lifetime. In the existing literature, as examined by Mishra D.P. et al. [41], [42] the term *microexplosion* is often used in place of *jetting* to characterize the disruptive combustion behavior of gel fuel droplets. However, microexplosion and jetting represent two distinct types of disruption events, which have completely different initiation mechanisms and impacts on the droplet. If the explosion is confined to a segment of the parent droplet and is of lower intensity, it is termed puffing, which is characterized by the

blowing out of vapor, along with a stream of fine droplets. Microexplosion was first reported by Law [74], [96], [97] in the context of multiphase multicomponent fuel droplets, corresponding to an abrupt catastrophic fragmentation of the droplet due to the rapid gasification of the high-volatility species entrapped in the droplet core. In multicomponent droplets possessing species with a high volatility differential, the lower-boiling-point (or the higher-volatility species) species becomes diffusively entrapped in the core, while the lower-volatility-species accumulates on the surface and governs the droplet surface temperature. With the increasing droplet temperature, the entrapped species is superheated to its homogenous boiling limit and undergoes explosive boiling, which is accompanied by a rapid pressure rise. Since homogenous boiling is accompanied by a sudden release of a large amount of stored superheat, this event (termed as microexplosion) shatters the entire droplet into smaller fragments and marks an end to the droplet lifecycle. In contrast to microexplosion, jetting events are unique to gel fuels and occur continuously during their lifetime, which features the initiation, coalescence, growth, and eventual collapse of bubbles to release the jets of unreacted fuel vapors [47], [70], [71], [98]. The continuous formation and collapse of multiple bubbles are representative of heterogeneous boiling. Because heterogeneous boiling is characterized by a low degree of stored superheat compared to homogenous boiling, the jetting events triggered by heterogeneous boiling have a visibly low intensity compared to a microexplosion event [47], [99], [100].

With respect to the disruptive events that are triggered by heterogeneous boiling, the jetting of the unreacted fuel vapors is like the bubble ejection events that govern the combustion behavior of nanofluid fuel droplets [99]–[103]. However, in terms of the mass, momentum, and energy transport processes that control their behavior, starting with initiation and ending with their termination, and their subsequent effects on droplet combustion, these are widely different disruptive events. First, in nanoparticle-laden fuel droplets, the particles agglomerate either via orthokinetic or perikinetic mechanisms to form micrometer-sized aggregates that behave as *sites* of bubble nucleation, as reported by Miglani A et al. [101]. In contrast, when burning gel fuel droplets, the inner surface of the gellant shell acts as a surface for

bubble nucleation. Secondly, in nanoparticle-laden fuel droplets, the pressure upsurge due to internal boiling is released via the rupture of the shell formed of agglomerated nanoparticles. The shell rupture is accompanied by the formation of *child droplets* that break off from the parent nano fuel droplet [101], [102]. These child droplets may further undergo microexplosion to form more child droplets [104], [105]. In comparison, the rupture of the gellant shell in the case of gel fuel droplets does not form any *child droplets*. Instead, the internal pressure build-up is released by the jetting of unreacted fuel vapors via the ruptured location. Details of the lifecycle of a vapor jet and the mechanisms governing it can be found in Miglani A. et al. [47]. Thirdly, the shell formation process, in the case of nanoparticle-laden droplets, is controlled by the interplay between two competing mechanisms, namely, particle agglomeration and the secondary atomization of the droplet, both of which change the mass fraction of NPs within the droplet at any time instant. The former helps to build the shell via particle agglomeration, while the latter impedes shell formation directly by rupturing it and indirectly by depleting the population of NPs through atomization, as reported by Miglani A. and Basu S.[99]. In contrast, the shell formation, in the case of gel fuel droplets, occurs via the phase separation of the gellant [38], [69]–[73], [106] from the mixture of the base fuel, the gellant, and the gellant solvent. In this case, the entire mass of the gellant is retained by the droplet until the end of the droplet's lifetime, when the shell carbonizes and is consumed. Fourthly, in nanoparticle-laden droplets, the child droplets resulting from secondary atomization and their subsequent fragmentation (tertiary atomization) aid in improving the droplet burn rate by enhancing the net surface area and dispersing the fuel charge evenly, as reported by Rao D.C. et al. [105]. Furthermore, the child droplets behave as nanoparticle carriers and transport them to the flame, where the particle ignites and releases energy [100], [103]. In contrast, the jetting allows the unreacted fuel vapors to be transported advectively from the droplet to the flame envelope. This helps to improve the droplet burn rate by increasing the fuel mass flux, in addition to pure vaporization. Since the droplet burn rates are significantly influenced by the type of jetting events and variations in their number density during the droplet lifetime, it is imperative to characterize

the jetting events. This is particularly crucial for rocket motor applications utilizing gel propellants, which exhibit higher ignition delays and low burning rates due to their inherently high heat of vaporization [69]. To this end, a key objective of this study is to characterize the jetting events and investigate their effects on the droplet flame as a function of the nature of the gellant shell.

In this study, two fuel combinations were taken for the experiments. The gel fuels used were non-metalized ethanol-based fuels containing organic gellants. Gelled ethanol fuel is a tri-component fuel that consists of two different organic gellant combinations: (1) research-grade ethanol (99.8% pure; CAS No. 64-17-5) as the base fuel and (2) the gelling agents or gellants i.e., hydroxypropyl methylcellulose (HPMC; CAS No. 9004-65-3, $\rho_b \sim 689.19 \text{ kg/m}^3$) and methylcellulose (MC; CAS No. 9004-67-5, bulk density $\rho_b \sim 503.92 \text{ kg/m}^3$). MC has a methoxy group ranging from 27.5 to 31.5%, while HPMC has both active hydroxyl and methoxy groups ranging between 7–12% and 28–30%, respectively [46]. (3) Double-distilled water served as the base solvent for organic gellants. The properties and compositions of both fuel formulations are detailed in Table 3.1. Note that while the HPMC-based gels fuels were prepared over a range of concentrations from 3 to 6%, with a range of 8–9% for the MC-based fuels, for brevity, the results are presented for only two cases, because these fuels represent two extreme cases of jetting behavior.

The details of fuel formulation steps, the high-speed-imaging setup at droplet and flame scale, and geometric parameter extraction at droplet and flame scales are given in Chapter 3.

4.2 Results and Discussion

The disruptive burning behavior of gel fuel droplets is characterized by the jetting of unreacted fuel vapors [41], [42], [70], [71] that occur unevenly during the droplet's lifetime. A typical jet is initiated through a three-step process that occurs inside the droplet [41], [42], [70], [71], as shown in Figure 4.1. First, during the transient heat-up period, the gellant phase separates from the base fuel/gellant

solvent, which results in the formation of a gellant crust near the droplet surface. Second, the trapped fuel (inside the droplet) undergoes boiling. Third, the gellant shell bursts due to internal pressure build-up and jetting of the unreacted fuel vapors (across the droplet–gas interface). In this way, the pressure energy within the bubble is converted to the kinetic energy of the jet, which is released via the rupture site on the droplet shell. Subsequently, the jet travels to the flame envelope, where it interacts with the flame and disturbs the symmetric tear-drop shape of the diffusion flame. Figure 4.1 shows an example of a typical jetting event and its interaction with the flame during the combustion of an HPMC 3 ethanol gel droplet. The entry of the fuel jet into the flame envelope is visible at 2 ms. At 4 ms, the jet causes localized flame extinction to occur, as is evident from the broken flame front. Subsequently, the flame begins to propagate around the jet of the unreacted fuel vapors and reconnects at 9 ms. Note that in addition to pure vaporization, jetting enables the advective efflux of the unreacted fuel vapors from the droplet and, therefore, jetting represents a key mechanism of the mass transport of fuel vapors that have the potential to improve the droplet gasification rate significantly [39]. This is crucial for gellant-based fuels because they tend to have high heats of formation and, hence, low gasification rates [69]. Therefore, in this section, the different types of jetting events are characterized in terms of their average velocity, and their impacts on the flame envelope are analyzed first. Second, the effects of the gellant type and, hence, the nature of the gellant shell on the number and average velocity of the jetting events are presented.

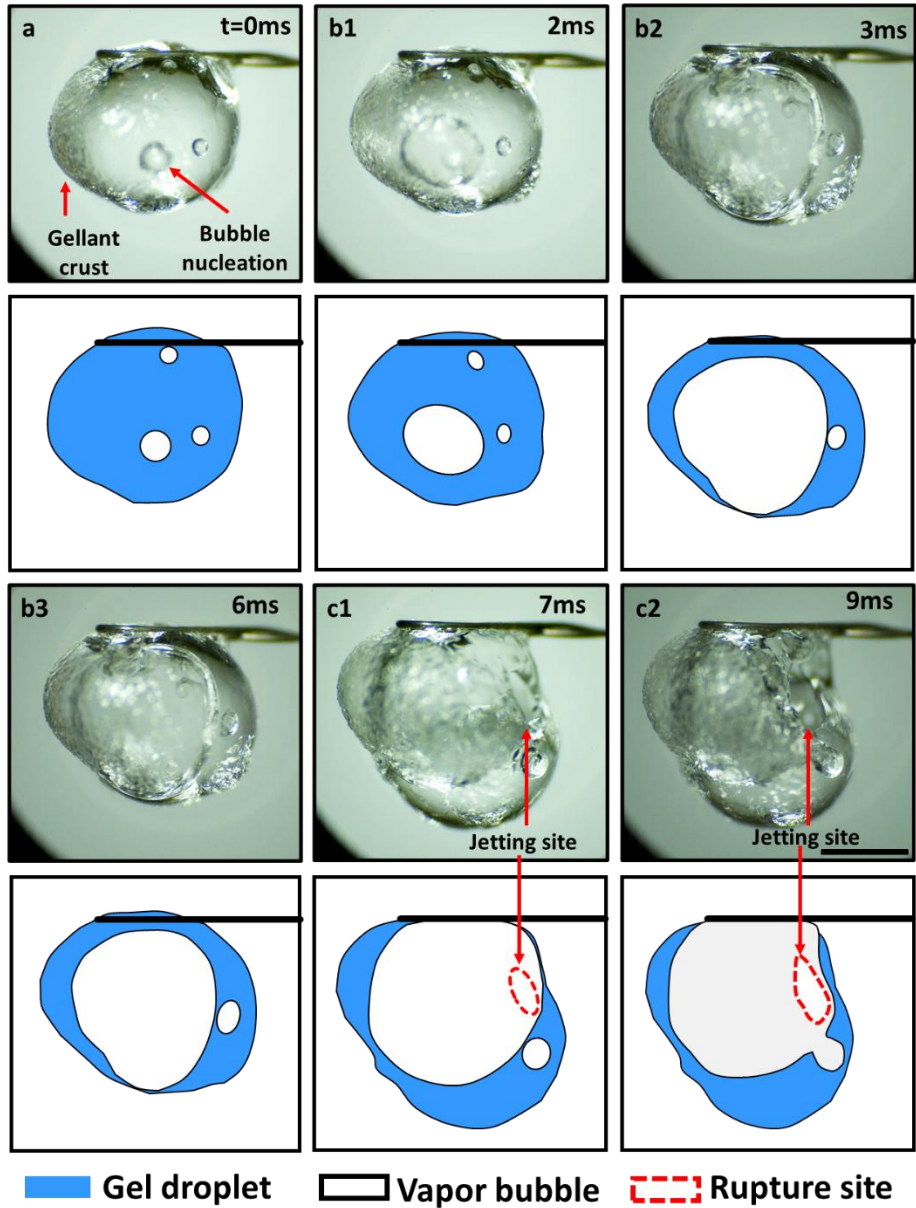


Figure 4. 1. High-magnification images (**top**) and the accompanying schematic representations (**bottom**) of the precursor events that lead to the initiation of jets. **(a)** Formation of gellant crust/shell and bubble nucleation, **(b)** bubble growth and droplet expansion (**b1**: initial bubble growth, **b2**: bubble expansion occupying large droplet vapor fraction, and **b3**: swelled droplet state prior to rupture, and **(c)** shell rupture and jetting of unreacted fuel vapors (**c1**: formation of rupture site, and **c2**: expansion of rupture site due to viscoelastic nature of the gellant shell). The scale bar equals 1 mm.

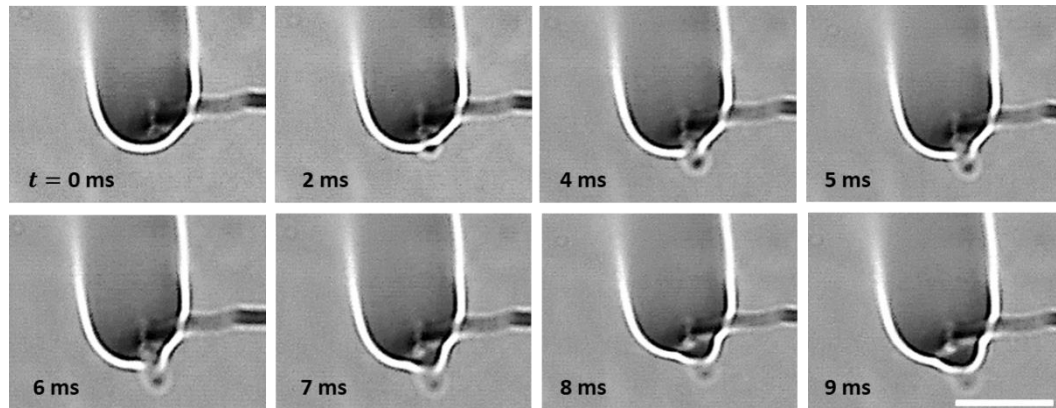


Figure 4. 2. High-speed images showing a representative jetting event and its interaction with the droplet flame envelope. The scale equals 10 μ m.

4.2.1 Jetting Modes

Depending on the interplay between the degree of pressure rise within the droplet and the ability of the shell to restrain this pressure due to its rheo-physical properties, the droplet may exhibit different jetting modes, namely, either isolated jetting or oscillatory jetting, or both (see Figure 4.3). Oscillatory jetting features the periodic release of jets from the same region of the droplet and occurs in gel fuels that tend to form viscoelastic shells that are weak but flexible [47]. This allows the shells to undergo oscillatory bursting cycles featuring shell rupture and recovery. As shown in Figure 4.4, a single bursting cycle comprises two phases: first, the active jetting period, where the jets are initiated due to shell rupture and the jetting continues until the shell recovers, and second, the inactive jetting period, where the shell recovers and, subsequently, the pressure builds up to initiate the next bursting cycle. In this way, the oscillatory bursting cycles of the shell result in oscillatory jetting. In HPMC-based gel fuel droplets, which form a weak-flexible viscoelastic shell, oscillatory jetting occurs over ~ 10 – 70% of the droplet lifetime, depending on the gellant concentration [47]. Therefore, oscillatory jetting is a key jetting mode that governs the droplet burn rate via the efflux of unreacted fuel vapors. In contrast, the gel fuels that tend to form strong-rigid shells feature isolated jetting [47]. The

effect of the gellant type on the nature of the shell and its effect on the jetting behavior are discussed later in Section 4.2.3.

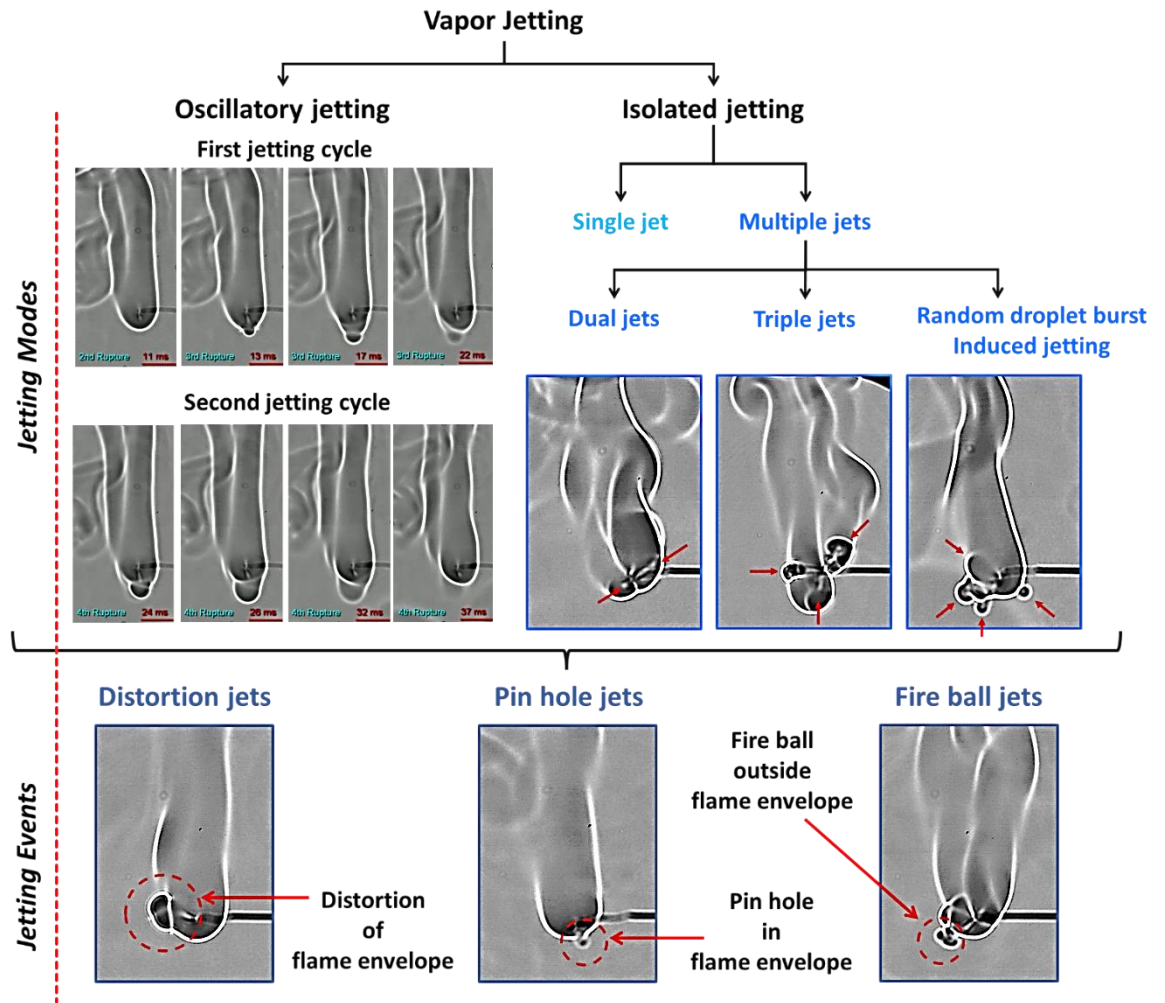


Figure 4. 3. A classification chart showing the jetting modes and events that govern the combustion behavior of organic-gellant-laden gel fuel droplets.

The isolated jetting mode is characterized by the release of individual jets, which may occur as either single isolated jets or as multiple simultaneous jets at different spatial locations across the droplet surface. Multiple jets occur either when the droplet shell ruptures at more than one location or in a random event where the shell is blown apart due to a transient pressure upsurge, as shown in Figure 4.5. In both these cases, the ruptured shell forms multiple jetting sites, which results in the large-scale distortion of the flame envelope.

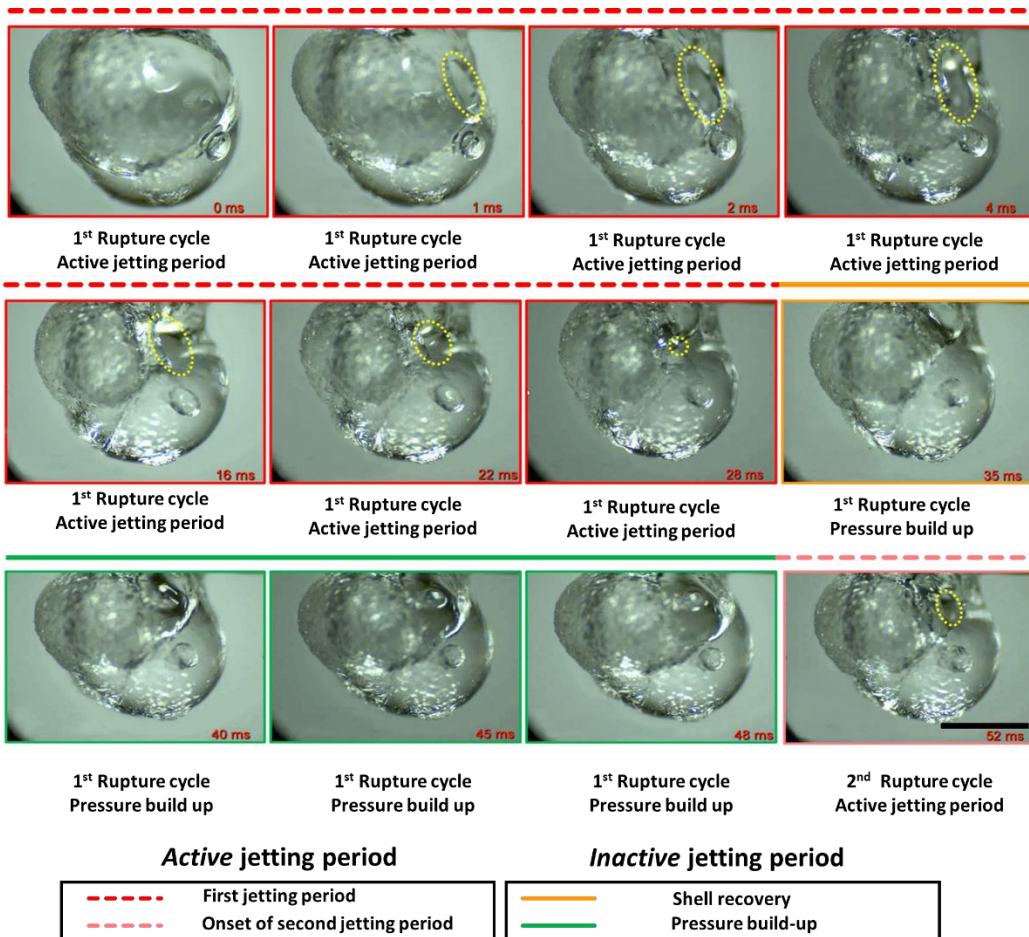


Figure 4. 4. Rupture sequence of a combusting gel fuel droplet undergoing oscillatory bursting. The scale bar equals 1mm.

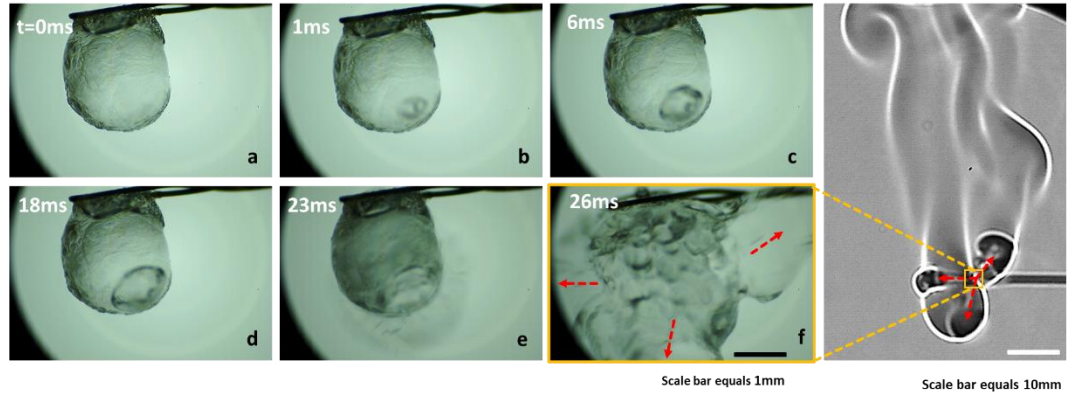


Figure 4. 5. High-magnification images showing the random bursting of a burning gel fuel droplet. (a). Gel droplet with the gellant shell. (b) Bubble nucleation on the inside surface of the gellant shell. (c,d) Bubble growth inside the droplet. (e) Initiation of droplet burst at a single rupture site. (f) Droplet bursting at multiple random locations. The resultant jetting and its interaction with the flame envelope are shown on the right. The red arrows indicate the directions of jetting at the droplet and flame scale respectively. The scale bar equals 1 mm for the droplet images and 10 mm for the flame image.

4.2.2 Jetting Events

While the jetting modes are governed by the competition between the internal boiling activity that tends to build up pressure (due to bubble growth) and the ability of the viscoelastic shell to contain this pressure rise, the resulting individual jets interact with the flame in one of the following ways: first, the jet distorts the flame envelope without breaking it; second, the jet breaks and moves past the flame envelope, where the unreacted fuel vapors ignite to form a fireball outside the droplet flame envelope; and third, the jet punctures the flame envelope and creates a pinhole in the flame envelope. Accordingly, the three distinct types of jetting events are termed flame distortion, a fireball outside the flame, and pinhole ejections, respectively, which are shown at the bottom of Figure 4.3. These jetting events are characterized based on their average velocity and their effects on the flame envelope in terms of the temporal variation in the flame perimeter during the jet lifetime.

Table 4.1 details the average velocities of these three events, which indicate that pinhole jets have the highest speed, while flame distortion events have the lowest speed.

Table 4.1 Average velocities of jets of flame-disrupting events.

Flame disruption event	HPMC-3% (mm/s)	MC-9% (mm/s)
Flame distortion	$800 \pm 5\%$	$873 \pm 7\%$
Fireball outside the flame	$1095 \pm 10\%$	$1030 \pm 8\%$
Pin ejections	$1313 \pm 9\%$	$1155 \pm 6\%$

Figure 4.6 shows the time sequence images of a flame distortion event, where the jet emanates at approximately 180° from the droplet at time $t = 0$ ms, travels to the flame front, and hits the envelope at 5 ms. This jet induces distortion in the flame envelope due to its radial momentum and its expansion as it hits the high-temperature flame envelope. For such events, the average velocities are low enough that the flame curvature undergoes distortion but remains intact, i.e., it does not undergo localized extinction. The fact that the flame remains distorted for a long enough period instead of being spontaneously restored to its initial shape demonstrates that the evaporated fuel is discharged continuously via the ruptured shell. In this representative flame distortion event, the speed is ~ 884 mm/s, and a noticeable distortion is observed in the flame front, as seen by a change in its perimeter (see the bottom plot in Figure 4.6). Note that while the maximum variation in the normalized perimeter is just 5%, the perimeter of the flame front can change significantly during several other flame distortion events that occur in the droplet’s lifetime. Next, Figure 4.7 shows the time-frozen snapshots of the jetting event that leads to fireball formation outside the flame envelope. Fireball formation involves a two-step process: first, the jet breaks the flame front, and second before the flame propagates around the jet and repairs this break in the flame envelope, the unburned fuel vapors that are the outside the flame envelope begin to

react to form a fireball, which grows over time. Here, the first step of the break in the flame occurs rapidly in ~ 6 ms, with a negligible change of less than 2% in the flame perimeter. In contrast, the second step of fireball formation and growth occurs over a longer timescale of ~ 60 ms and features a significant increase in the flame perimeter by $\sim 15\%$ before the flame envelope is restored to its initial steady-state value. Therefore, the fireball events tend to form a separate flame front away from the parent flame, and the effect of these events lasts for a longer time, as seen by the time scale O (70 ms). The speed of the fireball event shown in Figure 4.7 is 1012 mm/s. The jets that tend to break the flame front are characterized by high speeds, which are higher compared to both flame distortion and fireball events. Figure 4.8 shows a typical pinhole jetting event with a speed of 1356 mm/s, which hits and breaks the flame front just ~ 2 ms after its initiation. Subsequently, the flame propagates around the vapor jet to repair the break in the flame envelope and restores the complete envelope at 10 ms. This indicates that the pinhole jets are the fastest (and, hence, the shortest jetting events in terms of the timescale) and, therefore, have a negligible impact on the flame perimeter, as shown in the bottom plot of Figure 4.8. These events are caused by a high-pressure build-up within the droplet and its subsequent release from a tiny rupture site (in the form of either a small crack or a pinhole) in the shell in the form of a high-velocity jet. The formation of localized tiny rupture sites is characteristic of gellants that tend to form strong-rigid shells, which have high tensile strength and can sustain high pressures before undergoing rupture. The fact that the flame perimeter reduces slightly as soon as a pinhole jet is initiated and remains at the reduced value for the entire jetting duration indicates that the droplet shell sustains high pressure, which is released suddenly in a short duration. This pressure release is accompanied by droplet shrinkage and, hence, a reduction in the flame size. Additionally, the high speed of the pinhole jet ensures that the time duration for the jet's interaction with the high-temperature flame envelope is minimal, which prevents jet expansion and, hence, its large-scale distortion. Note that compared to the pinhole jets, where the jet-flame interaction occurs over short timescales of <10 ms, the flame distortion

events occur for a substantial duration $\sim O(100 \text{ ms})$, which allows the jet to distort the flame structure significantly.

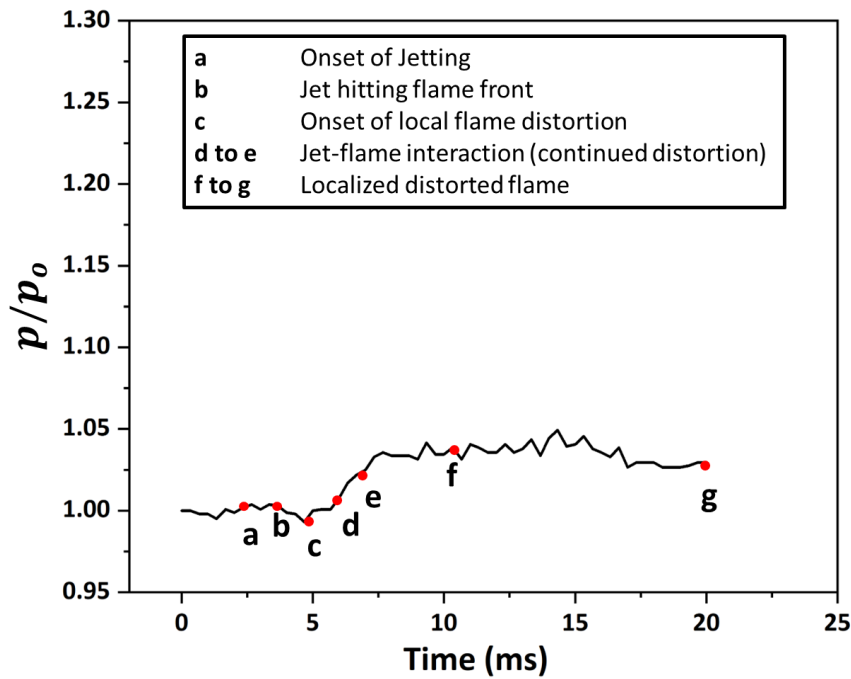
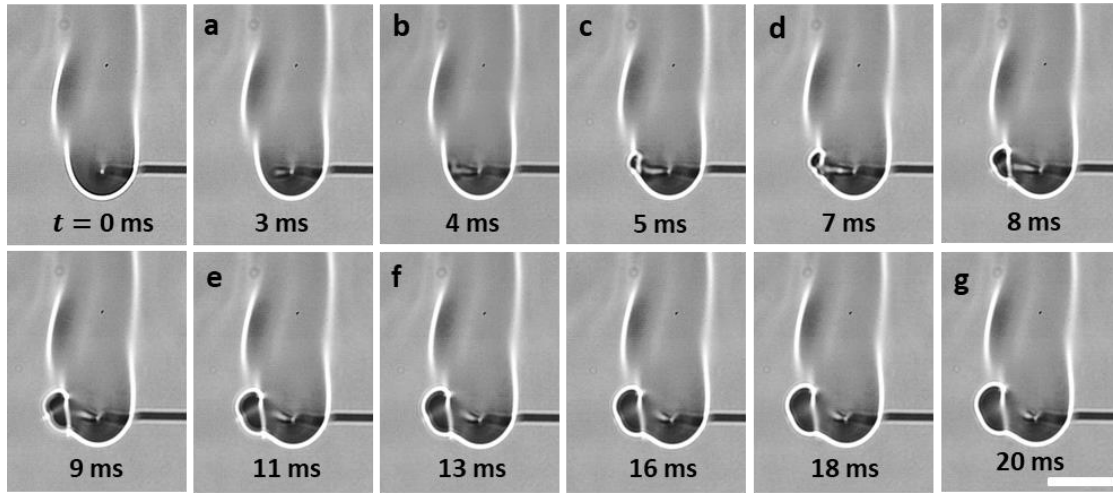


Figure 4. 6. (Top) Time-frozen snapshots of a jet causing flame distortion. The scale equals 12 mm. **(Bottom)** Temporal variation in the normalized flame perimeter characterizing the flame envelope disruption. Each point in the plot corresponds to the respective image in the top figure.

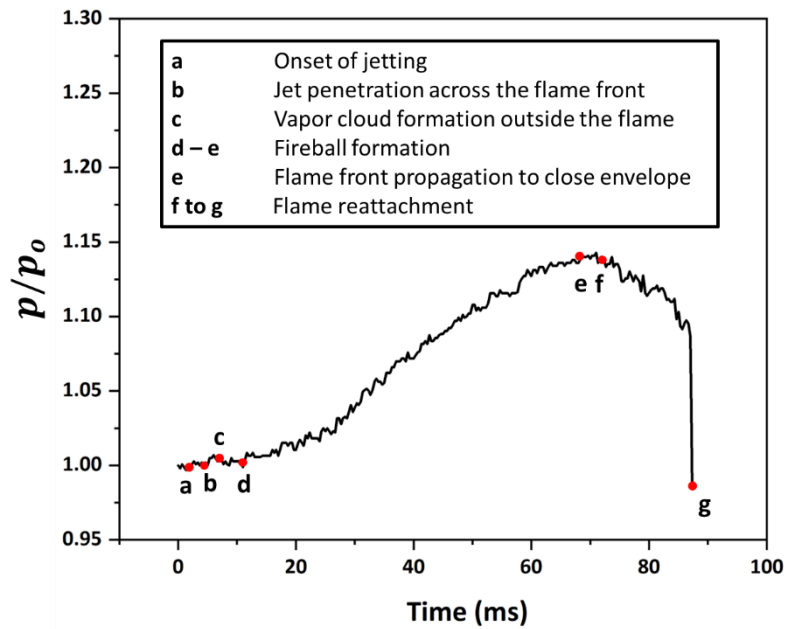
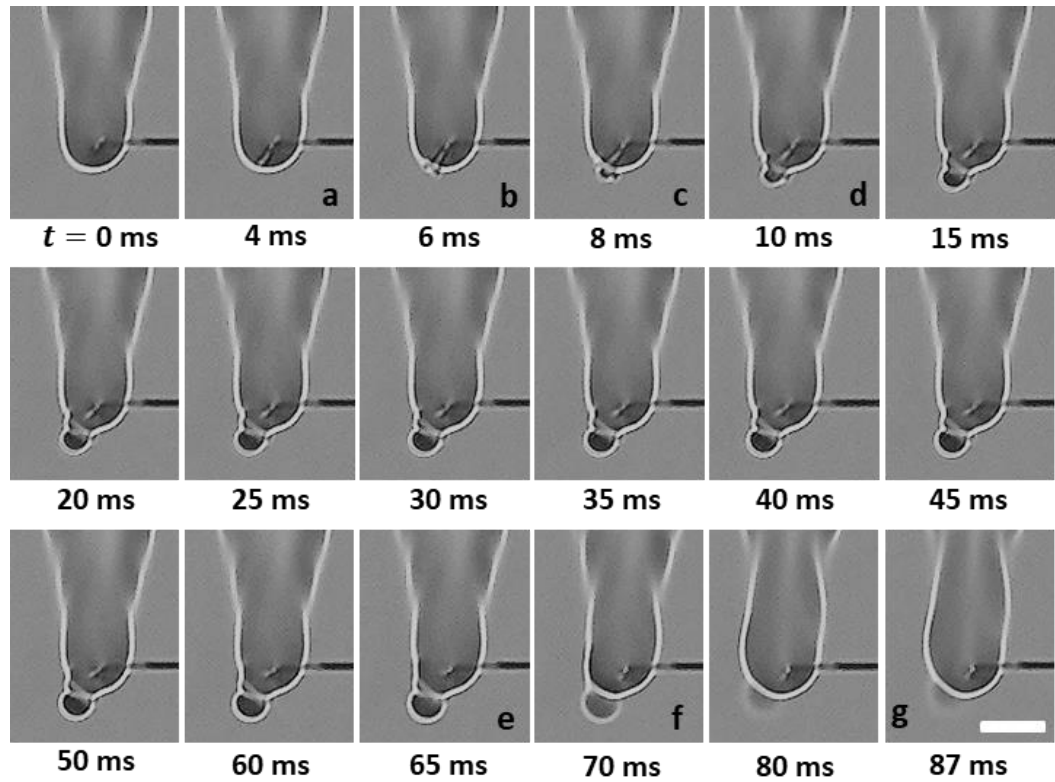


Figure 4. 7. (Top) Time-frozen snapshots of a jet forming a fire ball outside the flame envelope. The scale bar equals 5 mm. (Bottom) Temporal variation in the normalized flame perimeter for characterizing the flame envelope disruption. Each point in the plot corresponds to the respective image in the top figure.

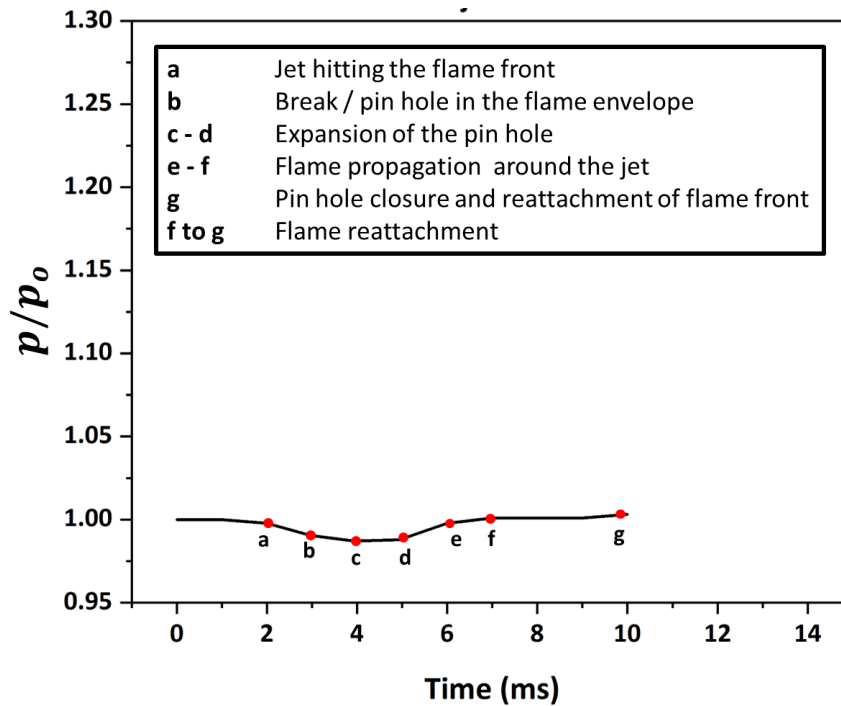
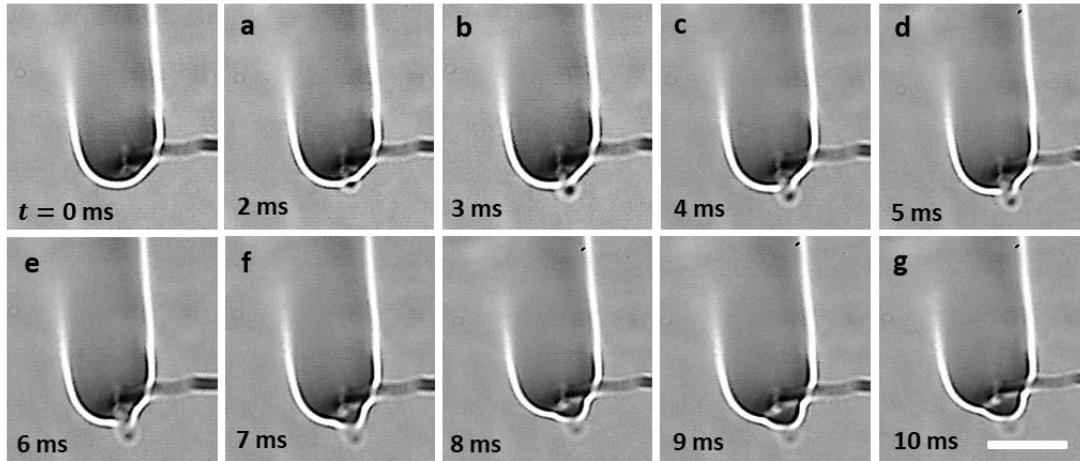


Figure 4. 8. (Top) Time-frozen snapshots of a jet breaking the flame front. The scale bar equals 10 mm. **(Bottom)** Temporal variation of the normalized flame perimeter for characterizing the flame envelope disruption. Each point in the plot corresponds to the respective image in the top figure.

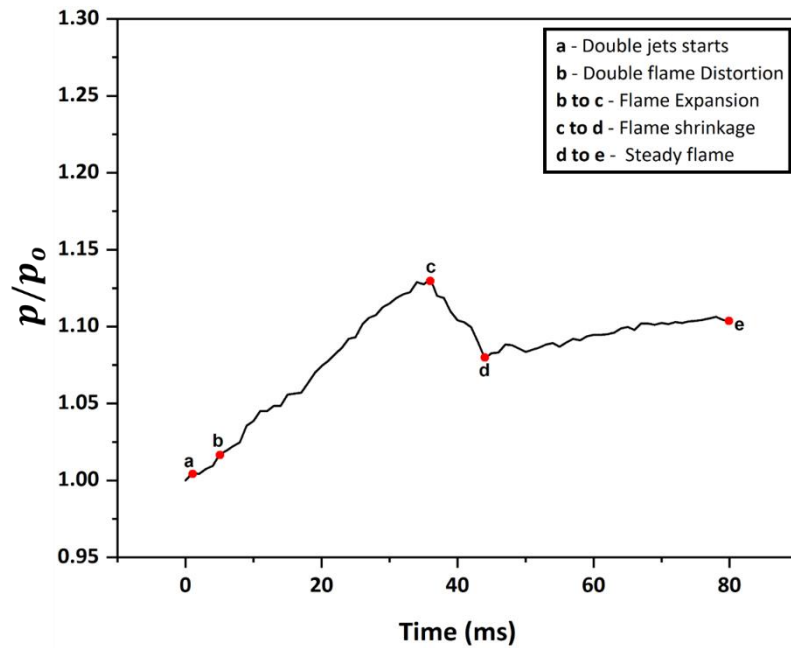
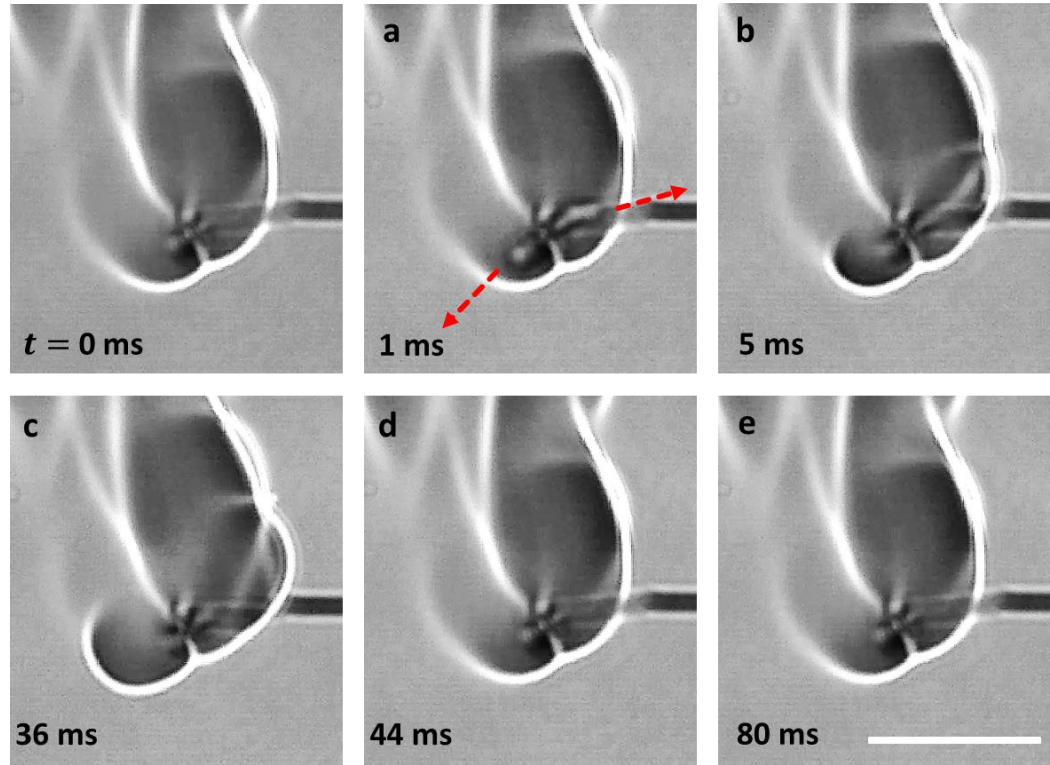


Figure 4. 9. (Top) Time-frozen snapshots of a double-jet event comprising two flame distortion events aligned at two different angular locations. The scale bar equals 15mm. **(Bottom)** Temporal variation of the normalized flame perimeter characterizing the flame envelope disruption.

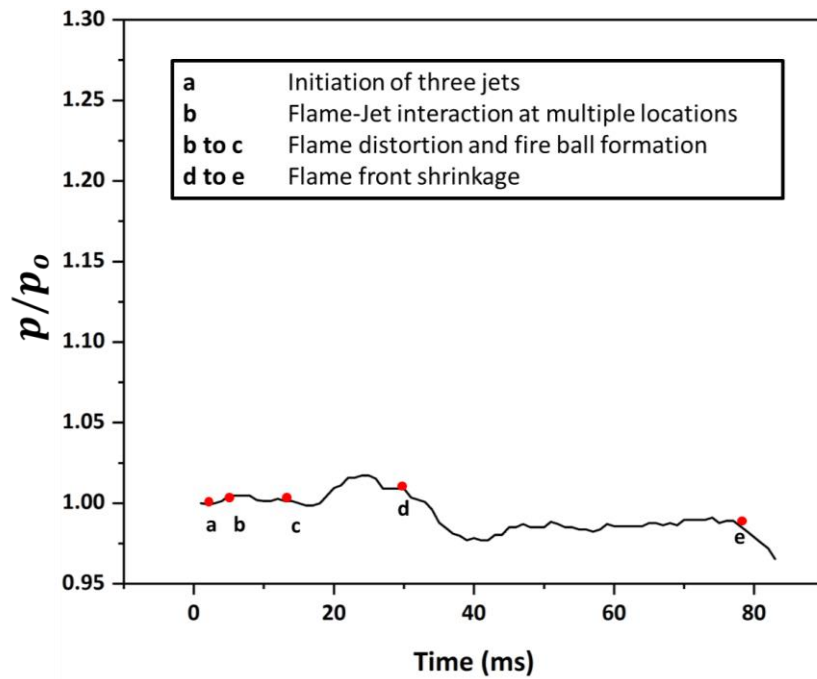
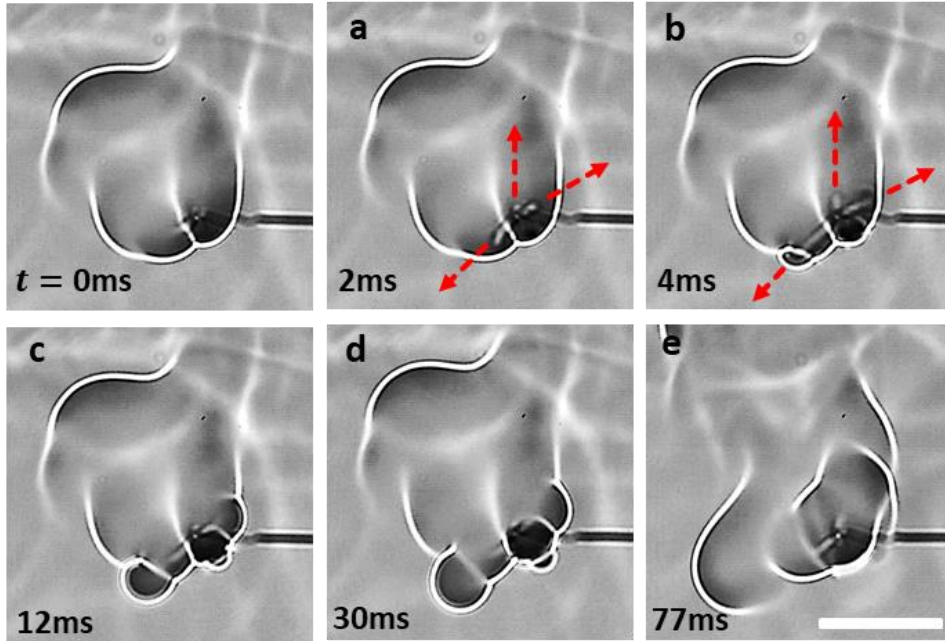


Figure 4. 10. (Top) Time-frozen snapshots of a triple-jet event comprising two fire balls and one flame distortion event, each aligned at a different angular location. The scale bar equals 20 mm. **(Bottom)** Temporal variation of the normalized flame perimeter for characterizing the flame envelope disruption.

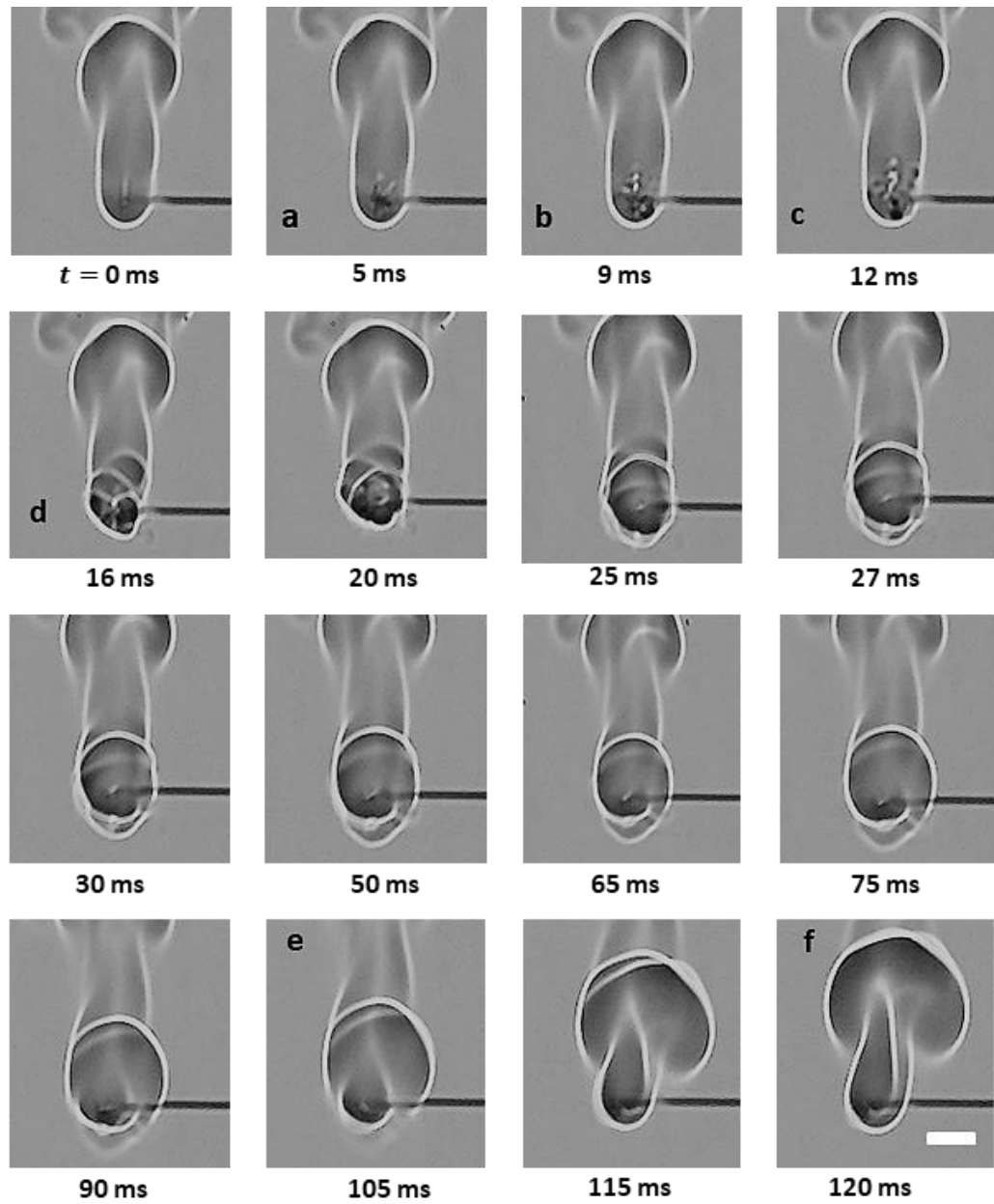
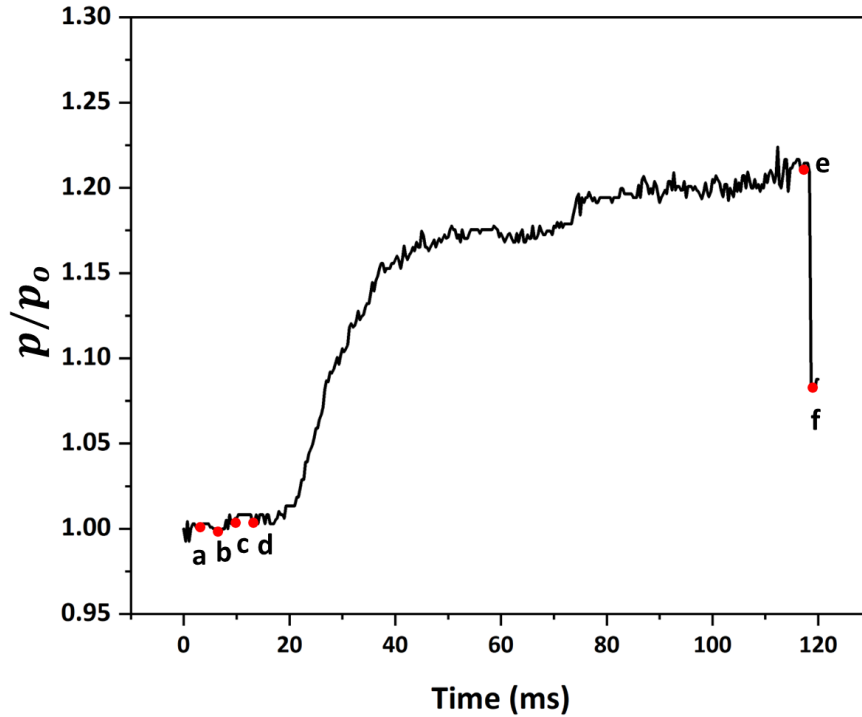


Figure 4. 11. Time-frozen snapshots of multiple jetting events caused by the random bursting of a gel fuel droplet. The scale bar equals 5 mm.



a	Droplet bursting at random locations
b	Ejection of jets at multiple locations
c	Jets touching the flame
d	Flame disruption
d - e	Flame disruption and expansion in multiple directions
e - f	Flame shrinkage and reattachment

Figure 4. 12. Temporal variation of the normalized flame perimeter resulting from the disruption caused by a random bursting event with multiple jets.

Due to the inhomogeneous structure of the gellant shell [47], the shell may rupture at more than one location, and therefore, the three types of jetting events may not occur individually, i.e., only one at a time. Instead, multiple events may either overlap or occur simultaneously. This is evident in Figures 4.9 and 4.10, which show the occurrence of two and three simultaneous jetting events, respectively. These are termed double and triple jetting events, respectively. Depending on the shell structure and the size of the ruptured hole, any combination of flame distortion, pinhole, and fireball events can occur during multiple jetting events. For instance, the double-jet event in Figure 4.9 constitutes a set of two flame distortion events occurring at 55° and 235° at speeds of 927 mm/s and 960 mm/s, respectively.

However, the triple-jet event shown in Figure 4.10 constitutes a set of two fireball events and one flame distortion event aligned at 38° , 178° , and 262° , respectively and their corresponding velocities are 1415 mm/s, 1562 mm/s, and 1121 mm/s, respectively. Due to interactions of multiple different types of jetting events with the flame, it is expected that the flame envelope undergoes random shape changes over time. This is corroborated by the non-monotonic trend of the normalized flame perimeter over time (see Figures 4.9 and 4.10). Note that a drop in the flame perimeter is observed between 36 and 44 ms in the case of a double-jet event and between 30 and 77 ms for a triple-jetting event. This is due to the termination of one of the flame distortion events in this timeframe in both cases, which reduces the degree of distortion in the flame envelope. The occurrence of multiple jetting events is also observed in a random event when the droplet undergoes sudden bursting, as shown in Figure 4.11. This random bursting event occurs following the droplet's transient heat-up period, when the bubble nucleates on the shell's inner surface and expands rapidly in a short time (< 2 ms), causing the shell to rupture at multiple sites. Since the sudden bursting of the droplet is an uncertain event and occurs rapidly with the formation of multiple rupture sites (and, hence, multiple jets), it disrupts the flame randomly. This is primarily because the jets have no specific spatial orientation, and any combination of the three types of jetting events may occur. This is evident from the nonmonotonic variation in the flame perimeter over time (see Figure 4.12), which shows that the flame perimeter remains nearly constant until 20 ms, then increases rapidly from 20 to 40 ms by $\sim 15\%$, then increases gradually from 40 to 110 ms by $\sim 5\%$, and finally exhibits a sharp drop of $\sim 13\%$ in less than 5 ms. In comparison to the other flame disruption events, the random bursting event has a lasting impact on the flame structure, as the flame remains distorted for longer timescales on the order of $\sim O(200)$ ms. It is important to note that even though the jetting event has finished, the flame may continue to be disrupted due to the expansion of the unreacted fuel vapors and their local interaction with the flame envelope. Subsequently, as the flame envelope stabilizes and reaches a steady state, its shape and perimeter may not be the same in this new state as they were before the commencement of a flame disruption event.

4.2.3 Effect of the gellant type on the jetting events

Figure 4.13 shows a comparison of the temporal variation in the jetting velocity of the burning gel fuel droplets of HPMC-3 versus MC-9 for six experimental runs. It is evident that for both types of gel fuels, the average velocity is highest in the case of the pinhole jets and lowest in the case of flame distortion events. In addition, within the experimental uncertainty, the average velocity of the three types of jetting events is the same for both the gel fuels (see Table 4.1). While the average jetting velocities are nearly the same (Figure 4.14a), the number of jetting events during the droplet lifetime is significantly higher in the case of the MC-gellant-based gel fuel droplets. The HPMC-3 fuel tends to form flame distortions (~500–870 mm/s) in substantial numbers in comparison to pin ejection (~1000–1550 mm/s) disruptions and fireballs outside the flame (~800–1530 mm/s). In the case of MC-9, along with flame distortions, pin ejections and fireballs outside the flame are found to be in abundance (Figure 4.14b). However, from Figure 4.13a,b, it can be observed that the range of the velocity distribution of each of the flame disruption events differs for both fuels. Therefore, it is worth mentioning that the velocities depicted in Figure 4.13a,b correspond to the interaction of the jets with the flame, irrespective of the magnitude of the velocity. Moreover, the number of flame distortion, fireball, and pinhole jets in the MC-based gel fuel droplet are ~1.15 times, 4 times, and 4.5 times the number of corresponding events in the case of the HPMC-based fuel droplet (Figure 4.14b). It is also apparent from the bottom plot in Figure 4.14b that the jetting behavior of the HPMC-based gel fuel droplets is dominated by the flame distortion events, which are approximately 4 times more frequent compared to the high-velocity fireball and the pinhole jetting events. In contrast, in the case of the MC-based gel fuel droplets, the number of flame distortion events is comparable to the number of fireballs and pinhole ejections.

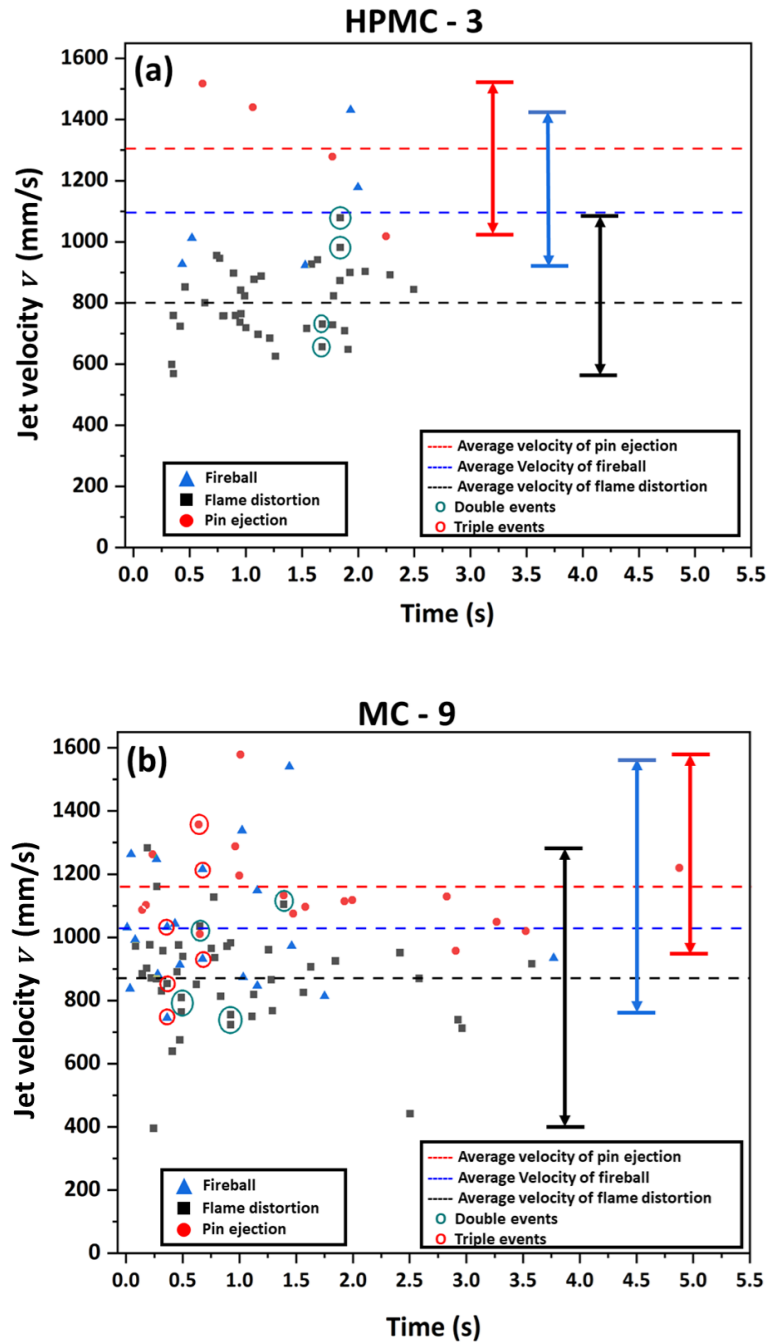


Figure 4. 13. The variation in the jet velocities as a function of time during the combustion of a gel fuel droplet: (a) HPMC-3 and (b) MC-9. The range of the velocities (vertical double-headed arrows) is shown for all three jetting events and are color-coded as black for the flame distortion events, blue for fireball events, and red for pin ejection events, alongside their average values (horizontal dotted lines) to show the range over which the jet velocities are distributed.

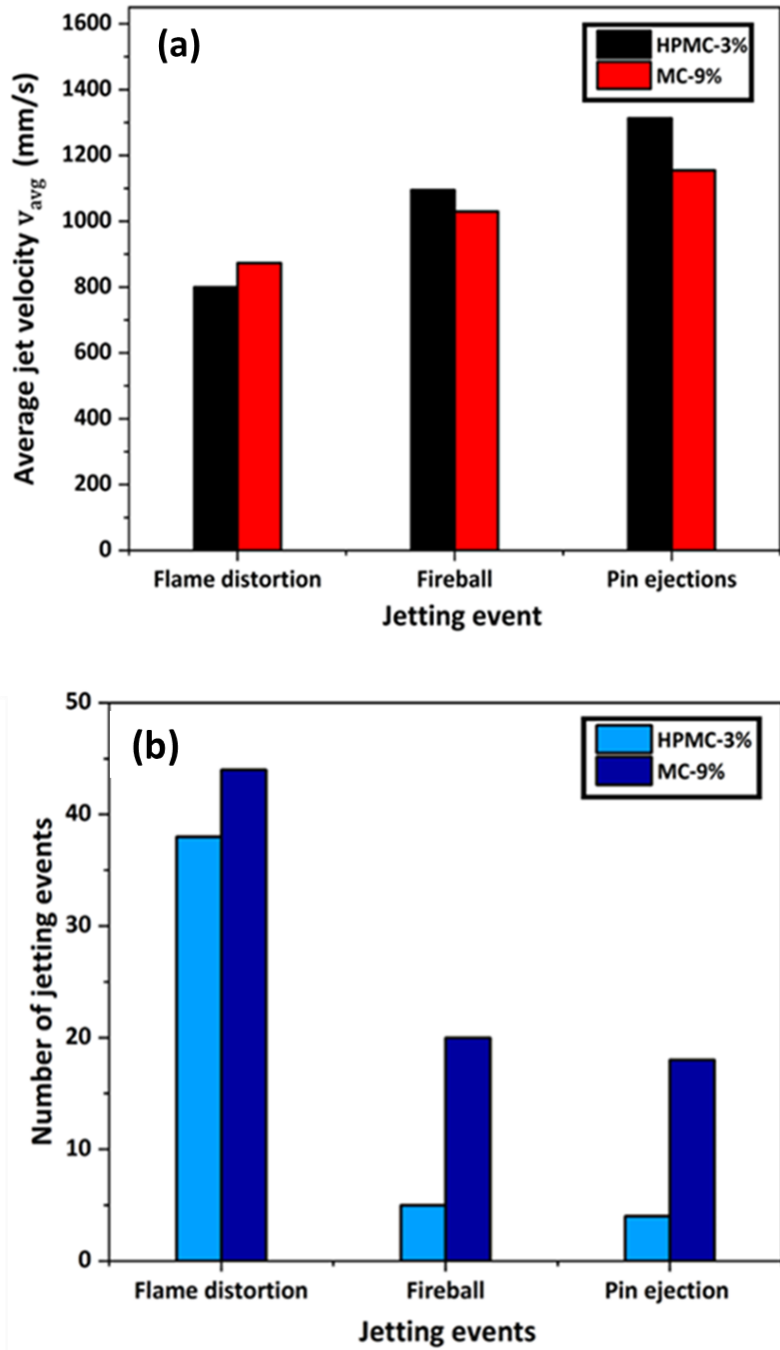


Figure 4. 14. (a) Histograms showing a one-to-one comparison of the variation in the average velocities of three types of jetting events for both the gel fuels. (b) The number of each type of jetting event (flame distortion, pinhole ejection, and fireball) for both the gel fuels.

Furthermore, for the MC-based droplets, the number of double and triple jetting events, together, is more than twice the number of corresponding events in the case of the HPMC-based droplets. In summary, jetting in HPMC-based fuels is governed by low-velocity flame distortion events, while jetting in MC-based gel fuel droplets is significantly influenced by high-velocity fireballs and pinhole jets. The difference observed in the jetting behavior of the HPMC- versus the MC-based gel fuel droplets can be explained as follows. Prior to rupture, the viscoelastic shell restrains the internal pressure in a sequential manner by stretching, thinning, and yielding, and therefore, the nature of the jetting events is governed by the rheo-physical properties of the shell, such as its thickness, yield stress, and the strain that it undergoes before and after its yield point. While it is exceedingly difficult to measure these shell properties in a dynamic combusting environment, an estimate of the properties of the freshly prepared gel fuel can provide critical insights into the nature of the shell that these gellants would form. For instance, the yield stress of HPMC-3 is ~ 25 Pa, while that of MC-9 is ~ 400 Pa [46], which indicates that the MC-9 gel fuels would facilitate a stronger shell formation compared to HPMC-3 fuels. In addition, dynamic creep analysis in previous studies [46], [47] showed that, at the same magnitude of applied shear stress below the yield stress values of both fuels, the strain endured by HPMC-3 was two orders of magnitude higher compared to the MC-9 gel fuel [46], [47]. This means that HPMC-3 gel fuel droplets have a propensity to form weak-flexible shells, while the MC-9 gel fuel droplets tend to form a strong-rigid shell. A higher strength indicates that the shell will sustain higher pressures, while a high rigidity indicates that the shell will undergo minimal deformation/expansion prior to rupture. Such a strong-rigid shell tends to rupture with small, localized cracks through which the high pressure is released in the form of fireballs and pinhole jets, i.e., the jetting events that have nominally high velocities. In contrast, a weak-flexible shell indicates that it responds to pressure build-up by stretching and expansion, i.e., its flexibility. However, as the shell is weak compared to that of MC-9 gel fuels, it is unable to sustain very high pressures.

Due to the combined effects of lower internal pressures and a high shell flexibility, the HPMC-3 gel fuel droplets form larger rupture sites that result in low-velocity jets, which are typical of flame distortion jetting events. A qualitative comparison of the rupture sites in the HPMC-3 versus MC-9 gel fuels is shown in Figure 4.15.

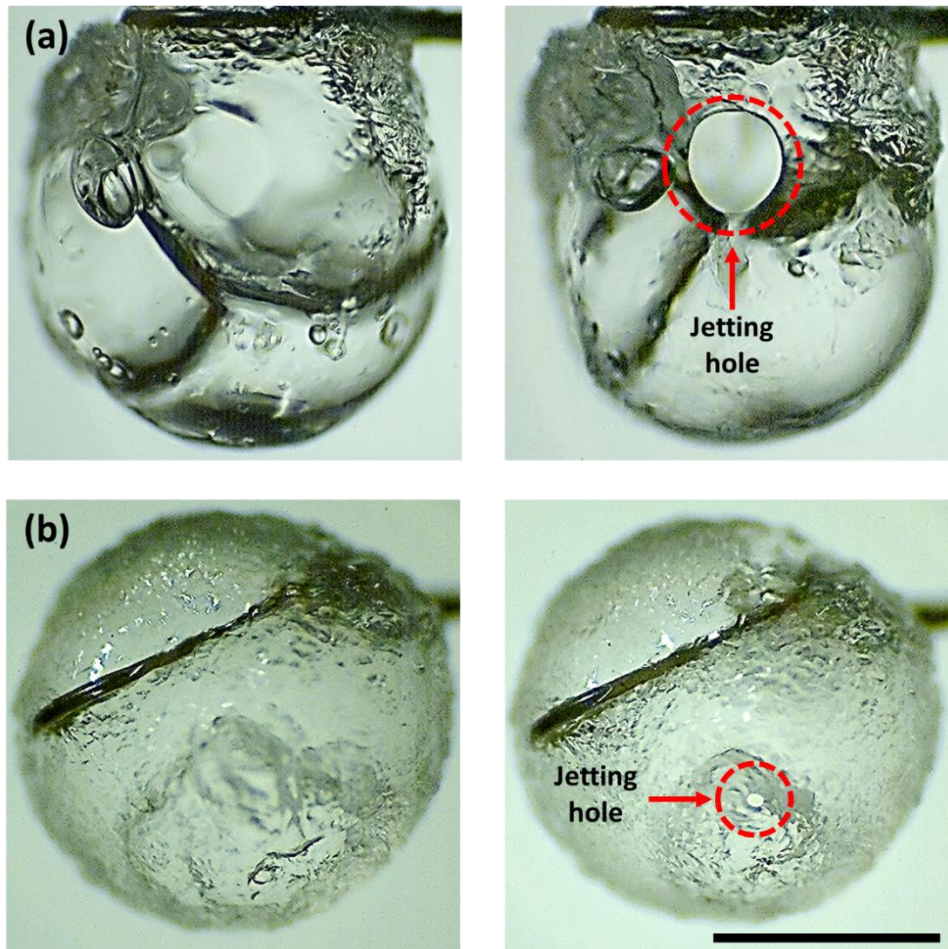


Figure 4. 15. Representative images of rupture site (dashed red circle) formation during a jetting event: (a) HPMC-3, (b) MC-9. The scale equals 1 mm.

4.3 Conclusions

Jetting is a critical phenomenon in the burning of gel fuel droplets that enables the efflux of the unreacted fuel vapors and, therefore, is likely to affect the local fuel–oxidizer ratio, gas phase mixing, and the droplet trajectory (due to the recoil thrust) in rocket engine environments. In this study, dual-mirror Z-type Schlieren imaging was used to investigate the jetting dynamics of burning gel fuel droplets at a temporal resolution of 0.33 ms and an optical resolution of 126.3 $\mu\text{m}/\text{pixel}$. The jetting behavior was investigated in ethanol gel fuels laden with two different types of organic gellants, namely, HPMC at 3 wt.% and MC at 9%. The following key conclusions are drawn from the study:

- The jetting of fuel vapors is responsible for the disruptive combustion behavior of gel fuel droplets and occurs in two potential modes, namely, either oscillatory bursting or isolated bursting, or both, where the latter features single or multiple jets initiating simultaneously.
- Both the jetting modes constitute jetting events that may either distort the flame front or form a fireball outside the enclosed flame envelope or, alternatively, break the flame front locally and form a pinhole therein. Accordingly, these events are identified as flame distortion, fireball, and pinhole jets, respectively. The pinhole jets are the highest-velocity jets ($\sim 1000\text{--}1550$ mm/s) and, hence, apply a high local shear to the flame front, thereby causing its localized extinction, which appears as a break in the flame.
- The type of the gellant and the nature of the shell that it forms determine the types of jetting events that will dominate the combustion behavior of a gel fuel droplet.
- The gellants that tend to form thin-weak-flexible shells (HPMC at 3 wt.% in this study) are associated with a low degree of internal pressure build-up and the formation of large rupture sites, which result in low-velocity flame distortion jets (500–870 mm/s). In contrast, the gellants that form thick-strong-rigid shells (MC at 9 wt.% in this study) are associated with a high degree of internal pressure build-up and the formation of tiny, localized rupture sites,

which result in the high-velocity flame ball (800–1530 mm/s) and pinhole jets (1000–1550 mm/s).

While some models can predict the bursting of burning gel droplets, they cannot quantify the types of jetting events, their spatiotemporal evolution, and their interplay with the flame envelope. In this light, the jetting dynamics deciphered in this study using Schlieren imaging provide a fundamental understanding of the chaotic combustion behavior of organic-gellant-laden gel fuel droplets.

CHAPTER 5: COMBUSTION STAGES OF ORGANIC-GELLANT-LADEN FUEL DROPLETS

Gel fuels are multi-component fuels, and their combustion behavior is different from conventional solid and liquid propellants. To develop a fundamental understanding of the vaporization and combustion of gel fuels, pendant mode experiments are performed for ethanol-based organic gel fuels by capturing high-speed video data. Primarily, two non-metalized ethanol-based gel fuels containing organic gellants Hydroxypropyl methylcellulose (HPMC) and methylcellulose (MC) are taken for experiments. Both fuels have shown three distinct combustion stages namely transient heat up (stage I), disruptive burning (stage II), and carbonization (stage III). The demarcation of the stages is done by visual evidence backed by high-fidelity high-speed video data. In stage I, phase separation occurs which leads to the formation of gellant shells. Organic gellants tend to form viscoelastic shells which significantly influence the jetting behavior during the disruptive burning (stage II). The combustion of gel droplets in stage II exhibits characteristic differences in bursting mechanism, for instance, oscillatory and transient bursting in HPMC and transient bursting in MC. Moreover, droplet-bursting traits influence jetting attributes and burn rates. Besides, the bursting of gel droplets is also dependent on the thickness of the gellant shells. The thin and weak shells are prone to bulk droplet motion due to active jetting, whereas the thick and rigid shells act as kinetic energy dampeners and thereby inhibit the bulk motion of droplets. Apart from disruptive burning, carbonization is a significant part of the combustion during which the suppressed jetting behavior is seen due to the traces of fuel trapped in the gellant shells. Jetting influences burn rate significantly which can be seen during the disruptive burning in contrast to the other two stages of combustion for both the gel fuels under study. Furthermore, combustion residue analysis is carried out to assess the variation in shell morphology across the stages.

5.1 Introduction

Modern-day aerospace propulsion systems are scaling new heights of innovation in technology and performance [107]. Alongside performance, parameters like reusability, ease of processing, reliability, and ecological safety fuel sources [32], [55]–[58] are of prime interest in the contemporary era. Gelled propellants are such propellants that can potentially replace conventional solid and liquid fuels by integrating their benefits and concurrently negating their disadvantages, therefore they are considered promising candidates for hybrid rocket and ramjet propulsion systems[36]. The liquid propellant is widely used as either a mono or bipropellant. It is pumped/fed under pressure and an atomization system is used to spray the liquid into the combustion chamber [54]. The easy throttle control of liquid propellants makes them superior to solid propellants, but they have their inherent drawbacks. A major issue to be considered with all the classes of liquid propellants is sloshing in the storage tanks, which has long been identified during the landing of the Apollo 11 lunar module[54], [60] . A major disadvantage of the typical liquid propellants is the likelihood of leakage and spills during handling, this becomes a key concern specifically in the case of hazardous hypergolic liquids [32], [54]–[58]. Modern-day high-performance and energy-dense cryogenic liquid propellants have their utility, but these liquid propellants are more difficult to handle and suffer from high evaporation losses [108], embrittlement of the storage vessel, and difficulty in storage under zero gravity [54]. A liquid propellant is susceptible to accidents due to leakage that can occur in-flight or on the ground. Hence, incorporating gelling into all the above liquid propellants can nullify or mitigate these disadvantages to a certain extent [54]. Solid propellants do not have issues with storage and handling [32], [55]–[58], but they also have certain disadvantages. The solid propellants are vulnerable to impact, friction, and electrostatic discharge and are susceptible to accidental ignition [32]. The gel propellants are relatively less sensitive to accidental ignition. Moreover, the viscoelasticity associated with the gel propellants aids during the storage and solid-to-liquid transformation within the delivery system thereby eliminating the possibility of cracks in the propellant structure and

thus preventing uncontrolled combustion [32]. Gel propellants have proved longevity in terms of storage without settling or separation [24], [28], [33], [63], [109], and phase separation occurs only at high acceleration levels [24]. The high viscosity of the gel fuels during the storage facilitates the suspension of metal additives like Boron (B), Aluminum (Al), Magnesium (Mg), etc. into the fuel matrix which has proven to increase energy density and specific impulse with a stable suspension of the additives [23], [24], [28], [33], [57], [63], [109], [110]. Furthermore, the shear-thinning behavior of gel propellants at high shear enables the ease of pumping into the combustion chamber analogous to liquid propellants leading to effective atomization through the fuel injectors [26], [64], [65], [94].

Despite all these potential advantages gel propellants have certain issues too which are needed to be considered. Too much stability makes the gel invariably viscous thus resulting in difficult flow and atomization during the injection. Therefore, the viscosity of the gel propellants must have a magnitude within the range suitable for atomization [54]. Gel propellants have complex combustion nature compared to solid/liquid counterparts. A characteristic of gel propellants is disruptive burning which is accompanied by jetting of unreacted fuel vapors [70], [71]. The jetting caused by unreacted fuel vapors impacts the flame and distorts it [39], [40]. Moreover, jetting can be affected by the alteration of different parameters like initial droplet diameter [41], ambient conditions [41], [42], [106], and by varying the base fuel, gellant concentration, or type (inorganic, organic or cryo-gels) [48]–[50]. For the interpretation of the combustion mechanism of the gel propellants, many experiments, and theoretical models [73] have been proposed among which Spalding's d^2 law model [111] is widely used. However, due to the complexity of gel droplet combustion, almost all models are established under some assumptions. Consequently, it is challenging to establish a universal model to precisely describe single droplet combustion. Furthermore, due to the existence of gelling agents and energetic particles, the combustion of gelled droplets is more complex than that of liquid droplets.

Literature review on gel droplet combustion reveals that most of the studies are done either on a droplet scale or jet visualization at the flame scale [39]–[42], [70], [71], [106]. Also, some studies are focused on the characterization of combustion stages of gel fuel droplets. Initially, the study was conducted by Solomon et.al.[71] for organic gellant-based fuel which gave insights into the demarcated stages of combustion. They classified the combustion into four stages comprising classic droplet combustion, phase separation of gel fuel components, Viscous gellant shell formation, and lastly, combustion gellant shell. D.P. Mishra et.al performed studies on aviation turbine fuel (Jet A1) based organic gel fuel [41], [42] and concluded that the combustion of Jet A1 organic gel fuel takes place via four stages namely, 1) the phase separation of the fuel components 2) formation of gellant layer, bubble nucleation and the onset of microexplosion 3) Vigorous microexplosion 4) subsequent uniform regression of droplet. Liu et.al performed experiments on freely falling Unsymmetrical Dimethylhydrazine (UDMH) fuel droplets to simulate the real-time combustion situation of a combustion chamber [106] and classified the combustion of UDMH in three distinct phases: gellant layer formation, bubble formation, and growth, vapor jetting. These studies provide a perspective into the combustion behavior of gel fuels and there exists an agreement on the fact that the combustion of gel fuels takes place in stages. But there is still ambiguity associated with the demarcation of stages and the role of the gellant shell during combustion. Moreover, there has not been much information available on the carbonization phase which occurs only at the end of the gel droplet's lifetime. It is worth mentioning that the terms jetting and microexplosion [101]–[103] have often been used in the classification of the combustion stages to account for the disrupting burning behavior of the gel fuel droplets. However, these phenomena are completely different from each other. A Micro explosion event is inherently a sudden catastrophic break-up of the droplet caused by rapid internal gasification of a highly volatile component. During this, the low boiling points entities get entrapped in the droplet core due to diffusion and further get superheated to their homogenous boiling limit. This leads to an immense pressure buildup inside the droplet and subsequently a catastrophic rupture of the droplet occurs. Hence the

micro explosion is a one-time event, and its occurrence leads to the end of the droplet's lifetime as reported by Law[74], [96], [97]. On the contrary, jetting events are not a single-time event, they occur throughout the entirety of the droplet lifespan in the form of perpetual bubble formation, growth, and collapse, which leads to jetting of unreacted fuel vapors [47]. Inherently, continuous bubble formation and growth are characteristics of heterogeneous boiling, unlike microexplosions [47]. In the current study, an effort is made to study the combustion characteristics of organic gel fuel droplets and their subsequent combustion stage classification. Primarily, two fuel combinations are taken for experiments. The gel fuels are non-metalized ethanol-based fuels containing organic gellants Hydroxypropyl methylcellulose (HPMC) and methylcellulose (MC). Both fuels are categorized into three distinct combustion stages namely transient heat up (stage I), disruptive burning (stage II), and carbonization (stage III). The demarcation of the combustion stages is supported by high-fidelity high-speed video data. The organic gellants tend to form viscoelastic shells hence their effect on the combustion behavior cannot be disregarded, therefore during the disruptive burning stage (stage II), the characteristics of the gellant shell and their effect on combustion are studied, as in both the fuels the shell bursting mechanisms differ viz. oscillatory and transient bursting in HPMC-3% and transient bursting in MC-9%. The jetting-associated bulk motion of gel droplets is also assessed to gauge droplet trajectory during the three stages of combustion. The current work also aims to explain the distribution of flame disruption events taking place across the three combustion stages. Alongside this, burn rate and combustion residue analysis are done for all the stages of combustion. A detailed discussion of the above is done in the sections to follow.

In this study, two fuel combinations were taken for the experiments. The gel fuels used were non-metalized ethanol-based fuels containing organic gellants. Gelled ethanol fuel is a tri-component fuel that consists of two different organic gellant combinations: (1) research-grade ethanol (99.8% pure; CAS No. 64-17-5) as the base fuel and (2) the gelling agents or gellants i.e., hydroxypropyl methylcellulose (HPMC; CAS No. 9004- 65-3, $\rho_b \sim 689.19 \text{ kg/m}^3$) and methylcellulose (MC; CAS No. 9004-67-5, bulk density $\rho_b \sim 503.92 \text{ kg/m}^3$). MC has a methoxy group ranging

from 27.5 to 31.5%, while HPMC has both active hydroxyl and methoxy groups ranging between 7–12% and 28–30%, respectively [46]. (3) Double-distilled water served as the base solvent for organic gellants. The properties and compositions of both fuel formulations are detailed in Table 3.1. Note that while the HPMC-based gels fuels were prepared over a range of concentrations from 3 to 6%, with a range of 8–9% for the MC-based fuels, for brevity, the results are presented for only two cases, because these fuels represent two extreme cases of combustion behavior.

The details of fuel formulation steps, the high-speed-imaging setup at droplet and flame scale, geometric parameter extraction at droplet and flame scales, and thermogravimetric analysis is given in Chapter 3.

5.2 Results and Discussion

In the current study, the characterization of combustion stages is done for both the fuels (Ethanol-based HPMC-3% and MC-9%) The demarcation of stages is done into three namely: Stage I Transient heat up, stage II disruptive burning, and stage III carbonization. The stages are categorized based on visual evidence captured during the high-speed imaging of the droplet combustion which is discussed in detail in the subsequent sections.

5.2.1 Stage I: Transient heat up

In Figure 5.1 during the combustion of both fuels, nearly the first 20% of the droplet lifetime marks up for the transient heat-up stage. After the ignition of the droplet, the heat flux is supplied to the outermost part of the droplet which is in the closest proximity to the flame. Gradually, the flame front engulfs the entire droplet's peripheral surface. Furthermore, with time, the amount of heat energy absorbed by the droplet increases. Consequently, phase separation of tri-component gel fuels initiates from the outer layer of the droplet and thus the gellant shell formation begins [39]–[42], [70], [71]. However, the inner layer core region of the droplet still has a pristine gel composition [42], [47], [71]. Moreover, in stage I the gel droplets

of both gel regress due to heating and evaporation. During the transient heat-up stage, for both fuels, gellant shells formed due to phase separation.

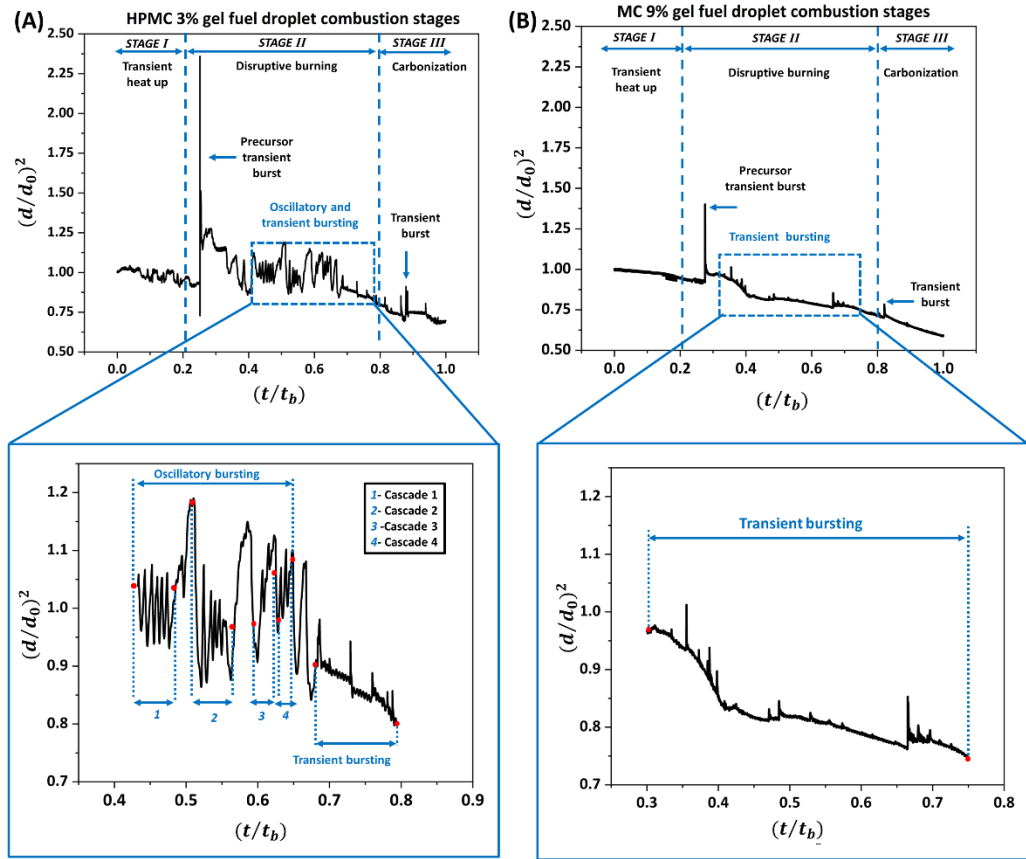


Figure 5. 1. Combustion stage characterization based on droplet diameter and time histories for ethanol-based gel fuels droplet of (A). HPMC-3% (B) MC-9 %.

5.2.2 Stage II: Disruptive Burning

In the transient heat-up stage, the gel fuels undergo phase separation leading to the formation of the gellant shell. Underneath the shell, the base fuel and solvent are trapped which begins to boil. The boiling of the individual components of the gel fuels follows the order of volatility. In both HPMC-3% and MC-9%, ethanol, and water have boiling points at 78.37 °C and 100 °C, while for the gellants the boiling points are 1101.5 °C (HPMC) and 507°C (MC) respectively at atmospheric pressure. Evidently, ethanol and water are the most volatile, leading to the formation of respective vapors, while the gellants HPMC and MC being least

volatile aid in the further formation of the shell which surrounds the vapors during this stage.

In Figure 5.1 initially, during the second stage of combustion, it is observed that the changes in the volume of the gel droplets for both cases of fuels are negligible. During this duration, the vapors of the volatile components form bubbles and subsequently coalesce to form bigger bubbles. Consequently, bubbles accumulate in the inner periphery of the gellant shell leading to a rise in pressure inside the shell (Figure 5.2b and c). In the case of both fuels due to the accumulation of bubbles a transient burst initiates that leads to the escape of unreacted fuel vapors. The transient bursting event is the first jetting event hence it is termed a precursor transient bursting event and for both the gel fuel combinations it is observed as shown in Figures 5.2(d and e) and 5.4 (b and c). Moreover, the sudden rupture of the gel droplet has a drastic effect on the instantaneous volume, and hence huge volume change is seen in the cases of gel fuels. In the case of HPMC-3% gel fuel the change of volume is about 2.3 times while for the MC-9% gel fuel, it is nearly 1.3 times the original volume (Figures 5.3 and 5.5). The differences in the volume expansion can be due to the variation in gellant shell traits as HPMC-3% forms thin, weak, and flexible shells contrary to the thick, strong, and rigid shell for MC-9%.

The precursor transient burst event is marked by the sudden rupture of gel droplets at various locations. These locations formed provides pathways for the escape of unreacted vapors of base fuel (Figures 5.2 and 5.4). The precursor burst event is a high intensity rupture event. Therefore, it is difficult to pinpoint the rupture locations during these events. However, there are observable differences in the sudden rise of volume for both cases of fuels under study, this can be attributed to the differences in the characteristics of the gellant shell. The thin-weak-flexible shell of HPMC-3% undergoes precursor transient burst via stretching, thinning, and yielding as reported by Kunin et.al. and Miglani et. al.[47], [73] .In the case of MC-9%, the strong and rigid shell (yield stress ~ 17 times HPMC-3%) does not undergo

significant expansion and leads to a gradual pressure build-up. Consequently, a sudden rupture of MC-9% shell occurs that manifests as a precursor transient burst.

In succession to the precursor transient burst event, the gel droplets for both fuels undergo shell recovery owing to the viscoelasticity of the gellants. The shell recovery is achieved by shell re-attachment and re-orientation as shown in Figures 5.2(g to i) and 5.4(d to f).

The disruptive burning occupies a significant duration of the droplet lifetime for both sets of fuels and it is nearly 60% of the droplet lifetime as shown in Figure 5.1. However, it is seen that during this stage of combustion, significant differences in the droplet rupture behavior exist.

The HPMC-3% gel fuel composition during the disruptive burning stage shows oscillating behavior in fluctuations on the diametrical plot (Figure 5.1A). This is an indication of the oscillatory bursting behavior of the gel droplet which takes place as sequential ruptures. Consequently, the gellant shell ruptures at a weak spot leading to the formation of a hole that provides a preferential escape route for the outflux of the unreacted fuel vapors via jetting as shown in Figure 5.6. During this jetting phase, the rupture site goes through irregular cycles of inflation and deflation. The phenomenon is known as the oscillatory rupture cascade which was studied by Miglani et.al. [47] for HPMC-3%. In a cascade, the droplet bursting at any instant of time is governed by a competing state taking place between the boiling of unreacted ethanol fuel which has an affinity towards causing pressure surges inside the gellant shell and the viscoelasticity of the shell. Moreover, the shell restrains this pressure surges through stretching, thinning, and yielding of the gellant shell [47].

In the case of the MC-9% gel fuel combination, the gel fuel droplet experiences rapid expansion and contraction taking place during very short time scales due to pressure surges. Since the rigid shell of MC-9% inhibits the rapid expansion of the gellant shell, therefore, the diametrical plot shows transient spikes unlike oscillatory bursting in HPMC-3% based gel fuel as shown in Figure 5.1B. Thus, MC-9% gel fuel is subjected to a transient pressure buildup. The pressure release

takes place via jetting holes and cracks in the hardened shell. The cracks not only nullify the pressure upsurge but also act as preferential sites for the accumulation of the fresh gel from the droplet core, which on receiving the heat flux from the flame help in escaping unreacted ethanol vapors as jets.

The progression of combustion during the disruptive burning (stage II) leads to the hardening of the gellant shell. Consequently, the droplet rupture behavior changes. In HPMC-3% the oscillatory behavior diminishes, and the ensuing ruptures occur in the form of transient droplet bursts. These transient bursts can occur in different modes like single or multiple (double). The representative cases of single and multiple bursts are illustrated in Figures 5.7 and 5.8 respectively. In the case of MC-9%, the rupture of the gellant shell continues to take place as transient bursts in single and multiple modes due to hardening. A representative case of a single mode is shown in Figure 5.9 for MC-9%. At the end of the disruptive burning stage, a decrease in the diametrical fluctuation is seen for both fuels (Figure 5.1) which indicates a substantial loss of unreacted ethanol fuel due to evaporation and jetting. Most of the components which remained are the gellants (HPMC and MC) due to their high boiling points. Also, at this juncture, gellants are the key contributor to the burning of the flame.

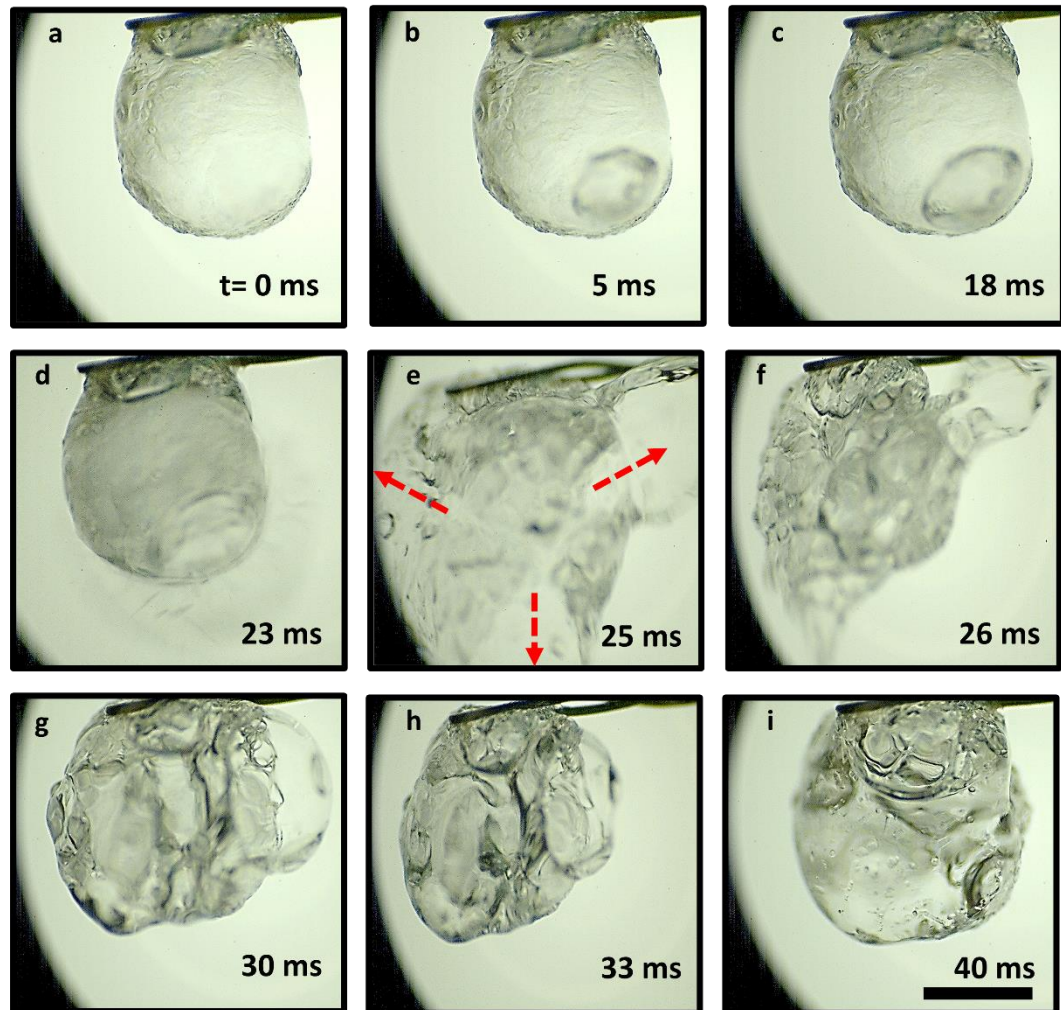


Figure 5. 2. Bursting dynamics of a precursor transient burst event for ethanol based HPMC-3% gel fuel. **(a)** Swollen droplet at $t= 0$ ms. **(b to c)** localization of bubbles at the preferential site $t=5$ to 18ms. **(d)** Sudden rupture due to drastic pressure build-up and beginning of precursor transient burst at $t=23$ ms. **(e to f)** Initiation and progression of burst from multiple locations at $t= 25$ and 26ms respectively of the ruptured gellant shell (red arrows). **(g to h)** Beginning of formation of shell following shell retraction from $t=30$ to 33ms. **(i)** Completely recovered gellant shell after the precursor random burst. At $t=40$ ms. The scale bar equals 0.7 mm.

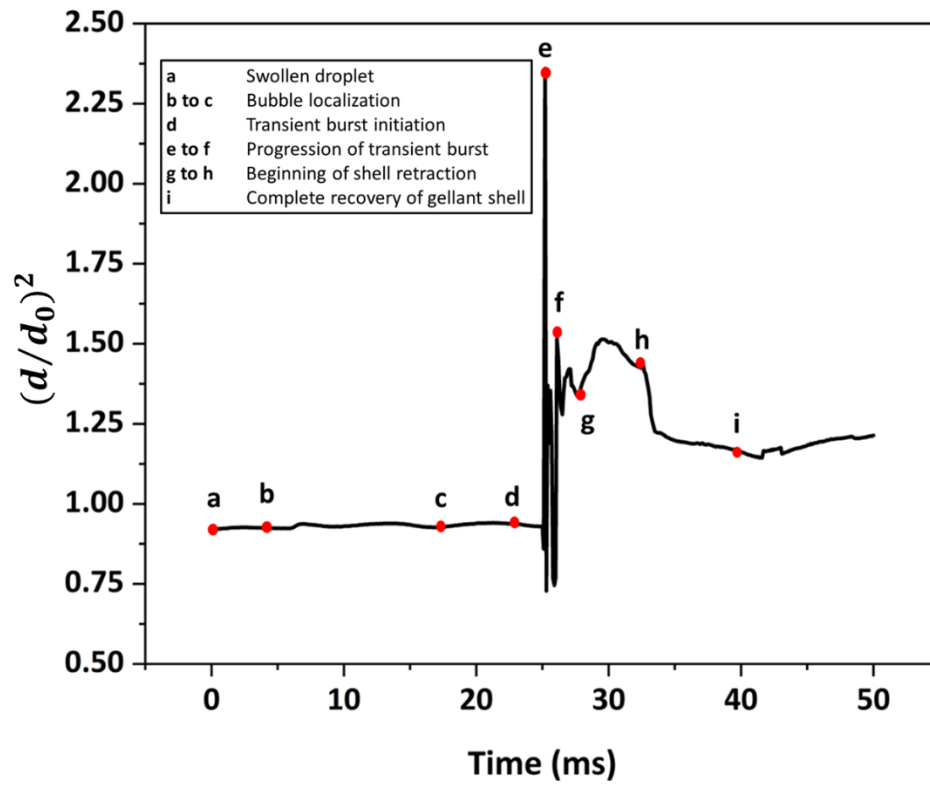


Figure 5. 3. Temporal variation of droplet diameter during a precursor transient burst in sync with the bursting dynamics for ethanol-based HPMC-3% gel fuel.

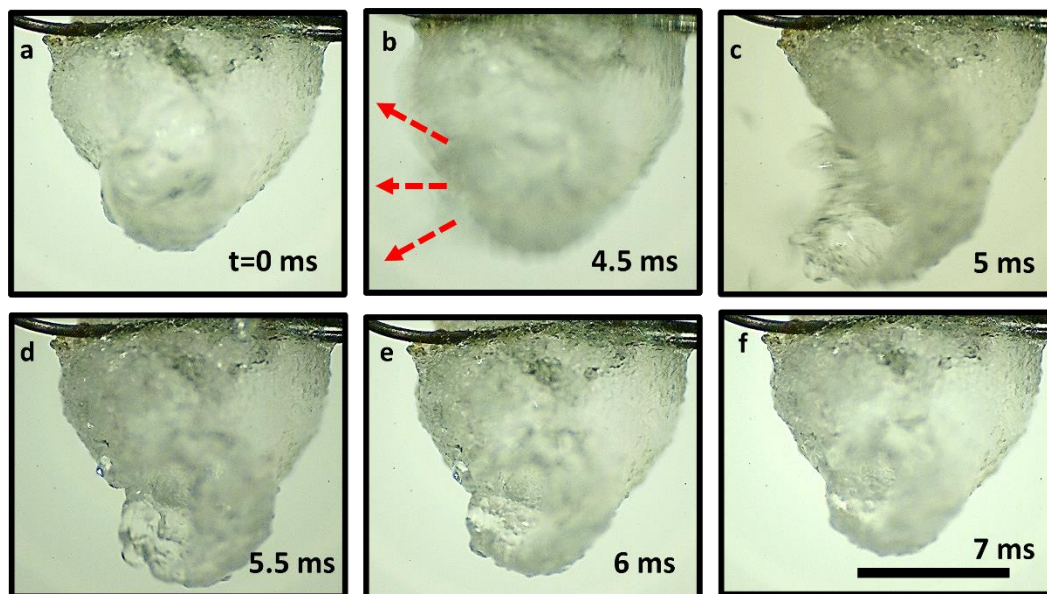


Figure 5. 4. (Top) Bursting dynamics of a precursor transient burst ethanol-based MC-9% are as follows: **(a)** swollen droplet state at $t=0$ ms. **(b)** Initiation of burst at $t=4.5$ ms (red arrows). **(c)** Rupturing of droplet causing it to open at $t= 5$ ms. **(d to e)** retraction of the gellant shell at the site of the rupture at $t= 5.5$ to 6 ms. **(f)**. Complete closure of the rupture site at $t= 7$ ms. The scale bar equals 1mm.

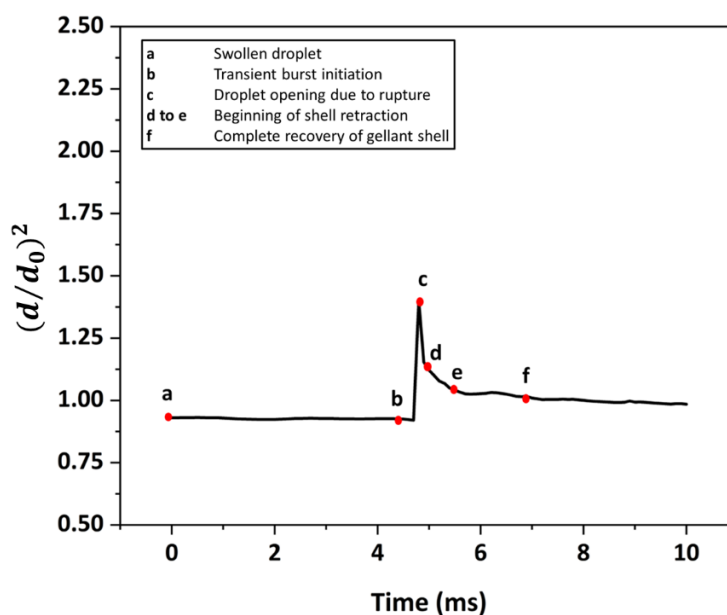


Figure 5. 5. Temporal variation of droplet diameter during a precursor transient burst in sync with the bursting dynamics for ethanol-based MC-9% gel fuel.

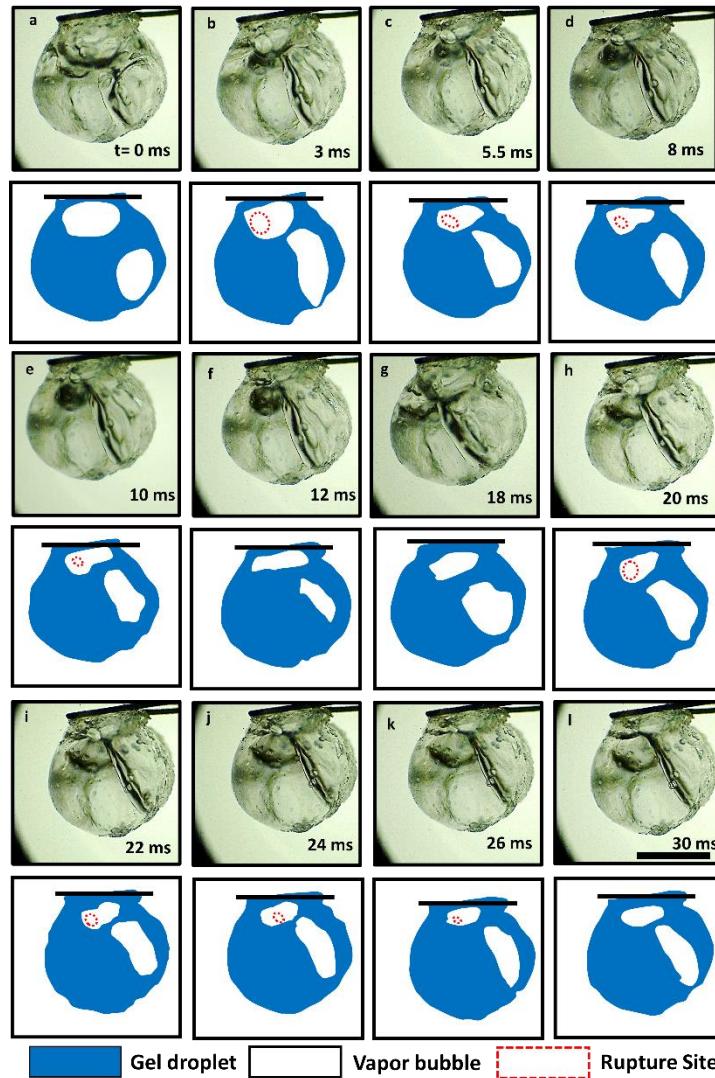


Figure 5. 6. Sequential progression of jetting due to oscillatory rupture cascades consisting of 6 bursting cycles of HPMC-3% based ethanol gel fuel droplet fuel. The corresponding schematic of each image is shown beneath for clarity. Out of the 6 cycles, the first 2 cycles (**a to f and g to l respectively**) have been represented. Cycle 1 (**a**) Swelling of droplet due to pressure surge $t=0$ ms. (**b**) Formation of a jet hole at $t=3$ ms. (**c to e**) retraction of jet hole at $t=5.5$ ms to 10ms. (**f**) complete shell recovery and closure of the jet hole and inflation of droplet begins $t=12$ ms. (**g**) The onset of cycle 2 at $t=18$ ms (**h**) formation of the jet hole at $t=20$ ms. (**i to k**) retraction of the jet hole at $t=22$ ms and 24ms respectively (**l**). Complete closure of hole and further initiation pressure build-up for subsequent rupture cycles $t=30$ ms. The scale bar represents 1mm.

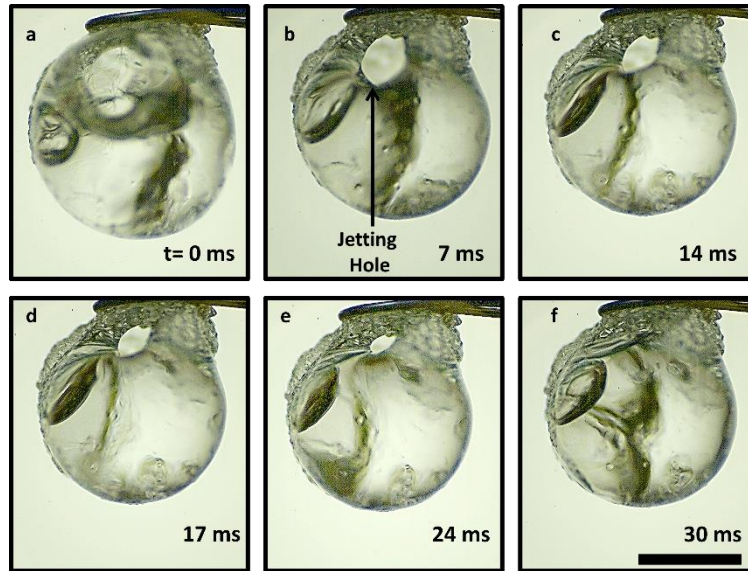


Figure 5. 7. Dynamic rupture sequence of single burst for ethanol based HPMC-3% gel fuel. **(a)** Swelled droplet at $t=0$ ms **(b)** Creation of rupture site to release pressure via jetting $t=7$ ms. **(c to e)** Initiation of hole retraction from $t=14$ to 24ms. **(f)**. Complete closure of hole at $t=30$ ms. The scale bar equals 0.7mm.

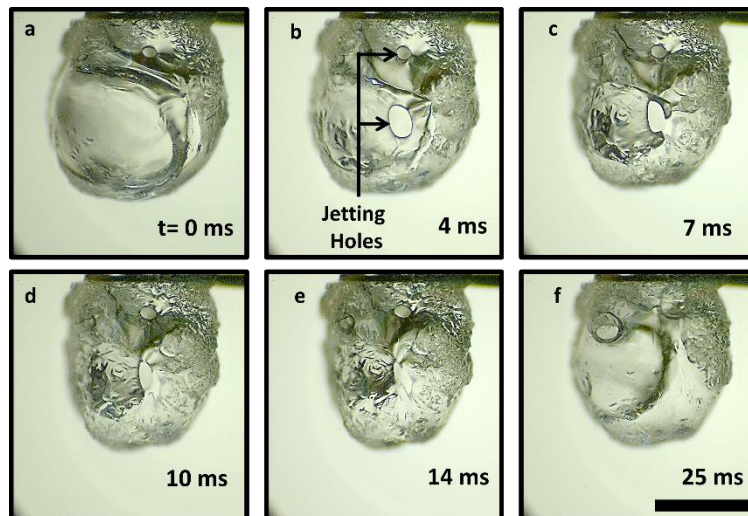


Figure 5. 8. Representative Image sequence demonstrating the double bursting of HPMC-3% gel droplets causing double jets. **(a)** gel fuel droplet at the initial position with a pre-existing hole at $t=0$ ms. **(b)** Rupture initiation and formation of two simultaneous holes for jetting at $t=4$ ms. **(c to e)** initiation of hole closure via retraction at $t=7$ to 14 ms **(f)**. closure of the holes at $t=25$ ms. The scale bar equals 0.7mm.

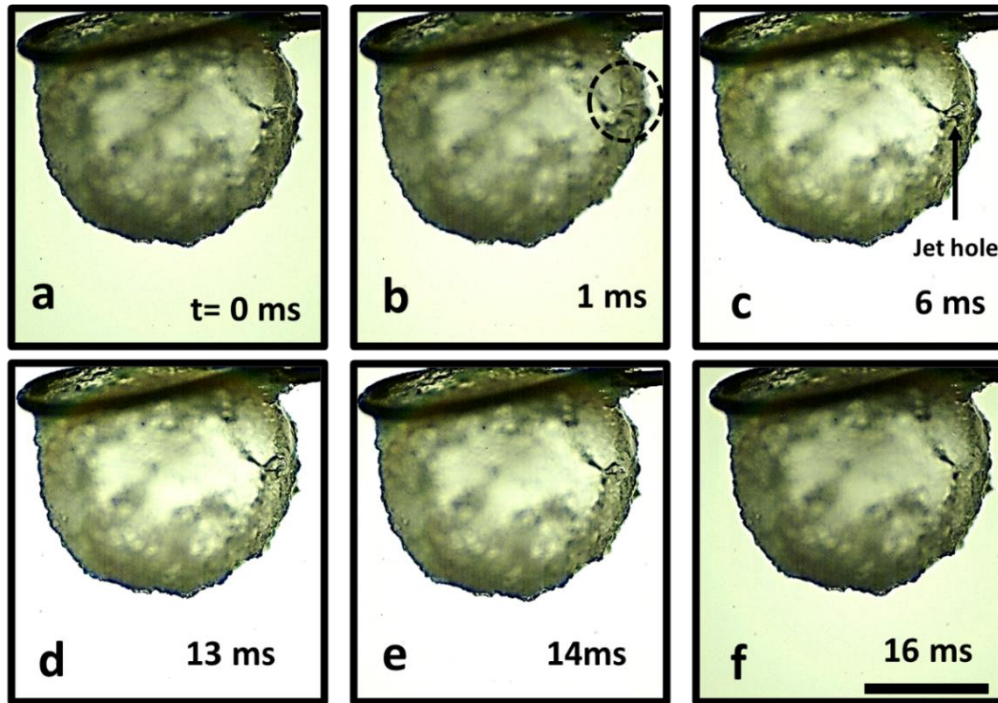


Figure 5. 9. The dynamic single burst sequence for MC-9% follows: **(a).** Inflated droplet state at $t = 0$ ms. **(b).** Starting of rupture at $t = 1$ ms (black dashed circle). **(c.)** Initiation of jetting hole $t = 6$ ms. **(d & e)** hole retraction at $t = 13$ and 14 ms. **(f).** complete closure of hole at $t = 16$ ms. The scale equals 0.5 mm.

5.2.3 Stage III: Carbonization

As already discussed in the previous section about evaporation and jetting of the base fuel (ethanol), now comes an instant during combustion where gellants begin to burn. In Figure 5.1 due to the high boiling point of the gellants, the fluctuations in the diametrical plots smoothen up. Only a few droplet rupture events are observed during this stage because of jetting. The jetting happening during the carbonization stage is an outcome of the remnants of the ethanol vapors trapped inside during the formation polymeric network of the gellants. Moreover, the gellant shell starts to burn, and the flame is in contact with these remaining traces of ethanol which leads to jetting in both fuel combinations. The jetting is caused by the transient bursting of the gellant shell.

The visual evidence for the inception of the carbonization stage is the formation of a carbonaceous crust on the gellant shell, which is independent of the location of the droplet surface (Figures 5.10 and 5.11). Furthermore, there are two possibilities with the combustion of the gellants shells, either it gets consumed entirely or it leaves behind a crusty shell residue. The plausibility which can be ascertained from this residue is that during the combustion, the flame does not have enough heat flux for complete combustion.

Thermogravimetric analysis was done for the sets of fuel under study. The purpose of these experiments was to identify the phase transitions associated with the combustion of gel fuel samples. Figure 5.12 is a depiction of the thermogravimetric (TG) and differential thermogravimetric (DTG, first derivative of TG curve) thermograms of gel fuel samples (HPMC-3 and MC-9). It is observed that the gel fuel samples go through a two-step thermal decomposition. In the case of HPMC-3, the first step of decomposition experiences a mass loss of ~85% occurring in the range of 35 to 220°C. While for MC-9 the first step of decomposition a mass loss of ~81% occurs in the temperature range of 43 to 220°C. The second step of decomposition occurs in the range of 290 to 398°C which is found to be common for both HPMC-3 and MC-9 gel fuels. Furthermore, the DTG curve shows a peak at ~350°C and 355°C which corresponds to the melting temperature of the gellants HPMC and MC respectively [112]. Therefore, it can be said that during combustion, organic gellants go through carbonization.

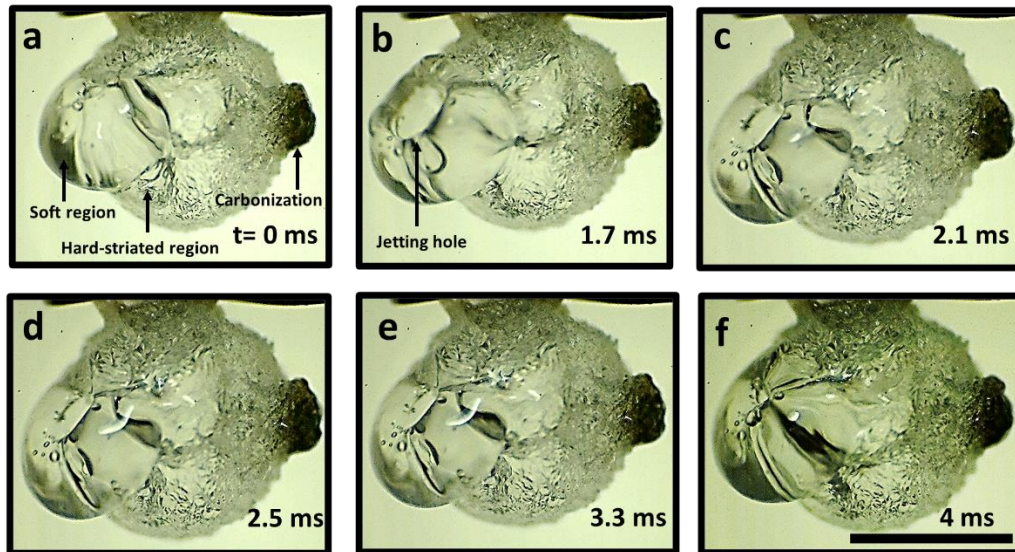


Figure 5. 10. The carbonization sequence of HPMC-3% ethanol-based gel fuel shows the sequential progression of the carbonization front. **(a)**. The gellant shell has a localized appearance of carbonaceous regions along with hard-striated and soft regions in coexistence at $t=0$ ms. **(b)**. Formation of the jet hole at $t= 1.7$ ms. **(c)**. Initiation of hole closure via retraction at $t=2.1$ ms. **(d to e)** Hole closure continues at $t= 2.5$ to 3.3 ms. **(f)** Closure of hole at $t= 3.3$ ms. The scale bar equals 1 mm.

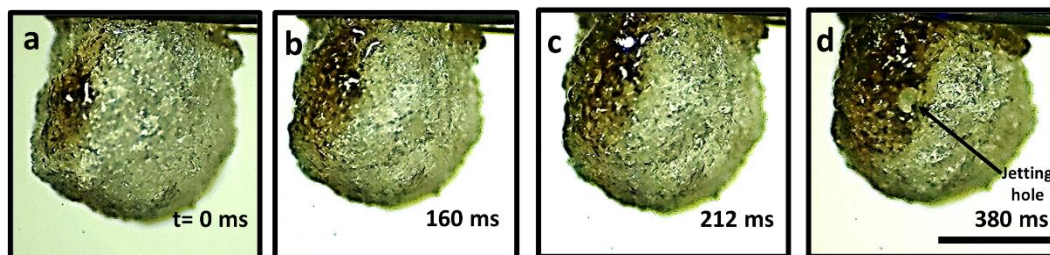


Figure 5. 11.The bursting dynamics of the carbonization sequence for MC-9% ethanol-based gel fuel is represented as **(a)**. The appearance of the localized carbonaceous region at $t=0$ ms. **(b to c)**. Growth of the carbonization front $t= 160$ and 212 ms respectively. **(d)**. Formation of the jet hole at $t=380$ ms. The scale bar equals 1 mm.

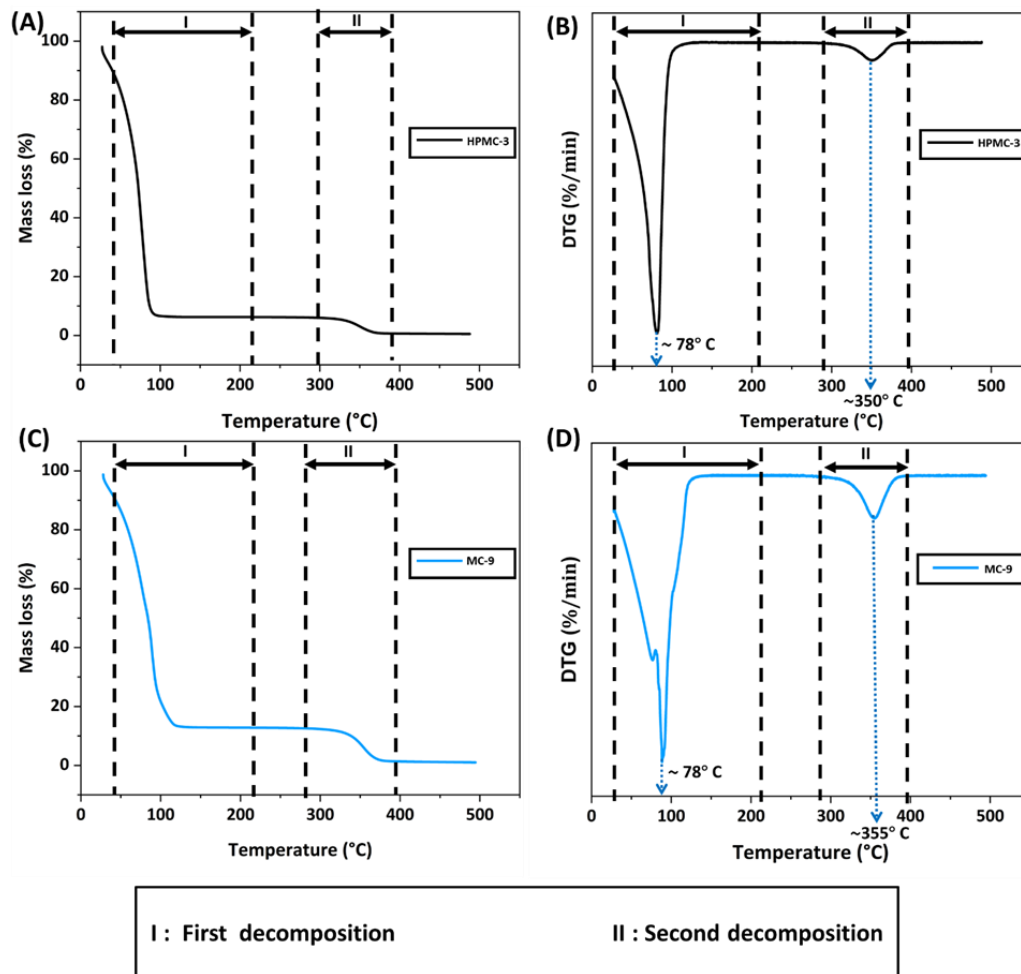


Figure 5. 12. (Top) The TGA **(A)** and DTG **(B)** thermograms for HPMC-3 gel fuel. **(Bottom)** The TGA **(C)** and DTG **(D)** thermograms for MC-9 gel fuel. In both cases, gel fuel samples were subjected to a heating rate of 10°C/min in an inert nitrogen atmosphere.

5.2.4 Bulk motion of gel fuel droplets: Centroidal Shift

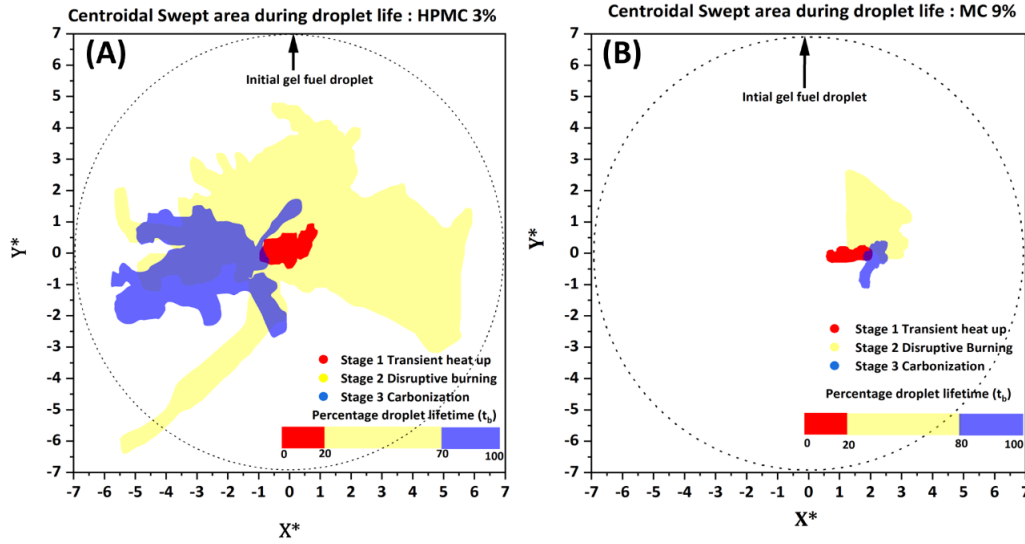


Figure 5. 13. Dynamic spreading of the area swept (A_s) by the droplet centroid due to jetting induced bulk motion. The spreading area is shown across the three stages of combustion during the droplet lifespan (t_b) for (A). HPMC-3% (B) MC-9 %.

The gel fuel droplets experience rupture due to pressure rise inside the gellant shell caused by phase separation and subsequent boiling of gel fuel's volatile components. Consequently, jetting is observed in gel fuels, and during a typical jetting event the gel fuel droplet goes through bulk motion. The bulk motion can be explained with the help of the centroidal shift of the gel fuel droplets occurring during the entirety of the combustion life span.

Figure 5.13 is an illustration of the bulk motion of gel fuel droplets i.e., Centroidal Shift [99]. The centroidal fluctuations were characterized in accordance with the gel fuel droplets and their respective combustion stages as discussed in previous sections. The insights into the details of the transients of the centroidal fluctuation are depicted by swept area (A_s) which represents the area covered by droplets in each of the combustion stages with time. The relative coverage of area during each stage of combustion has been classified in correspondence to combustion stages for both HPMC-3% and MC-9% gel fuels.

During the transient heat up (stage I) centroidal shift is due to phase separation and hence droplet motion is not dominant. The ratio of swept areas of HPMC-3% to MC-9% is ~ 1.6 and thus the centroidal motion is rather confined.

During the disruptive burning (stage II), centroidal fluctuations are seen predominantly for both fuels. The swept area increases drastically. In the case of HPMC-3% gel droplets, a dilating trend is observed in contrast to MC-9% which also shows an increment in the swept area but to a lesser extent. Thus, the ratio of area for this stage indicates a huge bulk motion of gel fuel droplets, and the ratio of swept areas of HPMC-3% to MC-9% is ~ 6.4 . Since stage II is usually dominated by jetting, hence larger swept areas are seen for both fuels.

During the carbonization (stage III) a drastic decrement in the swept area is observed in both the gel fuels in the form of shrinkage. However, the extent of area shrinkage is different in both cases. MC-9% fuel combination the bulk motion of droplet is not substantial in contrast to HPMC-3%. As already discussed, during the carbonization stage the quantity of base fuel is not in abundance which results in a decrease in jetting frequency. Consequently, less bulk motion of droplets in contrast to stage II. However, the ratio of swept areas in this stage of HPMC-3% to MC-9% is ~ 6.9 . To suffice for the variation swept areas of droplet centroids, the nature of the gellant shell must be the plausible cause across all three stages of combustion for the gel fuels. HPMC-3% gellant shells are weak and flexible while MC-9% gellant shells are hard and rigid. Thus, the HPMC-3% gellant shell does not inhibit the droplet motion caused by jetting of unreacted ethanol contrary to MC-9% gellant shells.

The bulk motion of the gel fuel droplets during combustion is also quantified by calculating the net centroidal shift for all three combustion stages. The net shift in centroid (X_{net} , Y_{net}) is evaluated in comparison to the initial droplet centroid position at the beginning of combustion which is having an initial projected area $A_0 = \pi.R_0^2$. The swept area during the combustion of gel droplets (HPMC-3% and MC-9%) is a representation of the droplet's bulk motion due to jetting. Therefore,

it can be inferred that the centroid is offset during the combustion lifespan due to jetting from its initial position.

Therefore, the net shift of centroid for HPMC-3% is found to be significantly displaced from the initial position i.e. $\sqrt{X_{net}^2 + Y_{net}^2} \sim 0.24R_o$ while in the case of MC-9% fuel combination the droplet is almost immovable from the initial position i.e. $\sqrt{X_{net}^2 + Y_{net}^2} \sim 0.082R_o$. The net shift of centroid is nearly 3 times for HPMC-3% in contrast to MC-9% which again explains thin and flexible shell of HPMC-3% enables the bulk motion of the droplet due to jetting while the strong and rigid shell of MC-9% inhibits the bulk motion of droplet caused by jetting. Thus, from Figure 5.13 key insights into the droplet trajectory (due to recoil thrust caused by jetting) [39], [40] can be understood which can provide a perspective into the combustion behavior inside a hybrid rocket motor engine that can affect the local fuel-oxidizer ratio and gas phase mixing significantly.

5.2.5 Effect of droplet rupture due to jetting at flame scale

The classification of combustion stages was also studied in terms of the effect of jetting on flame disruption events. The details of flame scale disruptions in correspondence to droplet combustion stages are discussed in this section.

The pressure surge inside the gel droplets is released via jetting of unreacted ethanol vapors. These jets hit the flame envelope repeatedly during the droplet's lifetime. The pressure energy build-up is transformed into the kinetic energy of jets which further gets manifested in the form of flame disruptions events caused by jetting occurring at the flame. Thus, it can be said that at the local level, droplet rupture takes place due to pressure buildup and its subsequent release via jetting of unreacted ethanol fuel vapor causes flame disruptions at the global level i.e., flame scale. The flame disruptions are usually observed as flame distortions, pin ejections, fireball outside the flame, and random burst-induced jetting events at the flame [39], [40].

The flame disruption events can be single or multiple (double and triple) jets which are caused by single or multiple droplet ruptures (Figures 5.7 and 5.8 respectively). It is observed that pin ejection and fireball outside the flame events are high-velocity events and flame distortion events are relatively low-velocity events in contrast to the other two flame disruption events. Apart from these, a random burst event at the flame scale is also seen. In the case of multiple jetting events, the combination of any of the three flame disruption events (flame distortions, pin ejections, and fireball outside the flame) can occur in no fixed manner.

In Figure 5.14 the velocity distribution of the flame disruption events caused by jetting is discussed. This is done in correspondence to the combustion stages at the droplet scale for the set of fuels. During the transient heat-up stage, no jetting is observed at the droplet scale hence no flame disruptions are observed. In the disruptive burning stage, both fuels demonstrate an active jetting behavior. However, the frequency of jetting and type of flame disruption are key differentiating factors. In HPMC-3% gel fuel the number of jetting events (flame disruptions) is found to be less in comparison to MC-9% gel fuel. The HPMC-3% fuel tends to form flame distortions (~500 to 870 mm/s) in substantial numbers in comparison to pin ejection (~ 1000 to 1550 mm/s) and fireball outside the flame (~ 800 to 1530 mm/s) disruptions. In the case of MC-9% along with flame distortions, pin ejections, and fireball outside the flame is found to be in abundance. This occurs due to the differences in the gellant shell characteristics, as in the case of HPMC-3% the weak and flexible gellant shell compensates for the pressure rise caused by ethanol vapors in the form of inflation-deflation cycles of the droplet [47]. On the contrary, in MC-9% the strong and rigid gellant causes the droplet to experience an unstable state of transient pressure. Furthermore, due to the combined effects of lower pressure build-up, flexible shells, and the larger areas of rupture sites (0.0075 to 0.1256 mm²) in HPMC-3% (Figure 5.15A) the tendency to form low-velocity flame-disrupting (flame distortions) jets increases. On the contrary in MC-9%, the propensity to form strong rigid shells leads to the formation of rupture sites of smaller areas (0.002 to 0.0104 mm²) i.e., Figure 5.15B. Therefore, in MC-9% the gellant shell's capacity to sustain high pressure and inability to undergo severe

expansion leads to high-velocity disrupting jets (Fireball and pin ejection). Ultimately, in the carbonization stage, only a few flame disruptions are observed for both HPMC-3% and MC-9% due to the deficiency of the base fuel.

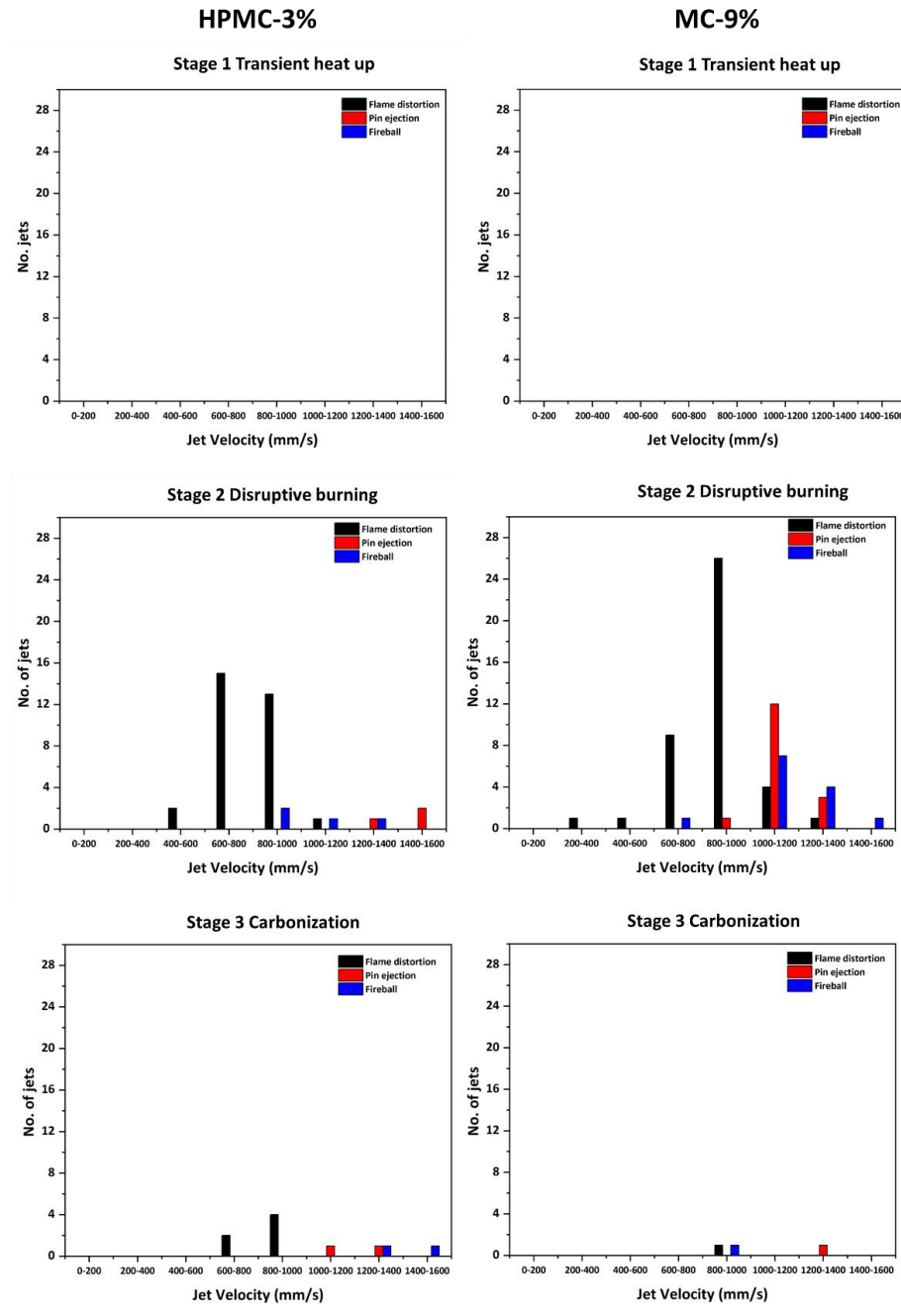


Figure 5. 14. Histograms of variation of velocities of flame disruptions caused by jetting during the individual combustion stages of ethanol-based HPMC-3% and MC-9% gel fuels.

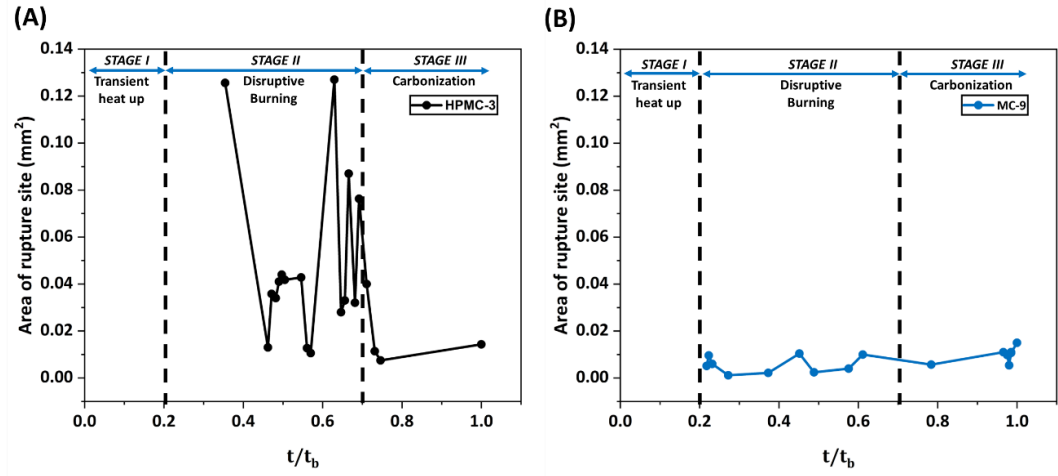


Figure 5. 15. The temporal variation of areas of rupture sites during the combustion of ethanol-based (A) HPMC-3% and (B) MC-9% gel fuels across the combustion stages.

5.2.6 Burn rate estimation of combustion stages

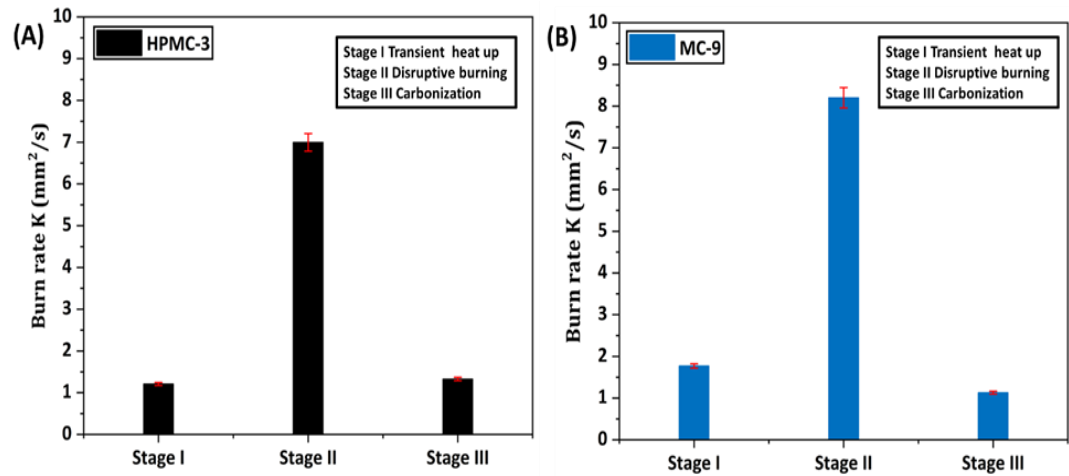


Figure 5. 16. Variation of burn rates across the combustion stage for ethanol-based (A) HPMC-3% and (B) MC-9% gel fuels.

Figure 5.16. shows the variation of burn rate for both the gel fuels (HPMC-3% and MC-9%) across all three combustion stages i.e., Transient heat up (stage I), Disruptive burning (stage II), and Carbonization (stage III). The estimation of the burn rate is done by applying Spalding's d^2 law model [111]. It is observed that similar to the combustion of gel fuels, the variation of the burn rates must be in correspondence to the individual combustion stages as proposed by Mishra and Patyal [42]. Thus, in the current study, to begin with, it is found that during the transient heat up the burn rate is marginal as during this duration the gel droplets tend to form gellant shells and experience heating and evaporation only. As the combustion proceeds to disruptive burning, a substantial increase (~ 5.8 times in HPMC-3% and ~ 4.8 times in MC-9%) in burn rate occurs due to jetting. The increase in burn rate in stage II is found to be a common feature for both the gel fuels. However, for MC-9% the burn rate is ~ 1.2 times HPMC-3%. This can be attributed to a high frequency of jetting (~ 1.8 times) for MC-9% as shown in Figure 16. Furthermore, as the combustion enters carbonization (stage III), the burn rates drop (~ 5.3 times in HPMC-3% and ~ 7.3 times in MC-9%). The plausible reason for this drop in burn rate is the scarcity of base fuel as discussed earlier. Hence, the combustion during stage III is largely due to a single component i.e., gellants. Also, it is observed that during stage III, the burn rate of MC-9% is ~ 0.85 times that of HPMC-3% due to the decrease in the jetting frequency as shown in Figure 5.14.

It is noteworthy to consider the occurrence and distribution of the flame disruption events influencing the burn rate characteristics of both the gel fuels. Evidently, from Figures 5.14 and 5.16 it is seen that the flame disruptions events largely occur during stage II and thus it has the highest burn rate. During stage III, the flame disruption events occur sparsely (Figure 5.14) due to the combustion of leftover traces of ethanol. The burn rate in stage I is found to be independent of jetting in both cases.

5.2.7 Combustion residue characterization

The post-combustion residue analysis is carried out to assess the morphological transformation of gellant shells for both the set of fuels i.e., HPMC-3% and MC-9%. This was done by using scanning electron microscopy (SEM), carried out under a high vacuum. The samples were made conducting by gold coating for the duration of ~2min under a vacuum-sealed chamber. In this section, from Figure 5.17 to 5.20 the transformation in gellant shell morphology is explained across the three droplet combustion stages (transient heat-up, disruptive burning, and carbonization). Furthermore, a representative case of MC-9 % gellant shell residue is detailed in Figure 5.19 to provide insights into the carbonization stage.

To begin with, figure 5.17 is a representation of gellant shell residue for HPMC-3% (Figure 5.17a and b) and MC-9% (Figure 5.17c and d) for stage I (transient heat-up) of the combustion. As discussed in the previous sections, during stage I the phase separation of the gel fuel components is the driving force that leads to the formation of the gellant shell. Although, this is a common trait demonstrated by both the set fuels under study. However, it is observed that there are inherent differences in the morphology of the shells of HPMC-3% and MC-9% compositions. From figures 5.17a and b for HPMC-3%, the gellant shell is crumpled and striated. This can be attributed to the thin, weak, and flexible shell which allows ease of internal circulation of the base fuel prior to boiling inside the shell. Moreover, the gellant shell skins over during stage I hence striations and the crumpled shell is seen. On the contrary, in the case of MC-9% (Fig. 5.17c and d) the gellant shell during stage I is observed to have a blistered appearance. This can be accounted for by the thick, strong, and rigid shell of MC-9% which inhibits the internal circulation of the base fuel.

Furthermore, following the precursor transient burst, in both cases, the gel droplet proceeds toward disruptive burning (stage II) which is accompanied by jetting events. However, the jetting occurrence is significantly influenced by the trait of the gellant shells. In the case of the HPMC-3% gel droplet, the dominant mode of jetting is oscillatory bursting induced, and thus, in Figures. 5.18 a and b striated

gellant shell has jetting holes. These striations can be ascertained from the cycles of inflation and deflation occurring during the oscillatory bursting [47]. Generally, it is seen that in the case of HPMC-3% the jetting holes usually occur in softer regions[47] and can be seen from Figures 5.18 a and b. While in the case of MC-9% the gellant shell is accompanied by blisters and jet holes (Figures 5.18 c and d). As the combustion proceeds, the gellant shell eventually hardens and thus shell cracks up (Figures 5.18 e and f) which also acts as preferential jetting sites along with the jet holes.

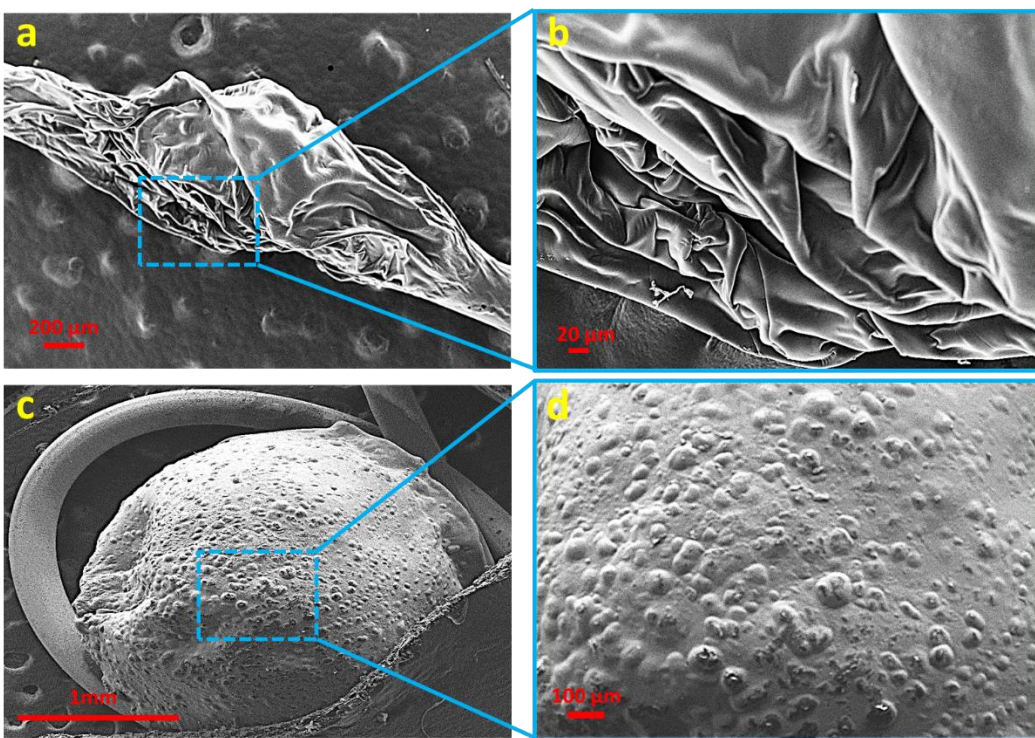


Figure 5. 17. SEM micrographs showing the combustion residue during stage I of the combustion for HPMC-3% (a & b) and MC-9% (c & d). (a). Overall view showing crumpled and striated shell for HPMC-3% (122X magnification). (b). Magnified view of the striations in HPMC-3% shell (501X magnification). (c). Overall view illustrating the blistered MC-9% shell (27X magnification). (d). Magnified view of blistered MC-9% droplet surface (85X magnification).

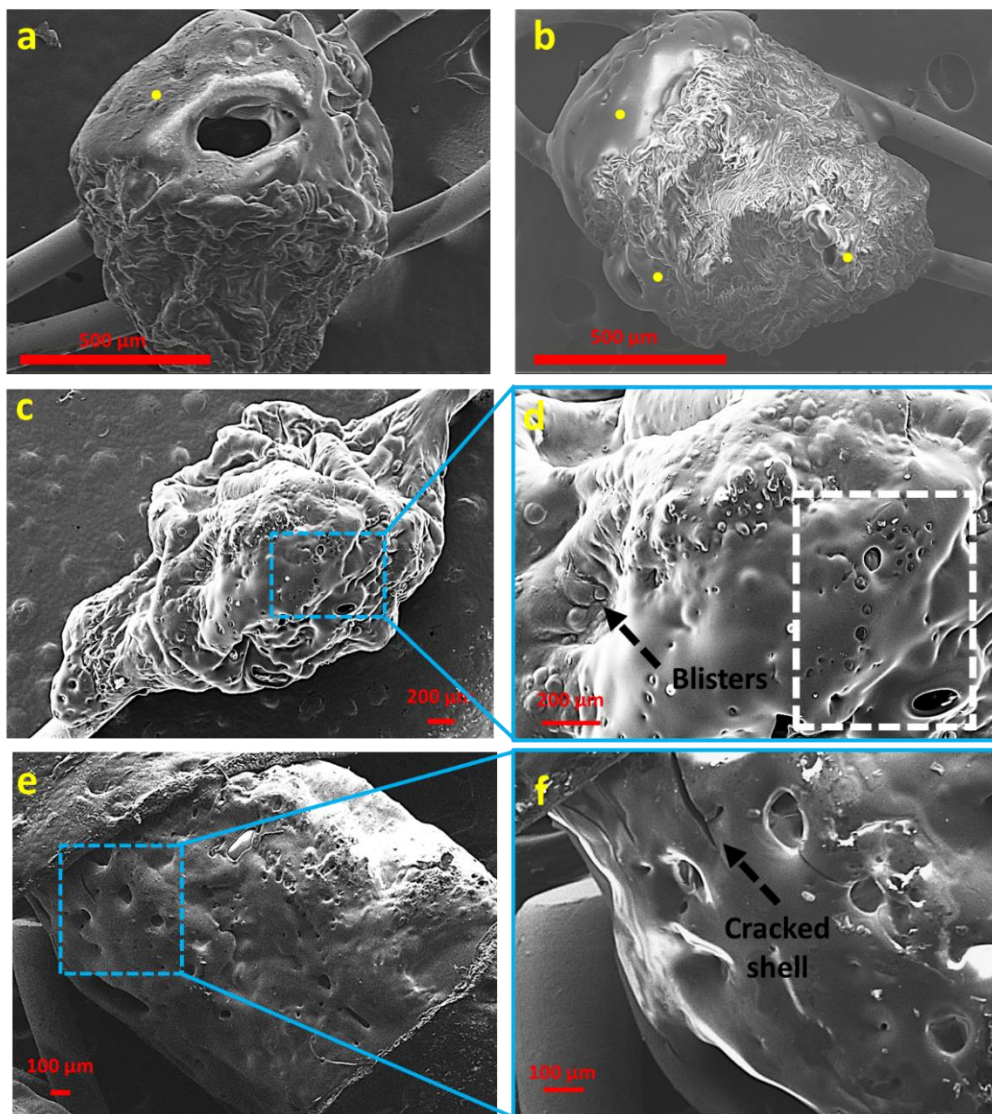


Figure 5. 18. SEM micrographs showing the combustion residue during stage II of the combustion for HPMC-3% (a & b) and MC-9% (c to f). (a). Overall view showing crumpled and striated shell for HPMC-3% with jetting holes in softer regions (yellow dots) (100X magnification). (b). Bottom view of the jet holes in softer regions (yellow dot) striations in HPMC-3% shell (80X magnification). (c). Overall view illustrating the blistered MC-9% shell with jet holes. (82X magnification). (d). Magnified view of blistered MC-9% droplet surface with jet holes (white dashed rectangle) (200X magnification). (e). Overall view illustrating the MC-9% shell with jet cracks and jet holes. (35X magnification). (f). Magnified view of the MC-9% shell with jet cracks and jet holes. (200X magnification).

In Figure 5.19, a representative case of carbonization (stage III) is discussed for the gellant shell of MC-9% gel fuel composition. It is observed that the remnant of MC-9% has a porous bottom region laden with jetting holes which suffice for the jetting taking place during the final moments of the gel droplet combustion. The SEM-EDX elemental analysis of the porous region in Figures 5.19 c and d provides a key understanding of the elemental composition of the combustion residue. Primarily, Carbon (C) and oxygen (O) are present with carbon (67.79%) in substantial amounts in contrast to oxygen (32.21%). Furthermore, the presence of large amounts of carbon in the residue reinforces the fact that organic gel fuels undergo carbonization during the combustion process and further act as a fuel source[112].

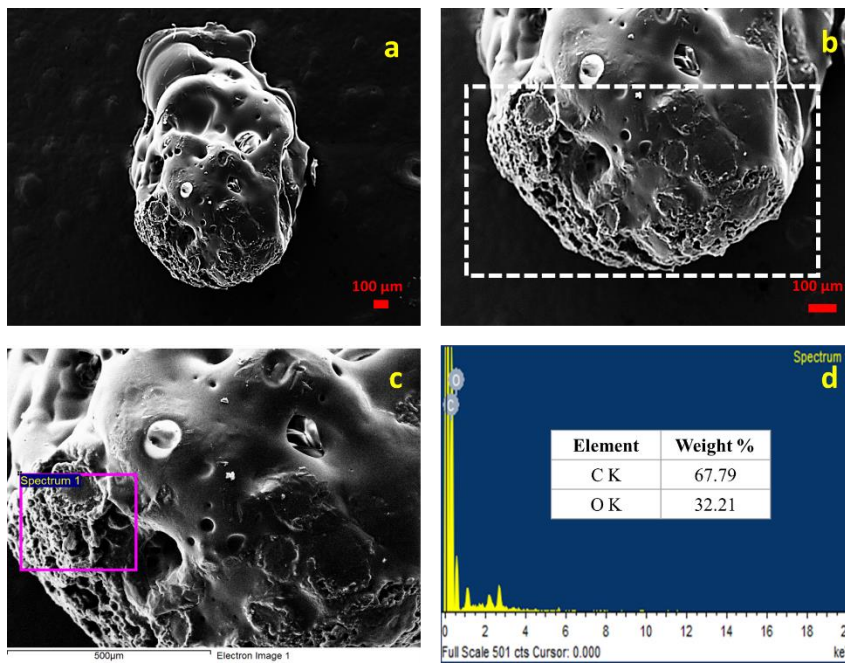


Figure 5. 19. SEM micrographs (a & b) and EDX mapping spectra (c & d) show the representative combustion residue during stage III of the combustion for MC-9%. (a). Overall view showing carbonized porous region with jetting holes (100X magnification). (b). Magnified view of the carbonized porous region with jetting holes (dashed white rectangle) for MC-9% shell (201X magnification). (c & d). EDX surface mapping spectra of the carbonized region.

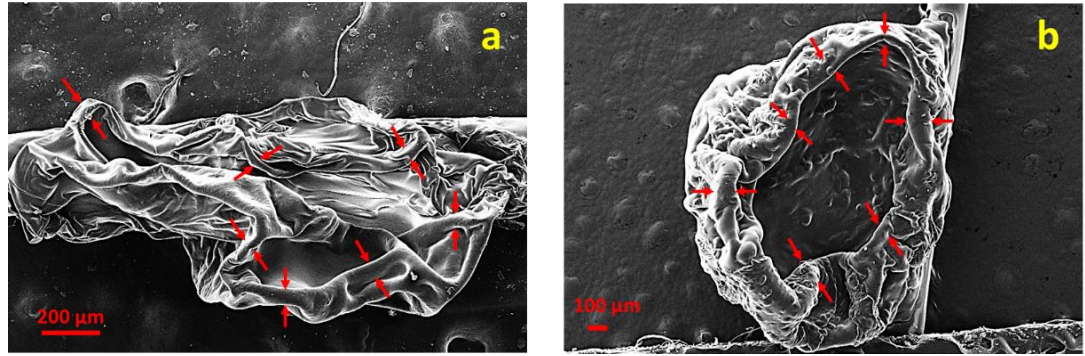


Figure 5. 20. SEM micrographs showing the non-homogenous thickness and hollow combustion residue for **(a).** HPMC-3% (180X magnification) and **(b.)** MC-9% (84X magnification). The red arrows represent the locations of thickness measurements along the periphery of the shell residue.

In Figures 5.20 a and b overall views of the hollow gellant shells of HPMC-3% and MC-9% are depicted respectively. In both sets of gel fuels an estimate of shell thickness is taken at multiple locations along the periphery. The shell thickness is found to be $38 \pm 5 \mu\text{m}$ for HPMC-3% and $66 \pm 6 \mu\text{m}$ for MC-9% gel composition. The variation in thickness of the gellant shell residues illustrates the presence of shell thickness inhomogeneity [47] and thus it is appropriate to say that gellant shells formed during the combustion of organic gel fuels are of non-uniform thickness and hollow. Moreover, the thickness of the MC-9% gellant shell is ~ 1.7 times that of HPMC-3% which can plausibly explain the formation of thinner shells in HPMC-3% and thicker shells in MC-9% gel fuels respectively [47].

5.3 Conclusions

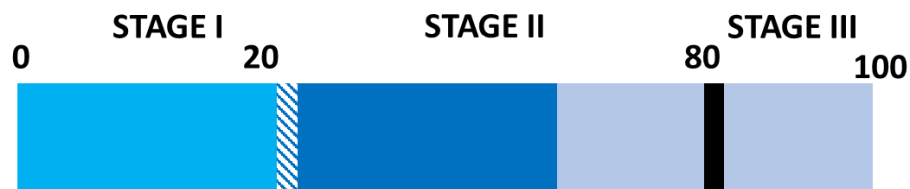
The current study dealt with understanding the combustion behavior of organic gel fuels. The gel fuels utilized for this purpose are composed of ethanol as base fuel with Hydroxypropyl Methylcellulose (HPMC) and Methylcellulose (MC) as organic gellants. Two non-metalized gel fuels are formulated with 3% of HPMC and 9% of MC as these two compositions demonstrated extreme combustion behavior.

- It can be inferred that the combustion of organic gel fuels takes place in namely three stages, transient heat up (stage I), disruptive burning (stage II), and carbonization (stage III) (Figure 5.21). These findings are backed by high-fidelity and high-speed video data. In stage I, the phase separation of gel fuel components occurs into base fuel, solvent, and gellant. Furthermore, gellant aids in the formation of gellant shells. In stage II i.e., disruptive burning, the jetting of unreacted fuel vapors takes place which initiates with a precursor transient burst event. Stage III i.e., carbonization initiates with the appearance of a carbonaceous region on the gellant shell. At this juncture stage II ends. During stage III, a suppressed jetting behavior is observed due to the paucity of the base fuel and further, the combustion of the gellant shell occurs.
- The gellant shell formed during the combustion of organic gel fuels governs the droplet bursting and jetting behavior (Figure 5.22). In stage II, it is found that in HPMC-3% composition, the gel droplet preferably undergoes oscillatory and transient bursting. On the contrary, in stage II for MC-9% composition, only transient bursting occurs. The oscillatory bursting behavior of HPMC can be attributed to the thin, weak, and flexible gellant shells. While in MC the transient bursts are caused by thick, rigid, and impervious shells.
- Due to the jetting, the bulk motion of the gel fuel droplet takes place. For both compositions, the severe bulk motion of the gel droplets is observed during the disruptive burning stage. However, for HPMC-3%, the bulk motion of the droplet is substantially larger than the MC-9% gel fuel composition, which is due to the differences in the gellant characteristics. Moreover, the net shift of droplet centroid is found to be nearly 3 times HPMC-3% in contrast to MC-9%. The assessment of the bulk motion gel droplets provided crucial insights into the droplet trajectory (due to the recoil thrust caused by jetting).

- The jetting of unreacted ethanol vapors causes flame disruptions in the vicinity of the droplet in the form of flame distortion, fireball, and pin ejections. These flame disruptions usually occur in stages II and III. The frequency of flame disruptions is found to be highest in stage II for both fuels. However, due to the difference in gellant shell characteristics, the MC-9% gel fuel had ~ 1.8 times the flame disruption events in comparison to HPMC-3%. Furthermore, due to the paucity of the base fuel in stage III, the frequency of flame disruptions gradually decreases. The type and frequency of flame disruptions are directly influenced by the nature of the gellant shells. The thick shell of MC-9% composition leads to an unstable state of transient pressure leading to the formation of large numbers (~3.5 times) of high-velocity fireball and pin ejection flame disruption events in comparison to the thin shell of HPMC-3%. The burn rate analysis carried out across the combustion stages reveals that the burn rate increases substantially during disruptive burning (stage II) due to active jetting.
- The combustion residue analysis reveals morphological differences in the gellant shells, and it has been reported across all three stages. The SEM analysis of residues provided insights into the evolution of gellant shells during combustion. For HPMC-3% the shells in stage I are striated and crumpled while for MC-9% it is blistered. During stage II, the HPMC-3% shells are striated with jetting holes in soft regions contrary to blistered shells accompanied by cracks with large and small holes of MC-9% shells. The carbonization (stage III) has a porous region laden with jetting holes. The combustion residues of both gel fuels demonstrated thickness inhomogeneity. Also, differences in the shell thickness were observed with MC-9% forming thicker shells in contrast to HPMC-3%.

Combustion stages of HPMC-3 % and MC-9% gel fuel droplets

Percentage (%) of total droplet lifetime (HPMC-3%)



Percentage (%) of total droplet lifetime (MC-9%)



STAGE I : Transient heat up
STAGE II : Disruptive burning
STAGE III : Carbonization
 Precursor transient burst
 Oscillatory bursting
 Transient bursting
 Carbonization initiation

Figure 5. 21. Characterization of combustion stages of HPMC-3% and MC-9% gel fuel compositions.

Comparison of droplet rupture modes due to jetting during stages II and III of combustion of HPMC-3 % and MC-9% gel fuel droplets

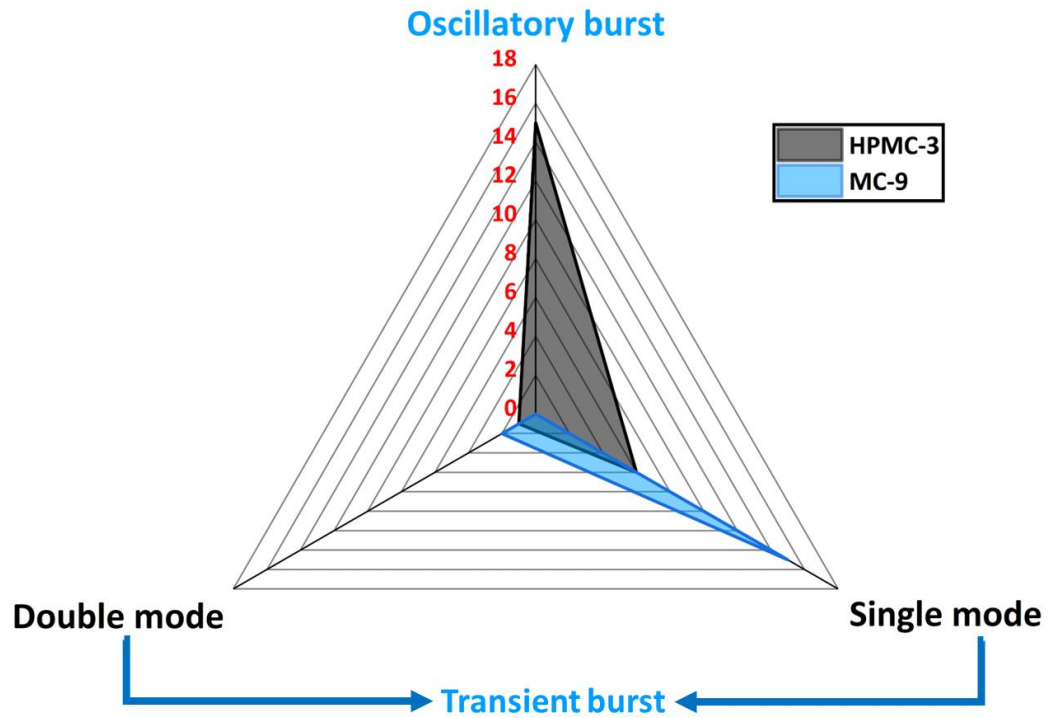


Figure 5. 22 Comparison of droplet bursting modes of HPMC-3% and MC-9% gel fuel droplets.

CHAPTER 6: TIME-VARYING OSCILLATORY RESPONSE DURING DISRUPTIVE BURNING PHASE

The disruptive burning of gel fuel droplets causes the release of unreacted fuel vapors from the droplet interior to the flame in the form of jets. In addition to pure vaporization, this jetting allows convective transport for fuel vapors, which accelerates gas-phase mixing and is known to improve droplet burn rates. Using high-magnification and high-speed imaging, it is seen that the viscoelastic gellant shell at the droplet surface evolves during the droplet's lifetime, which causes the droplet to burst at different frequencies, thereby triggering a time-varying oscillatory jetting. In particular, the continuous wavelet spectra of the droplet diameter fluctuations show that the droplet bursting exhibits a nonmonotonic (hump-shaped) trend, where the bursting frequency first increases and then decreases to a point where it stops oscillating. The changes in the shell structure are captured by tracking the temporal variation of the area of rupture sites, spatial movement of their centroid, and the degree of overlap between the rupture areas of successive cycles. During the initial period (immediately following its formation) when the shell is newly formed, it is weak and flexible, which causes it to burst at increasingly high frequencies. This is because the area at and around the rupture site becomes progressively weaker with each rupture in an already weak shell. This is shown by a high degree of overlap between the areas of successive ruptures. On the contrary, the shell flexibility during the initial period is demonstrated by a reversal in the motion of rupture site centroids. However, at later stages when the droplet has undergone multiple ruptures, the depletion of the fuel vapor causes accumulation of gellant on the shell, thus causing the shell to become strong and rigid. Which in turn suppresses droplet oscillations. Overall, this mechanistic study provides an understanding of the evolution of the gellant shell during the combustion of a gel fuel droplet. This study can be used to devise gel fuels that result in gellant shells with tailored properties, and therefore, control the jetting frequencies to tune droplet burn rates.

6.1 Introduction

Modern-day aerospace propulsion systems are scaling new heights of innovation in technology and performance. Alongside performance, there are key parameters like operational safety, reliability, ease of processing, reusability, and environmental safety [32], [36], [55]–[58] of fuel sources that are currently of prime concern. Gelled propellants are such propellants that have the potential to fulfill all the above-mentioned needs and can replace conventional solid and liquid fuels by incorporating their benefits and simultaneously negating their disadvantages. Therefore, they are considered favorable candidates for rocket and ramjet propulsion systems [36]. The commonly used liquid propellants offer ease of throttle control, but they have inherent drawbacks. A major disadvantage of the typical liquid propellants is the likelihood of leakage and spills during handling, which becomes a key concern specifically in the case of hazardous hypergolic propellants [54]. The gel propellants provide safety from spillage and leaks during handling in a manner akin to that of the solid propellants [23], [24], [54], [59]. Moreover, the shear thinning behavior of gel fuels provides better injection and atomization that is analogous to liquid fuels [26], [64], [65], [94]. Due to gelation, the stable suspension of metal additives can be completed in the gel fuel matrix. This can aid in improving performance characteristics, such as a specific impulse and energy density [36], [69]. Interestingly, gel propellants resemble solid propellants in terms of storability and handling, but they have shown certain advantages over solid propellants. Unlike solid propellants, gel propellants are less sensitive to impact, friction, and electrostatic discharge, and thus have a decreased susceptibility to accidental ignition, deflagration, detonation, or thermal runaway [32]. The viscoelasticity of the gel propellants during the storage and the tendency to transform from solid-like to liquid-like within the delivery system eliminates the possibility of cracking the propellant structure and its consequent uncontrolled combustion [57].

Although gel propellants offer various advantageous avenues, as discussed earlier, their combustion behavior has nonetheless yet to be understood and deciphered.

The combustion of gel propellants is often considered to be disruptive combustion behavior, which is accompanied by disruptive jetting events, as reported by Solomon et al. [71]. These disruptive jetting events are the jets of fuel vapors from the droplet interiors which occur aperiodically and asymmetrically throughout the droplet's lifetime. A usual jetting event occurs sequentially as first the gellant crust/shell forms due to the phase separation of the gelling agent from its components (base fuel and solvent) in the vicinity of the droplet surface. Second, underneath the gellant shell, the trapped fuel begins to boil. Third, the inner surface layer of the gellant shell acts as nucleation sites for bubble growth, leading to an increase in pressure inside the shell. Eventually, the gellant shell ruptures, and subsequently, there is a release of internal pressure via the jetting of unreacted fuel vapor occurs. Finally, the jet travels to the flame envelope in the vicinity which causes disruptions in the flame. This mechanism of jetting has been reported in the literature by different studies conducted on organic gel-based propellants. The studies conducted by Solomon et al. [71] on multicomponent gel fuel droplets revealed that during combustion, a nonpermeable elastic layer of gellant is formed which prevents the evaporation of the fuel, which in turn causes the swelling of the droplet. This eventually leads to the jetting of unreacted fuel vapors and further shrinkage of the gel droplet. Moreover, in this study, the gel droplet diameter and time history revealed a fluctuation in the form of an increasing–decreasing trend for droplet diameters. Similarly, Mishra et al. [41], [42] examined the combustion behavior of Jet A1 fuel gelled with Thixotrol ST as gellant and Xylene as the solvent and concluded that the key phenomena involved in the combustion were phase separation (gellant shell formation), bubble nucleation, and microexplosions, which occurred in a staged manner. They also reported a fluctuating trend in the volume time history of the gel droplets due to jetting. Cho et al. [39], [40] utilized high-speed OH-PLIF experiments to characterize the trimodal behavior of flame-disrupting jets. They proposed that these jets occur from the same location repeatedly which can be attributed to the weakening of the gellant shell during subsequent jetting due to the viscoelastic nature. Furthermore, the combustion behavior of the unsymmetrical dimethylhydrazine (UDMH) droplets gelled with

organic gellant was investigated by Feng et al. [75] under the oxidant convective environment, and these authors also reported that the combustion proceeds in four stages: (1) transient heat-up with phase separation of gel propellant components, (2) gellant-layer formation and bubble nucleation leading to an onset of microexplosions, (3) vigorous microexplosions, (4) and uniform regression of the droplet. It was observed that during stages 2 and 3, substantial jetting takes place, which also manifested in the form of fluctuating trends in the volume–time history. Research performed by Miglani et al. [47] provided key insights into the bursting and jetting behavior of ethanol-based organic gelled droplets of varying gellant concentrations. The findings of this study confirmed that due to the viscoelasticity of the gellant shells, volumetric fluctuations occur due to the oscillatory bursting of the gel droplets. They reported that the lower concentration of gellant exhibited an oscillatory bursting behavior in the form of rupture cascades that occurred in the same region of the droplet. On the contrary, for the high concentration of gellant, the ruptures took place at dispersed locations of the droplet surface.

A survey of the relevant literature reveals that the combustion behavior of gel fuel has been analyzed either as a function of the initial droplet size and the ambient conditions [41], [42] or the functional properties such as the parent fuel, the type of gellant (organic, inorganic, and cryogel) and their concentration [41], [42], [47]–[50], [71], [72]. While these studies have focused on determining droplet burn rates, a key mechanism that governs the combustion and jetting behavior in gel fuel droplets is the formation of a gellant shell, whose evolution during the droplet lifetime has been unexplored. Therefore, a key objective of this study was to investigate the temporal evolution of the gellant shell in burning ethanol-based organic gel fuel with hydroxypropyl methylcellulose (HPMC-3%) as a gellant. By analyzing one of the modes of jetting, namely, the oscillatory jetting [47], and extracting the key parameters such as the droplet oscillation frequency (using continuous wavelet spectra, CWT) [101], the area and overlap of rupture sites, as well as the movement of their centroid transformation in the gellant shell with time, can be inferred as being initially thin, weak, and flexible to become thick, strong, and rigid at later stages.

The steps of fuel formulations, droplet imaging, and geometric parameter extraction are given in Chapter 3 for reference.

6.2 Results and Discussion

6.2.1 Data Reduction

Since gel fuels are non-Newtonian, it is difficult to dispense a perfect spherical-shaped gel droplet, and therefore, the projected area-based equivalent diameter is used to determine the droplet diameter fluctuations with time. The HED algorithm-based image processing captures all the four parameters accurately namely, the area of rupture sites, centroid of rupture sites, the spatial movement of rupture sites, and the percentage overlap between successive rupture areas. The projected-area diameter is determined using an in-house developed deep learning-based holistically nested edge detection (HED) algorithm, as reported previously [91]–[93]. HED enables automated learning of multiscale and multilevel features in a droplet image and reconstructs a continuous droplet. Furthermore, the extracted droplet shape is verified by recreating the droplet boundary by taking a polar plot of the distances from the centroid to the droplet edge based on their angle. This is carried out by feeding an array of computed radial distances and their corresponding angles to the standard polar plot function from the matplotlib python library. Based on the edge detection, the maximum error in determining the droplet diameter is 3% [92]. The temporal evolution of the droplet oscillation frequencies is determined via the continuous wavelet spectra (CWT) of the time series signal of droplet diameter fluctuations in-built into the MATLAB R2021b version software. The continuous wavelet spectra (CWT) or the scalogram represent the frequency-time domain analyses, where the analyzing function is a wavelet. The CWT compares the time series signal to the versions of a wavelet that is shifted in time and compressed or stretched, i.e., scaled. By comparing the signal to the wavelet at various scales and positions, a function of two variables is generated. It has two implications, if the wavelet is complex-valued, the CWT is a complex-valued function of scale and position. If the signal is real-valued, the CWT is a real-

valued function of scale and position. (“Continuous Wavelet Transform and Scale-Based Analysis”) For a scale parameter, $a > 0$ and the position, b , the CWT is given as follows:

$$C[a, b; f(t)\psi(t)] = \int_{-\infty}^{\infty} f(t) \frac{1}{a} \psi^* \left(\frac{t-b}{a} \right) dt$$

where * denotes the complex conjugate. By continuously varying the values of the scale parameter a and position parameter b , the CWT coefficients $C(a, b)$ are obtained, and multiplying each coefficient by the appropriately scaled and shifted wavelet yields the constituent wavelets of the original signal. In the CWT analysis, scale and frequency have a crucial relationship. A smaller scale leads to compression of the wavelet function, and hence a higher frequency resolution is obtained but a low time resolution is subsequently observed. On the contrary, a longer scale a lead to the stretching of the wavelet function, which results in a low-frequency resolution but high time resolution. In the CWT spectral distribution shown in Figure 6.1, the white line represents the cone of influence, below which the area in the scalogram is affected by edge-effect artifacts, and therefore, treated as unreliable. These effects in the scalogram arise from areas where the stretched wavelets extend beyond the edges of the observation interval. Above the white line, the information provided by the scalogram is an accurate time-frequency representation of the data. In this study, the morse wavelet is used for generating the scalogram of the time-varying droplet diameter fluctuations.

The droplet diameter history (Figure 6.1a) shows that in the disruptive burning phase, the gel fuel combustion is characterized by the occurrence of intermittent oscillations, which appear as four distinct bands. This is evident from the continuous wavelet spectra (CWT or scalogram) of the time series signal of the droplet diameter fluctuations, which shows the occurrence of four distinct frequency bands (Figure 6.1b). Each of these frequency bands corresponds to an oscillatory cascade which is composed of a series of rupture–recovery cycles of the gel fuel droplet.

Figure 6.2 shows the temporal evolution of the burning gel fuel droplet during a single rupture–recovery cycle. As seen in Figure 6.2, each cycle is divided into three stages: First, the gellant shell ruptures at a weak spot with the formation of a hole or site, which marks the beginning of the cycle (see Figure 6.2(a1)). Second, the jets of unreacted fuel vapor are released via this rupture site. This represents the time period of active jetting (t_a); see Figure 6.2(a2)–(a7). Third, the ruptured site recovers due to the viscoelastic nature of the shell (Figure 6.2b), which allows the bubbles inside the droplet to grow and dilate the droplet (Figure 6.2(c1)–(c4)). This, in turn, stresses the gellant shell to the point where it ruptures again and initiates the next rupture–recovery cycle. This implies that the complete recovery of the gellant shell, i.e., the closure of the ruptured site marks the end of the active jetting period, and therefore, serves as a prerequisite condition to initiate the next rupture–recovery cycle. In this way, each rupture–recovery cycle can be divided into two-time durations, one with jetting (t_a) and the other without it (t_{ia}). Since the shell rupture corresponds to the efflux of unreacted fuel vapors via jetting, the jetting frequency is the same as the droplet oscillation frequency.

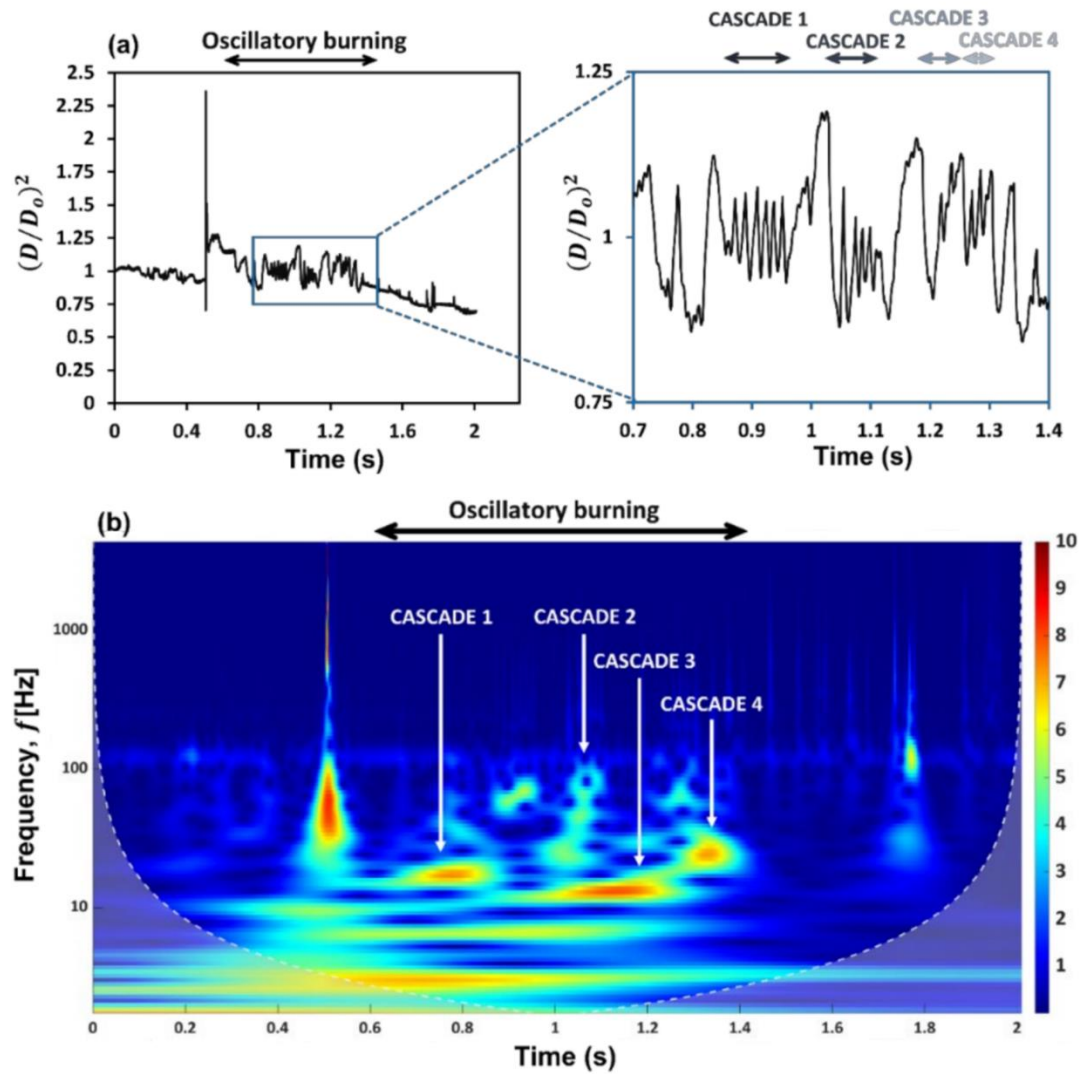


Figure 6. 1.(a) Diameter time history of HPMC-based ethanol gel fuel droplet. (b) Continuous wavelet spectra (CWT) or scalogram of the diameter time signal showing frequencies for diametrical fluctuations.

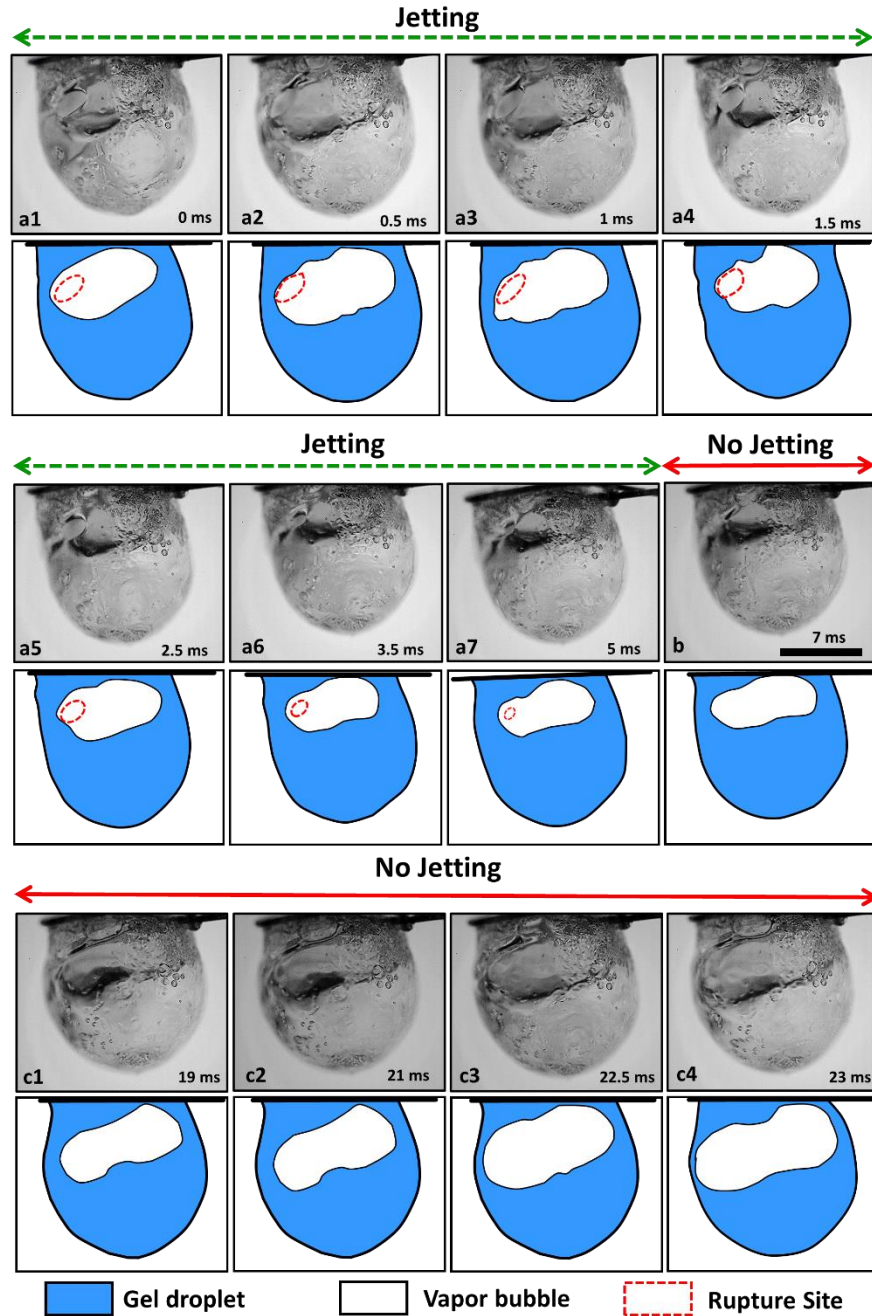


Figure 6. 2.High-magnification images of a burning gel fuel droplet undergoing a single rupture–recovery cycle. The accompanying schematics are shown at the bottom of each image. (a1) Rupture of the gellant shell and (a2–a7) jetting of unreacted fuel vapors from the rupture site. (b) Recovery of the rupture site. (c1–c4) Bubble growth and droplet expansion. The time stamps are shown on each image, and the scale bar equals 1 mm.

The CWT (see Figure 6.1b) shows that the droplet diameter fluctuations exhibit a hump-shaped trend with time, where the oscillation frequency first increases and then decreases. Specifically, the oscillation frequencies range from $\sim 15\text{--}18$ Hz in the first band, increase by $\sim 3\text{--}4$ times to $\sim 55\text{--}72$ Hz in the second band, then decrease significantly to $\sim 12\text{--}14$ Hz in the third band, and finally, increase slightly to $\sim 23\text{--}26$ Hz in the fourth band. Note that these frequency ranges are extracted from the CWT of the droplet diameter fluctuations and are corroborated with the oscillation frequencies calculated directly from the high-speed videos as follows: $f_{cycle} = 1/(t_a + t_{ia})$. The observed change in the oscillation frequency of the droplet is due to the change in the relative dominance of the two competing mechanisms over its lifetime, namely, the jetting of unreacted fuel vapors versus the gellant shell formation. The time evolution of the gellant shell can be understood based on Figure 6.3, where the top figure shows the spatial movement of the centroid of the rupture site $(x_r/D_o, y_r/D_o)$ with time for each rupture–recovery cycle, while the bottom figure shows the total distance traversed by the rupture sites during each cascade. The rupture site, its centroid coordinates, and the spatial movement of these centroid coordinates for a single cycle are shown schematically in Figure 6.4. First, it is evident from Figure 6.3b that the total distance traveled by the centroids of the rupture sites is significantly more for cascades 1 and 2 compared to the following cascades 3 and 4.

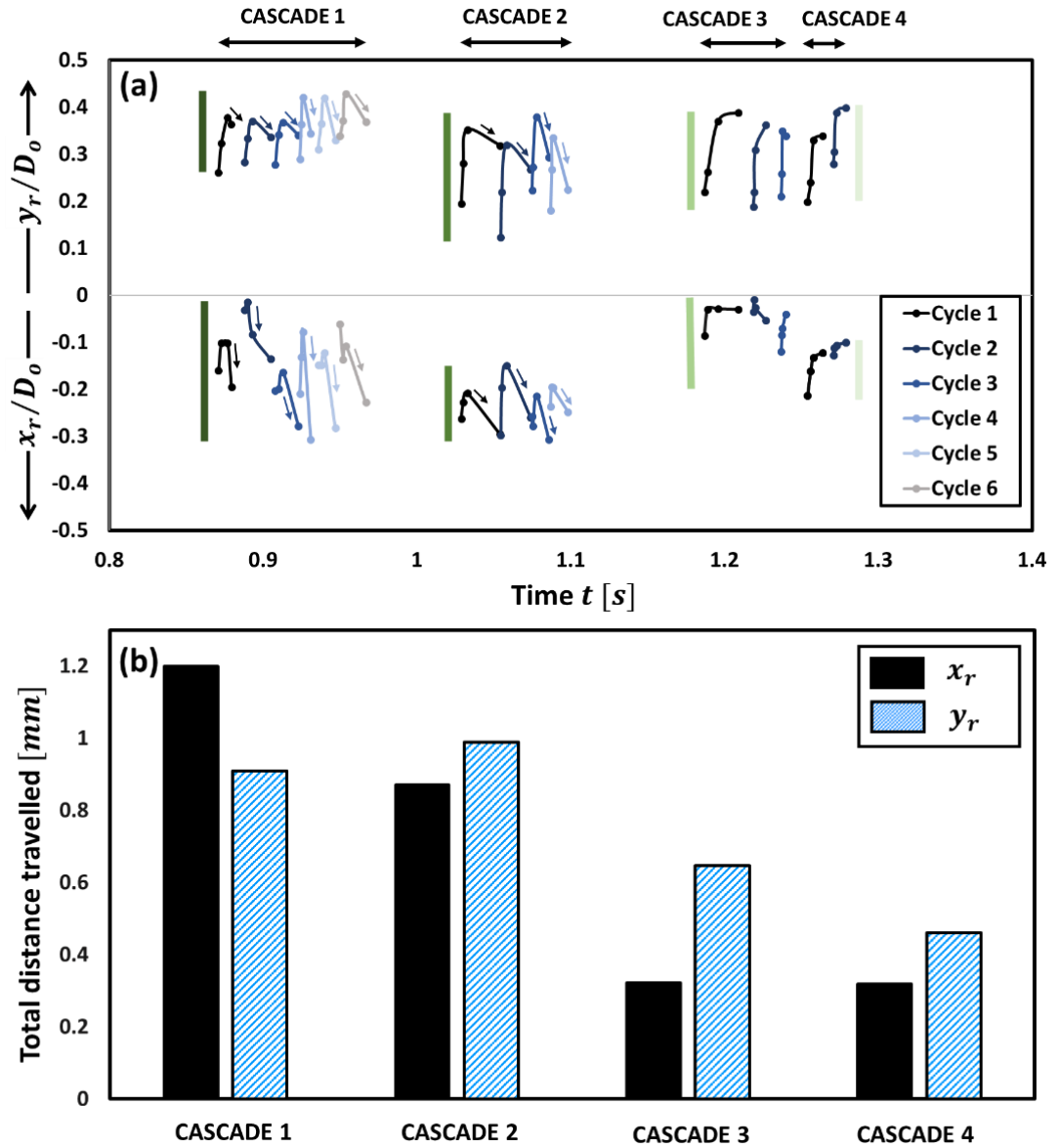


Figure 6.3. (a) Spatial movement of the centroid coordinates (x_r, y_r) of rupture sites with time for each cascade. The double-headed arrows on the top show the time duration of each cascade. The vertical bars indicate the extent of spatial shifting. (b) The total distance traversed by both the centroid coordinates during each cascade.

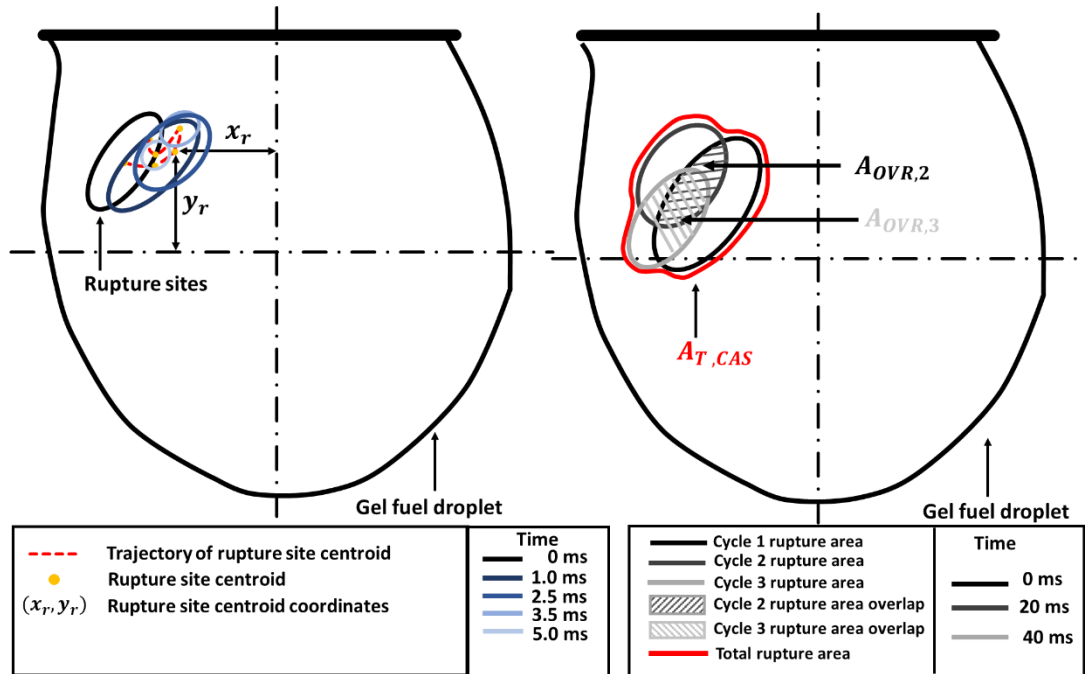


Figure 6. 4. Schematic diagram showing the key geometrical parameters for analyzing the temporal evolution of the gellant shell. **(a)** Spatial movement of the rupture site centroid (x_r, y_r) during a single rupture–recovery cycle for a representative case. **(b)** The maximum rupture area of each cycle, with the rupture area overlapping between successive cycles ($A_{O,2}$ and $A_{O,3}$), and the total rupture area for the cascade ($A_{T,CAS}$).

For instance, the distance traversed by the rupture sites in x-direction during cascades 1 and 2 is ~ 3 times that traveled during cascades 3 and 4, respectively, while that traveled in the y-direction is ~ 1.7 times compared to that traveled during cascades 3 and 4, respectively. This indicates that the gellant shell remains flexible during the first two cascades but becomes increasingly rigid with the following cascades. An important indicator of the shell flexibility during cascades 1 and 2 is the retraction or reversal in the movement of the rupture site centroids, as shown by the arrows in Figure 6.3a. This reversal means that the gellant shell expands as it ruptures and then contracts as the rupture site recovers. Note that the reversal of the rupture site centroid coordinates is absent in the case of cascades 3 and 4, thus indicating that the gellant shell is stiffer or more rigid during these cascades.

Secondly, the total distance traveled by the centroids of rupture sites increases from cascade 1 to cascade 2 and is the highest for the latter among all cascades. This is because, with several rupture cycles occurring in cascade 1, the gellant shell becomes progressively weaker at and around the rupture site, which makes it prone to more frequent ruptures.

The weakening of the rupture site can be inferred from Figure 6.5, which shows the total ruptured area for each cascade. From a droplet-level perspective, it is clear from Figure 6.5 that the shell ruptures repeatedly in the same region of the droplet (second quadrant), which becomes a weak spot, and therefore, a preferential rupture site. However, the total rupture area corresponding to each cascade increases from cascade 1 to 2 and then decreases for cascades 3 and 4, with cascade 2 having the maximum rupture area. In particular, the total rupture area of cascade 2 is ~ 1.8 times higher compared to cascade 1 and ~ 1.7 and 5.8 times higher compared to cascades 3 and 4, respectively (Figure 6.5a). The occurrence of maximum rupture area for cascade 2 means that a larger portion of the gellant shell becomes weaker, and therefore, the droplet naturally bursts at higher frequencies. Figure 5.1 shows that the droplet oscillation frequency resulting from its shell rupture and recovery is highest in cascade 2. The fact that the total rupture area reduces after cascade 2 means that the weak region of the gellant shell shrinks with progressive cascades. This is an indicator of the increasing shell stiffness, i.e., the shell becoming more rigid.

The weak and flexible nature of the gellant shell during the initial two cascades and its strong and rigid nature during the following cascades are further confirmed by analyzing the extent of overlap between the rupture areas of successive cycles for each cascade, as shown in Figure 6.6.

Figure 6.6 illustrates the normalized projected rupture area for each cycle (solid bar) and the amount of overlap of rupture area between successive cycles (hatched bar) for each cascade. The overlap area exhibits the expected hump-shaped trend, where the amount of overlap between the rupture site areas increases from cascade 1 to 2, reaches a maximum at cascade 2, and then reduces for cascades 3 and 4. The

average overlap area of rupture sites for each cascade is shown by the horizontal dotted line in Figure 6.6. The average overlap area for cascade 2 is ~ 10 , 5, and 25 times higher compared to cascades 1, 3, and 4, respectively. A large degree of overlap means that the ruptures occur regularly in the same region of the gellant shell. This weakens the shell and causes it to rupture frequently, thereby increasing the droplet bursting frequency. In contrast, the low degree of overlap in cascades 3 and 4 implies that the tendency of successive ruptures to occur repeatedly at the same location declines after the second cascade.

Another indicator of the gellant shell becoming increasingly rigid is the decreasing number of cycles per cascade from six cycles in Cascade 1 to just two cycles in Cascade 4. Furthermore, the absence of cascades after the fourth cascade indicates that by the time the droplet reaches the fourth cascade, the gellant shell becomes rigid enough that it eventually prevents the occurrence of any further oscillatory rupture–recovery cycles. Therefore, a gradually increasing rigidity of the gellant shell eventually suppresses the oscillatory burning behavior of the gel fuel droplet.

The increasing strength and rigidity of the gellant shell with time can be attributed to two processes: the efflux of unreacted fuel vapors from the droplet via jetting and the evaporation of base fuel (ethanol). Both these processes cause depletion of the base fuel from the droplet, and therefore, lead to an increase in the gellant concentration inside the droplet. This, in turn, leads to a gradual accumulation of the gellant on the shell, thereby increasing the shell thickness. During the initial two cascades (i.e., cascades 1 and 2), it is the efflux of unreacted fuel vapors via jetting that promotes the shell build-up process, as seen by high oscillation or jetting frequency. In contrast, during cascades 3 and 4, the jetting or the oscillation frequency is reduced due to a relatively strong and rigid shell, and therefore, it is the fuel vaporization that governs the shell build-up process. At a point where the shell becomes sufficiently rigid, it is unable to undergo the rupture–recovery oscillatory cycles. This is marked by the end of cascade 4. Note that while the oscillatory jetting terminates with cascade 4, the jetting continues in the form of individual isolated jets that occur randomly during the remaining droplet lifetime.

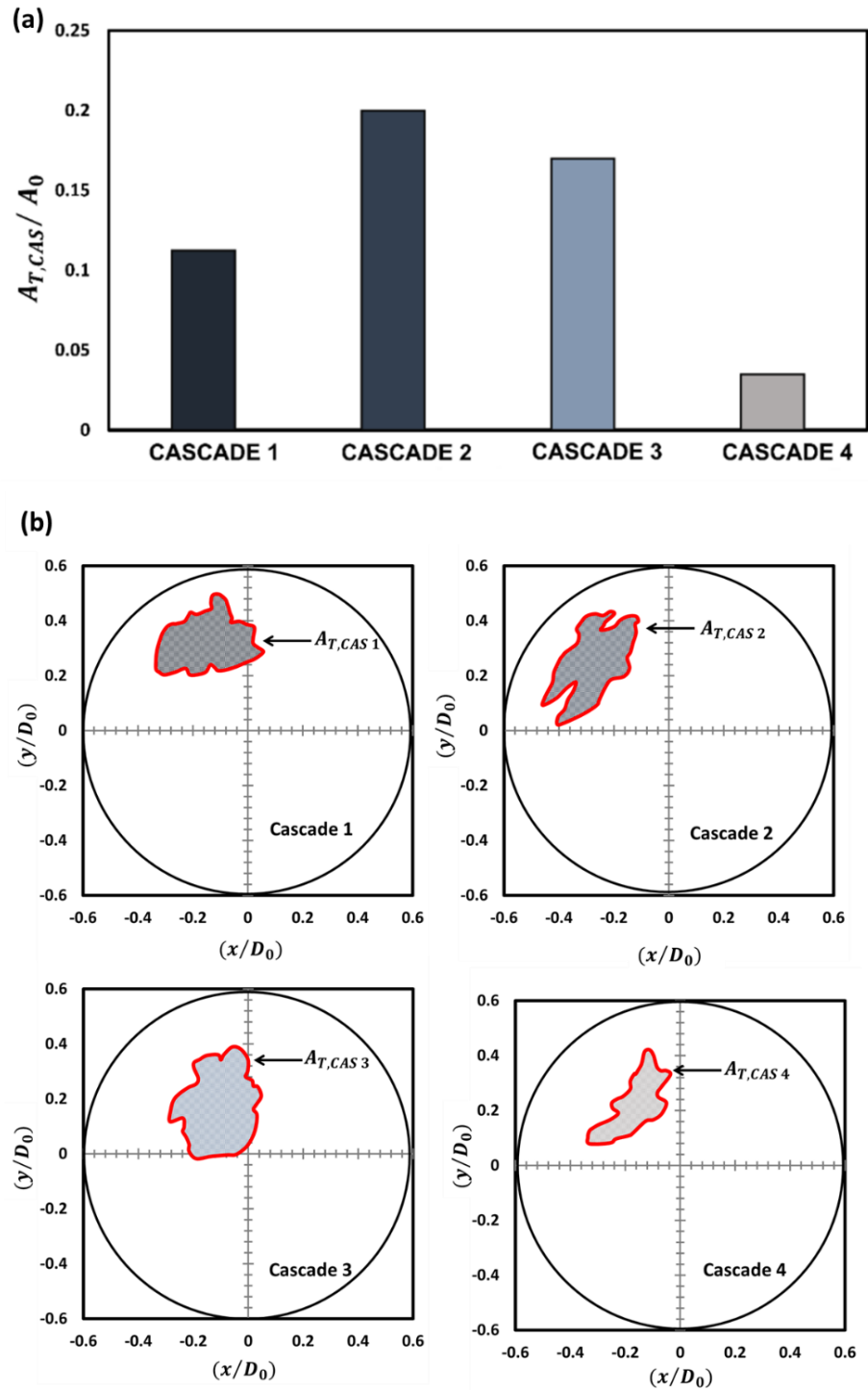


Figure 6. 5. A comparison of the total rupture area for each cascade: (a) graphical representation and (b) schematic representation showing the area relative to the initial droplet area.

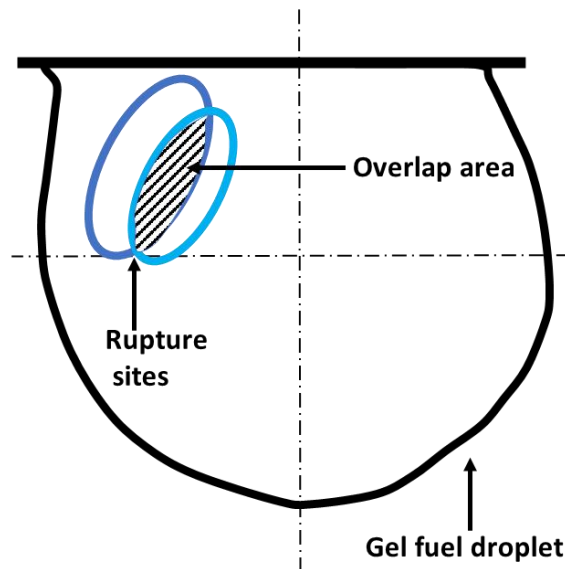
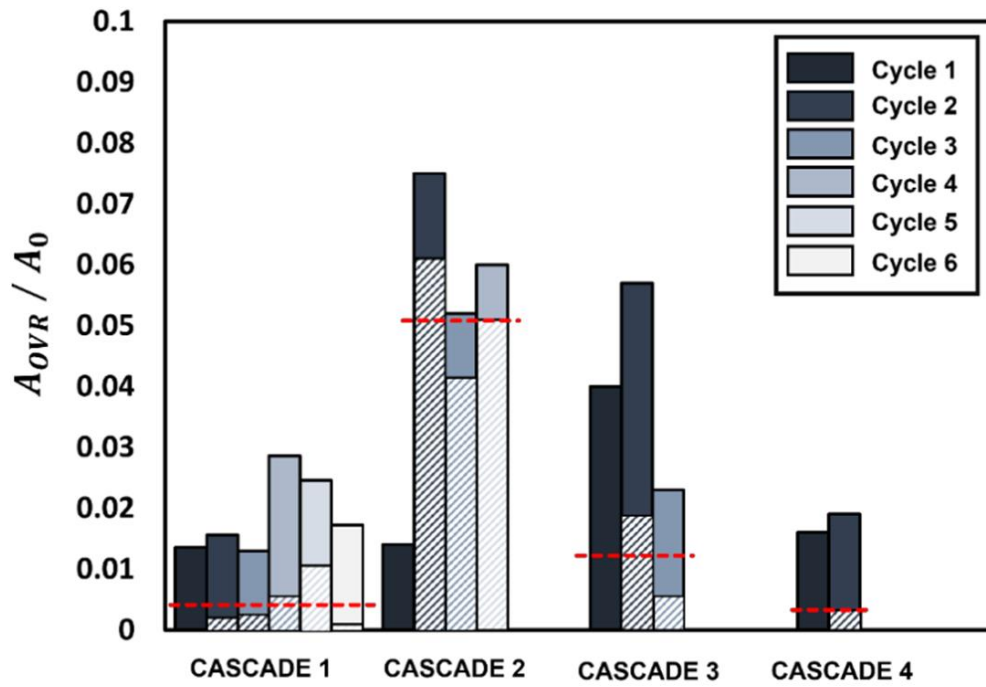


Figure 6. 6. The variation of the normalized overlap area of the rupture sites (A_{OVR}/A_0) between successive cycles with each cascade. Solid bars represent the rupture site area for each cycle while the shaded bars represent the percentage overlap between successive cycles. The horizontal red dotted lines represent the average overlap for each cascade.

6.3 Conclusions

In general, the results presented in Figures 6.1–6.6 demonstrate a time-varying oscillatory response in the combustion of an organic gel fuel droplet with ethanol as the base fuel and hydroxypropyl methylcellulose (HPMC-3%). This study provides a phenomenological understanding of the evolution of the gellant shell during the combustion of gel fuel droplets that burst at different frequencies. Furthermore, these insights can be incorporated to formulate gel fuel compositions that result in gellant shells with customized properties. Consequently, controlling and altering the jetting frequencies can enhance droplet burn rates. The following are the conclusions that can be drawn from this study.

- The high-magnification and high-speed imaging of the gel droplet combustion reveals that the viscoelastic gellant shell at the droplet surface evolves during the droplet's lifetime, which leads to the bursting of gel fuel droplet at different frequencies, thereby triggering a time-varying oscillatory jetting in the form of rupture cascades. In each of these cascades, it is observed that the number of rupture cycles differs and has a decreasing trend. The highest number of rupture cycles is found in cascade 1 with 6 cycles, while the lowest is in cascade 4 with 2 cycles. Furthermore, in cascades 2 and 3, the number of rupture cycles is 4 and 3, respectively.
- The continuous wavelet spectra of the droplet diameter fluctuations elucidate the droplet bursting trait which exhibits a nonmonotonic (hump-shaped) trend. Indeed, the bursting frequency first increases from cascade 1 (15–18 Hz) to cascade 2 (55–72 Hz) and then decreases in cascade 3 (12–14 Hz) and cascade 4 (23–26 Hz), respectively to an extent at which the droplet stops oscillating.
- The assessment of variations in the gellant shell (from thin-flexible to thick-strong and rigid) during the combustion was captured by tracking the temporal variation of the area of rupture sites, the spatial movement of their centroid, and the degree of overlap between the rupture areas of successive cycles for each cascade.

- The newly formed gellant shell during the initial period (immediately after its formation), is weak and flexible; consequently, bursting can be observed at increasingly high frequencies. This is because the area at and in the vicinity of the rupture site becomes progressively weaker with each ensuing rupture in an already weakened shell. This was indicated by a high degree of overlap between the areas of successive ruptures, which was found to be highest in cascade 2 (~81%).
- The shell flexibility during cascades 1 and 2 exhibited a retraction and reversal in the motion of rupture site centroids. However, in the ensuing cascades 3 and 4, when the droplet had undergone multiple ruptures, this retraction and reversal of the rupture site vanished. Consequently, the depletion of the fuel vapor aids in the accumulation of gellant on the shell, thus leading to the formation of a thick, strong, and rigid shell, which suppresses the droplet oscillations.

CHAPTER 7: EVOLUTION OF THE GELLANT SHELL

The disruptive combustion behavior of gel fuel typically occurs in the form of jetting of unreacted fuel vapors. Disruptive combustion is dependent on the gellant shell and its structure throughout the combustion. In this study, we have utilized the DSC (differential scanning calorimetry) to decipher the temperature-dependent structural changes in the gellant during combustion. The study reveals that the gellant shell undergoes glass transition which not only affects the gellant shell bursting but also influences the convective transport of fuel vapors to the flame envelope. Overall, this study provides insights into the mechanism of combustion for organic gel fuels.

7.1 Introduction

In the contemporary era of innovation and futuristic technology, in the domain of aerospace propulsion systems, there is a necessity for high-performance propellants with reliability, ecological safety, reusability, and ease of processing. The promising candidates for achieving these feats are the gelled propellants. The gelled propellants have the potential to replace the existing solid and liquid propellants [32], [54]–[58], [66]. Moreover, gelled propellants can incorporate the advantages of both propellants, for instance, easy storage and handling traits of solid propellants alongside throttle control and atomization of liquid propellants [32], [54]–[58], [66]. Gelled propellants have demonstrated easy handling of hazardous and toxic hypergolic propellants [54] and have shown less sensitivity to accidental ignition unlike solid propellants [54]. The incorporation of gelling agents into cryogenic liquid fuels can mitigate evaporation losses and can also overcome the storage issues associated with zero gravity [54], [108]. Moreover, the high viscosity of gel propellants facilitates the suspension of metal additives into the fuel matrix and has demonstrated an increase in energy density and specific impulse [36]. The use of gelled propellants for sounding rockets, hybrid rocket

motors, and ramjet engines has provided a perspective into its applications [32], [54], [57], [108].

Despite all the potential advantages and application avenues, the complex combustion of gel propellants is yet to be deciphered. The typical combustion behavior of gel propellants is accompanied by disruptive burning in the form of jets of unreacted fuel vapors that impact the flame in its vicinity and distort the flame [39], [40], [70], [71]. A usual jetting event occurs sequentially as firstly the gellant crust /shell formation due to the phase separation of the gelling agent from its components in the vicinity to the droplet surface. Secondly, underneath the gellant shell, the trapped fuel begins to boil. Thirdly, the inner surface layer of the gellant shell acts as nucleation sites for bubble growth, this leads to an increase in pressure inside the shell. Eventually, the gellant shell ruptures, and subsequently release of internal pressure via jetting of unreacted fuel vapor occurs. Lastly, the jet travels to the flame envelope in the vicinity which causes disruptions in the flame [39]–[42]. Therefore, in the disruptive combustion of the gel propellants, the gellant shells play a crucial role in jetting. Hence, the objective of our study is to understand the temperature-dependent evolution of the gellant shell during combustion, as it significantly influences the gel droplet bursting behavior and consequently the jetting behavior.

Two non-metalized organic gel fuel combinations are examined in this study comprising ethanol as base fuel. The tri-component gel fuel consists of two different organic gellant combinations which have:(1). Research grade ethanol (99.8% pure; CAS No. 64-17-5) as the base fuel. (2). The gellants i.e., Hydroxypropyl methylcellulose (HPMC; CAS No. 9004-65-3, bulk density $\rho_b \sim 689.19 \text{ kg/m}^3$) and Methylcellulose (MC; CAS No. 9004-67-5, bulk density $\rho_b \sim 503.92 \text{ kg/m}^3$). The methoxy group in MC ranges from 27.5 to 31.5%. On the contrary, HPMC consists of both hydroxyl and methoxy groups ranging between 7-12% and 28-38 % respectively [46] (3). De-ionized water as the base solvent. All these components were procured from Sigma Aldrich Co. Notably, the gel fuels were prepared over a range of concentrations. In the case of HPMC, it was from 3

to 6% while for MC the range was 8–9%. For succinctness, two cases of extremities of jetting behavior are studied and the details of the compositions of the test fuels and yield strength are given in Table 3.1.

7.2 Results and Discussion

The combustion of an organic gel fuel droplet proceeds in three stages namely: Stage I: Transient heat up, Stage II: Disruptive burning, and Stage III: Carbonization as shown in Figure 7.1. In the transient heat-up, phase separation of the multicomponent gel fuel takes place and consequently, the formation of the gellant shell takes place. In disruptive burning, significant jetting behavior of unreacted fuel vapors is observed. The carbonization stage initiates with an appearance of a carbonaceous region appearing on the gellant shell. Moreover, during this stage suppressed jetting is observed due to the burning of traces of base fuel present in the gellant shell. Interestingly, it is seen that the gellant shell is evolving across the stages of combustion.

In Figures 7.1 and 7.2 initially, the newly formed shell after phase separation is weak and flexible underneath which the boiling of trapped fuel takes place. Further, the pressure surge caused by the unreacted fuel vapors leads to the bursting of the viscoelastic gellant shell and subsequently jetting occurs. This is followed by the closure of the rupture site due to the viscoelasticity of the gellant shell and further pressure surge initiates again due to unreacted fuel vapors underneath the shell. As the combustion progresses during stage II, the gellant shell exhibits structural changes like an increase in strength and rigidity which can be attributed to two scenarios: the efflux of unreacted fuel vapors from the droplet via jetting and the evaporation of base fuel. Both scenarios lead to the depletion of base fuel from the droplet and hence causing an increase in gellant concentration inside the droplet. Consequently, the gellant shell increases.

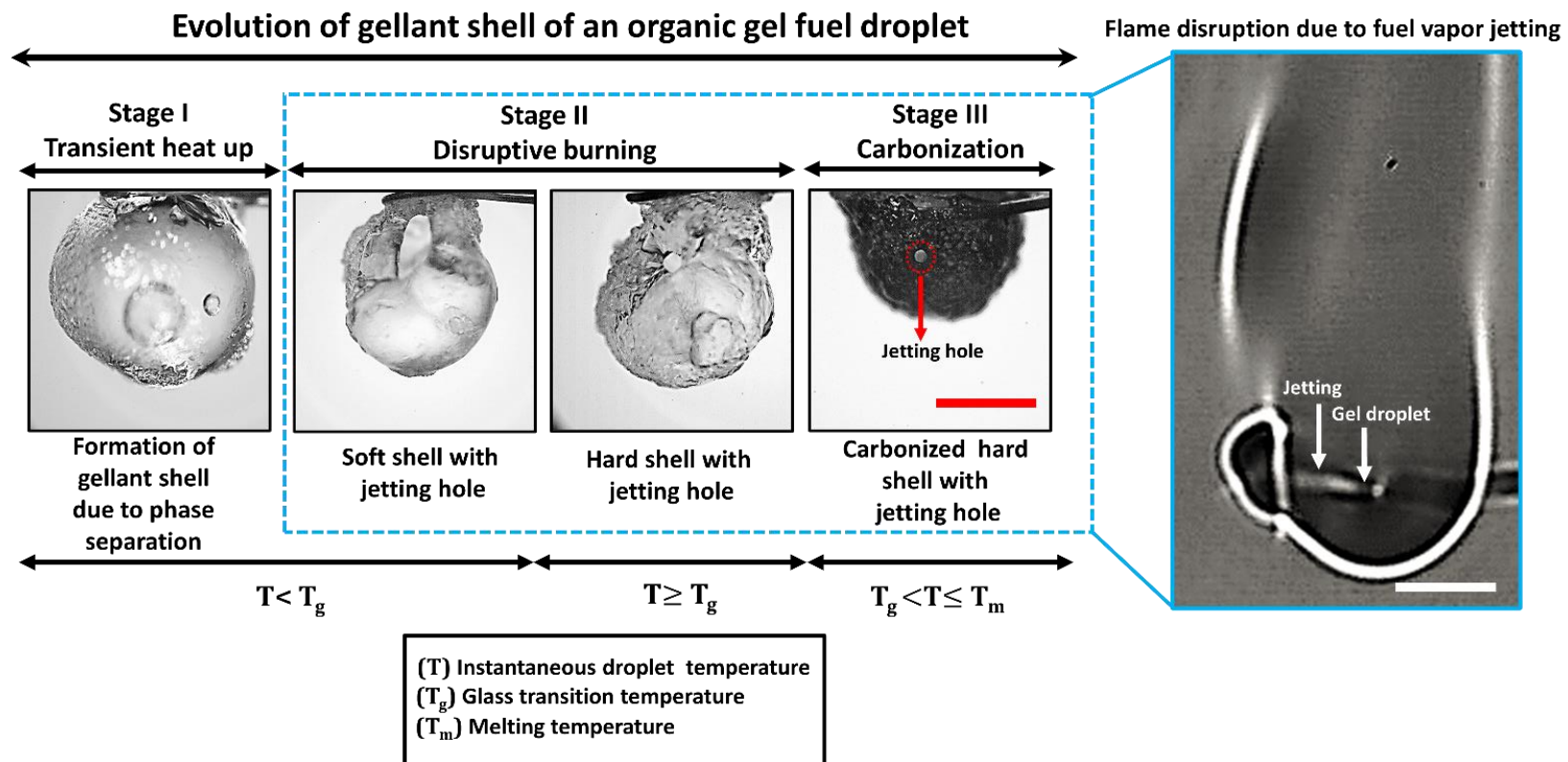


Figure 7. 1. High-magnification representative images showing the temperature-dependent structural variation of gellant shell during the disruptive combustion of gel fuel droplet. The scale bar equals 1mm at the droplet scale and 6mm at the flame scale.

Evolution of gellant shell of an organic gel fuel droplet

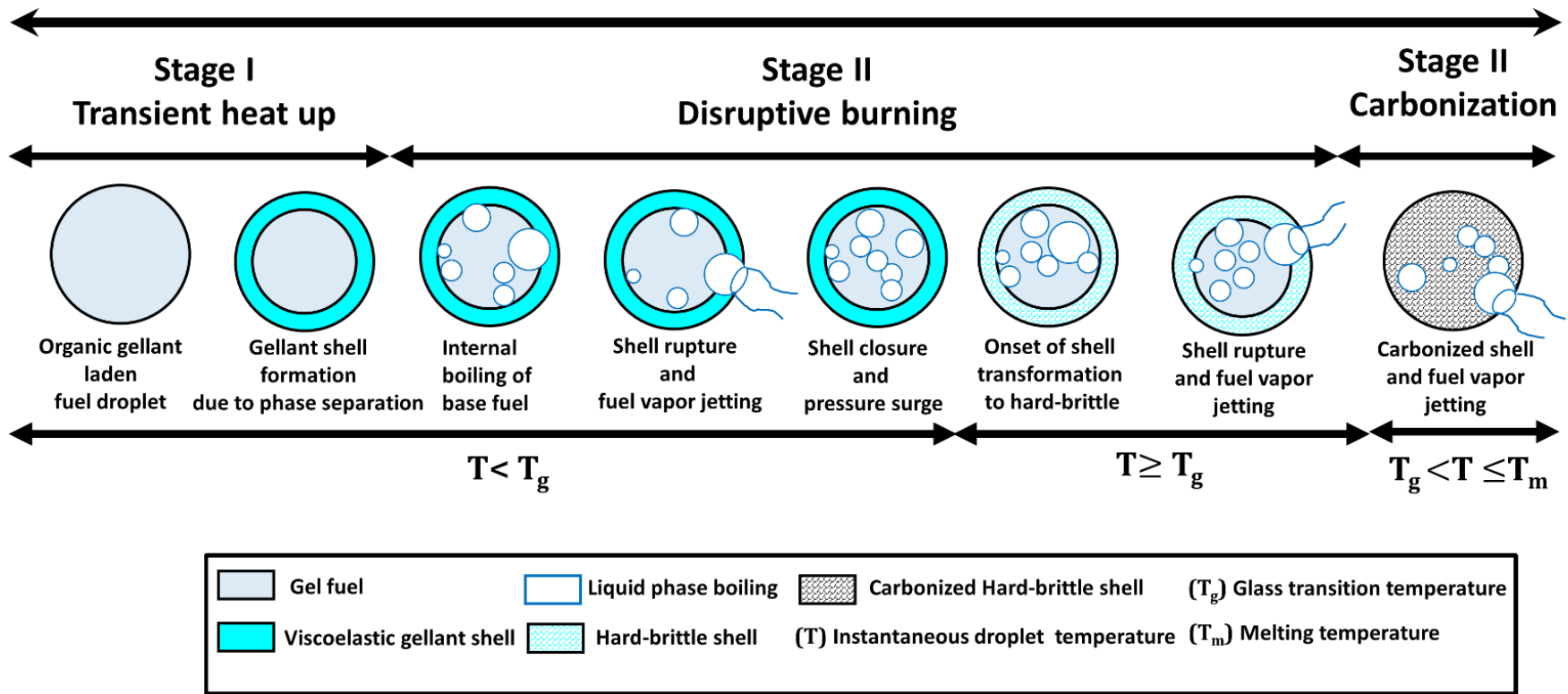


Figure 7. 2. Schematic illustration depicting the variation of jetting behavior due to temperature-dependent gellant shell changes during combustion.

During the combustion of organic gel fuel droplets, the structure of the gellant shell and its temperature dependence cannot be ignored. Hence in our study, differential scanning calorimetry (DSC) was performed for the gel fuels (HPMC-3% and MC-9%). Note that it is extremely difficult to predict the variation of gellant shell structure as a function of temperature in a dynamic combustion environment. Therefore, the DSC thermograms can provide crucial insights into the temperature-dependent structural variation of the gellant shells.

The DSC analysis was carried out using a Perkin Elmer STA 8000 analyzer. The samples of 30mg were loaded onto the ceramic pan and heated in the alumina crucible from 30 to 500 °C in an inert nitrogen atmosphere. The nitrogen was purged at 20ml/min. The DSC thermograms for the fuel under study are illustrated in Figure 7.3.

In Figure 7.3, the DSC thermograms illustrate two endotherms and a step change in the heat flow signal [113]. The large endotherm peak corresponds to the phase separation of the gel fuel components into base fuel and polymeric gellant (shell). Contrary to this, the smaller endothermic peak corresponds to the melting of the polymeric gellant shell [112]. Further, in between these two endotherms, the step in the heat flow signals signifies the glass transition of the polymeric gellant shell [113]. During the glass transition, the newly formed soft gellant shell transforms structurally to hard-brittle (glassy) [114]. This thermally induced (due to combustion) glass transition is opposite to the conventional glass transition of the conventional glassy to rubbery transition [114]. The reverse glass transition occurs due to the coupling of phase separation followed by an increase in the inter/intra polymeric interactions [114]. Hence, in our study, during the thermally induced glass transition (due to combustion) the structural change in the polymeric gellant shell causes an increment in the stiffness, strength, and toughness [114]. The thermally induced glass transition in HPMC-3% occurs at ~133 °C while for MC-9% it is ~166 °C. These temperature values lie in the range of glass transition temperatures for both HPMC and MC [115]–[117]. Notably, from Figure 7.3, the glass transition temperature for HPMC-3% is less than MC-9% fuel composition.

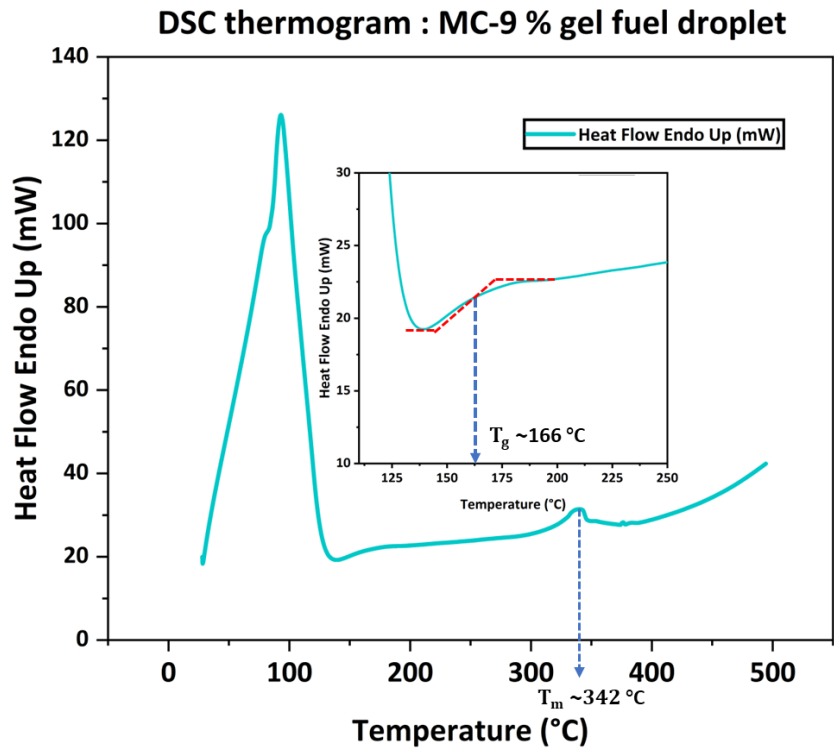
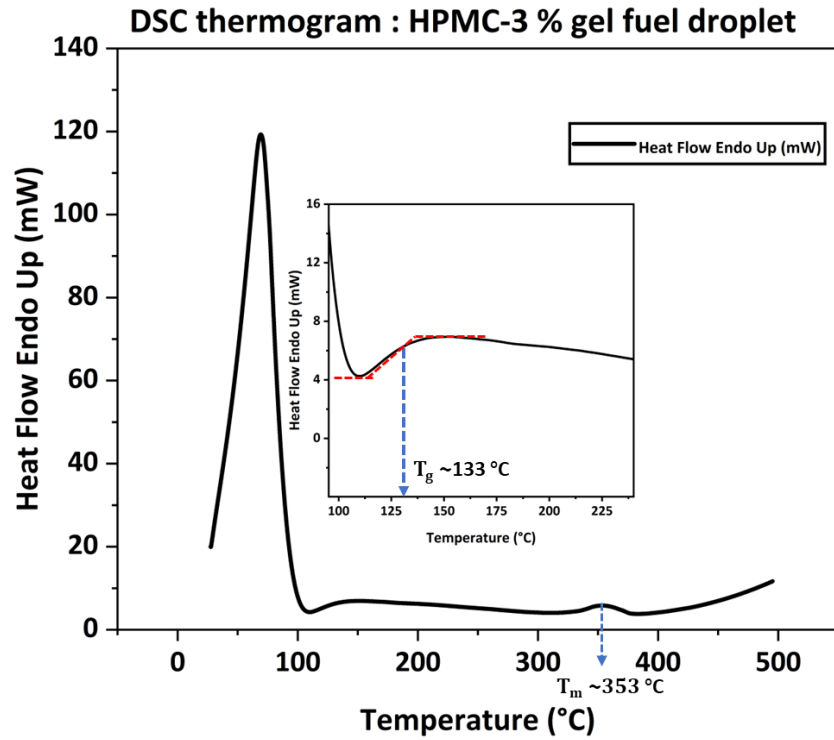


Figure 7. 3. The DSC thermograms for HPMC-3% and MC-9% gel fuel compositions depict their respective glass transition and melting temperatures.

This can be attributed to the presence of a bulkier hydroxyl group which results in larger fractional free volume due to the expansion of intermolecular distance and shorter chain length. Consequently, a disruption in the hydrogen bonding takes place due to the bulkier hydroxyl group between the adjacent polymer chains and thus the glass transition temperature decreases for HPMC [115]–[118].

The temperature-dependent structural changes in the polymeric gellant shell after phase separation (Figures 7.1 and 7.2) not only influence the compensation mechanism of pressure surge but also the jetting behavior of gel fuels. It has been observed that initially, HPMC-3% composition tends to form thin-weak-and flexible shells which in turn accommodates the intense pressure surges via shell elongation [47]. Furthermore, these traits of the HPMC-3% gellant shell demonstrate an oscillatory bursting behavior [47] which leads to oscillatory jetting of unreacted fuel vapors which disrupts the flame in proximity [47]. However, for MC-9% composition, the newly formed shell after phase separation is thick-rigid and strong in comparison to HPMC-3% (yield stress ~ 17 times HPMC-3% as seen in Table 3.1). Thus, the gel fuel droplet encounters rapid expansion and contraction due to pressure surges at very short time scales. Moreover, the rigid shell of MC-9% inhibits the rapid expansion of the gellant shell. Furthermore, this unstable state of pressure transients leads to the transient bursting of the gellant shell which manifests in the form of isolated jetting of unreacted fuel vapors which further disrupts the flame in the vicinity. As the combustion progresses, in HPMC-3% and MC-9%, the glass transition occurs which leads to the structural changes in the gellant shells as discussed earlier. The effect of the glass transition significantly affects the shell-bursting behavior and subsequently the jetting behavior. For HPMC-3% the oscillatory bursting ceases and the ensuing ruptures occur in the form of transient bursts which leads to transient jetting behavior at the flame scale. While for MC-9%, the shell further hardens and continues to burst in transient mode.

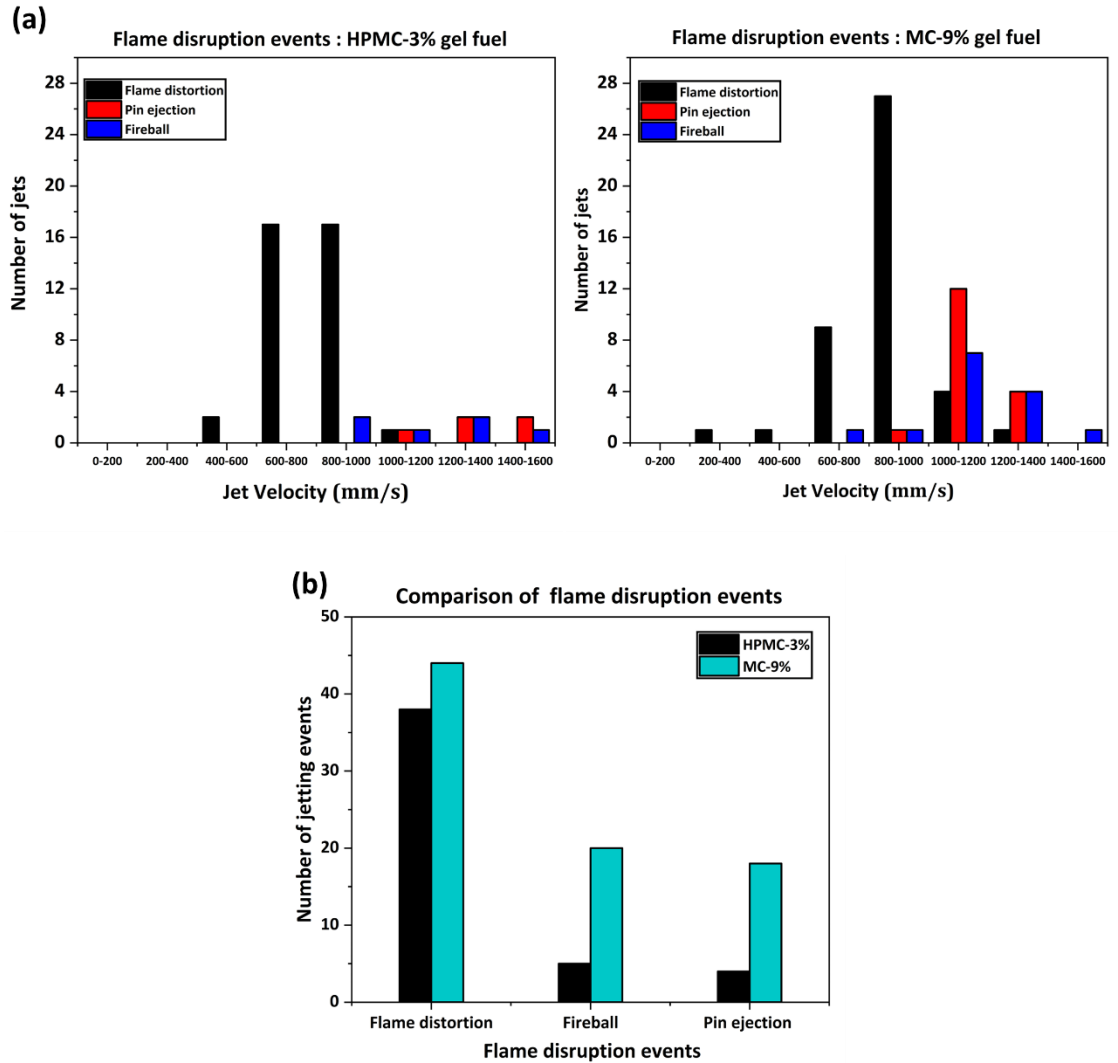


Figure 7. 4. (a) Distribution of velocities of flame disruption events caused by jetting during the combustion of ethanol-based HPMC-3% and MC-9% gel fuels. **(b).** One-to-one comparison of flame disruptions events for HPMC-3% and MC-9%.

The temperature-dependent structural changes in gellant shells not only affect the shell bursting behavior but also significantly governs the degree to which these jets disrupt the flame periphery in the vicinity. The flame disruptions are usually observed in the form of flame distortions (~500 to 870 mm/s), pin ejections (localized flame extinction, 1000 to 1550 mm/s), and fireball outside the flame (~800 to 1530 mm/s). In our study, from Figure 7.4a, HPMC-3% gel fuel droplet tends

to form substantial numbers of flame-distorting jets in comparison to pin ejections and fireball jets. While in the case of MC-9% (Figure 7.4a) gel fuel droplets, along with flame distortions; pin ejections, and fireballs for found in abundance. The difference in the jetting behavior of MC-9% (Figure 7.4b) can be attributed to the propensity to form strong-rigid shells which on glass transition hardens further. Consequently, the pressure built-up inside the gellant shell increases, and due to its inability to undergo severe expansion, high-velocity flame-disrupting jets (fireball and pin ejections) are formed.

7.3 Conclusions

In summary, the current study provides insights into the thermally induced structural changes in the gellant shell of an organic gel propellant. The gellant shell after its formation proceeds towards the glass transition which significantly influences the shell bursting mechanism and subsequent jetting behavior. The study also gives discernment into the disruptive combustion behavior of organic gel which can help in devising strategies to fabricate gel propellants in the future.

CHAPTER 8: REGRESSION RATE ANALYSIS OF SOLIDIFIED ETHANOL FUELS FOR HYBRID ROCKETS

The success of hybrid rockets in future military and commercial applications will depend on their ability to utilize fuels that are not only easy-to-process, safe, and environmental-friendly but also meet operational demands of high regression rate and efficient combustion. In this study, the eco-friendly ethanol fuel is solidified using Methylcellulose (MC) and Hydroxypropyl Methylcellulose (HPMC) as organic gellants and de-ionized water as the solvent and proposed for usage as a fuel for hybrid rocket applications. The gellant concentration is varied in the range of 10 – 14 % while the nano aluminum concentration is varied in the range of 2 - 6 wt.% for HPMC and 2 - 4 wt.% for MC samples. Subsequently, the regression rate of solid fuels is investigated as a function of the oxidizer flux ranging from 0.97 – 11.7 kg/m²-s in an opposed flow burner facility (OFB). Over the range of oxidizer fluxes, the regression rate of solid ethanol fuels is higher than the conventional fuels such as HTPB and DCPD and comparable to that of paraffin wax. The high regression rate is attributed to their low melting points and enthalpy of melting, strongly shear thinning behavior, and the occurrence of vapor jetting, which in addition to fuel gasification aids in the advective transport of unreacted fuel vapors to the flame zone. Finally, the effect of oxidizer flux and nanoparticle concentration on the regression rate is analyzed. Irrespective of the fuel, the regression rate increases monotonically with the oxidizer flux whose degree depends on the flow regime i.e., laminar versus turbulent; being higher for the latter. Further, in the laminar regime, there is no effect of increasing nanoparticle loading on the regression rate while in the turbulent flow regime, the regression rate increases rapidly with increasing concentration.

8.1 Introduction

Hybrid rocket systems are fast becoming an attractive choice for space exploration as they overcome the safety, environmental, reliability, and cost issues concerning rocket engines based on conventional solid or liquid propellants or both [119], [120]. Hybrid rockets constitute a chemical propulsion system where the inert solid grain (solid) and the oxidizer (liquid) have different phases and are physically separated in the engine. Once the solid grain is ignited and combusts with the injected liquid or the gaseous oxidizer flow (at high pressure), it forms a diffusion flame. This configuration allows throttling by varying the oxidizer flow rate, thereby providing a means for thrust modulation, greater controllability, and on-off capability compared to conventional rocket engines. However, the classical hybrid motors using polymeric fuels such as Hydroxy-Terminated Polybutadiene (HTPB) and paraffin wax suffer from larger oxidizer volumes, low densities of the exhaust, low fuel regression rates (\dot{r}_b), low specific impulse, and a low combustion efficiency [62], [121]. Since the regression rate and combustion efficiency are the key design and performance parameters, several past studies have devised methods to improve these parameters, namely, designing fuel grains with multiport geometries, energizing the fuel grain either via the addition of metallic particles or via oxidizer doping [122], [123], and by adding energetic nanoparticles [100], [124]–[127]. The use of energetic nano additives is a density enhancement technique that has been reported to accelerate the regression rate substantially. For instance, at moderate oxidizer mass flux, adding 13% of energetic nano-aluminum powders to the HTPB-based fuels enhanced their regression rate by 123% compared to their unloaded counterpart [128]. Risha et al. [129] reported a 62% augmentation in the regression rate of HTPB in comparison to the neat fuel and combustion efficiency of 88 – 92% with the addition of 84.8% Aluminum nanoparticles. Strand et al. [130] showed that by adding 40% Aluminum and 30% coal particles (remaining 30% HTPB) the regression rate increased by 17% compared to pure HTPB. This enhancement in regression rate was attributed to the high heat release and radiation heat transport resulting from the combustion of

nanoscale metal additives. Despite their desirable characteristics, metallic particles become less reactive over time due to the development of a passive oxide layer over their surface, which is mostly inert due to its significantly high melting point. To overcome the oxide layer problems, Li, and Jin [131] used oxidizing agents such as Ammonium and Potassium Perchlorates, and catalysts such as Lithium Fluoride (LiF) with the micron-sized boron particles and found that the burning rate increased by 10-36 %. A few studies demonstrated an improvement in the regression rate by using energetic binders such as 3-azidomethyl-s-methyloxetane (AMMO), 3-nitramethyl-3-methyloxene (NMMO), and Glycidyl Azide Polymer (GAP) in HTPB fuel [16, 17]. The usage of GAP as the replacement for HTPB has gained attention due to its higher density (1.30 g/cm^3) and high heat of formation [132], [133]. The solid propellant formulation based on GAP is found to have higher burning rates and high specific impulse with reduced smoke [132], [134]. Harting [135] explored the usage of GAP as the inert solid fuel for hybrid rocket motors and demonstrated that its burning rate with gaseous oxygen (GOX) was 1-2 orders greater than that of HTPB. While the methods discussed above help in achieving high regression rates, they may not be attractive if they are accompanied by poor combustion performance. Therefore, to overcome the limitations of hybrid propellants, it is imperative to either identify or formulate an alternative fuel that is not only cost-effective and environmentally friendly but also offers a high energy density, lower ignition delay, and faster burn rates.

Ethanol is an eco-friendly biofuel that has proven to be an energy-efficient fuel for liquid rocket engines such as PGM-11 Redstone and German V2 engines [136]. However, the usage of ethanol in hybrid rocket engines would require it to be solidified using a suitable gelling agent, and depending on the choice of gelling agent *i.e.*, organic versus inorganic, the combustion performance may vary. The cellulose-derived gelling agents such as Methylcellulose (MC), Hydroxy-Propyl Methylcellulose (HPMC), and Sorbitol are consumed completely during combustion (via carbonization), and therefore, contribute directly to the combustion heat release. For example, with a 7 wt. % increase in the MC concentration, the heat of combustion of solidified ethanol increases by 3.25 %

[81]. On the contrary, the inorganic gelling agents such as fumed silica have been reported to reduce the burn rates of Kerosene, JP-5, JP-8 turbine fuel, and UDMH, since they have high melting points, and therefore, difficult to combust [137], [138].

A cost-effective Ethanol-based gel fuel and the formulation thereof for hybrid rocket engines was first proposed by Brandenburg et al. [136]. It was demonstrated that using organic gellants such as Methylcellulose in conjunction with Calcium acetate or independently can increase the fuel stiffness, and hence, its yield stress, which enables rapid acceleration of the rockets. A single-stage rocket was successfully tested using a fuel consisting of ~85 wt.% ethanol, 5 wt.% water; and 10 wt.% methyl cellulose as the gellant with a burn time of ~20 s and thrust generation of 50 lbs. This low-cost bio-fuel-based gel fuel was shown to have a high mass fraction of ethanol, produce mechanically strong fuel grains, and low molecular weight exhaust, which is non-toxic and eco-friendly. In the early 2000s, the solidification of liquid fuels was achieved by cryogenic freezing of the organic liquids [137]. With these cryogenically solidified fuels, a regression rate improvement of 3-4 times could be achieved compared to HTPB at the same magnitude of oxidizer mass flux. In another work, Gramer et al. [137] reported that the regression rate of two fuel-oxidizer combinations, namely, solidified kerosene-GOX and methane-GOX was 20-40 times higher compared to the HTPB-based fuels. The higher regression rates compared to the conventional hybrid fuels have been reported for several other cryogenically solidified fuels that are formulated using methane, oxygen, and pentane as well as for the non-cryogenic wax [139]–[142]. These studies reported that the liquefying melt layer of the solid fuel and the regression rate is strongly correlated. This is because, when the grain melt surface is subjected to high shear by the oxidizer stream, a thin liquid layer forms over the melt surface due to its shear-thinning behavior. This liquid layer is hydrodynamically unstable and eventually breaks into ligaments. These ligaments break down further into smaller, fine droplets, that are entrained by the high-pressure oxidizer stream injected into the combustion chamber. These entrained droplets vaporize and burn quickly, which accelerates surface regression. Since the reduction in viscosity promotes the formation and break-up of ligaments, the shear

thinning property of the fuel plays a key role in improving combustion performance. This is enabled by the high shear rates encountered in hybrid rocket engines that lead to a reduction in the viscosity of the melt layer by several orders of magnitude. This way, the decrease in viscosity with applied shear translates directly to an enhancement in regression rate. However, under actual pressure conditions, the liquid layer developed over the melt area (at the surface of the fuel grain) is highly unstable, and therefore, difficult to maintain. Furthermore, the methodology of formulating and developing solid cryogenic fuels is costly as well as practically challenging. Consequently, Brandenburg[136] developed a tri-component fuel consisting of Plexiglass, and ethanol that is gelled using methylcellulose and calcium acetate while Nitrous oxide was used as an oxidizer. With this solid fuel, an improvement of approximately 6% (on an average) was observed in the specific impulse under static motor firing at 1100 psi. While these studies focused on performance-based tests, they lacked data on the molecular interaction, characterization, and stability of solidified fuels, which are crucial in understanding and tuning the fuel's rheo-physical properties. This is important from the viewpoint of optimizing the storage, handling, and processability of the fuel grains during casting since they are governed by the rheo-physical properties [143], [144]. While the determination of the regression rate of solidified fuels using lab-scale static firing has been the focus of many studies, the experiments therein have been limited to traditional fuels such as HTPB (a cross-linked rubber), Paraffin wax, and Bee wax, and plastics such as Polyethylene[46], [145]–[148].

Based on the above discussion it can be inferred that solidified ethanol enriched with energetic nanoparticles can be a promising environmental-friendly fuel for hybrid rockets applications. However, evaluating its efficacy requires considerable experimental effort, which is currently lacking in the open literature. Therefore, this study focuses on formulating solidified ethanol fuels containing organic gellants and high energy density Aluminum nanoparticles and enabling their molecular structural characterization. Furthermore, an opposed flow burner (OFB) facility is developed to evaluate the performance of these fuels in terms of their regression rate (\dot{r}_b) at different magnitudes of oxidizer mass flux and at ambient pressure. The

regression rate of solidified fuel (with and without the energetic nano additives) is compared with that of the paraffin and 2080 Boron wax using the data from the literature under the same value oxidizer mass flux in an OFB. The opposed flow burner mimics the multi-dimensional environment of a hybrid rocket motor through a simplified one-dimensional representation, which has been used as a vital tool for the initial screening and characterization of hybrid rocket fuels [57]. Such screening may be beneficial during the design and development phase and before the pilot/full-scale testing of promising fuels for hybrid rockets.

8.2 Materials and Methods

8.2.1 Materials

The solidified ethanol fuels both with and without metallic nano additives are formulated. The metalized fuels consist of four components, namely, the base liquid fuel, an organic gellant, gellant solvent, and aluminum nanoparticles, while the nanoparticles are absent in non-metalized fuels. The base liquid fuel is research-grade ethanol (CAS No. 64-17-5) with a purity of $\geq 99.5\%$. The organic gellants selected for solidifying ethanol are macromolecular Methylcellulose (MC; CAS No. 9004-67-5) and Hydroxypropyl Methylcellulose (HPMC; CAS No. 9004-65-3), which have bulk densities $\rho_B \sim 504 \text{ kg/m}^3$ and $\sim 689.2 \text{ kg/m}^3$ respectively. Both the organic gellants consist of microscale particles and appear as white solid powders at room temperature conditions. MC has a Methoxy group ranging from 27.5 – 31.5% while HPMC has both active Hydroxyl and Methoxy groups ranging between 7–12% and 28–30 % respectively [46]. The gellant solvent used is de-ionized water. All the chemicals are obtained from Sigma Aldrich Co. and used as it is for formulating the solidified ethanol fuels. Aluminum nanoparticles (NP) are used as energetic additives in fuels. The spherical nano aluminum particles with an average diameter of 50 nm and a bulk density $\rho_B \sim 193 \text{ kg/m}^3$ are supplied by the Agency of Defense Development (ADD), Republic of Korea. Aluminum is selected as the energetic nano additive on account of two key factors. *First*, historically, Aluminum is the most explored energetic nano additive for solid-fuel formulations

and several studies have investigated the role of Aluminum nanoparticles in both conventional polymeric binders as well as nonpolymeric binders such as paraffin solid fuel. This is due to its nominally high heat of oxidation (31,100 kJ/kg), a relatively high density (2.7 g/cc), and easy ignitability in the high-pressure high-temperature combustion environment of a rocket motor [13,14]. *Second*, while the majority of the energetic nano additives (Li, Mg, Ti, C, B, Be, Si, Fe, Al, W, etc.) offer a higher volumetric heat release compared to HTPB, from a viewpoint of gravimetric heat release *i.e.*, on a per unit mass basis, Beryllium (Be) possesses the highest heat of oxidation. However, its oxidation product (BeO) is carcinogenic, which rules out its candidature as a viable additive [143]. From a viewpoint of energy density *i.e.*, volumetric heat release, Boron offers the highest heat of oxidation. However, the difficulty with its ignition and propensity for incomplete combustion to form oxides such as BO_2 (other than B_2O_3) as final products present obstacles to its adoption[128]. In this regard, Aluminum nanoparticles are a promising additive due to their thermal properties, low melting point, ease of processing, and relatively low cost. However, the presence of a passive, inert oxide layer of Al_2O_3 on the surface of the nanoparticle is undesirable as it impedes burning. Fortunately, this Al_2O_3 layer is brittle, which causes it to crack when the Al-nanoparticle expands on heating, thereby, permitting the pure/active Aluminum to react with the oxidizer [149]. Furthermore, the relative percentage of active Aluminum versus the oxide layer in the nanoparticle can be controlled by tuning the manufacturing and storage conditions. These factors make nano aluminum an attractive choice as an energetic additive for enhancing the performance of a volume-limited propulsion system.

Combustion of aluminum nanoparticles involves a spectrum of thermal, physical, and chemical processes where the transfer of mass, momentum, and energy are tightly coupled between the particle and the gas phase transformations occurring in the oxide layer on the particle surface. The aluminum oxide (Al_2O_3) layer is 2–4 nm thick [128] and the combustion occurs heterogeneously on the particle surface. The three key stages that typically govern the burning rate of aluminum nanoparticles are (1) diffusion of oxidizer molecules through the gas-phase

mixture; (2) diffusion of oxidizer across the oxide layer, and (3) chemical reactions between oxygen molecules and active aluminum in the particle core [128]. The subsequent energy released during the reaction process heats up the particle, which is then transferred to the ambient through conduction and radiation.

Sundaram et al. [150] reported that the combustion of aluminum nanoparticles happens heterogeneously on the particle surface and that their burning time is an exponential function of the temperature. The activation energy of aluminum nanoparticles ranges between 50 – 145 kJ/mol. Since the oxide layer has a significantly high melting point the mass diffusion across the oxide layer can impede the burning process at temperatures lower than the melting temperature of aluminum. Fortunately, the aluminum oxide layer is brittle, which causes it to crack/fracture either during ignition or during the melting of the particle core and/or during the period when the oxide layer undergoes polymorphic phase transformations. This aids in significantly reducing the diffusion resistance during particle burning.

8.2.2 Fuel Formulation

The chemical composition of the fuel samples analyzed in this study is listed in Table 8.1. These solidified ethanol fuel samples (both with and without nanoparticles) are formulated using a three-step process: Firstly, the organic gellant (HPMC or MC) is added to ethanol (base liquid fuel) and the resulting mixture is stirred vigorously by hand using a spatula for ~ 60 s at room temperature. Secondly, in metalized samples, to avoid the oxidation of energetic Aluminum NPs during the handling process they are weighed and dispersed (in 2, 4, and 6 wt. %) into the ethanol-gellant mixture in an inert environment *i.e.*, a N₂ filled glove box. Subsequently, the gellant solvent *i.e.*, DI water is added to complete the fuel formulation. In non-metalized fuel samples, the DI water is mixed directly with the ethanol-gellant blend to complete the solidification procedure. In the third and final step, the resulting mixture is stirred vigorously at 600 rpm for ~ 180 s by using a mechanical stirrer. The resulting solid-like ethanol is then left undisturbed at room temperature for ~ 2 days. This rest duration allows the 3D-network formation

process to complete and form a stable gel phase. Additionally, this period is utilized to perform a visible check for any phase separation that may occur during the network formation process.

A key objective when preparing solidified fuel is to obtain a phase structure that contains a maximum amount of base fuel (including nanoparticles) and a minimum amount of gellant and solvent while retaining long-term stability. To achieve this objective, a lower and an upper threshold concentration of the gellant is identified for this four-component system comprising of the liquid base fuel (ethanol), organic gellant (HPMC or MC), the gellant solvent (de-ionized water) and metal nanoparticles (Aluminum). Below the lower threshold concentration, this four-component fuel system behaves as a gel, while at gellant concentrations beyond the upper threshold, a stable fuel cannot be obtained. Specifically, a continuous 3D fibrous network spread across the entire volume of the fuel cannot be realized and the fuel formulation separates to form granular clusters. The test samples that are stable and lie within the lower and upper threshold limits of the gellant concentration are enlisted in Table 8.1. To determine these threshold limits, different fuel samples with the gellant concentration varying from 1 - 20wt. % (in 1wt. % increments) are formulated and then testing the samples qualitatively.

Table 8. 1 The chemical composition, density, and yield stress of solid ethanol fuel samples both with and without aluminum nanoparticles.

Solidified fuel	Chemical composition (wt. %)					Density (g/cc)	Yield Stress (Pa)
	Base fuel	Organic gellant	Nano additive	Solvent			
	Ethanol	HPMC	MC	Aluminum	DI water		
HPMC 10	80	10	-	-	10	0.539	578.8
HPMC 12	78	12	-	-	10	0.584	659.3
HPMC 10 Al 2	78	10	-	2	10	0.608	612.4
HPMC 10 Al 4	76	10	-	4	10	0.622	742.6
HPMC 10 Al 6	74	10	-	6	10	0.641	1233
MC 13	72	-	13	-	15	0.617	576.5
MC 14	71	-	14	-	15	0.648	621.7
MC 13 Al 2	70	-	13	2	15	0.691	738.5
MC 13 Al 4	68	-	13	4	15	0.728	1287

8.2.3 Opposed Flow burner test rig for linear regression rate studies

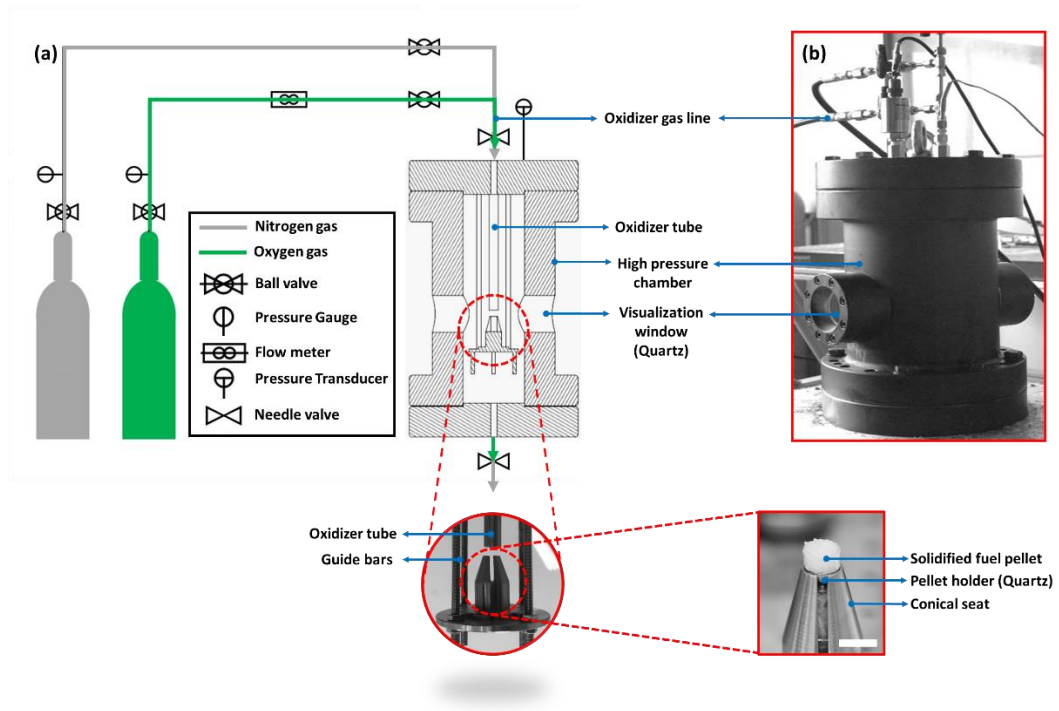


Figure 8. 1. Experimental test facility. (a) Schematic diagram of the flow loop for measurement of regression rates of solidified-ethanol fuel. Inset at the bottom shows the image of a MC 13 sample pressed into the quartz tube (pellet holder) for combustion experiments. Scale bar corresponds to 10 mm.

Figure 8.1 shows a schematic diagram of the oxidizer flow loop and an actual photograph of the opposed or counter flow burner, which is utilized for investigating the combustion of solidified-ethanol fuels and enabling visualization for measuring the regression rates. The burner consists of an oxygen supply tube, a pellet holder (quartz tube), a conical seat for the pellet holder and the guide bars with thread screw for adjusting the distance between the surface of the pellet and the exit of oxidizer tube. The burner is designed to hold a quartz tube (9 mm ID, 1mm wall thickness and 6 mm height) where the fuel pellets are pressed. To prepare pellets of solidified ethanol fuels for linear burn rate studies, the sample fuels were manually pressed into a Lucite cylinder (with same dimensions as the quartz tube)

while taking care to avoid any voids or cracks. The Lucite cylinder with the fuel pellet is placed in a cold-water bath maintained at 4°C. This ensures that the pellet conforms with the shape of the pellet holder and attains a cylindrical shape. The fuel pellet was removed from the Lucite 15 min. prior to experiments to avoid any loss of ethanol from the sample due to its volatility. Inset in Figure.8.1 (inset) shows a representative image of the fuel pellet loaded in the quartz pellet holder for the regression rate tests. The quartz tube is so located that the surface of the fuel pellet is situated ~7.5 mm below the exit of the tube (1/2") carrying the gaseous oxidizer. This distance is finalized after several iterations (by varying in increments of 1 mm starting from 2 mm) considering the range of oxidizer mass flux used for testing. With this distance, the exit of the oxidizer tube is neither too close to the pellet surface that spatters the top melt-layer of the fuel (at pellet surface) nor is it too far that the fuel surface receives an insufficient amount of oxygen. The oxidizer can be supplied at various flow rates by regulating the ball valves and these flow rates are measured using an inline mass flow meter with a coupled controller (Line Tech M3100VA). The oxygen mass flux is varied between 0.97 – 11.7 Kg/m²-s and calculated by dividing the oxygen flow rate (measured using flow meter) with the cross-section area of the oxidizer tube exit. Ignition of the fuel pellet is achieved electrically by using a 150 µm Nichrome wire which is pressed at the pellet surface. The nichrome wire is heated by supplying electric current to it using the igniter electrodes, which are powered using a 12 V, 7 A battery connected via a variac and an ignition switch. This low voltage source ensures that the current supplied to the wire is minimum and produces just enough heat to ignite the fuel and then gets cut-out, without pre-heating the fuel pellet. The burner is mounted inside a cylindrical pressure vessel with a volume of 7.85 liters. The vessel is equipped with two diametrically opposite placed 60 mm quartz windows, which allow optical access for visualizing the burning process.

The vessel is capable of withstanding high pressure up to 10 MPa and is hydrostatically tested up to 6 MPa before conducting any tests. A Canon 550D DSLR camera coupled with an EF 100 mm Macro lens is used to record the ignition and combustion of the fuel pellet at 50 fps and an optical resolution of 1280 × 760

pixels. The images are extracted and analyzed using ImageJ software and the reported data for linear regression rate obtained using these images is averaged over six trials. A variable intensity LED light source is used with different settings to allow the visualization of the flame structure as well as the tracking of the regressing surface during different experiment trials. During combustion, the pressure and temperature of the chamber is monitored using an absolute pressure transducer (Honeywell TJE AP122DJ) and a K-type thermocouple respectively, which are connected to NI-DAQ (NI 9211). The data is recorded and analyzed using the NI LabVIEW software.

8.3 Results and Discussion

8.3.1 Regression rate measurements

The linear regression rate (\dot{r}_b) of the solidified ethanol fuel samples is measured using the opposed flow burner (described in section 8.2.3) at medium oxidizer mass fluxes (G_{ox}) ranging from 0.97 - 11.7 kg/m²-s. This corresponds to the nozzle oxidizer velocity of 75 – 900 cm/s with the corresponding Reynolds number (Re) ranging from ~ 615 – 7430. The burning behavior of the fuel pellet and its burn-out length (Δx) during the steady-burning period is tracked directly from the images. Figure. 8.2 illustrates the nominal burning behavior for a representative case of HPMC 10 in terms of the burn-out length as a function of time along with the corresponding images of the regressing pellet. This curve is obtained for all the fuel samples and their slopes under steady state burning conditions are used to calculate their linear regression rates or burning rates. The regression rate is calculated as the ratio of the burnout length (Δx) to the steady burning duration (Δt) *i.e.*, $\dot{r}_b = \Delta x / \Delta t$. For each sample the test lasted for ~ 60 s and the steady-burning period varied between 10 - 20 s. Figure.8.3 shows the regression rate characteristics of non-metallized solid fuels as a function of oxidizer flux. It is apparent from the regression rate trends that it is strongly influenced by the oxidizer mass flux. In particular, the regression rate increases monotonically for all non-metallized fuel samples, and therefore, improves with an increase in the oxidizer mass flux. For

instance, when mass flux is increased from 0.97 to 4 kg/m²-s, the regression rate of HPMC 12 increases by ~35%. Similarly, in case of MC 13 the regression rate doubles on increasing the mass flux from 0.97 – 10 kg/m²-s. Further, for all the solidified fuels the slope of regression rate increases beyond 4 kg/m²-s, which corresponds to an oxidizer exit Reynolds number $Re = 2540$, and therefore, marks a transition from laminar to turbulent flow regime.

Figure. 8.3 also shows a comparison of regression rates of solidified fuels with DCPD, HTPB, and paraffin wax under same oxidizer mass flux conditions in an opposed flow burner configuration. It is noteworthy to mention that for the same operating range of oxidizer mass fluxes, the \dot{r}_b for non-metallized solidified ethanol is higher than the conventional DCPD, comparable with (or greater in some cases) HTPB, and at par with paraffin wax [151]. The nominally high regression rates exhibited by solidified-Ethanol fuels can be attributed to: First, these solid fuels are strongly shear thinning (yield thixotropic [46]), and therefore, the large aerodynamic force (or the shear rate) produced by the oxidizer flow decreases the viscosity of the pellet surface. This aids in freeing Ethanol by converting into the fine liquid droplets at the surface of the pellet, which enhances the mass transfer rate. Second, the solidified-Ethanol fuels have a low melting point of 61.5 – 75.1 °C, which is comparable to that of paraffin wax (46 – 68 °C), and significantly lower than HTPB (~241 °C) [57]. This indicates that the solidified Ethanol fuels can melt easily, which is a prerequisite condition to form droplets for subsequent entrainment and contributing to an increase in regression rate. Third, the combustion of organic gellant-laden solidified fuels is uniquely characterized by the jetting of unreacted fuel vapors, which in addition to the vaporization also allows the fuel vapors to be transported to the flame zone advectively. This jetting of fuel vapors accelerates the efflux of fuel and shortens the timescale of fuel-oxidizer mixing, thereby facilitating efficient combustion and a faster burn rate. Figure. 8.4 shows the time-sequence images of the events leading to vapor jetting with the accompanying schematics and are explained next.

In solidified fuel, the organic gellant, MC and HPMC used for the solidification process traps the liquid ethanol in the 3D-network formed between the gellant and the solvent (water). At the beginning of the burning process, the fuel burns regressively like conventional hybrid fuels, where the fuel surface gets heated and the most volatile component *i.e.*, ethanol vaporizes. As ethanol gets depleted from the surface layer this layer becomes rich in gellant. This gellant eventually melts down to form a melted layer at the top of the pellet surface and ethanol in the layers below the melt layer *i.e.*, in the bulk gets entrapped. As the temperature rises, the net heat transfer from flame front heats the layer beneath the melt layer. This results in boiling of the entrapped liquid fuel and therefore the bubble formation (see Figure 8.4). As more is heat transferred via the melt layer to the bubbles, they grow and coalesce to form bigger bubbles, which leads to an internal pressure rise. The pressure build-up ruptures the melt layer at the pellet surface to release jets of fuel vapors. In this way, besides vaporization, a faster outflow of fuel from the pellet is enabled via the jetting of fuel vapors, which contributes to a faster regression rate. Such preferential entrapment of low volatility component and its subsequent boiling leading to jetting has been reported previously in the context of combustion of ethanol gel fuels [152], [153].

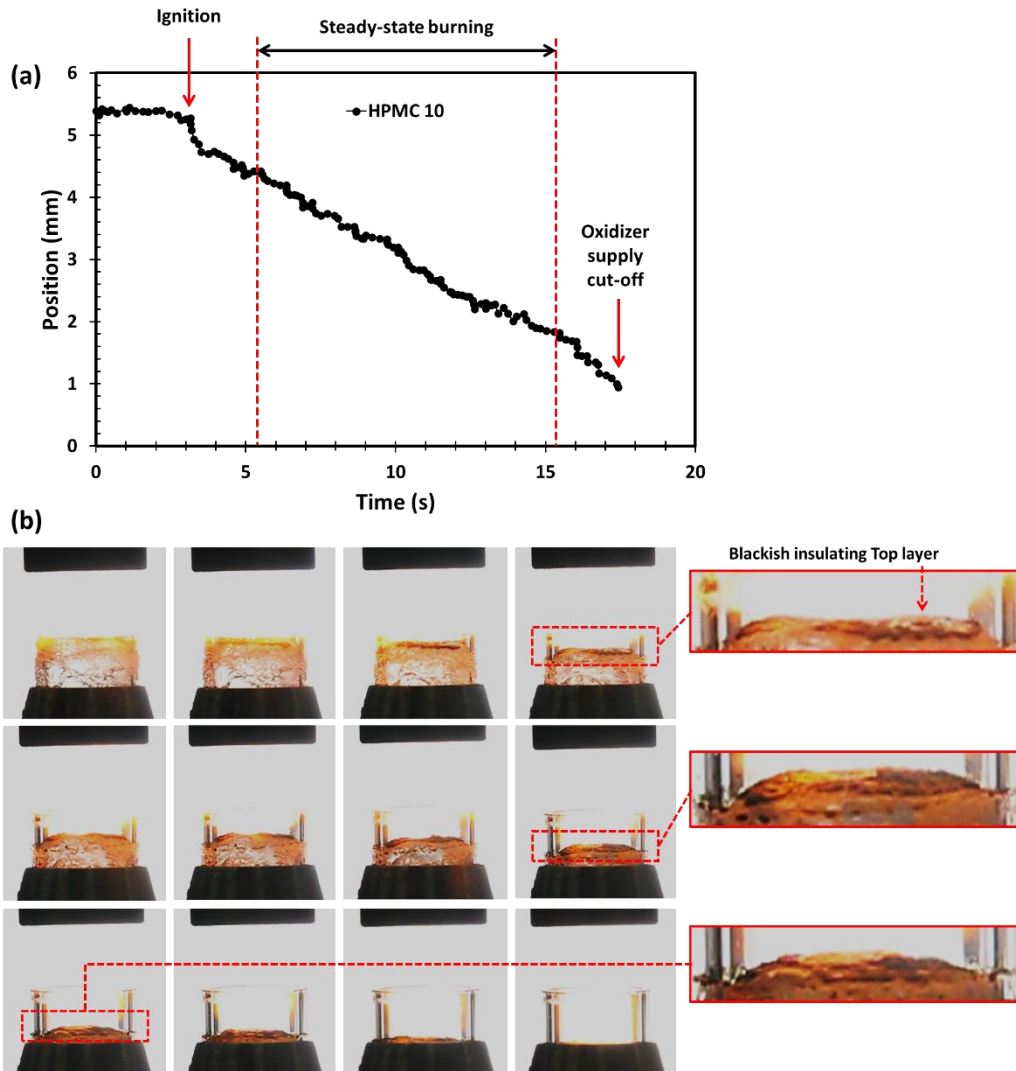


Figure 8. 2. The linear burning rate of HPMC 10 using gaseous oxygen at $1.95 \text{ kg/m}^2\text{-s}$. (a) Displacement-time trace of the pellet top surface obtained from the 50-fps video, whose slope in the steady-state burning period is used to determine the regression rate (\dot{r}_b). (b) The corresponding burning sequence of the solidified fuel pellet. The time stamps corresponding to images starting from left to right and top down are: 3.15s (ignition), 3.27s, 3.75s, 5.55s, 7.25s, 10.08s, 13.38s, 15.3s, 16.05s, 16.78s, 17s, 17.42s (oxidizer cut-off).

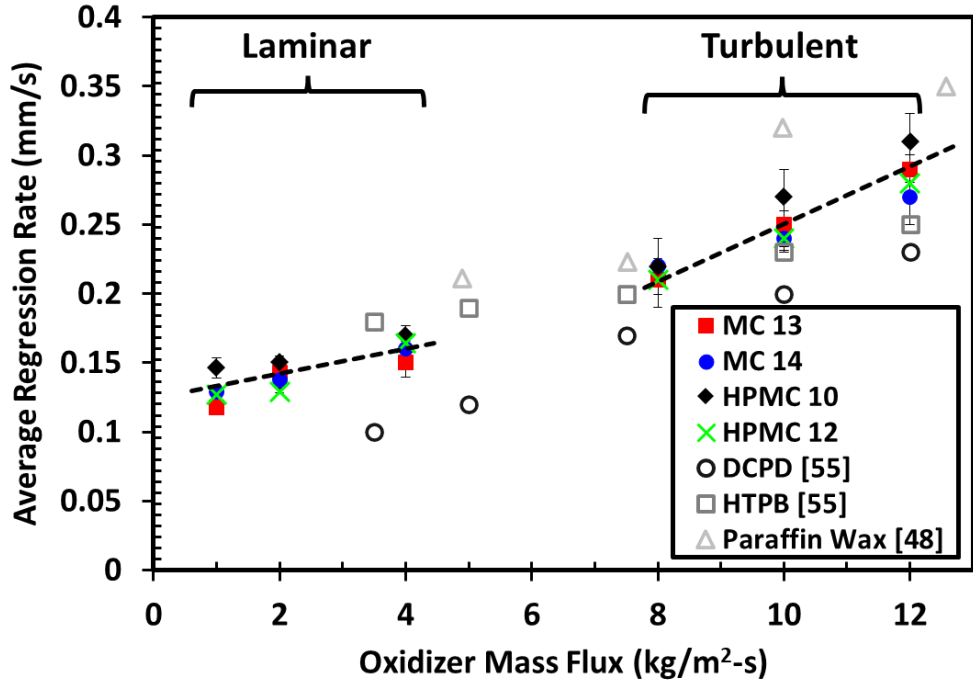


Figure 8. 3. Mean linear regression rate of MC and HPMC-based unloaded fuel at varying oxidizer flux conditions.

Therefore, the classical combustion model for the regression rate of liquefying fuels, which considers the summation of the gasification rate (\dot{r}_{gas}), and the entrainment rate (\dot{r}_{ent}) as the overall regression rate ($\dot{r}_{o,liq} = \dot{r}_{gas} + \dot{r}_{ent}$) can be modified for organic gellant-laden solidified Ethanol fuels (SEF) to account for advective mass transfer due to jetting i.e., $\dot{r}_{o,SEF} = \dot{r}_{gas} + \dot{r}_{ent} + \dot{r}_{jet}$. Note that the intensity of the bubble growth in the fuel pellet depends on the yield stress and the elastic nature of the fuel sample. While the bubble dynamics and the resulting jetting behavior has not been quantified in this study, our previous studies [45], [46] have demonstrated that the jetting has significant impact on the combustion behavior of MC and HPMC-based Ethanol gel fuel droplets. It was shown that the active jetting of unreacted fuel vapors can occur for as much as 75 % of the droplet lifetime, and therefore, govern the gasification rate of gellant-laden fuels in a reacting environment.

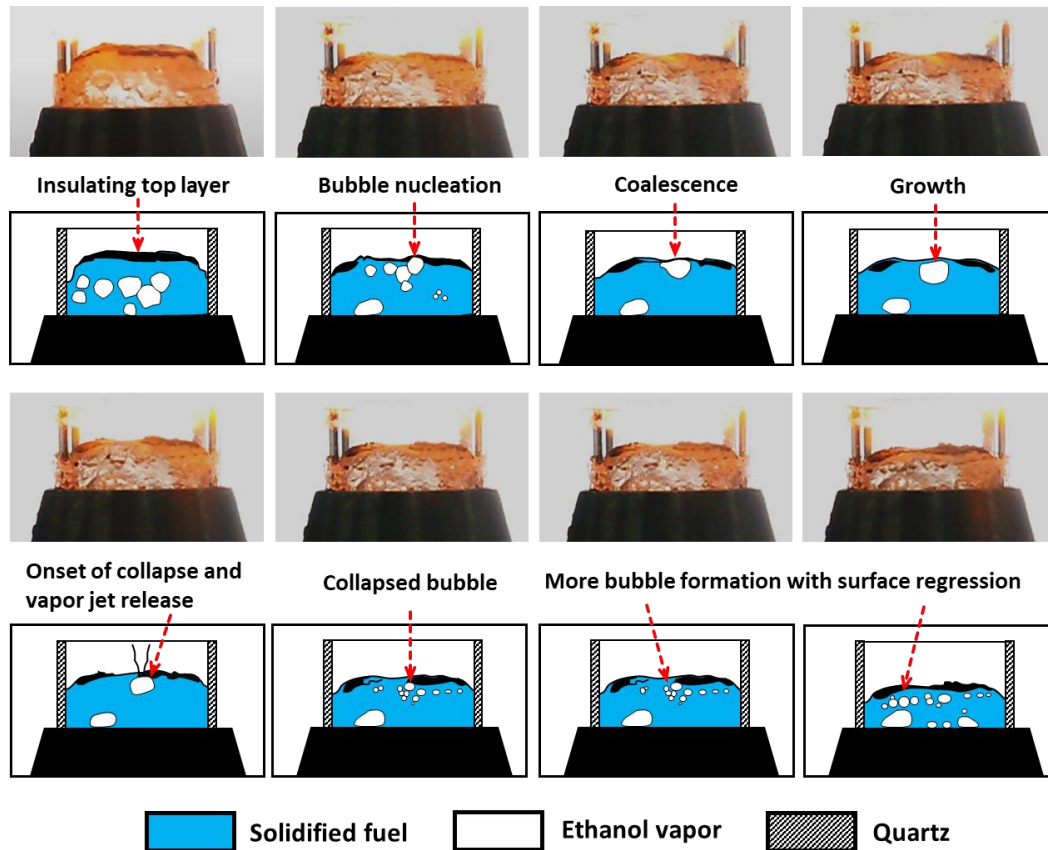


Figure 8. 4. Burning sequence of the HPMC 10 fuel pellet at $1.95 \text{ kg/m}^2\text{-s}$ with the accompanying schematics showing bubble formation below the melt layer. Red arrows show the key events including bubble, nucleation, growth, coalescence, and subsequent collapse to release unreacted fuel vapors in form of jets. The time stamps of the images from top to bottom and left to right in order are: 7s, 8s, 8.75s, 9s, 10s, 11s, 12s.

8.3.2 Regression behavior of nano-Al laden solid fuels

The solidification of ethanol provides an opportunity to load energetic metal additives during the formulation process, which aids in tailoring rheo-physical properties. Furthermore, the use of metal additives is known to enhance the regression rate of the hybrid propellants as well as their mechanical strength and the combustion efficiency [154]. In this section, the effect of aluminum nanoparticles on the linear regression rate of solidified ethanol fuels (liquefying type) is analyzed under varying oxidizer flux conditions. The nano-Al particle loading is varied ranging from 2 - 6 wt.% and 2 - 4 wt.% respectively for the HPMC 10 and MC 13 cases.

Figure. 8.5 shows comparative trends of the regression rate with oxidizer flux for HPMC-laden versus MC-laden fuels both with and without aluminum nanoparticles. It is observed that the regression rate of metallized fuels exhibits a non-monotonic trend with oxidizer flux, which is characterized by a change in the slope of the regression rate at oxidizer flux of $4 \text{ kg/m}^2\text{-s}$. The oxidizer nozzle exit Reynolds number corresponding to this mass flux is 2540, which lies in the range of 2000 – 3000, and therefore, falls within the range where laminar to turbulent transition occurs for a pipe flow [153]. Thus, for low oxidizer fluxes ($0.97 - 4 \text{ kg/m}^2\text{-s}$) the flow field at the nozzle exit is laminar while at higher mass fluxes ($8 - 11.7 \text{ kg/m}^2\text{-s}$) the nozzle exit flow is turbulent. Figure. 8.6 shows a comparison of the flame zone in the laminar versus the turbulent flow regimes. When the nozzle exit flow is laminar the visible flame tends to curve upwards uniformly along the streamlines and away from the pellet surface. However, in the turbulent regime, the visible flame stays parallel to the pellet surface before curving downwards and dispersing non-uniformly into the shear layer with the surroundings. This changeover in the flow structure marks a transition from laminar to turbulent flow. These regimes have different convective heat transfer behavior [151], and therefore, they directly influence the regression rate of solidified fuels.

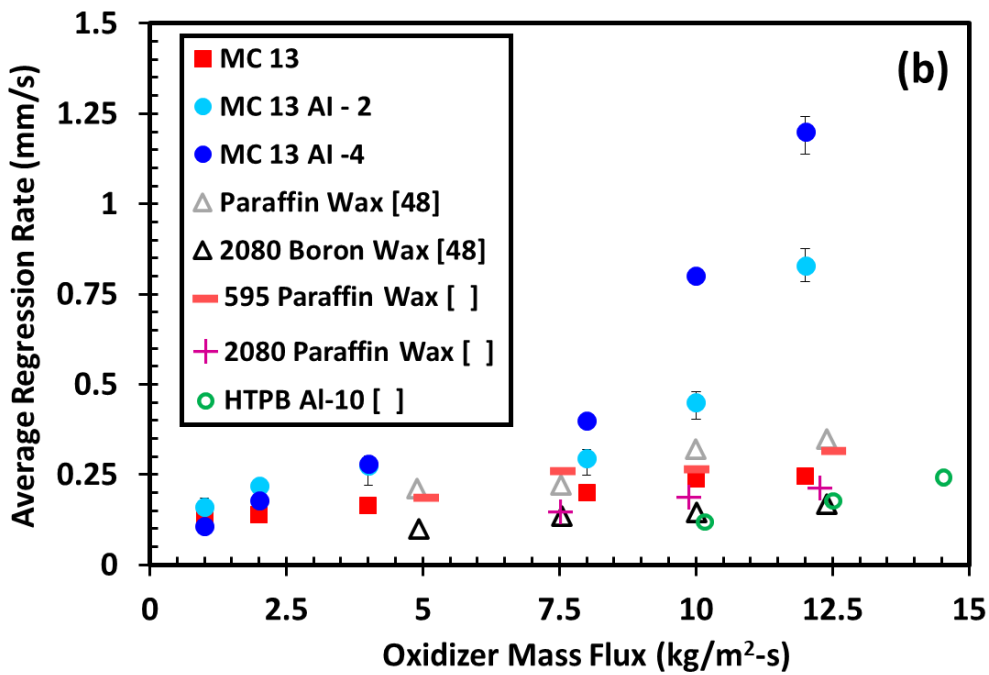
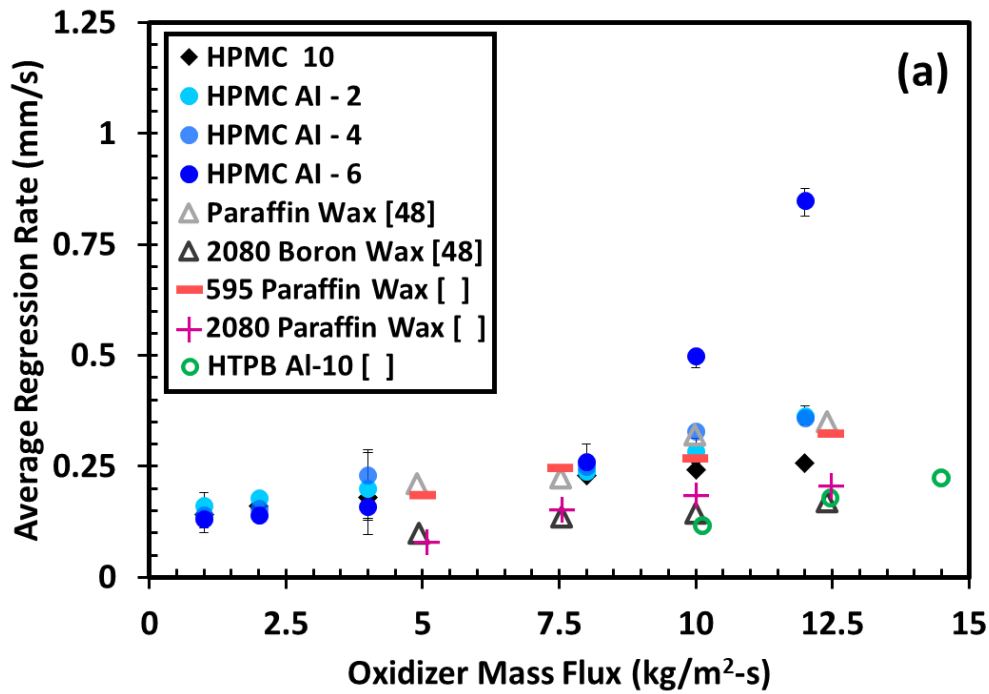


Figure 8. 5. Linear regression rate of (a) HPMC, and (b) MC based nano-Al loaded fuel at varying oxidizer flux conditions.

In the laminar regime, the addition of nano aluminum has no effect on the regression rate i.e., both the metallized and the non-metallized fuels exhibit the same regression rate. This is because at low oxidizer fluxes a thick black layer (see right side of Figure. 8.2) forms on the pellet surface which impedes the fuel gasification and insulates the pellet surface, thereby, inhibiting the regression rate [148]. This layer likely results from the oxidation and melting of aluminum nanoparticles and other combustion products. Figure. 8.6a visibly confirms that even at high loading rates the number of ignited aluminum particles/particle aggregates that leave the pellet surface are very few. However, in the turbulent flow regime, the high oxidizer velocities are adequate to strip off this layer, which allows the thermal energy to be transported effectively to the fuel pellet. This in turn will enable aluminum nanoparticles to burn close to the pellet surface and the accompanying release of energy during this metal oxidation process will result in more heat transport to the diffusion flame zone, thereby improving the fuel regression rate. The removal of this insulating layer under turbulent flow conditions and its positive role in improving regression rate has also been reported previously in the context of HTPB and DCPD fuels in an opposed burner setting [148]. Figure. 8.6b qualitatively shows that under turbulent flow conditions, a significantly larger number of aluminum particles/particle aggregates are released from the pellet compared to that under laminar flow conditions. The burning of aluminum nanoparticles/particle aggregates in the vicinity of the pellet surface can be observed throughout the regression period, as shown in the burning sequence of HPMC 10 Al-6 fuel in Figure 8.7 at an oxidizer mass flux of $11.7 \text{ kg/m}^2\text{-s}$. Figure. 8.5 further confirms that the improvement in regression rate starts becoming noticeable at the transition oxidizer flux of $4 \text{ kg/m}^2\text{-s}$ ($Re \sim 2540$). At higher oxidizer fluxes i.e., in the turbulent regime, the regression rate increases monotonically with oxidizer flux, and the slope of regression rate trends increases with an increase in the concentration of aluminum nanoparticles. For instance, the regression rate of HPMC 10 Al-6 is ~ 6 times higher at the highest tested oxidizer flux of $11.7 \text{ kg/m}^2\text{-s}$ compared to HPMC 10 and HPMC 10 Al-6 at $4 \text{ kg/m}^2\text{-s}$. Similarly, the regression rate of MC 13 Al-4 solidified fuel is ~ 4.8 times higher at

11.7 kg/m²-s compared to MC 13 and MC 10 Al-4 at 4 kg/m²-s. Thus, the turbulent flow regime combined with energetic nano-aluminum additives in the fuel can enhance the regression rate by an order of magnitude.

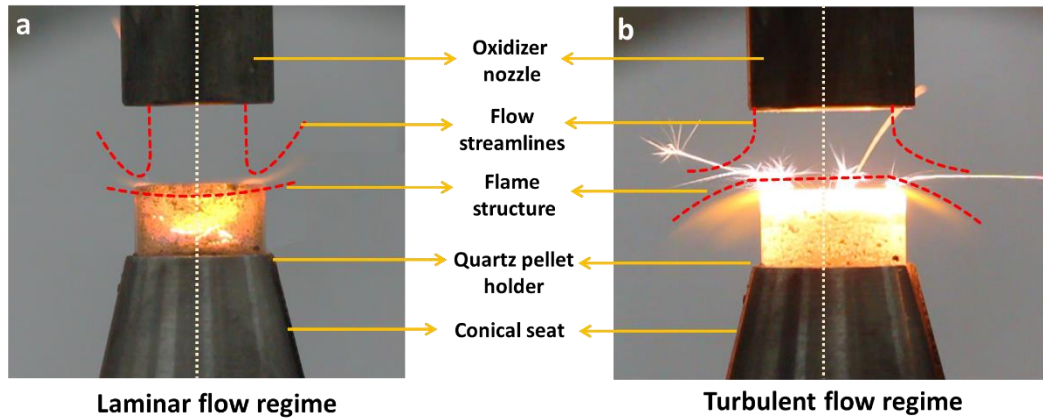


Figure 8. 6. Burning sequence of HPMC 10 Al-6 fuel pellet at an oxidizer flux of 11.7 kg/m²-s in turbulent flow regime: (a) pre-ignition, (b) ignition, (c) nano-aluminum particles/particle aggregate combustion near pellet, (d), ejection of burning particles/particle aggregates, (e) continued burning of particles/particle aggregates in end stages, and (f) extinction. The time stamps of images in order from top to bottom and left to right is 0s, 2s, 3s, 6s, 7s, 8s, 9s, 10s, 13s, 14s, 17s, 20s, 22s, 25s, 26s, 29s.

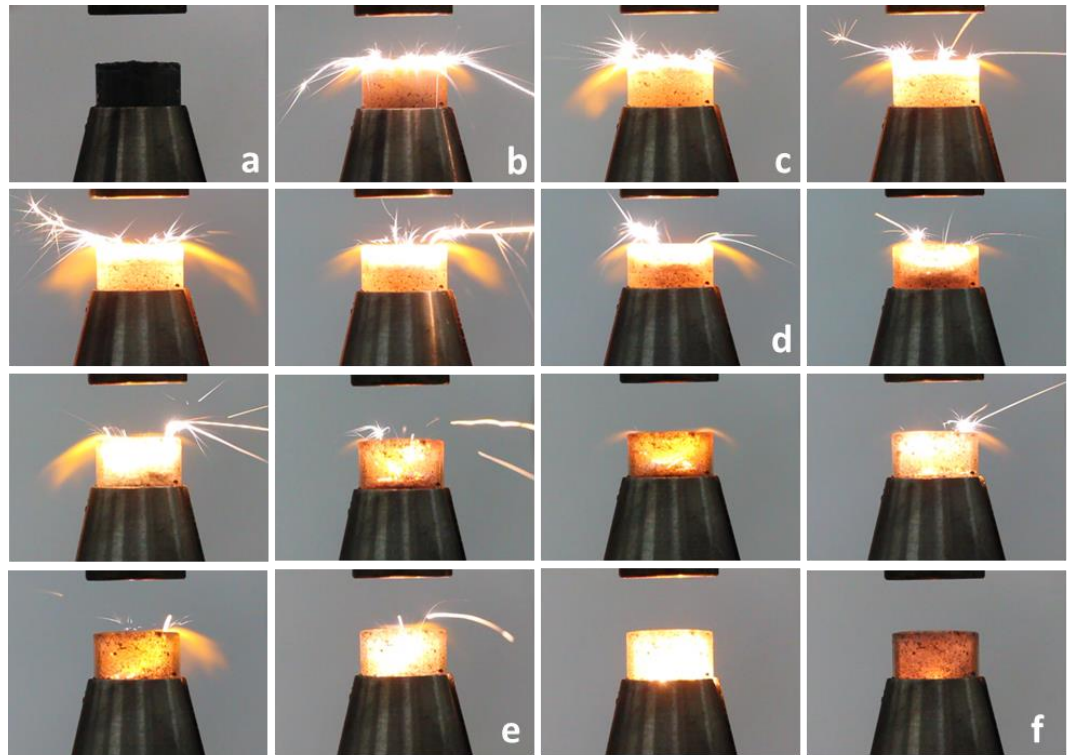


Figure 8.7. Burning sequence of HPMC 10 Al-6 fuel pellet at an oxidizer flux of $11.7 \text{ kg/m}^2\text{-s}$ in turbulent flow regime: (a) pre-ignition, (b) ignition, (c) nano-aluminum particles/particle aggregate combustion near pellet, (d), ejection of burning particles/particle aggregates, (e) continued burning of particles/particle aggregates in end stages, and (f) extinction. The time stamps of images in order from top to bottom and left to right are 0s, 2s, 3s, 6s, 7s, 8s, 9s, 10s, 13s, 14s, 17s, 20s, 22s, 25s, 26s, 29s.

A comparison of the regression rate data for metallized fuels versus paraffin wax, 595 Paraffin wax, 2080 Paraffin wax [149], 2080 Boron wax, and HTPB Al-10 [81] are shown in Figure 8.5 for the same conditions of oxidizer flux in an opposed flow burner. Figure 8.5 indicates that in the turbulent flow regime the regression rate of metallized fuels is higher compared to paraffin wax and 2080 Boron wax, and the extent to which it is higher increases with both the oxidizer flux and the concentration of nanoparticles. Particularly, the regression rate of HPMC 10 Al-6 and MC 13 Al-4 at $11.7 \text{ kg/m}^2\text{-s}$ is ~ 2.85 times, and ~ 5.4 times respectively compared to paraffin wax, while the corresponding numbers compared to 2080

Boron wax are ~ 6.12 times and 11 times respectively. This indicates that a significant enhancement in regression rate can be obtained by doping the solidified ethanol fuels with nominally small amounts (2 – 6 wt.%) of energetic aluminum nanoparticles.

8.4 Conclusions

In the study, the eco-friendly ethanol fuel is solidified via the gelation technique using two organic gellants and proposed for usage as a solid fuel in hybrid rocket applications. Two organic gellants, namely, Methylcellulose (MC) and Hydroxypropyl Methylcellulose (HPMC) are used to solidify ethanol. Both metallized and non-metallized samples are formulated by varying the gellant concentration in the range of 10 wt.% to 14 wt.% and the concentration of aluminum nanoparticles varying in the range of 2 wt.% to 6 wt.% for HPMC and 2 wt.% to 4 wt.% for MC samples respectively. Subsequently, the regression rates of these fuel formulations are measured using an opposed flow burner at oxidizer flux ranging from 0.97 – 11.7 kg/m²-s and compared with corresponding data for conventional hybrid propellants such as HTPB, DCPD, and paraffin wax from the literature. The following key conclusions are drawn from the study:

- For the range of tested oxidizer fluxes, the regression rate of solid ethanol fuels is higher than the conventional fuels such as HTPB and DCPD and at par with paraffin wax under the same experimental conditions. This is attributed to three factors: First, their low melting points and enthalpy of melting, which allows the melting stage to be reached easily and rapidly. Second, their strongly shear thinning behavior, which promotes droplet entrainment, and hence the mass transport, and third, the occurrence of vapor jetting, which in addition to fuel gasification aids in advective transport of unreacted fuel vapors to the flame zone.
- For both metallized and non-metallized solid fuels that regression rate increases monotonically with an increase in the oxidizer flux and its slope depends on the flow regime *i.e.*, laminar versus turbulent.

- In the laminar flow regime, aluminum nano additives have no effect on the regression rate trends. This is due to the formation of an insulating top layer from the products of combustion and melted aluminum particles that impede gasification and heat transfer from the flame.
- In the turbulent flow regime, the regression rate increases significantly with an increase in particle concentration. At the highest tested oxidizer flux of $11.7 \text{ kg/m}^2\text{-s}$, the regression rate of most loaded fuels *i.e.*, HPMC 10 Al-6 and MC 13 Al-4 is ~ 2.85 times, and ~ 5.4 times respectively compared to paraffin wax.

CHAPTER 9: CONCLUSIONS & FUTURE SCOPE

In this chapter, the summary of key results and conclusions from the present thesis is illustrated. The scope for future work based on the experiments performed and proposed mechanisms is mentioned in the last part of the chapter.

9.1 Major Conclusions

The thesis presents a systematic investigation of understanding the combustion dynamics of organic-gellant-laden ethanol fuel. The gel fuels of different formulations were prepared and subjected to combustion studies at droplet and flame scales. To understand the droplet scale jetting behavior, ultra-high-speed imaging was utilized. At the flame scale, Schlieren Imaging was incorporated to gauge the flame-disrupting jet emanating from the gel droplet. The high-speed video data provided key insights into the characterization of the disruptive combustion behavior of organic gel fuels. Furthermore, solidified nano-particle-laden ethanol-based gel fuels were also formulated, and their regression burn rate studies were investigated in comparison to conventional fuels (HTPB, DCPD, and paraffin wax). Overall, the current study provides detailed insights into the combustion characterization of organic gel fuels, which can help in fabricating gel fuel compositions. The culmination of the findings for this dissertation is summarized in Figures 9.1 and 9.2.

The following key conclusions can be drawn from the current investigations:

- The jetting behavior of organic gel fuel droplets is dependent on the type of gellant shell and its nature. These two factors also determine the domination of jetting events which govern combustion. The gellants which tend to form thin-weak-flexible shells result in low-velocity flame disruption events (flame distortion) due to a lower degree of pressure buildup. On the contrary, the gellants that form thick-strong-rigid shells tend to have higher

pressure buildup thereby leading to high-velocity flame disruption events (fireball and pin ejections).

- Jetting is a crucial phenomenon in the burning of gel fuel droplets that aids the efflux of the unreacted fuel vapors and, therefore, is likely to affect the local fuel–oxidizer ratio, gas phase mixing, and the droplet trajectory (due to the recoil thrust) in the rocket engine environment.
- The combustion of organic gel fuels has shown three distinct combustion stages namely transient heat up (stage I), disruptive burning (stage II), and carbonization (stage III). In the stage, I, phase separation occurs which leads to the formation of gellant shells. Organic gellants tend to form viscoelastic shells which substantially influence the jetting behavior during the disruptive burning (stage II). Apart from disruptive burning, carbonization is a significant part of the combustion during which the suppressed jetting behavior is seen due to the traces of fuel trapped in the gellant shells.
- The combustion behavior of an individual gel droplet evolves as a function of time. The newly formed gellant shell after phase separation is thin-weak and flexible which with the progression of combustion transforms into thick-strong and rigid. This temporal evolution not only affects the droplet bursting frequencies but also dictates the combustion and jetting behavior.
- During the combustion, the newly formed gellant shells formed after phase separation are soft. But being in a reactive environment they eventually undergo a thermally induced glass transition. i.e., the gellant shell transforms structurally to hard brittle (glassy). This temperature-dependent structural change in the polymeric gellant shell after phase separation not only influences the compensation mechanism of pressure surge but also the jetting behavior of gel fuels.
- For the range of tested oxidizer fluxes, the regression rate of solid ethanol fuels is higher than the conventional fuels such as HTPB and DCPD and at par with paraffin wax under the same experimental conditions. This is attributed to three factors: First, their low melting points and enthalpy of melting, which allows the melting stage to be reached easily and rapidly.

Second, their strongly shear thinning behavior, which promotes droplet entrainment, and hence the mass transport, and third, the occurrence of vapor jetting, which in addition to fuel gasification aids in advective transport of unreacted fuel vapors to the flame zone.

9.1 Future Scope

In the current work, an effort is made to understand the combustion traits of ethanol-based organic gellant-laden fuels. However, many avenues in the exploration of gel propellant technology have a potential scope in the future.

- Inorganic gellants are often used with conventional propellants like Kerosene. However, there is a paucity of combustion studies in this regard. The incorporation of ultra-high-speed imaging at droplet scale and Schlieren imaging at flame scale can provide crucial insights into combustion dynamics.
- Due to the multi-component nature of the gel fuels, simulation studies are a tedious task, however, the mechanistic insights provided by the current research can throw some light on this regard.
- Rheology is a key parameter in the development of gel fuels. The high temperature and high-pressure rheological studies can be beneficial in deciphering the conditions analogous to the combustion environment.
- Gel fuels offer ease of suspension of particles which can help manufacture hybrid fuels. These hybrid fuels can be a combination of organic, inorganic gellants, and metal particles. This can benefit in utilizing the benefits of these entities.
- Currently, a few studies have been carried out at the lab-scale and prototype level concerning gel fuels as potential propellants. These studies can be beneficial in the development of future hybrid rockets, tactical missiles, and sounding rockets.

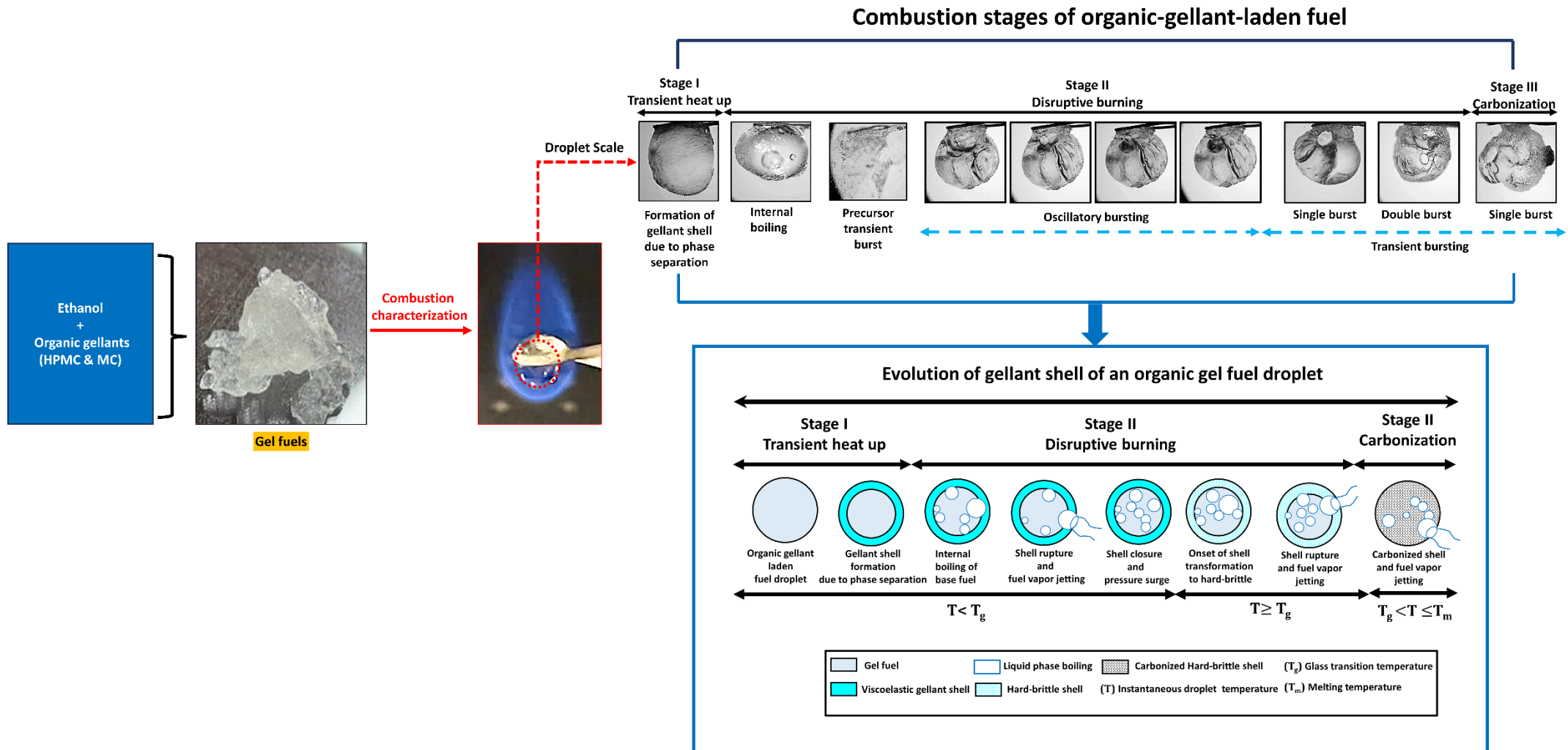


Figure 9. 1 Combustion dynamics of ethanol-based organic gel fuel droplets.

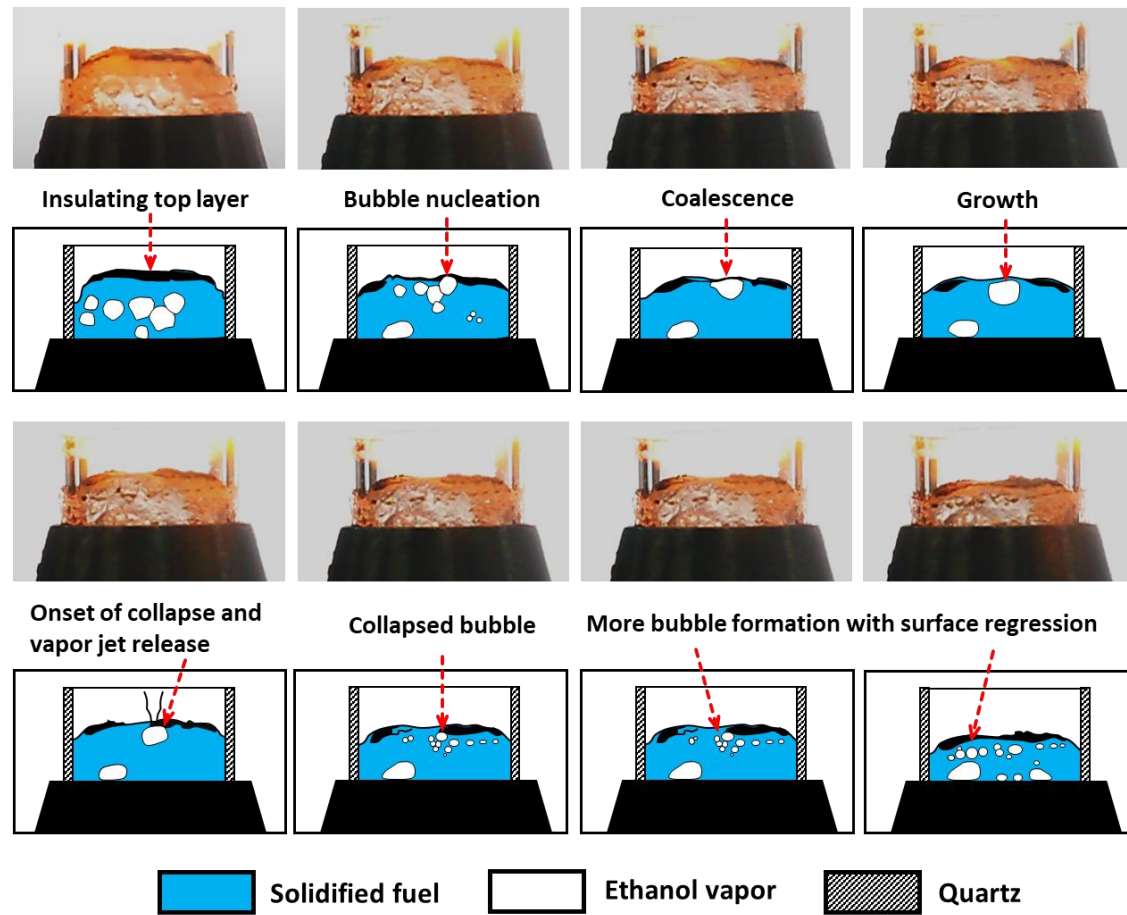


Figure 9. 2 The combustion dynamics of solidified ethanol-based organic gel fuel tested in an opposed flow burner facility for the evaluation of regression rates.

REFERENCES

- [1] “Brief History of Rockets.” Accessed: Jun. 28, 2023. [Online]. Available: https://www.grc.nasa.gov/www/k-12/TRC/Rockets/history_of_rockets.html
- [2] “The History of Rocket Science | Innovation| Smithsonian Magazine.” Accessed: Jun. 28, 2023. [Online]. Available: <https://www.smithsonianmag.com/innovation/the-history-of-rocket-science-4078981/>
- [3] “The History of Rockets | Space.” Accessed: Jun. 28, 2023. [Online]. Available: <https://www.space.com/29295-rocket-history.html>
- [4] “Brief history of rockets – timeline — Science Learning Hub.” Accessed: Jun. 28, 2023. [Online]. Available: <https://www.sciencelearn.org.nz/resources/1868-brief-history-of-rockets-timeline>
- [5] G. Vasant and B. N. Suresh, “History of rocketry in India,” *Acta Astronaut.*, vol. 65, no. 11–12, pp. 1515–1519, Dec. 2009, doi: 10.1016/j.actaastro.2009.03.083.
- [6] “Rocket - Black Powder, Liquid-Propellant Engines, and Solid-Propellant Motors | Britannica.” Accessed: Jun. 28, 2023. [Online]. Available: <https://www.britannica.com/technology/rocket-jet-propulsion-device-and-vehicle/Development-of-rockets>
- [7] “R-7 family of launchers and ICBMs.” Accessed: Jun. 28, 2023. [Online]. Available: <https://www.russianspaceweb.com/r7.html>
- [8] “7 Accidents and Disasters in Spaceflight History | Britannica.” Accessed: Jun. 28, 2023. [Online]. Available: <https://www.britannica.com/list/7-accidents-and-disasters-in-spaceflight-history>
- [9] V. (Slava *et al.*, “Hazards Induced by Breach of Liquid Rocket Fuel Tanks: Conditions and Risks of Cryogenic Liquid Hydrogen-Oxygen Mixture Explosions.”
- [10] I. Muniz De Almeida and C. W. Johnson, “Extending the Borders of Accident Investigation: Applying Novel Analysis Techniques to the Loss of the Brazilian Space Programme’s Launch Vehicle VLS-1 V03.” [Online]. Available: <http://www.dcs.gla.ac.uk/~johnson>
- [11] J. A. Dallas, S. Raval, J. P. Alvarez Gaitan, S. Saydam, and A. G. Dempster, “The environmental impact of emissions from space launches: A comprehensive review,” *Journal of Cleaner Production*, vol. 255. Elsevier Ltd, May 10, 2020. doi: 10.1016/j.jclepro.2020.120209.
- [12] “The environmental impact of rocket launches: The ‘dirty’ and the ‘green’ | Space.” Accessed: Jun. 28, 2023. [Online]. Available: <https://www.space.com/rocket-launches-environmental-impact>
- [13] N. Fue and A. B. Ray, “Process of producing solidified fuel,” Feb. 1934.
- [14] H. P. Bieber John Longwell, B. R. Nawakau, F. P. John Longwell, S. Plains, and H. Bieber, “Gelled solid rocket propellant reinforced with unoriented microfibers,” Dec. 1959.

- [15] “Thixotropic organic liquid propellant compositions with solid storage characteristics,” Sep. 1959.
- [16] “Thixotropic oxidizer propellant mixtures,” Apr. 1960.
- [17] M. H. Stans, A. V. Astin, A. S. Rapial, and D. E. Daney, “UNITED STATES DEPARTMENT OF COMMERCE PREPARATION AND CHARACTERIZATION OF SLUSH HYDROGEN AND NITROGEN GELS.”
- [18] A. S. Rapial, “Preparation and characterization of slush hydrogen and nitrogen gels,” Gaithersburg, MD, 1969. doi: 10.6028/NBS.TN.378.
- [19] J. CABEAL, “System analysis of gelled space storable propellants,” in *6th Propulsion Joint Specialist Conference*, Reston, Virginia: American Institute of Aeronautics and Astronautics, Jun. 1970. doi: 10.2514/6.1970-609.
- [20] B. L. Gupta, M. Varma, and N. L. Munjal, “Rheological Studies on Virgin and Metallized Unsymmetrical Dimethyl Hydrazine Gelled Systems,” *Propellants, Explosives, Pyrotechnics*, vol. 11, no. 2, pp. 45–52, Apr. 1986, doi: 10.1002/prop.19860110204.
- [21] B. L. Gupta, M. Varma, and S. B. Goel, “Rheological Characterization of Fuming Nitric Acid Gel,” *Propellants, Explosives, Pyrotechnics*, vol. 11, no. 3, pp. 85–90, Jun. 1986, doi: 10.1002/prop.19860110304.
- [22] N. L. Munjal, B. L. Gupta, and M. Varma, “Preparative and mechanistic studies on unsymmetrical Dimethyl Hydrazine-Red Fuming Nitric Acid Liquid Propellant Gels,” *Propellants, Explosives, Pyrotechnics*, vol. 10, no. 4, pp. 111–117, Aug. 1985, doi: 10.1002/prop.19850100406.
- [23] D. RAPP and R. ZURAWSKI, “Characterization of aluminum/RP-1 gel propellant properties,” in *24th Joint Propulsion Conference*, Reston, Virginia: American Institute of Aeronautics and Astronautics, Jul. 1988. doi: 10.2514/6.1988-2821.
- [24] K. Hodge, T. Crofoot, and S. Nelson, “Gelled propellants for tactical missile applications,” in *35th Joint Propulsion Conference and Exhibit*, Reston, Virginia: American Institute of Aeronautics and Astronautics, Jun. 1999. doi: 10.2514/6.1999-2976.
- [25] S. Rahimi and B. Natan, “Atomization characteristics of gel fuels,” in *34th AIAA/ASME/SAE/ASEE Joint Propulsion Conference and Exhibit*, Reston, Virginia: American Institute of Aeronautics and Astronautics, Jul. 1998. doi: 10.2514/6.1998-3830.
- [26] S. Rahimi and B. Natan, “Flow of Gel Fuels in Tapered Injectors,” *J Propuls Power*, vol. 16, no. 3, pp. 458–464, May 2000, doi: 10.2514/2.5590.
- [27] S. Rahimi, B. Natan, S. Rahimi, and B. Natan, “The injection process of gel fuels,” in *33rd Joint Propulsion Conference and Exhibit*, Reston, Virginia: American Institute of Aeronautics and Astronautics, Jul. 1997. doi: 10.2514/6.1997-2972.
- [28] S. Rahimi, D. Hasan, and A. Peretz, “Development of Laboratory-Scale Gel Propulsion Technology,” *J Propuls Power*, vol. 20, no. 1, pp. 93–100, Jan. 2004, doi: 10.2514/1.9235.
- [29] H. Ciezki, A. Robers, and G. Schneider, “Investigation of the Spray Behavior of Gelled Jet-A1 Fuels using an Air Blast and an Impinging Jet Atomizer,” in *38th AIAA/ASME/SAE/ASEE Joint Propulsion Conference & Exhibit*, Reston, Virginia: American Institute of Aeronautics and Astronautics, Jul. 2002. doi: 10.2514/6.2002-3601.

- [30] K. Naumann, H. Ciezki, ... R. S.-20th S. on, and undefined 2011, "Rocket propulsion with gelled propellants for sounding rockets," *adsabs.harvard.edu*, Accessed: Jun. 28, 2023. [Online]. Available: <https://adsabs.harvard.edu/full/2011ESASP.700..143N>
- [31] H. K. Ciezki, K. Wieland Naumann, and V. Weiser, "STATUS OF GEL PROPULSION IN THE YEAR 2010 WITH A SPECIAL VIEW ON THE GERMAN ACTIVITIES."
- [32] H. K. Ciezki and K. W. Naumann, "Some Aspects on Safety and Environmental Impact of the German Green Gel Propulsion Technology," *Propellants, Explosives, Pyrotechnics*, vol. 41, no. 3, pp. 539–547, Jun. 2016, doi: 10.1002/prop.201600039.
- [33] P. Caldas Pinto, N. Hopfe, J. Ramsel, W. Naumann, A. Thumann, and G. Kurth, "Scalability of Gelled Propellant Rocket Motors", doi: 10.13009/EUCASS2017-158.
- [34] B. Natan, V. Perteghella, and Y. Solomon, "Hypergolic Ignition of Oxidizers and Fuels by Fuel Gelation and Suspension of Reactive or Catalyst Particles," in *46th AIAA/ASME/SAE/ASEE Joint Propulsion Conference & Exhibit*, Reston, Virginia: American Institute of Aeronautics and Astronautics, Jul. 2010. doi: 10.2514/6.2010-7144.
- [35] J. von Kampen, F. Alberio, and H. K. Ciezki, "Spray and combustion characteristics of aluminized gelled fuels with an impinging jet injector," *Aerosp Sci Technol*, vol. 11, no. 1, pp. 77–83, Jan. 2007, doi: 10.1016/j.ast.2006.08.006.
- [36] A. Haddad, B. Natan, and R. Arieli, "The performance of a boron-loaded gel-fuel ramjet," in *Progress in Propulsion Physics*, Les Ulis, France: EDP Sciences, Oct. 2011, pp. 499–518. doi: 10.1051/eucass/201102499.
- [37] J. G. Lee, S. Fakhri, and R. A. Yetter, "EFFECT OF NOZZLE GEOMETRY ON THE ATOMIZATION AND SPRAY CHARACTERISTICS OF GELLED-PROPELLANT SIMULANTS FORMED BY TWO IMPINGING JETS," *Atomization and Sprays*, vol. 20, no. 12, pp. 1033–1046, 2010, doi: 10.1615/AtomizSpr.v20.i12.20.
- [38] Y. Solomon, S. Jo DeFini, T. L. Pourpoint, and W. E. Anderson, "Gelled MMH Hypergolic Droplet Investigation," 2011.
- [39] K. Y. Cho, T. L. Pourpoint, S. F. Son, and R. P. Lucht, "Microexplosion Investigation of Monomethylhydrazine Gelled Droplet with OH Planar Laser-Induced Fluorescence," *J Propuls Power*, vol. 29, no. 6, pp. 1303–1310, Nov. 2013, doi: 10.2514/1.B34853.
- [40] K. Cho, T. Pourpoint, S. Son, and R. Lucht, "High Repetition Rate OH Planar Laser Induced Fluorescence of Gelled Propellant Droplet," in *47th AIAA/ASME/SAE/ASEE Joint Propulsion Conference & Exhibit*, Reston, Virginia: American Institute of Aeronautics and Astronautics, Jul. 2011. doi: 10.2514/6.2011-5792.
- [41] D. P. Mishra and A. Patyal, "Effects of initial droplet diameter and pressure on burning of ATF gel propellant droplets," *Fuel*, vol. 95, pp. 226–233, May 2012, doi: 10.1016/j.fuel.2011.09.041.
- [42] D. P. Mishra, A. Patyal, and M. Padhwal, "Effects of gellant concentration on the burning and flame structure of organic gel propellant droplets," *Fuel*, vol. 90, no. 5, pp. 1805–1810, May 2011, doi: 10.1016/j.fuel.2010.12.021.
- [43] S. Y. Jejurkar, G. Yadav, and D. P. Mishra, "Visualizations of sheet breakup of non-Newtonian gels loaded with nanoparticles," *International Journal of Multiphase Flow*, vol. 100, pp. 57–76, Mar. 2018, doi: 10.1016/j.ijmultiphaseflow.2017.12.003.

- [44] S. Y. Jejurkar, G. Yadav, and D. P. Mishra, "Characterization of impinging jet sprays of gelled propellants loaded with nanoparticles in the impact wave regime," *Fuel*, vol. 228, pp. 10–22, Sep. 2018, doi: 10.1016/j.fuel.2018.04.138.
- [45] A. Miglani, P. Nandagopalan, J. John, and S. Wook Baek, "Disruptive Combustion Behavior of Gelled Ethanol Fuel droplets," 2016.
- [46] J. John, P. Nandagopalan, S. W. Baek, and A. Miglani, "Rheology of solid-like ethanol fuel for hybrid rockets: Effect of type and concentration of gellants," *Fuel*, vol. 209, pp. 96–108, Dec. 2017, doi: 10.1016/j.fuel.2017.06.124.
- [47] A. Miglani, P. Nandagopalan, J. John, and S. W. Baek, "Oscillatory bursting of gel fuel droplets in a reacting environment," *Sci Rep*, vol. 7, no. 1, p. 3088, Jun. 2017, doi: 10.1038/s41598-017-03221-x.
- [48] Q. Cao, W. Liao, W.-T. Wu, and F. Feng, "Combustion characteristics of inorganic kerosene gel droplet with fumed silica as gellant," *Exp Therm Fluid Sci*, vol. 103, pp. 377–384, May 2019, doi: 10.1016/j.expthermflusci.2019.01.031.
- [49] D. O. Glushkov, K. K. Paushkina, A. O. Pleshko, and V. S. Vysokomorny, "Characteristics of micro-explosive dispersion of gel fuel particles ignited in a high-temperature air medium," *Fuel*, vol. 313, p. 123024, Apr. 2022, doi: 10.1016/j.fuel.2021.123024.
- [50] D. O. Glushkov, G. V. Kuznetsov, A. G. Nigay, and O. S. Yashutina, "Heat and mass transfer induced by the ignition of single gel propellant droplets," *Journal of the Energy Institute*, vol. 92, no. 6, pp. 1944–1955, Dec. 2019, doi: 10.1016/j.joei.2018.10.017.
- [51] D. O. Glushkov, A. O. Pleshko, and O. S. Yashutina, "Influence of heating intensity and size of gel fuel droplets on ignition characteristics," *Int J Heat Mass Transf*, vol. 156, Aug. 2020, doi: 10.1016/j.ijheatmasstransfer.2020.119895.
- [52] D. O. Glushkov, K. K. Paushkina, A. O. Pleshko, and V. A. Yanovsky, "Ignition and combustion behavior of gel fuel particles with metal and non-metal additives," *Acta Astronaut*, vol. 202, pp. 637–652, Jan. 2023, doi: 10.1016/j.actaastro.2022.11.027.
- [53] K. KAJIWARA, "Structure of gels," in *Gels Handbook*, Elsevier, 2001, pp. 122–171. doi: 10.1016/B978-012394690-4/50081-5.
- [54] M. B. Padwal, B. Natan, and D. P. Mishra, "Gel propellants," *Prog Energy Combust Sci*, vol. 83, p. 100885, Mar. 2021, doi: 10.1016/j.pecs.2020.100885.
- [55] L. Q. Maurice, H. Lander, T. Edwards, and W. E. Harrison, "Advanced aviation fuels: a look ahead via a historical perspective," *Fuel*, vol. 80, no. 5, pp. 747–756, Apr. 2001, doi: 10.1016/S0016-2361(00)00142-3.
- [56] T. Edwards, "Liquid Fuels and Propellants for Aerospace Propulsion: 1903-2003," *J Propuls Power*, vol. 19, no. 6, pp. 1089–1107, Nov. 2003, doi: 10.2514/2.6946.
- [57] B. Natan and S. Rahimi, "THE STATUS OF GEL PROPELLANTS IN YEAR 2000," *International Journal of Energetic Materials and Chemical Propulsion*, vol. 5, no. 1–6, pp. 172–194, 2002, doi: 10.1615/IntJEnergeticMaterialsChemProp.v5.i1-6.200.
- [58] K. W. Naumann *et al.*, "Green Gelled Propellant Throtteable Rocket Motors for Affordable and Safe Micro-Launchers," 2015, doi: 10.13009/EUCASS2017-154.
- [59] K. W. Naumann and P. C. Pinto, "Green, Controllable, Safe, Affordable and Mature Gelled Propellant Rocket Motor Technology for Space and Sub-Orbital Launchers," in *2018 Joint*

Propulsion Conference, Reston, Virginia: American Institute of Aeronautics and Astronautics, Jul. 2018. doi: 10.2514/6.2018-4854.

- [60] E. J. Hopfinger and V. Baumbach, "Liquid sloshing in cylindrical fuel tanks," in *Progress in Propulsion Physics*, Les Ulis, France: EDP Sciences, Sep. 2009, pp. 279–292. doi: 10.1051/eucass/200901279.
- [61] Y. Gan and L. Qiao, "Combustion characteristics of fuel droplets with addition of nano and micron-sized aluminum particles," *Combust Flame*, vol. 158, no. 2, pp. 354–368, Feb. 2011, doi: 10.1016/j.combustflame.2010.09.005.
- [62] G. P. (George P. Sutton and Oscar. Biblarz, *Rocket propulsion elements*. John Wiley & Sons, 2001.
- [63] M. Varma and R. Pein, "OPTIMISATION OF PROCESSING CONDITIONS FOR GEL PROPELLANT PRODUCTION," *International Journal of Energetic Materials and Chemical Propulsion*, vol. 8, no. 6, pp. 501–513, 2009, doi: 10.1615/IntJEnergeticMaterialsChemProp.v8.i6.30.
- [64] S. Rahimi and B. Natan, "Numerical Solution of the Flow of Power-Law Gel Propellants in Converging Injectors," *Propellants, Explosives, Pyrotechnics*, vol. 25, no. 4, pp. 203–212, Sep. 2000, doi: 10.1002/1521-4087(200009)25:4<203::AID-PREP203>3.0.CO;2-E.
- [65] J. GREEN, D. RAPP, and J. RONCACE, "Flow visualization of a rocket injector spray using gelled propellant simulants," in *27th Joint Propulsion Conference*, Reston, Virginia: American Institute of Aeronautics and Astronautics, Jun. 1991. doi: 10.2514/6.1991-2198.
- [66] H. K. Ciezki, K. Wieland Naumann, and V. Weiser, "STATUS OF GEL PROPULSION IN THE YEAR 2010 WITH A SPECIAL VIEW ON THE GERMAN ACTIVITIES."
- [67] S. Rahimi, A. Peretz, and B. Natan, "On Shear Rheology of Gel Propellants," *Propellants, Explosives, Pyrotechnics*, vol. 32, no. 2, pp. 165–174, Apr. 2007, doi: 10.1002/prep.200700018.
- [68] G. Nahamoni and B. Natan, "Investigation of the combustion process of gel propellants," in *33rd Joint Propulsion Conference and Exhibit*, American Institute of Aeronautics and Astronautics Inc, AIAA, 1997. doi: 10.2514/6.1997-2973.
- [69] G. NACHMONI and B. NATAN, "Combustion Characteristics of Gel Fuels," *Combustion Science and Technology*, vol. 156, no. 1, pp. 139–157, Jul. 2000, doi: 10.1080/00102200008947300.
- [70] Y. SOLOMON and B. NATAN, "EXPERIMENTAL INVESTIGATION OF THE COMBUSTION OF ORGANIC-GELLANT-BASED GEL FUEL DROPLETS," *Combustion Science and Technology*, vol. 178, no. 6, pp. 1185–1199, Jun. 2006, doi: 10.1080/00102200600620259.
- [71] Y. Solomon, B. Natan, and Y. Cohen, "Combustion of gel fuels based on organic gellants," *Combust Flame*, vol. 156, no. 1, pp. 261–268, Jan. 2009, doi: 10.1016/j.combustflame.2008.08.008.
- [72] R. Arnold and W. E. Anderson, "Droplet Burning of JP-8/Silica Gels," 2010.
- [73] A. Kunin, B. Natan, and J. B. Greenberg, "Theoretical Model of the Transient Combustion of Organic-Gellant-Based Gel Fuel Droplets," *J Propuls Power*, vol. 26, no. 4, pp. 765–771, Jul. 2010, doi: 10.2514/1.41705.

- [74] C. H. Wang, X. Q. Liu, and C. K. Law, “Combustion and microexplosion of freely falling multicomponent droplets,” *Combust Flame*, vol. 56, no. 2, pp. 175–197, May 1984, doi: 10.1016/0010-2180(84)90036-1.
- [75] S. Feng *et al.*, “Experimental studies the burning process of gelled unsymmetrical dimethylhydrazine droplets under oxidant convective conditions,” *Fuel*, vol. 111, pp. 367–373, 2013, doi: 10.1016/j.fuel.2013.03.071.
- [76] M. Ghamari and A. Ratner, “Combustion characteristics of diesel and Jet-A droplets blended with polymeric additive,” *Fuel*, vol. 178, pp. 63–70, Aug. 2016, doi: 10.1016/j.fuel.2016.03.052.
- [77] Rm. Muthiah, V. N. Krishnamurthy, and B. R. Gupta, “Rheology of HTPB Propellant: Development of generalized correlation and evaluation of pot life,” *Propellants, Explosives, Pyrotechnics*, vol. 21, no. 4, pp. 186–192, Aug. 1996, doi: 10.1002/prop.19960210405.
- [78] N. Q. Dzuy and D. V. Boger, “Yield Stress Measurement for Concentrated Suspensions,” *J Rheol (N Y N Y)*, vol. 27, no. 4, pp. 321–349, Aug. 1983, doi: 10.1122/1.549709.
- [79] J. D. Dennis, T. D. Kubal, O. Campanella, S. F. Son, and T. L. Pourpoint, “Rheological Characterization of Monomethylhydrazine Gels,” *J Propuls Power*, vol. 29, no. 2, pp. 313–320, Mar. 2013, doi: 10.2514/1.B34611.
- [80] P. Li, L. Yang, Q. Fu, and Z. Fang, “Spray characteristics of the nanoparticle-containing gel propellants by using an improved single-phase nozzle,” *Fuel*, vol. 315, May 2022, doi: 10.1016/j.fuel.2021.122968.
- [81] J. JOHN and J. John, “Experimental study of metalized and non-metalized ethanol based solid propellant for hybrid rocket engine,” 2015, Accessed: Jun. 28, 2023. [Online]. Available: <https://koasas.kaist.ac.kr/handle/10203/206484>
- [82] M. H. J. S. T. H. M. S. A. U. F. E. SIEWERT, “Visualization of Gas Flows in Welding Arcs by the Schlieren Measuring Technique”.
- [83] A. M. E.-D. Faik, Y. Zhang, and S. de M. Hanriot, “Droplet Combustion Characteristics of Biodiesel–Diesel Blends using High Speed Backlit and Schlieren Imaging,” *Heat Transfer Engineering*, vol. 40, no. 13–14, pp. 1085–1098, Aug. 2019, doi: 10.1080/01457632.2018.1457209.
- [84] O. C. Bixler, “Color Schlieren as a Quantitative Tool for Acoustic Measurements in Ballistics,” *J Acoust Soc Am*, vol. 44, no. 1, pp. 375–375, Jul. 1968, doi: 10.1121/1.1970556.
- [85] E. T. Jens, A. C. Karp, V. A. Miller, G. S. Hubbard, and B. J. Cantwell, “Experimental Visualization of Hybrid Combustion: Results at Elevated Pressures,” *J Propuls Power*, vol. 36, no. 1, pp. 33–46, Jan. 2020, doi: 10.2514/1.B37416.
- [86] E. J. Rice, G. Raman, and E. J. Rice, “Enhanced Mixing of a Rectangular Supersonic Jet by Natural and Induced Screech.”
- [87] M. Staymates, “Flow visualization of an N95 respirator with and without an exhalation valve using schlieren imaging and light scattering,” *Physics of Fluids*, vol. 32, no. 11, p. 111703, Nov. 2020, doi: 10.1063/5.0031996.
- [88] F. Tomaschek, D. Arnold, K. Sering, and F. Strauss, “A corpus of Schlieren photography of speech production: potential methodology to study aerodynamics of labial, nasal and vocalic processes,” *Lang Resour Eval*, vol. 55, no. 4, pp. 1127–1140, Dec. 2021, doi: 10.1007/s10579-021-09550-8.

- [89] G. S. Settles and M. J. Hargather, "A review of recent developments in schlieren and shadowgraph techniques," *Meas Sci Technol*, vol. 28, no. 4, p. 042001, Apr. 2017, doi: 10.1088/1361-6501/aa5748.
- [90] C. Tropea, A. L. Yarin, and J. F. Foss, Eds., *Springer Handbook of Experimental Fluid Mechanics*. Berlin, Heidelberg: Springer Berlin Heidelberg, 2007. doi: 10.1007/978-3-540-30299-5.
- [91] Bhupendra, K. Moses, A. Miglani, and P. Kumar Kankar, "Deep CNN-based damage classification of milled rice grains using a high-magnification image dataset," *Comput Electron Agric*, vol. 195, p. 106811, Apr. 2022, doi: 10.1016/j.compag.2022.106811.
- [92] V. Agarwal, P. Chitkariya, A. Miglani, P. Nandagopalan, J. John, and P. K. Kankar, "Deep learning-based image processing for analyzing combustion behavior of gel fuel droplets," in *Smart Electrical and Mechanical Systems*, Elsevier, 2022, pp. 65–85. doi: 10.1016/B978-0-323-90789-7.00011-7.
- [93] S. Patil, A. Miglani, P. K. Kankar, and D. Roy, "Deep learning-based methods for detecting surface defects in steel plates," in *Smart Electrical and Mechanical Systems*, Elsevier, 2022, pp. 87–107. doi: 10.1016/B978-0-323-90789-7.00001-4.
- [94] K. Chojnacki and D. Feikema, "Atomization studies of gelled bipropellant simulants using planar laser induced fluorescence," in *31st Joint Propulsion Conference and Exhibit*, Reston, Virginia: American Institute of Aeronautics and Astronautics, Jul. 1995. doi: 10.2514/6.1995-2423.
- [95] "NAVAL POSTGRADUATE SCHOOL."
- [96] C. K. Law, "Internal boiling and superheating in vaporizing multicomponent droplets," *AIChE Journal*, vol. 24, no. 4, pp. 626–632, Jul. 1978, doi: 10.1002/aic.690240410.
- [97] C. H. Wang and C. K. Law, "Microexplosion of fuel droplets under high pressure," *Combust Flame*, vol. 59, no. 1, pp. 53–62, Jan. 1985, doi: 10.1016/0010-2180(85)90057-4.
- [98] B. He, W. Nie, and H. He, "Unsteady combustion model of nonmetalized organic gel fuel droplet," in *Energy and Fuels*, Nov. 2012, pp. 6627–6639. doi: 10.1021/ef300990d.
- [99] A. Miglani and S. Basu, "Coupled Mechanisms of Precipitation and Atomization in Burning Nanofluid Fuel Droplets," *Sci Rep*, vol. 5, no. 1, p. 15008, Oct. 2015, doi: 10.1038/srep15008.
- [100] S. Basu and A. Miglani, "Combustion and heat transfer characteristics of nanofluid fuel droplets: A short review," *Int J Heat Mass Transf*, vol. 96, pp. 482–503, May 2016, doi: 10.1016/j.ijheatmasstransfer.2016.01.053.
- [101] A. Miglani, S. Basu, and R. Kumar, "Insight into instabilities in burning droplets," *Physics of Fluids*, vol. 26, no. 3, p. 032101, Mar. 2014, doi: 10.1063/1.4866866.
- [102] A. Miglani, S. Basu, and R. Kumar, "Suppression of instabilities in burning droplets using preferential acoustic perturbations," *Combust Flame*, vol. 161, no. 12, pp. 3181–3190, Dec. 2014, doi: 10.1016/j.combustflame.2014.06.010.
- [103] A. Miglani and S. Basu, "Effect of Particle Concentration on Shape Deformation and Secondary Atomization Characteristics of a Burning Nanotitania Dispersion Droplet," *J Heat Transfer*, vol. 137, no. 10, Oct. 2015, doi: 10.1115/1.4030394.

- [104] J. Shinjo, J. Xia, L. C. Ganippa, and A. Megaritis, “Physics of puffing and microexplosion of emulsion fuel droplets,” *Physics of Fluids*, vol. 26, no. 10, Oct. 2014, doi: 10.1063/1.4897918.
- [105] D. C. K. Rao, S. Karmakar, and S. K. Som, “Puffing and Micro-Explosion Behavior in Combustion of Butanol/Jet A-1 and Acetone-Butanol-Ethanol (A-B-E)/Jet A-1 Fuel Droplets,” *Combustion Science and Technology*, vol. 189, no. 10, pp. 1796–1812, Oct. 2017, doi: 10.1080/00102202.2017.1333502.
- [106] Z. Liu, X. Hu, Z. He, and J. Wu, “Experimental Study on the Combustion and Microexplosion of Freely Falling Gelled Unsymmetrical Dimethylhydrazine (UDMH) Fuel Droplets,” *Energies (Basel)*, vol. 5, no. 8, pp. 3126–3136, Aug. 2012, doi: 10.3390/en5083126.
- [107] T. Zhang *et al.*, “Review on space energy,” *Appl Energy*, vol. 292, p. 116896, Jun. 2021, doi: 10.1016/j.apenergy.2021.116896.
- [108] Y. W. Liu, X. Liu, X. Zh. Yuan, and X. J. Wang, “Optimizing design of a new zero boil off cryogenic storage tank in microgravity,” *Appl Energy*, vol. 162, pp. 1678–1686, Jan. 2016, doi: 10.1016/j.apenergy.2015.01.104.
- [109] G. Baek and C. Kim, “Rheological properties of Carbopol containing nanoparticles,” *J Rheol (N Y N Y)*, vol. 55, no. 2, pp. 313–330, Mar. 2011, doi: 10.1122/1.3538092.
- [110] D. GALECKI, “Ignition and combustion of metallized propellants,” in *25th Joint Propulsion Conference*, Reston, Virginia: American Institute of Aeronautics and Astronautics, Jul. 1989. doi: 10.2514/6.1989-2883.
- [111] Spalding D.B., “COMBUSTION OF LIQUID FUELS 847-864, Proceedings of the Combustion Institute,” 1953.
- [112] J. John, P. Nandagopalan, S. W. Baek, and S. J. Cho, “Hypergolic ignition delay studies of solidified ethanol fuel with hydrogen peroxide for hybrid rockets,” *Combust Flame*, vol. 212, pp. 205–215, Feb. 2020, doi: 10.1016/j.combustflame.2019.10.029.
- [113] “Designation: D3418 – 12’112’1 Standard Test Method for Transition Temperatures and Enthalpies of Fusion and Crystallization of Polymers by Differential Scanning Calorimetry 1”, doi: 10.1520/D3418-12E01.
- [114] T. Nonoyama, Y. W. Lee, K. Ota, K. Fujioka, W. Hong, and J. P. Gong, “Instant Thermal Switching from Soft Hydrogel to Rigid Plastics Inspired by Thermophile Proteins,” *Advanced Materials*, vol. 32, no. 4, p. 1905878, Jan. 2020, doi: 10.1002/adma.201905878.
- [115] A. Meena, T. Parikh, S. Singh Gupta, and A. T. M. Serajuddin, “Investigation of thermal and viscoelastic properties of polymers relevant to hot melt extrusion-II: Cellulosic polymers.”
- [116] H. McPhillips, D. Q. M. Craig, P. G. Royall, and V. L. Hill, “Characterisation of the glass transition of HPMC using modulated temperature differential scanning calorimetry,” *Int J Pharm*, vol. 180, no. 1, pp. 83–90, Mar. 1999, doi: 10.1016/S0378-5173(98)00407-4.
- [117] A. Gómez-Carracedo, C. Alvarez-Lorenzo, J. L. Gómez-Amoza, and A. Concheiro, “Chemical structure and glass transition temperature of non-ionic cellulose ethers DSC, TMDSC®: Oscillatory rheometry study,” *J Therm Anal Calorim*, vol. 73, no. 2, pp. 587–596, 2003, doi: 10.1023/A:1025434314396/METRICS.

- [118] G. P. Simon *et al.*, “Molecular mobility of substituted poly(p-phenylenes) characterized by a range of polymer relaxation techniques,” *J Polym Sci B Polym Phys*, vol. 36, no. 9, pp. 1465–1481, Jul. 1998, doi: 10.1002/(SICI)1099-0488(19980715)36:9<1465::AID-POLB5>3.0.CO;2-J.
- [119] Altman D and Holzman A, “Overview and History of Hybrid Rocket Propulsion,” in *Fundamentals of Hybrid Rocket Combustion and Propulsion*, Reston ,VA: American Institute of Aeronautics and Astronautics, 2007, pp. 1–36. doi: 10.2514/5.9781600866876.0001.0036.
- [120] A. Mazzetti, L. Merotto, and G. Pinarello, “Paraffin-based hybrid rocket engines applications: A review and a market perspective,” *Acta Astronaut*, vol. 126, pp. 286–297, Sep. 2016, doi: 10.1016/j.actaastro.2016.04.036.
- [121] N. A. Davydenko, R. G. Gollender, A. M. Gubertov, V. V. Mironov, and N. N. Volkov, “Hybrid rocket engines: The benefits and prospects,” *Aerosp Sci Technol*, vol. 11, no. 1, pp. 55–60, Jan. 2007, doi: 10.1016/j.ast.2006.08.008.
- [122] *Fundamentals of Hybrid Rocket Combustion and Propulsion*. American Institute of Aeronautics and Astronautics, 2007. doi: 10.2514/4.866876.
- [123] H. NAGATA, “New Fuel Configurations for Advanced Hybrid Rockets,” *49th International Astronautical Congress, 1998-9*, vol. 116, no. 1134, pp. 323–326, 1998, doi: 10.1299/JSMEMAG.116.1134_323.
- [124] A. Sossi *et al.*, “Combustion of HTPB-Based Solid Fuels Loaded with Coated Nanoaluminum,” *Combustion Science and Technology*, vol. 185, no. 1, pp. 17–36, Jan. 2013, doi: 10.1080/00102202.2012.707261.
- [125] L. Galfetti, L. Merotto, M. Boiocchi, F. Maggi, and L. T. DeLuca, “Experimental investigation of paraffin-based fuels for hybrid rocket propulsion,” in *Progress in Propulsion Physics*, Les Ulis, France: EDP Sciences, Mar. 2013, pp. 59–74. doi: 10.1051/eucass/201304059.
- [126] S. C. Shark, T. L. Pourpoint, S. F. Son, and S. D. Heister, “Performance of Dicyclopentadiene/H₂O₂-Based Hybrid Rocket Motors with Metal Hydride Additives,” *J Propuls Power*, vol. 29, no. 5, pp. 1122–1129, Sep. 2013, doi: 10.2514/1.B34867.
- [127] J. H. Corpening, R. K. Palmer, S. D. Heister, and J. J. Rusek, “Combustion of advanced non-toxic hybrid propellants,” *International Journal of Alternative Propulsion*, vol. 1, no. 2/3, p. 154, 2007, doi: 10.1504/IJAP.2007.013018.
- [128] K. K. Kuo, G. A. Risha, B. J. Evans, and E. Boyer, “Potential Usage of Energetic Nano-sized Powders for Combustion and Rocket Propulsion,” *MRS Online Proceedings Library 2004 800:1*, vol. 800, no. 1, pp. 39–50, Jul. 2004, doi: 10.1557/PROC-800-AA1.1.
- [129] G. A. Risha, Risha, and G. Alexander, “Enhancement of hybrid rocket combustion performance using nano-sized energetic particles,” *PhDT*, 2003, Accessed: Jun. 28, 2023. [Online]. Available: <https://ui.adsabs.harvard.edu/abs/2003PhDT.....90R/abstract>
- [130] L. STRAND, R. RAY, F. ANDERSON, and N. COHEN, “Hybrid rocket fuel combustion and regression rate study,” in *28th Joint Propulsion Conference and Exhibit*, Reston, Virginia: American Institute of Aeronautics and Astronautics, Jul. 1992. doi: 10.2514/6.1992-3302.

- [131] S. Li and R. Jin, "Improvement of combustion characteristics of solid propellant with coated boron," in *35th Joint Propulsion Conference and Exhibit*, Reston, Virginia: American Institute of Aeronautics and Astronautics, Jun. 1999. doi: 10.2514/6.1999-2633.
- [132] I.-M. Shyu and T.-K. Liu, "Combustion characteristics of GAP-coated boron particles and the fuel-rich solid propellant," *Combust Flame*, vol. 100, no. 4, pp. 634–644, Mar. 1995, doi: 10.1016/0010-2180(94)00032-N.
- [133] K. Nagayama and Y. Oyumi, "Combustion Characteristics of High Burn Rate Azide Polymer Propellant," *Propellants, Explosives, Pyrotechnics*, vol. 21, no. 2, pp. 74–78, Apr. 1996, doi: 10.1002/prep.19960210205.
- [134] H. F. R. Schoeyer *et al.*, "High-performance propellants based on hydrazinium nitroformate," *J Propuls Power*, vol. 11, no. 4, pp. 856–869, Jul. 1995, doi: 10.2514/3.23911.
- [135] G. C. Harting, Harting, and G. C., "Pyrolysis and combustion of HTPB, GAP, and OXSOL for hybrid rocket motor applications," *PhDT*, pp. 9–10, 2000, Accessed: Jun. 28, 2023. [Online]. Available: <https://ui.adsabs.harvard.edu/abs/2000PhDT.....177H/abstract>
- [136] Brandenburg, "Ethanol based gel fuel for a hybrid rocket engine," May 2008.
- [137] D. Gramer, W. Knuth, E. Rice, and C. St. Clair, "Experimental investigation of a metallized cryogenic hybrid rocket engine," in *34th AIAA/ASME/SAE/ASEE Joint Propulsion Conference and Exhibit*, Reston, Virginia: American Institute of Aeronautics and Astronautics, Jul. 1998. doi: 10.2514/6.1998-3509.
- [138] C. Larson, K. Pfeil, M. DeRose, and P. Garrick, "High pressure combustion of cryogenic solid fuels for hybrid rockets," in *32nd Joint Propulsion Conference and Exhibit*, Reston, Virginia: American Institute of Aeronautics and Astronautics, Jul. 1996. doi: 10.2514/6.1996-2594.
- [139] C. Larson *et al.*, "Tube burner studies of cryogenic solid combustion," in *33rd Joint Propulsion Conference and Exhibit*, Reston, Virginia: American Institute of Aeronautics and Astronautics, Jul. 1997. doi: 10.2514/6.1997-3076.
- [140] M. A. Karabeyoglu, D. Altman, and B. J. Cantwell, "Combustion of Liquefying Hybrid Propellants: Part 1, General Theory," *J Propuls Power*, vol. 18, no. 3, pp. 610–620, May 2002, doi: 10.2514/2.5975.
- [141] A. Karabeyoglu, G. Zilliac, B. J. Cantwell, S. DeZilwa, and P. Castellucci, "Scale-Up Tests of High Regression Rate Paraffin-Based Hybrid Rocket Fuels," *J Propuls Power*, vol. 20, no. 6, pp. 1037–1045, Nov. 2004, doi: 10.2514/1.3340.
- [142] P. ESTEY and B. HUGHES, "The opportunity for hybrid rocket motors in commercial space," in *28th Joint Propulsion Conference and Exhibit*, Reston, Virginia: American Institute of Aeronautics and Astronautics, Jul. 1992. doi: 10.2514/6.1992-3431.
- [143] R. F. McALEVY and J. G. HANSEL, "Linear pyrolysis of thermoplastics in chemically reactive environments," *AIAA Journal*, vol. 3, no. 2, pp. 244–249, Feb. 1965, doi: 10.2514/3.2837.
- [144] J.-T. Cheng, N. W. Ryan, and A. D. Baer, "Oxidative decomposition of PBAA polymer at high heating rates," *Symposium (International) on Combustion*, vol. 12, no. 1, pp. 525–532, Jan. 1969, doi: 10.1016/S0082-0784(69)80434-0.

- [145] K. N. Ninan, K. Krishnan, R. Rajeev, and G. Viswanathan, “Thermoanalytical Investigations on the Effect of Atmospheric Oxygen on HTPB resin,” *Propellants, Explosives, Pyrotechnics*, vol. 21, no. 4, pp. 199–202, Aug. 1996, doi: 10.1002/prop.19960210408.
- [146] W. H. Beck, “Pyrolysis studies of polymeric materials used as binders in composite propellants: A review,” *Combust Flame*, vol. 70, no. 2, pp. 171–190, Nov. 1987, doi: 10.1016/0010-2180(87)90077-0.
- [147] V. K. Dubey, S. N. Mahottamananda, A. A. Khaleel, P. N. Kadiresh, and M. Thirumurugan, “Mechanical Characteristics of Paraffin Wax, Beeswax and HTPB as Rocket Propellant—A Comparative Study,” *Lecture Notes in Mechanical Engineering*, pp. 243–252, 2021, doi: 10.1007/978-981-33-6428-8_18/COVER.
- [148] S. C. Shark, C. R. Zaseck, T. L. Pourpoint, and S. F. Son, “Solid-Fuel Regression Rates and Flame Characteristics in an Opposed Flow Burner,” *J Propuls Power*, vol. 30, no. 6, pp. 1675–1682, Nov. 2014, doi: 10.2514/1.B35249.
- [149] S. A. Hashim, S. M. Kangle, S. Karmakar, and A. Roy, “Screening of Nano-Aluminum Based Solid Fuels for Hybrid Rocket Applications,” in *2018 AIAA Aerospace Sciences Meeting*, Reston, Virginia: American Institute of Aeronautics and Astronautics, Jan. 2018. doi: 10.2514/6.2018-0669.
- [150] D. S. Sundaram, V. Yang, and V. E. Zarko, “Combustion of nano aluminum particles (Review),” *Combust Explos Shock Waves*, vol. 51, no. 2, pp. 173–196, Mar. 2015, doi: 10.1134/S0010508215020045.
- [151] J. C. Thomas, E. L. Petersen, J. D. Desain, and B. Brady, “Hybrid Rocket Enhancement by Micro- and Nano-Scale Additives in HTPB Fuel Grains,” American Institute of Aeronautics and Astronautics (AIAA), Jul. 2015. doi: 10.2514/6.2015-4041.
- [152] V. A. Alvarez and A. Vázquez, “Thermal degradation of cellulose derivatives/starch blends and sisal fibre biocomposites,” *Polym Degrad Stab*, vol. 84, no. 1, pp. 13–21, Apr. 2004, doi: 10.1016/j.polymdegradstab.2003.09.003.
- [153] H. Schlichting and K. Gersten, “Boundary-Layer Theory,” *Boundary-Layer Theory*, pp. 1–799, Oct. 2016, doi: 10.1007/978-3-662-52919-5/COVER.
- [154] M. J. Chiaverini *et al.*, “Pyrolysis Behavior of Hybrid-Rocket Solid Fuels Under Rapid Heating Conditions,” *J Propuls Power*, vol. 15, no. 6, pp. 888–895, Nov. 1999, doi: 10.2514/2.5512.